Stellar population in the Magellanic Clouds: Star formation and evolution in diverse environments

A thesis
submitted for the degree of

Doctor of Philosophy

in

The Department of Physics,
Pondicherry University,
Puducherry - 605 014, India

by

Dhanush S.R
Indian Institute of Astrophysics,
Bangalore - 560 034, India

June 2025

Stellar population in the Magellanic Clouds: Star formation and evolution in diverse environments

Dhanush S.R
Indian Institute of Astrophysics

Indian Institute of Astrophysics
Bangalore - 560 034, India

Title of the thesis	:	**Stellar population in the Magellanic Clouds: Star formation and evolution in diverse environments**
Name of the author	:	**Dhanush S.R**
Address	:	Indian Institute of Astrophysics II Block, Koramangala Bangalore - 560 034, India
Email	:	dhanush.sr@iiap.res.in
Name of the supervisor	:	**Prof. Annapurni Subramaniam**
Address	:	Indian Institute of Astrophysics II Block, Koramangala Bangalore - 560 034, India
Email	:	purni@iiap.res.in

Declaration of Authorship

I hereby declare that the matter contained in this thesis is the result of the investigations carried out by me at the Indian Institute of Astrophysics, Bangalore, under the supervision of Prof. Annapurni Subramaniam. This work has not been submitted for the award of any other degree, diploma, associateship, fellowship, etc., of any other university or institute.

Signed:

Date: 11-11-2025

Certificate

This is to certify that the thesis entitled **'Stellar population in the Magellanic Clouds: Star formation and evolution in diverse environments'** submitted to Pondicherry University by Mr. Dhanush S.R for the award of the degree of Doctor of Philosophy is based on the results of the investigations carried out by him under my supervision and guidance, at the Indian Institute of Astrophysics. This thesis has not been submitted for the award of any other degree, diploma, associateship, fellowship, etc., of any other university or institute.

Signed:

Date: 11-11-2025

List of Publications

1. **Dhanush, S. R.**; Subramaniam, A.; Nayak, Prasanta K.; Subramanian, S., 2024, "Spatiotemporal map of star clusters in the Magellanic Clouds using *Gaia*: synchronized peaks and radial shrinkage of cluster formation", *Monthly Notices of the Royal Astronomical Society*, 528, 2
2. **Dhanush, S. R.**; Subramaniam, A.; Subramanian, S., 2024, "A Comprehensive Kinematic Model of the Large Magellanic Cloud Disk from Star Clusters and Field Stars using *Gaia* DR3: Tracing the Disk Characteristics, Rotation, Bar, and Outliers", *The Astrophysical Journal*, 968, 2
3. **Dhanush, S. R.**; Subramaniam, A.; Subramanian, S., 2025, "Unraveling the Kinematic and Morphological Evolution of the Small Magellanic Cloud ", *The Astrophysical Journal*, 980, 1
4. Hota, Sipra; Subramaniam, A.; **Dhanush, S. R.**; Cioni, Maria-Rosa L.; Subramanian, S., 2024, "UVIT Study of the Magellanic Clouds (U-SMAC) - I. Recent star formation history and kinematics of the Shell region in the north-eastern Small Magellanic Cloud ", *Monthly Notices of the Royal Astronomical Society*, 532, 1
5. Harsha, K H; Subramaniam, A.; **Dhanush, S. R.**; Cioni, Hariharan, DS, 2025, "A kinematic and structural study of young open clusters in the Milky Way Galaxy using Gaia DR3 catalogue ", *Journal of Astrophysics and Astronomy, under review*

Presentations

1. Presented a poster titled "**How do galaxy interactions impact cluster formation? – A case study using the Magellanic Clouds**" in *National conference Astronomical Society of India (ASI) 2022*, IIT Roorkee, India.

2. Presented a talk titled "**Spatio-temporal formation of star clusters in the Magellanic Clouds: age trend in cluster formation and LMC bar**" in *National conference Astronomical Society of India (ASI) 2023*, IIT Indore, India.

3. Presented a poster titled "**Spatio-temporal map of star clusters in the Magellanic Clouds using Gaia: Correlated peaks and shrinkage of cluster formation**" at *International Astronomical Union (IAU) 2023, IAUS379: Dynamical Masses of Local Group Galaxies*, Telegrafenberg, Germany.

4. Presented a poster titled "**Tracing the kinematic response of LMC to the recent SMC interaction: A case study with clusters and nearby field using Gaia DR3**" in *National conference Astronomical Society of India (ASI) 2024*, IISc Bengaluru, India.

5. Presented a poster titled "**Tracing the change in structure and kinematics of the Small Magellanic Clouds due to interactions**" in *National conference Astronomical Society of India (ASI) 2025*, NIT Rourkela, India.

6. Presented a talk titled "**Investigating the Kinematics of the SMC using Gaia DR3** " remotely at the conference *XMC II: Clouds over Yellowstone 2025*, Bozeman, Montana, United States.

Acknowledgements

I would like to sincerely acknowledge and express my heartfelt gratitude and regards to my supervisor, Prof. Annapurni Subramaniam, of the Indian Institute of Astrophysics (IIA), Bangalore, for her invaluable guidance, support, and encouragement throughout my PhD journey. It has been an immense privilege to work under her guidance, as she inspired me to work harder and provided essential academic direction for this thesis. I extend my sincere gratitude to my collaborators Assoc. Prof. Smitha Subramanian and Dr. Prasanta Nayak , for their assistance at every phase of my research.

I am grateful to the Director, Dean, and the Board of Graduate Studies (BGS) for providing me with the opportunity to work at this institute and for the resources needed for my research. I would also like to extend my sincere thanks to my Doctoral committee members, Prof. Sudhanshu Barway and Prof. V. V. Ravi Kanth Kumar, for their constant support and valuable suggestions. I also thank IIA for providing me with their facilities. I am very grateful to Ashok, Fayaz, and other 'Data Center' staff for their time-to-time technical support in computer and internet-related matters and to the administration of the University of Pondicherry for their support during my various research phases. I thank the IIA Administrative Officer, the Personnel Officer, the Account Officers, and all other Administrative staff for their timely assistance in the administrative work.

I extend my heartfelt thanks to the Bhaskara staff for their care and attention, especially Chandrashekhar, Manju, Vimal, and Lakshmi, for their immense support during the Covid times. I deeply appreciate their efforts to make hostel life feel like home.

I am extremely grateful to be a part of an excellent and supportive research group and appreciate the numerous valuable discussions that have happened during our

weekly meetings. I would like to thank my groupmates, Chayan Mondal, Prasanta Nayak, Gaurav Singh, Deepthi S. Prabhu, Vikrant Jadhav, Sipra Hota, Anju Panthi for their support and the productive discussions we had during my PhD journey. Their contributions have been invaluable and greatly appreciated.

I am thankful to my fellow batchmates Aratrika, Rishab, Ravi, and Anohita for their support during the initial phases of my PhD. I sincerely appreciate the company of my close friends, Athira, Amrutha, Bharat, Manjunath, and Sonith, for making my PhD life full of cherishable memories. They have always been a great source of inspiration to me, and I have learned so much from them. And I want to convey thanks to seniors as well as juniors for making my stay enjoyable and memorable at Bhaskara.

I am indebted to my parents, my sister and brother-in-law for their constant support and belief in me throughout this journey; without their love and blessings, it would not have been possible. Finally, I would take this opportunity to thank the Almighty for being with me every step of the way during this wonderful journey.

With this, I look forward to an exciting and joyful journey ahead of my PhD.

Dhanush

Data and software usage

I have made use of space-based telescope data for the study presented in this thesis. I gratefully acknowledge the use of this dataset and extend my sincere thanks to the members and affiliates of the facility for providing the data.

In this thesis work, we used the *Gaia* (Global Astrometric Interferometer for Astrophysics) Data Release 3 (DR3) catalog, which is obtained from the European Space Agency (ESA) mission *Gaia* (`https://www.cosmos.esa.int/gaia`) and processed by the *Gaia* Data Processing and Analysis Consortium (DPAC, `https://www.cosmos.esa.int/web/gaia/dpac/consortium`). Funding for the DPAC has been provided by national institutions, in particular, the institutions participating in the *Gaia* Multilateral Agreement.

We have used the `astroquery` package (Ginsburg et al. 2019) to access the *Gaia* asynchronous query service and retrieve archived *Gaia* data for our study. This work also made use of `astropy` (Astropy Collaboration et al. 2013), TOPCAT (Taylor 2011), `scipy` (Virtanen et al. 2020), `matplotlib` (Hunter 2007), `kalepy` (Kelley 2021), `numpy` (Harris et al. 2020), `numba` (Lam et al. 2015), `corner` (Foreman-Mackey 2017).

Dedicated to

my

family

Abstract

The Magellanic Clouds (MCs) are the closest interacting satellite dwarf galaxies of the Milky Way (MW). The Magellanic system comprises the Large Magellanic Cloud (LMC) and the Small Magellanic Cloud (SMC), which are connected by the Magellanic Bridge, a structure composed of gas and stars. The recent proper motion (PM) studies of the MCs suggest that they are interacting not only with each other but also with the MW. The interactions experienced by the MCs have also produced a prominent tail of neutral hydrogen gas, known as the Magellanic Stream, which stretches across $\sim 200^{\circ}$ of the southern sky. In addition, filamentary leading arms extend ahead of the Clouds' motion, arching over the MW disk. Interactions between the MCs trigger star formation and impact the internal kinematics of both galaxies. Therefore, studying the stellar populations residing within these galaxies is essential to unraveling their evolution and interaction history.

Star clusters serve as valuable tracers for unraveling the star formation history of galaxies. In the MCs, over 4000 clusters have been cataloged. Determining their ages provides insights into the cluster formation history (CFH) of the MCs. However, a comprehensive age estimation from the center to the outskirts of the LMC and SMC is still lacking. Such global age dating is essential for identifying the episodes of enhanced star/ cluster formation (CF) triggered by the LMC-SMC interactions. Also, modeling the internal kinematics of the LMC and SMC is crucial for revealing the disk response of the MCs to their mutual interaction. The goal of this thesis is to trace the CFH and model the kinematics of the MCs to gain insights into their interaction history. The analysis in our studies is based entirely on *Gaia* (Global Astrometric Interferometer for Astrophysics) Data Release 3 (DR3) data sets.

In this study, we present a detailed view of CF to trace the evolution and interaction history of the MCs in the last 3.5 Gyr. We parameterized 1710 and 280 star clusters in the LMC and the SMC, where 847 and 113 clusters are newly characterized in the outer LMC and SMC, respectively. We estimated the age-extinction-metallicity-distance parameters using an automated fitting of the color-magnitude diagram (CMD) after field star removal, followed by a Markov Chain Monte Carlo (MCMC) technique. We report a first-time detection of two synchronized CF peaks in the MCs at 1.5±0.12 Gyr and 800±60 Myr. We recommend that the choice of the metallicity (Z) values of isochrones for clusters with age $\leq$ 1 - 2 Gyr are $\mathrm{Z_{LMC}}$ = 0.004 - 0.008 and $\mathrm{Z_{SMC}}$ = 0.0016 - 0.004 for the LMC and SMC, respectively. We found evidence for spiral arms in the LMC, as traced by the cluster count profiles over the last 3.5 Gyr. The density maps provide evidence of ram-pressure stripping in the North-East of the LMC, a severe truncation of CF in the South of the LMC, and a radial shrinkage of CF in the SMC in the last 450 Myr. The last SMC-LMC interaction ($\sim$ 150 Myr) resulted in a substantial CF in the North and Eastern SMC, with a marginal impact on the LMC. This study brings out the CF episodes in the MCs and their connection to the LMC-SMC-MW interactions.

The internal kinematics of the LMC disk have been modeled by several studies using different tracers with varying coverage, resulting in a range of parameters. In this study, we modeled the LMC disk using 1705 star clusters and field stars, based on a robust MCMC method. The dependency of model parameters on the age, coverage, and strength of the clusters are also presented. This is the first comprehensive 2D kinematic study using star clusters. Red clump (RC) stars and young main-sequence stars are also modeled for comparison. The clusters and field stars are found to have distinctly different kinematic centers, disk inclination, position angle of the line of nodes, and scale radius. We also note a significant radial variation of the disk parameters. Clusters and young stars are found to have a large residual PM and a relatively large velocity dispersion when compared to the RC field population, which could be due to perturbation from the bar and spiral arms. We traced the presence of

large residual PM and non-circular motion among clusters likely to be due to the bar and detected a decrease in the scale radius as a result of the possible evolution of the bar. The kinematically deviant clusters point to a spatio-temporal disturbance in the LMC disk, matching the expected impact parameter and time of the recent collision between the LMC and the SMC.

Similar to the LMC, we modeled the kinematics of the SMC by analyzing the PM from nine different stellar populations, which include young main sequence stars ($<$ 2 Gyr), RGB stars, RC stars, red giants with line-of-sight (LOS) velocities, and three groups of star clusters. We trace the evolution from a non-rotating flattened elliptical system as mapped by the old population to a rotating highly stretched disk structure as denoted by the young main sequence stars and clusters ($<$ 400 Myr). We estimated that the inclination, i ($\sim$ 58° to 82°) decreases and the position angle, Θ ($\sim$ 180° to 240°) increases with age. We estimated an asymptotic velocity of $\sim$ 49 - 89 km s^{-1} with scale-radius of $\sim$ 6 - 9 kpc for the young main sequence populations with velocity dispersion of $\sim$ 11 km s^{-1}, suggesting a rotation-supported disk structure. Our models estimate a LOS extension of $\sim$ 30 kpc, in agreement with observations. We identified four regions of the SMC showing anomalies in the residual PM, the East Anomaly (EA), South East Anomaly (SEA), South Anomaly (SA), and West Anomaly (WA). The SEA appears like an infalling feature and is identified for the first time. The tidal imprints observed in the residual PM of the SMC suggest that the recent interaction with the LMC considerably shapes its evolution.

Contents

List of Figures

List of Tables

Abbreviations

2MASS	**T**wo **M**icron **A**ll **S**ky **S**urvey
APOGEE	**A**pache **P**oint **O**bservatory **G**alactic **E**volution **E**xperiment
ATCS	**A**ustralia **T**elescope **C**ompact **A**rray
CCD	**C**harge **C**oupled **D**evice
CF	**C**luster **F**ormation
CFH	**C**luster **F**ormation **H**istory
CMD	**C**olor **M**agnitude **D**iagram
COM	**C**enter **O**f **M**ass
DBSCAN	**D**ensity **B**ased **S**patial **C**lustering of **A**pplications with **N**oise
DECam	**D**ark **E**nergy **C**amera
DM	**D**istance **M**odulus
DPAC	**D**ata **P**rocessing and **A**nalysis **C**onsortium
DSS	**D**igitized **S**ky **S**urvey
EA	**E**ast **A**nomaly
ECF	**E**pisodic **C**luster **F**ormation
ESA	**E**uropean **S**pace **A**gency
ESO	**E**uropean **S**outhern **O**bservatory
FLAMES	**F**ibre **L**arge **A**rray **M**ulti **E**lement **S**pectrograph
FSD	**F**ield **S**tar **D**econtamination
Gaia	**G**lobal **A**strometric **I**nterferometer for **A**strophysics

GC	**G**lobular **C**luster
GASS	**G**alactic **A**ll **S**ky **S**urvey
HDBSCAN	**H**ierarchical **D**ensity **B**ased **S**patial **C**lustering of **A**pplications with **N**oise
H-R	**H**ertzsprung - **R**ussell
HST	**H**ubble **S**pace **T**elescope
IMF	**I**nitial **M**ass **F**unction
JWST	**J**ames **W**ebb **S**pace **T**elescope
LA	**L**eading **A**rms
LMC	**L**arge **M**agellanic **C**loud
LOS	**L**ine **O**f **S**ight
MC	**M**agellanic **C**loud
MCMC	**M**arkov **C**hain **M**onte **C**arlo
MCPS	**M**agellanic **C**louds **P**hotometric **S**urvey
MS	**M**ain **S**equence
MW	**M**ilky **W**ay
OC	**O**pen **C**luster
OGLE	**O**ptical **G**ravitational **L**ensing **E**xperiment
PARSEC	**PA**dova and t**R**ieste **S**tellar **E**volutionary **C**ode
PHANGS	**P**hysics at **H**igh **A**ngular resolution in **N**earby **G**alaxie**S**
PM	**P**roper **M**otion
RC	**R**ed **C**lump
RGB	**R**ed **G**iant **B**ranch
SA	**S**outh **A**nomaly
SEA	**S**outh **E**ast **A**nomaly
SEHO	**S**outh**E**ast **HI** **O**verdensity
SFH	**S**tar **F**ormation **H**istory
SMASH	**S**urvey of the **MA**gellanic **S**tellar **H**istory
SMC	**S**mall **M**agellanic **C**loud

VISCACHA	**VI**sible **S**oar photometry of star **C**lusters in t**A**pii and **C**oxi **H**ugu**A**
VISTA	**V**isible and **I**nfrared **S**urvey **T**elescope for **A**stronomy
WA	**W**est **A**nomaly

Chapter 1

Introduction

1.1 The Magellanic system

Galaxy interactions are among the most interesting phenomena that occur in our universe. These interactions impact the galaxy's morphology, dynamics, and star formation rates during their evolution. Such gravitationally interacting galaxies often leave evidence such as tidal tails, bridges, enhanced bars, and bursts of star formation, with some interactions eventually resulting in mergers. Interacting galaxies are plenty in our universe with most of them located far away. Detailed studies of such systems are however feasible only for those close to our Galaxy. Fortunately, our Galactic neighborhood has a pair of interacting galaxies, the Magellanic Clouds (MCs), which include the Large Magellanic Cloud (LMC) and the Small Magellanic Cloud (SMC), which serve as a test-bed for galaxy interactions. These galaxies are visible to the naked eye in the southern hemisphere. Studying the MCs will deepen our understanding of galaxy interactions in general. Also,

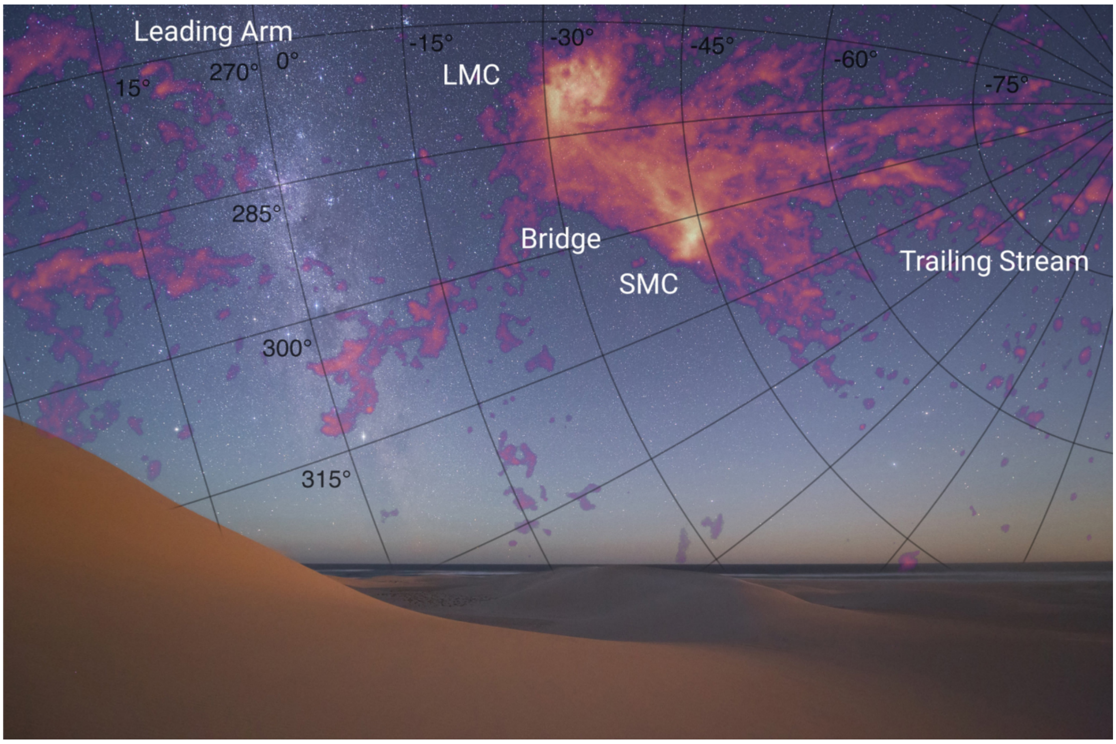

FIGURE 1.1: The Magellanic system is shown superimposed on a photograph captured by Colin Legg in Australia. Purple and orange overlays highlight the HI emission across the system. Prominent features such as the Leading Arm, the Bridge, and the Trailing Stream are distinctly marked. (credits: Colin Legg, Lucchini 2024)

the MCs can be used as a good template to understand similar galaxy systems far from the Milky Way (MW).

The Magellanic system, depicted in Figure 1.1, includes the LMC and SMC, prominent features such as the Magellanic Bridge, the Magellanic Stream, and the Leading Arms (LA). The LMC lies at a distance of ∼ 49.59±0.09 kpc, while the SMC is located farther away at ∼ 62.44±0.47 kpc (Pietrzyński et al. 2019; Graczyk et al. 2020).The Magellanic Stream appears as a trail of neutral hydrogen extending over more than 100° across the sky (Putman et al. 2003). The Magellanic Bridge is composed of gas and stars, which appear as an elongated structure, seemingly connecting the MCs (Gardiner et al. 1994; Muller & Bekki 2007; Jacyszyn-Dobrzeniecka et al. 2020). The LA, devoid of a stellar component (Putman et al. 1998; Nidever et al. 2008), are characterized by multiple filaments and are seen in front of the galaxy pair, arching across the MW's disk. All three structures result from repeated interactions between the MCs themselves and their interactions with the MW.

1.2 Morphology of the Clouds

(a) (b)

FIGURE 1.2: The optical images of the LMC (panel a) and the SMC (panel b) are shown here. (credits: Carlos Fairbairn, José Mtanous)

The LMC exhibits a disk structure along with an asymmetric stellar bar that is displaced from the isophotal center of the disk and is not evident in the galaxy's interstellar medium (van der Marel 2001; Subramaniam & Subramanian 2009; Besla et al. 2012; Rathore et al. 2025). Zaritsky (2004) suggested that the apparent levitation of the LMC's bar could be explained by the viewing perspective of a three-dimensional, elongated central stellar bulge partially hidden by a thick disk. The LMC is found to have a flared disk with a non-axisymmetric spiral structure (van der Marel et al. 2002, hereafter V02; Ripepi et al. 2022), with the presence of a star-forming complex at the end of the bar (de Vaucouleurs & Freeman 1972a). The disk of the LMC is warped, and its bar is found to be inclined relative to the plane of the galaxy (Subramaniam 2003; Choi et al. 2018; Choi et al. 2022, hereafter C22). The spatial distribution of red clump (RC) stars revealed that the disk of the LMC has a warp, predominantly in the outer southwestern regions

(Saroon & Subramanian 2022, hereafter S22). Over time, several studies estimated the LMC disk's viewing angles, with the inclination found ranging between ∼ 24° to 40° and the position angle of the line of nodes ranging between ∼ 125° and 160° (van der Marel & Kallivayalil 2014, hereafter V14; Wan et al. 2020, hereafter W20; Gaia Collaboration et al. 2021, hereafter G21; Niederhofer et al. 2022, hereafter N22). Studies by Saha et al. (2010) and Carrera et al. (2011) on the outer regions of the LMC suggest that the galaxy has an extended disk with no evidence of a halo.

The SMC, in comparison to the LMC, possesses a less pronounced bar. It features an eastern extension, known as the Wing, which was initially considered a separate structure projected in front of the SMC main body toward the northeast (Gardiner & Hawkins 1991). Traditionally, the SMC has been regarded as a 3D spheroidal or ellipsoidal system, with its structure primarily shaped by intrinsic hydrodynamic processes rather than by tidal interactions (Zaritsky et al. 2000). According to Cioni et al. (2000), younger stars in the SMC display an irregular structure characterized by tidal features. In contrast, the studies on the older population indicate that they are being distributed in a spherical or ellipsoidal manner (Subramanian & Subramaniam 2011, hereafter S12; Deb et al. 2015; Rubele et al. 2018, hereafter R18; El Youssoufi et al. 2019, hereafter Y19). Studies by Haschke et al. (2012), Subramanian & Subramaniam (2015, hereafter S15), and Di Teodoro et al. (2018, hereafter D18) suggest that the SMC can have a disk morphology as well. Deb et al. (2019) found that the northeastern region of the SMC bar is located nearer to us compared to the southwestern part. The estimated line-of-sight (LOS) depth of the SMC is found to be greater than that of the LMC and reaches more than ∼ 20 kpcs (S12; Jacyszyn-Dobrzeniecka et al. 2016, hereafter J16; Jacyszyn-Dobrzeniecka et al. 2017; Ripepi et al. 2017, hereafter R17; Muraveva et al. 2017).

1.3 Stellar population in the Clouds

Stellar populations in our Galaxy are classified based on their age and metallicity. Baade (1944) introduced the classification of Population I and Population II stars in our Galaxy. Population I stars are younger, metal-rich stars primarily located in the Galactic disk. These stars are relatively young, with ages ranging from a few million to a few billion years, and encompass a broad mass spectrum from low-mass to high-mass stars. The Sun is an example of a Population I star. Since they form from interstellar material enriched by previous generations of stars, they have a higher metallicity. Population I stars are spread across the Galactic disk, especially in regions of active star formation, including open clusters and star-forming nebulae. In contrast, Population II stars are older and metal-poor, predominantly found in the Galactic halo, bulge, and globular clusters. Globular clusters often have ages exceeding 10 billion years, making them important tracers of the Galaxy's early star formation.

The above definitions of the populations are valid only for our Galaxy and differ for the MCs. The MCs host both Population I & II stars, exhibit active star formation and are largely dominated by intermediate-age stellar populations (Milone et al. 2009; Subramanian & Subramaniam 2013). The MCs are located at high galactic latitudes, where the impact of Galactic reddening is relatively small (Zaritsky et al. 2004; Subramaniam 2005; Skowron et al. 2021), making their stellar populations excellent tracers for studying the properties of the Clouds. These stellar populations are generally metal-poor, but they exhibit a radial metallicity gradient, with metallicity decreasing toward the outskirts (Choudhury et al. 2016, 2018). The diverse range of ages of stars present in the MCs helps us understand the formation of interacting galaxies in general. The different stellar populations we used in our studies are introduced in the following sections.

1.3.1 Main sequence stars

Stars form within molecular clouds of gas and dust in the interstellar medium. Disturbances in these clouds cause them to collapse under gravity, breaking into dense clumps. As these clumps collapse under gravity, the internal pressure increases, raising the core temperature and leading to the formation of a rotating, dense region of hot gas called a protostar (Prialnik 2009). The protostar continues to gather material from the surrounding molecular cloud, growing in mass and evolving into a pre-main-sequence star as it approaches its final stellar mass. The evolutionary path of a star from the protostar depends on its mass, with low-mass and high-mass stars following different evolutionary processes (de Boer & Seggewiss 2008).

A protostar with a mass ranging from $\sim$ 0.08 M$\odot$ to 100 M$\odot$ initiates nuclear fusion once its core temperature reaches nearly 10 million kelvin. This process leads to hydrostatic equilibrium, where the outward pressure from heated gas balances the force of gravity. Once stabilized, the star enters the main sequence (MS) (Kippenhahn & Weigert 1990). Massive, hot O-type stars burn through their nuclear fuel quickly and leave the MS in just a few million years. In contrast, medium-sized stars like the Sun, classified as yellow dwarfs, spend around 10 billion years on the MS.

1.3.2 Red Giants and Red Clumps

Red giants represent a critical phase in stellar evolution when stars have exhausted their core hydrogen (Kippenhahn et al. 2013). As nuclear fusion shifts to a shell around the inert helium core, the star's envelope expands dramatically while its surface temperature decreases. This process results in a significant increase in

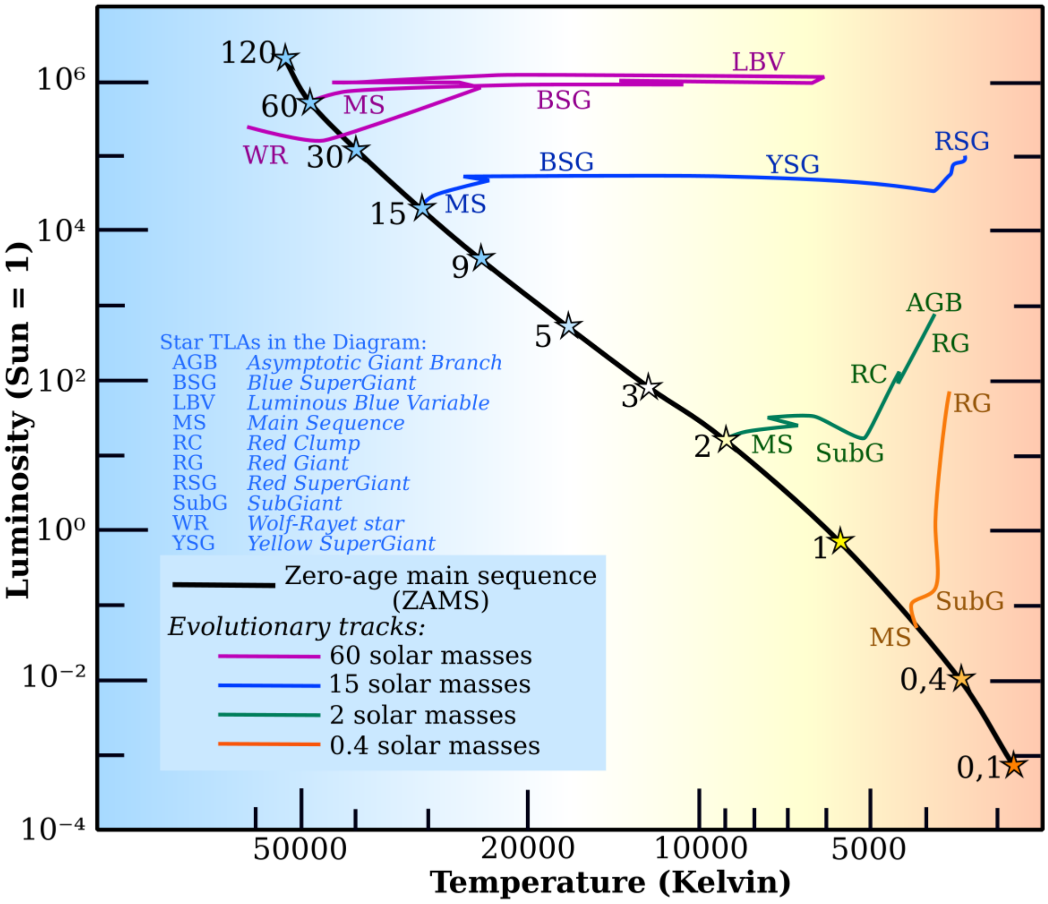

FIGURE 1.3: Evolutionary tracks of single stars with masses ranging from 0.5 to 60 $M_\odot$, highlighting the various phases of stellar evolution. (Credits: G.A.S, Rursus)

luminosity and radius, sometimes reaching hundreds of solar radii. The transition occurs as stars move horizontally across the HR diagram before ascending the red giant branch. For stars with masses ≤ 2 $M_\odot$, the helium core becomes electron-degenerate, leading to unique evolutionary characteristics (Iben 1991). The giant branch phase provides crucial insights into stellar aging processes and galactic chemical evolution.

Red Clump (RC) stars are core helium-burning stars that serve as excellent standard candles for distance measurements (Girardi 2016). They represent a more metal-rich population compared to horizontal branch stars, with masses typically ranging from 1-2.5 $M_\odot$ in the MCs. Their key characteristic is their nearly constant luminosity, which remains relatively independent of mass and age for populations between 2-9 Gyr old (Salaris & Girardi 2002). This property, combined with their well-defined color and magnitude in the color-magnitude diagram (CMD), particularly in I-band, make them invaluable for studying galactic structure (Stanek & Garnavich 1998). However, their use requires careful consideration of population effects, as their properties can be influenced by variations in metallicity and star formation history (SFH) across different galactic regions (Girardi & Salaris 2001).

1.4 Star clusters

Star clusters are gravitationally bound groups of stars that form from the same molecular cloud (Archinal & Hynes 2003). They typically have diameters ranging from a few parsecs to a few tens of parsecs, which is relatively small compared to their distances from Earth, often exceeding 100 parsecs. Stars within a cluster are positioned at nearly the same distance, causing them to experience similar interstellar absorption and reddening. This enables the accurate determination of each star's key properties, such as luminosity and effective temperature. Furthermore, they provide an ideal setting for studying stellar evolution and evaluating theoretical evolutionary models (Subramaniam et al. 1995; Subramaniam & Sagar 1999; Kalirai & Richer 2010). Star clusters are generally divided into two main categories: open clusters (OCs) and globular clusters (GCs).

OCs are typically young, loosely bound systems found in the Galactic disk. A series of studies utilizing *Gaia* data have significantly advanced our understanding of OCs and Galactic structure. Cantat-Gaudin et al. (2018) characterized 1229 OCs, revealing structural trends and improving membership assignment using *Gaia* DR2 astrometry. Building on this, Cantat-Gaudin et al. (2020) derived ages, distances, and extinctions for 1867 clusters by combining *Gaia* data with APOGEE metallicities, revealing age gradients, Galactic warp signatures, and a lack of old clusters in the inner disk. Castro-Ginard et al. (2020) discovered 582 new OCs using DBSCAN and a CMD-trained neural network, expanding the known population near the plane and Solar neighborhood. These works demonstrated the synergy of *Gaia* and machine learning in OC discovery. Further refinement came from Hunt & Reffert (2021), which used HDBSCAN to identify and classify OCs, detecting 41 new candidates. Hunt & Reffert (2023) extended this with *Gaia* DR3 to produce an all-sky catalog of 7167 clusters, including 2387 new detections and fundamental parameters. Most recently, Hunt & Reffert (2024) estimated photometric masses and Jacobi radii for over 6900 clusters, finding that only $\sim 79\%$ are gravitationally bound.

There are several other surveys beyond *Gaia* which analyzed the Galactic star clusters. The APOGEE survey provides precise radial velocities and chemical abundances for cluster members, aiding chemical tagging and internal dynamics studies (Donor et al. 2020; Myers et al. 2022). Hubble Space Telescope (HST) observations have yielded high-resolution star cluster catalogs in nearby galaxies like M83 and NGC 628, helping to constrain cluster age distributions and mass functions (Silva-Villa et al. 2014; Whitmore et al. 2021, hereafter W21). The PHANGS–HST project combines optical imaging with CO and HI data to link cluster properties with their natal environments (W21; Lee et al. 2022). The study by Pontoppidan et al. (2022) with JWST observations revealed infrared views of embedded clusters previously obscured in dust. In external galaxies, the PHANGS–HST survey compares human and machine classification across thousands of star cluster candidates, revealing not only biases in classification methods but also the importance of training data and morphological priors (W21).

GCs are older, more massive, and reside in the bulge and halo. GCs are used to trace the early epochs of galaxy formation. Their compact nature, along with their metallicities, kinematics, and spatial distributions, provides valuable insights into the formation and assembly history of their host galaxies. Studies suggest a dual formation pathway for GCs: some formed in situ in massive early starbursts, while others were accreted during hierarchical merging events (Kruijssen et al. 2015; Forbes et al. 2018; Massari et al. 2019). Observationally, surveys such as HST, APOGEE, and *Gaia* have revealed substructure in the GC system of the MW, including evidence for the accretion of entire GC systems from dwarf galaxies like the Sagittarius and Gaia-Enceladus progenitors (Myeong et al. 2019; Vasiliev 2019). Beyond the MW, deep imaging of GC systems in nearby galaxies like M31, M87, and Centaurus A demonstrates similar patterns, reinforcing the idea that GCs are powerful tracers of the hierarchical nature of galaxy assembly (Peng et al. 2006; Harris 2010; Usher et al. 2024).

Ultimately, the study of both open and globular clusters bridges the scales between individual star formation and galaxy evolution. Clusters provide benchmarks for stellar evolution, initial mass function (IMF) variations, feedback processes, and the role of environment in regulating star formation (Krumholz et al. 2019; Kuhn et al. 2019). Increasingly, the new sky surveys, and machine learning tools is unlocking the full potential of star clusters as chronological markers of galaxy evolution. From the local Universe to high redshifts, these stellar systems are emerging as vital probes of galaxy structure and their evolution.

1.4.1 Star clusters in the MCs

The star clusters in the MCs display a remarkably diverse and nearly continuous age distribution, spanning from very young stellar associations ($\leq$ 10 Myr) to old GCs that are older than 10 billion years. In contrast to the MW, which lacks a substantial population of intermediate-age clusters (1–10 Gyr), both MCs host a significant number of such systems, providing a more complete age sequence.

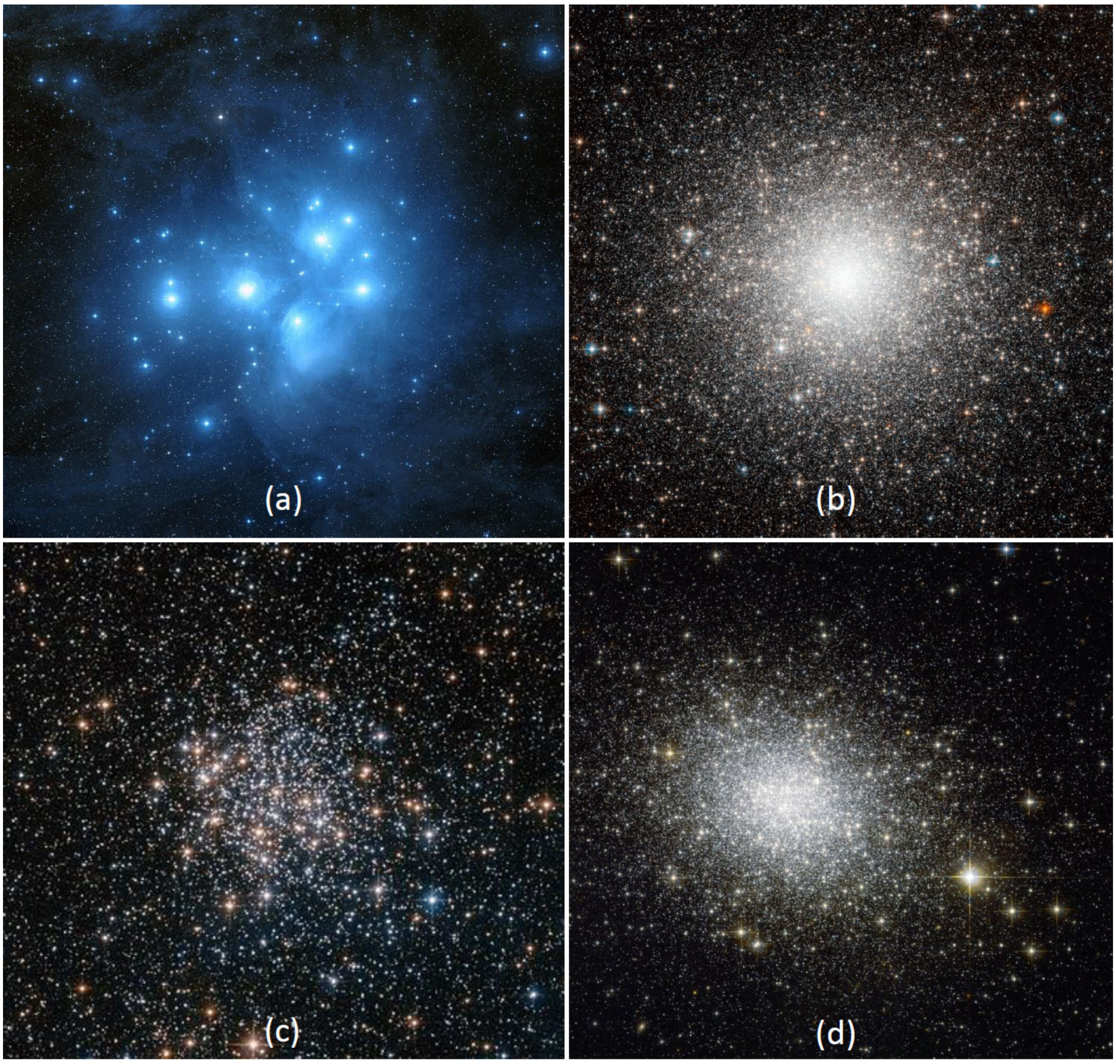

FIGURE 1.4: The figure shows optical color-composite images of open and globular clusters in the MW (top) and the MCs (bottom), demonstrating how stellar density varies among the different types of clusters. Panel (a): Galactic OC M45 (NASA, ESA, AURA/Caltech, Palomar Observatory), panel (b): Galactic GC M54 (ESA/Hubble & NASA), panel (c): OC in the LMC, NGC 1854 (NASA), panel (d): GC in the SMC, NGC 121 (ESA/Hubble)

Bica et al. (2008, hereafter B08) compiled a comprehensive catalog of star clusters, associations, and nebulae in the MCs, integrating data from a wide array of sources including photographic surveys like the ESO Schmidt and UK Schmidt Telescope Southern Sky Surveys, and CCD-based surveys such as the Magellanic Clouds Photometric Survey (MCPS), the Digitized Sky Survey (DSS), and Two Micron All Sky Survey (2MASS). This catalog contains $\sim$ 3700 objects. Expanding on this work, Sitek et al. (2016, hereafter S16) used Optical Gravitational Lensing

Experiment (OGLE) III photometry to identify and classify clusters in the SMC, particularly in its densely populated central regions. The effort was extended by Sitek et al. (2017, hereafter S17) to the LMC using deeper OGLE-IV data. Together, these two studies contributed 301 newly identified clusters, significantly enhancing the completeness of the MC cluster census.

The VISCACHA project conducted an in-depth observational study examining star clusters located in the MCs. The survey captured detailed photometric data to determine important parameters like age, mass, and structure across a diverse population of clusters. Dias et al. (2021) studied seven clusters in the SMC outskirts, finding associations with the Magellanic Bridge and Counter-Bridge. The kinematic and spatial evidence from the study revealed strong tidal interaction between the MCs, affecting the galaxies' evolution. Dias et al. (2022a) examined the West halo of the SMC, revealing structural trends correlated with galactocentric distance and confirming a large LOS depth to the galaxy. Bica et al. (2022) studied three faint SMC star clusters, which revealed they are significantly younger (2.6–4.8 Gyr) than previously estimated. The study updated metallicities ([Fe/H] $\approx$ –0.57 to –0.90), highlighting the value of high-quality data in estimation of the cluster parameters. Rodríguez et al. (2022) analyzed the internal structure of 82 star clusters in the MCs, using the Minimum Spanning Tree to measure how the stars are spread out inside each cluster. The study showed that older, more evolved clusters tend to have a more smooth, concentrated shape, while younger clusters are more clumpy or irregular. Oliveira et al. (2023) analyzed 33 star clusters in the Magellanic Bridge and SMC Wing to trace the assembly history of these regions. The study identified two main populations: older clusters (0.5–6.8 Gyr, [Fe/H] $<$ –0.6) likely stripped from the SMC, and younger clusters ($<$ 200 Myr, [Fe/H] $>$ –0.5) that formed in situ along the Bridge. This series of studies with the VISCACHA survey built a comprehensive view of cluster evolution, dynamics, and interaction-driven structure in the Magellanic system.

Recently, Milone et al. (2023) analyzed 113 star clusters using HST survey of the MCs. The study revealed extended main-sequence turn-offs (eMSTOs) in clusters like KMHK 361 and NGC 265, including new evidence of multiple stellar populations. Also, proper motion (PM) data uncovered kinematic links between young stars in the SMC and the LMC, highlighting ongoing dynamical interactions between the two galaxies. Ettorre et al. (2025) reported a high fraction of fast-rotating stars in several young LMC clusters, contributing to the eMSTOs seen in CMDs. The presence of both slow and fast-rotating stellar populations indicates that stellar rotation, mass loss, and age spreads all play roles in shaping cluster morphology.

Surveys such as SMASH, DECam, *Gaia*, VMC, and OGLE have enabled detailed mapping and characterization of star clusters in the MCs. Additionally, machine learning techniques have enhanced cluster detection and parameter estimation. These combined efforts are enhancing our understanding of the MCs by revealing insights into their structural properties, star formation patterns, past interactions, and overall evolutionary history through the study of star clusters.

1.5 Interaction history of the MCs

It was previously believed that the MCs had interactions both with our Galaxy and with each other (Westerlund 1997). Early PM measurements of the LMC using HST data implied that it might be unbound from the MW (Kallivayalil et al. 2006). Subsequent refinements, however, yielded lower velocity values, suggesting that the LMC is likely on its first infall toward the MW. Following this, Besla et al. (2007), Besla et al. (2010), and Besla et al. (2012, hereafter B12), introduced a first infall scenario for the MCs to the MW. Their models provided valuable insights into the Clouds' mutual interaction history, suggesting that a direct collision between the LMC and SMC occurred within the last 200 Myr. This interaction likely triggered tidal stripping of material from the SMC, with the resulting Magellanic Stream primarily attributed to the LMC–SMC encounter, rather than their motion through the MW's gravitational potential. Later, Lucchini et al. (2021) and Lucchini (2024) supported the first passage scenario and suggested the presence of a Magellanic Corona before the infall of the Clouds into the MW's potential.

The model proposed by Diaz & Bekki (2012) explored scenarios in which the MCs are gravitationally bound and have experienced multiple orbital passages around the MW. According to this, the MCs became a binary pair only within the last 2 Gyr. It is suggested that they may have initially evolved as separate satellites of the MW, originating at large separations (as also considered by Bekki & Chiba 2005). Over time, as the MCs moved through the Galactic halo, their trajectories gradually brought them closer together, eventually leading to the LMC capturing the SMC and forming a gravitationally bound binary system. This scenario better accounts for the observed bifurcation of the Magellanic Stream into two distinct filaments, suggesting that a prolonged interaction within the MW's halo may be crucial for the formation of such features.

Figure 1.5 illustrates the orbital trajectories of the MCs as predicted by several models (Yoshizawa & Noguchi 2003; Diaz & Bekki 2012; B12; Lucchini et al. 2021). These models demonstrate that assumptions regarding the MW's mass significantly influence the inferred orbital history of the MCs. Specifically, models with a lower MW mass suggest that the Clouds are currently on their first approach, whereas models with a higher MW mass indicate that the Clouds have undergone multiple orbital passages. Vasiliev (2023) investigated how uncertainties in the MW's mass influence the orbital evolution of the MCs, opening up the possibility of multiple-passage scenarios. However, the models suggest the LMC and the SMC have experienced three or five pericentric passages, which are

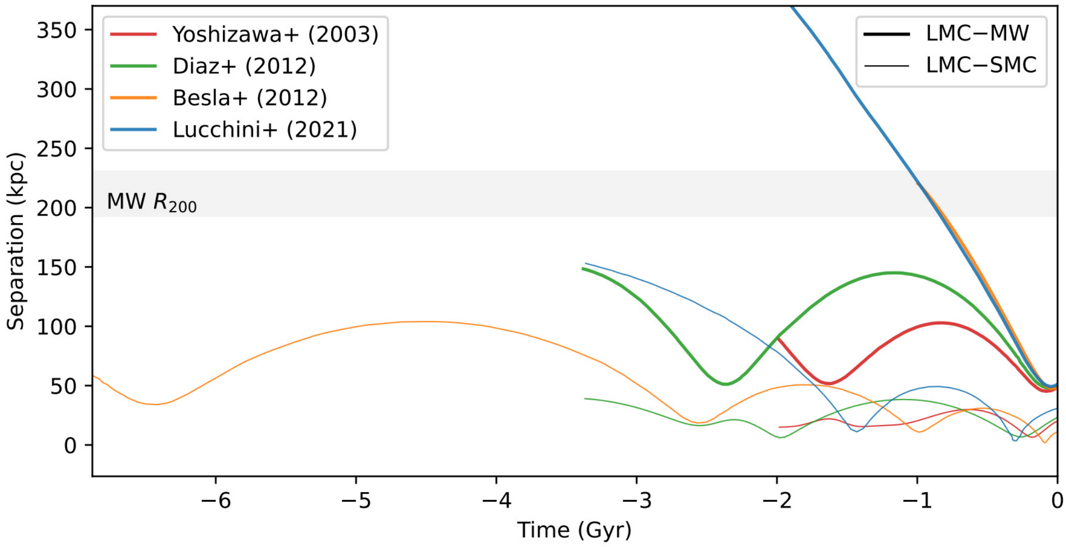

FIGURE 1.5: The figure presents orbital trajectories for the MCs under different models, showing their separations over time, with the present day set at t=0. Thick lines represent the distance between the LMC and the MW, while thin lines indicate the separation between the LMC and SMC. The multiple-passage scenarios from Yoshizawa & Noguchi (2003) and Diaz & Bekki (2012) are illustrated in red and green, respectively. Meanwhile, the first-passage models proposed by Besla et al. (2012) and Lucchini et al. (2021) are shown in yellow and blue. The shaded gray region represents the estimated virial radius of the MW, ranging between 192 and 231 kpc (Bland-Hawthorn & Gerhard 2016). (Credits: Lucchini 2024)

more frequent than their encounters with the MW. Their models indicate that the LMC and SMC may have undergone three to five close passages with each other, occurring more frequently than their encounters with the MW.

Both the first-passage and multiple-passage models by B12 and Diaz & Bekki (2012) reproduce the Magellanic Bridge during the recent encounter between the LMC and the SMC, which likely occurred between 100 to 300 Myr ago. The models propose that tidal forces led to the stripping of gas and stars from the SMC, with some material also being drawn from the LMC. Metallicity studies, such as Misawa et al. (2009), indicate that the Magellanic Bridge has a chemical composition closely resembling that of the SMC, suggesting it originated mainly from SMC material. Nonetheless, these models also predict a metallicity gradient along the Bridge, increasing in the direction of the LMC, likely due to the presence of the LMC gas.

The origin of the LA in the Magellanic system remains poorly understood and is subject to multiple interpretations. An initial investigation by Nidever et al. (2008) suggested that the LA might have formed from the SouthEast HI Overdensity (SEHO) region of the LMC. This region also includes 30 Doradus, known for its intense star formation activity. Based on positional and velocity measurements, the study suggested that a significant portion of the LA originates in the LMC. However, a later study by Yang et al. (2014) proposed that the LA comprises remnants of ancient tidal dwarf galaxies that preceded the MCs and were directed toward the MW's potential as a result of a past merger event near the location of M31. In contrast, simulations by Lucchini et al. (2020) showed that a pre-existing halo of warm ionized gas around the LMC, known as the Magellanic Corona, can account for the present-day location and structure of the LA, even before the LMC entered the MW's halo.

Hammer et al. (2015) performed hydrodynamical simulations to reproduce the crossing and twisted filamentary structure of the Magellanic Stream, as observed in the Galactic all sky survey (GASS, McClure-Griffiths et al. 2009). The simulations suggest that the MCs experienced a direct collision at ~ 250 Myr ago, after which two trailing tails formed and evolved under the influence of ram pressure from the dense MW halo. The study by Salem et al. (2015) demonstrated that ram pressure played a significant role during the LMC's recent pericentric passage, effectively truncating its gaseous disk. Craig et al. (2021) argued that tidal effect between the MCs and with the MW alone are insufficient to explain the observed properties of the Stream, highlighting instead the strong role of ram-pressure stripping by the MW's dense circumgalactic medium.

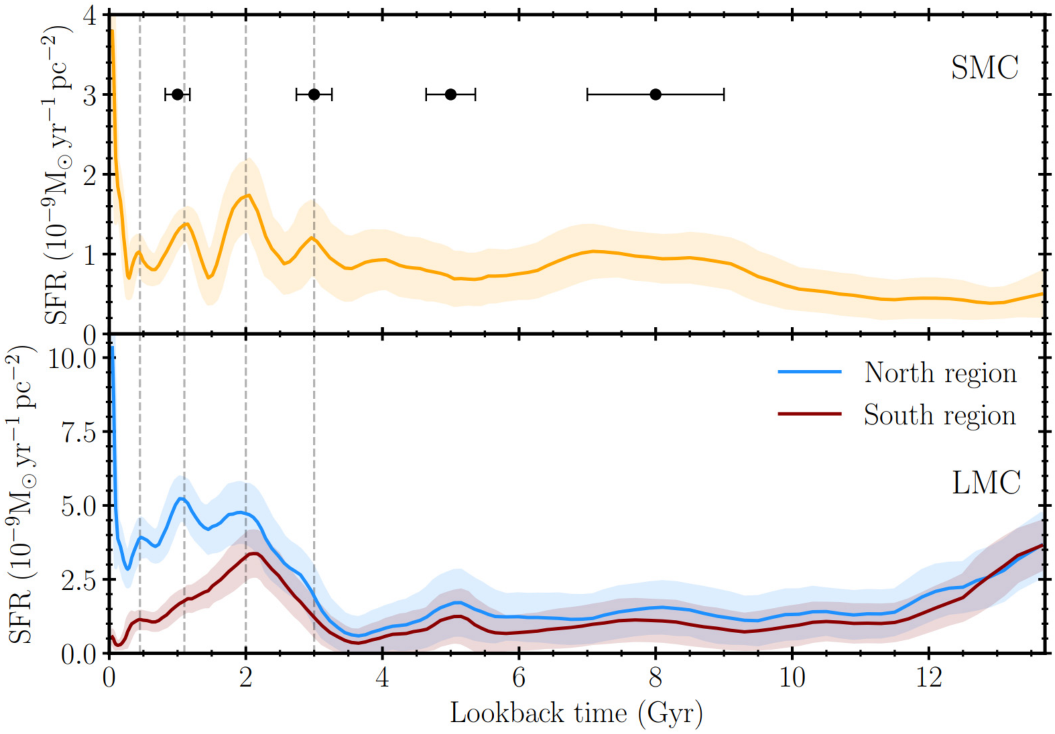

FIGURE 1.6: This figure presents a comparison between the global star formation rates of the SMC, as derived by Massana et al. (2022), and those of the LMC from Ruiz-Lara et al. (2020). Vertical dashed lines mark the approximate timing of corresponding star formation peaks at ∼ 0.45, 1.1, 2, and 3 Gyr ago in both galaxies. In the top panel, horizontal bars denote the duration of enhanced star formation episodes. The shaded regions illustrate the uncertainties in the SFHs, estimated using the methodologies described in Hidalgo et al. (2011) and Rusakov et al. (2021). (Credits: Massana et al. 2022)

1.6 Star formation history of the MCs

The SFH of a galaxy describes the variation of its star formation rate as a function of time over its lifetime. It provides insights into when and how efficiently a galaxy formed its stars, pointing to the effects of gas accretion, mergers, feedback, and environmental influences during the course of their evolution. The SFH of the MCs offer insights into their mutual interactions as well those with the MW.

Several studies have investigated the SFH of the MCs using both star clusters and field stars as tracers. The global and spatially resolved SFH of the MCs was studied by Zaritsky et al. (1997) using the MCPS. Pietrzynski & Udalski (2000) studied the age distributions of star clusters in the MCs and made comparisons. The studies have shown a close link between cluster formation (CF) and star formation in the MCs (Holtzman et al. 1999; Subramaniam 2004). Harris & Zaritsky (2009) analyzed the SFH of the LMC and observed a strong correlation between field star formation and CF, with significant peaks occurring at $\sim$ 2 Gyr, 500 Myr, and 100 Myr. In a similar study, Harris & Zaritsky (2004) identified star formation enhancements in the SMC at $\sim$ 2.5 Gyr, 400 Myr, and 60 Myr.

A significant number of studies have been performed with several of the cataloged star clusters to obtain their properties. Glatt et al. (2010, hereafter G10) using the MCPS data estimated peaks of CF at $\sim$ 125 Myr and $\sim$ 800 Myr for the LMC, and, $\sim$ 160 Myr and $\sim$ 630 Myr for the SMC, respectively. Nayak et al. (2016, hereafter N16) and Nayak et al. (2018, hereafter N18), utilizing OGLE III data, identified prominent CF episodes around 125 Myr in the LMC and $\sim$ 130 Myr in the SMC. To investigate the SFH of the MCs, catalogs of long-period variable stars (Spano et al. 2011; Soszyński et al. 2011) were employed by Rezaeikh et al. (2014). Their findings indicated that the early SFHs of the two galaxies diverged significantly, with major activity in the LMC dating back to $\sim$ 10 Gyr and in the SMC to $\sim$ 3–5 Gyr ago. More recently, Massana et al. (2022) used SMASH data to derive the SFHs and found that the MCs have exhibited synchronized and tidally influenced star formation over the last $\sim$ 3.5 Gyr. This identifies mutual interactions as the driver of their star formation in the last few Gyr.

1.7 Kinematics of the MCs

Significant efforts have been made to examine the internal kinematics of the LMC, with early efforts focusing on its HI gas and stellar content. Kim et al. (1998)

studied HI velocity fields using data from the ATCA and GASS, identifying a relatively symmetric HI disk characterized by a LOS velocity dispersion of ~ 15 km s^{-1}. They also observed indications of gas outflows, suggesting that material may be getting stripped from the area surrounding the LMC's bar. V02 used a sample of 1041 carbon stars to model the LMC disk, finding that the dynamical center is offset by $\sim 1^{\circ}.2$ from the HI disk center. This study also revised the PM of the LMC's center of mass(COM) and used LOS velocities of stars to estimate the disk thickness, finding a V/σ ratio of ~ 3, which is lower than that of the MW. Indu & Subramaniam (2015) reported velocity patterns indicative of gas outflows originating from the western part of the LMC disk as well as from the southern and southwestern regions of the Bridge. These features were interpreted as being caused by ram-pressure stripping.

More recently, W20 modeled the PM of the LMC using the all-sky data release of SkyMapper (Data Release 1), examining various stellar populations, including carbon stars, RGB stars, and young stars. Their study confirmed that both young and old populations exhibit disk rotation. However, the disk of the young population displayed an offset of $\sim 0^{\circ}.7$ in the kinematic center relative to the old population, suggesting it was due to the interaction between the MCs. N22 investigated the central PMs of the LMC using data obtained from the VISTA Magellanic Clouds (VMC) survey (Cioni et al. 2011). Their analysis revealed that the disk rotation velocity of the younger population differs from that of the older population, where the intermediate-age stars follow elongated orbits parallel to the LMC bar's major axis.

The observation with ATCA found that the HI gas in the SMC exhibits differential rotation, where a gradient in velocity fields is noted from the southwest to the northeast of the galaxy (Stanimirović et al. 2004). Dobbie et al. (2014) used 3037 RGB stars and found lower LOS velocities towards the Wing, which they associated with the Magellanic Bridge, and higher velocities at the southwestern end of the SMC bar, interpreted as the signature of the Counter-Bridge. The study suggested that these kinematic features observed in intermediate-age stars resulted from tidal stripping of the SMC due to its interactions.

Zivick et al. (2018) measured the systemic PM of 43 SMC fields with the HST Wide Field Camera 3 and suggested that the SMC does not show significant rotation. Also, the study reconstructed the past orbits of the LMC and the SMC, which indicated a direct collision at $\sim$ 147 Myr. The study by De Leo et al. (2020, hereafter D20) using red giant stars revealed that the SMC exhibits kinematic signatures of tidal disruption, specifically in the form of tangential velocity anisotropy, which is likely to be the result of tidal interactions with the LMC. Niederhofer et al. 2021, hereafter N21) used the VMC survey to study the PM of the old and young stellar population of the SMC, revealing that the SMC is experiencing outward stretching of its outer regions. The study also found that younger stars exhibited larger PMs towards the young Magellanic Bridge, while older stars showed a coordinated motion towards the older bridge of the SMC.

1.8 MCs with *Gaia*

Gaia is a groundbreaking mission launched by the European Space Agency (ESA) on December 19, 2013. It is dedicated to advancing astrometry by measuring celestial positions, distances, and motions with unprecedented precision. More details about the *Gaia* instrument and its specifications are presented in Chapter 2 (Section 2.1). This thesis exclusively uses the *Gaia* data, and below we summarize the previous studies utilizing the *Gaia* data to study the MCs.

Using the first data release (DR1) from *Gaia*, van der Marel & Sahlmann (2016, hereafter V16) analyzed the proper motions of 29 stars in the LMC and 8 in the

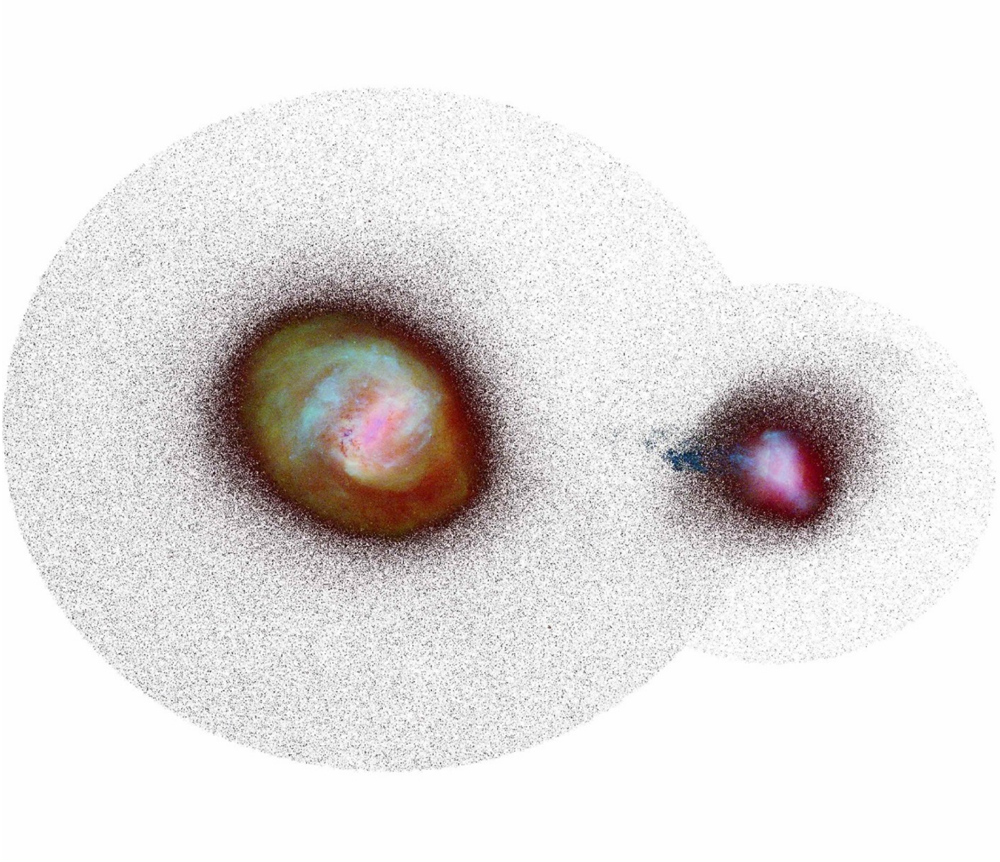

FIGURE 1.7: The selection of the MCs from *Gaia* Early Data Release 3 data is shown, with the LMC on the left ($\sim 20^\circ$ sky coverage) and the SMC on the right ($\sim 9^\circ$ sky coverage). (Image credit: ESA/Gaia/DPAC)

SMC. Their results showed a clockwise rotation of the LMC disk, but the accuracy of these *Gaia* measurements was lower than those from the HST. Belokurov et al. (2017) used the photometric catalog from *Gaia* DR1 to analyze star count maps, identifying a trail of RR Lyrae stars connecting the MCs, though not collocated with the Magellanic Bridge. The study also revealed density contours indicative of tidal stripping from the SMC. Using *Gaia* DR2 data, Zivick et al. (2021, hereafter Z21) analyzed the kinematics of red giant stars in the SMC, modeling its rotation and tidal expansion. The study revealed tidal distortions on the eastern side extending toward the Magellanic Bridge, along with a high inclination of $\sim 80^\circ$ and a line of nodes oriented nearly north-south.

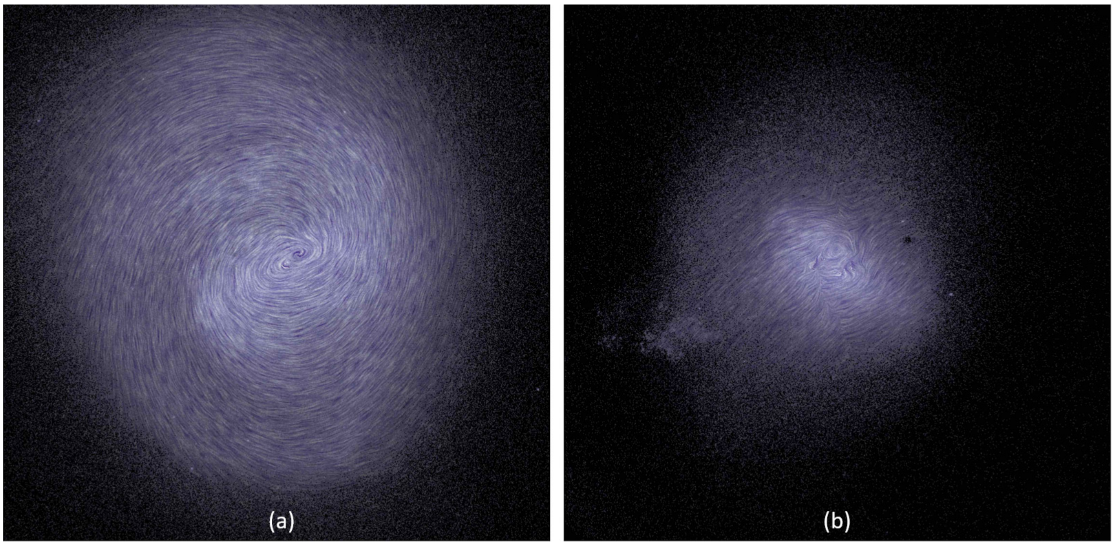

Figure 1.8: The internal PM of the MCs is shown, with panel (a) displaying the LMC and panel (b) the SMC, after subtracting their center-of-mass PMs. (Image credit: Gaia Collaboration et al. 2021)

G21 utilized *Gaia* Early Data Release 3 (EDR3) to investigate the stellar populations of the MCs based on age. Their analysis demonstrated that the EDR3 data show a significant enhancement in both PM precision and coverage compared to the previous DR2. Figure 1.8, panel (a) shows the coverage of the MCs with EDR3 data. The LMC is seen as a well-defined disk with a prominent central bar and a dense northern spiral arm, highlighting its asymmetry and internal structure. In contrast, the SMC exhibits a more irregular and elongated shape, without a well-defined disk, featuring a central concentration and an eastern stellar extension known as the Wing. The study also identified that the Magellanic Bridge contains both young (≤100 Myr) and intermediate-age (1–2 Gyr) stars, each exhibiting distinct kinematic signatures. Panel (b) of Figure 1.8 shows the internal PM of the LMC and SMC, respectively. The LMC shows clear signs of a rotating disk, with well-measured rotation curves indicating differential rotation around a central bar. Its velocity field also displays perturbations likely related to spiral arms and tidal interactions. In contrast, the SMC exhibits more complex and disturbed kinematics, lacking a coherent rotation pattern. Instead, it shows irregular motions and velocity gradients consistent with its disrupted morphology and ongoing tidal interaction with both the LMC and the MW.

S22 analyzed the asymmetric warp of the LMC disk using *Gaia* EDR3 data and red clump stars, finding that the distortion is more significant in the southwest, while it appears weaker in the northeast. This asymmetry suggests a U-shaped distortion in the outer LMC disk, likely resulting from tidal interactions between the MCs, and with the MW. C22 used *Gaia* PM of RC stars in the LMC disk, revealing asymmetric residual motions, particularly in the southern disk. Through comparisons with N-body simulations, the study identified that the observed kinematic asymmetries and vertical heating of the LMC disk are consistent with a recent direct collision with the SMC, occurring $\sim$ 140–160 million years ago with an estimated impact distance of $\sim$ 5 kpc. These findings strongly support the scenario of a close, recent encounter between the two galaxies, which has significantly affected the LMC's present-day kinematics.

The extensive sky coverage of the MCs with *Gaia* data provides a significant advantage for constructing spatial age maps of the galaxies with various stellar populations including star clusters. Age-dating clusters in the outskirts are crucial for unraveling the interaction history of the MCs. With *Gaia* DR3, it is now possible to study clusters located far from the centers of the galaxies, which was not possible with other surveys. The PM measurements of star clusters also enable kinematic modeling of the MCs, which has not been attempted so far. With *Gaia* DR3 offering improved accuracy in PM estimates for sources in the MCs, the kinematic properties of the MCs can be precisely modeled for star clusters. Furthermore, *Gaia* DR3 sources in the MCs can be classified based on their evolutionary phase with the CMD. This classification helps modeling of the MCs using both young and old stellar populations, providing key insights into their structure and evolution.

1.9 Motivation and goals of the thesis

The MCs are known to have had multiple interactions in the past that shaped their structural and dynamic evolution. It is therefore crucial to trace the interaction history so that the interactions can be linked to the observed features in the galaxies. The interaction episodes are known to trigger star formation in the MCs. Tracing the formation history of star clusters is one of the most effective ways to locate the episodic star formation events in the MCs triggered by interactions. Numerous studies have examined cataloged star clusters to determine their properties, including age, metallicity, and reddening (G10; N16; N18). However, previous studies that analyzed the age distribution were predominantly focused on the inner regions of the MCs. Clusters located in the outer regions of the LMC remain largely unexplored due to the need for extensive sky coverage for surveys. As the outer LMC is more susceptible to the effects of interactions, age-dating of star clusters in the outer LMC is crucial to tracing them. Additionally, statistical techniques for removing field stars from star clusters were not properly applied in many cases, which affect the accuracy of age estimations.

Several studies have performed the kinematic modeling of the LMC (V02; W20; G21), which resulted in kinematic parameters with values spanning a broad range. It also became evident that the modeled/ estimated parameters vary with respect to the age and nature of the stellar population used for the analysis (W20). Even though the LMC is known to host a rotation-supported disk, the kinematic parameters of the LMC are also known to vary with respect to the radial coverage of the study as well (N22). Modeling the internal kinematics of the LMC using various populations and coverage is therefore necessary to reveal the parameter range of the LMC disk and to trace the response of the disk to the direct collision with the SMC, if present.

The kinematic model of the SMC reveals discrepancies in the rotation signature, with the old stellar population exhibiting minimal rotation compared to the gas, which shows significant rotation (D18; Z21). An age-dependent kinematic model of the SMC is essential for revealing its structural properties and identifying its unusual internal kinematics. Additionally, looking at the residual velocity maps of both the LMC and the SMC from modeling is crucial for linking kinematic features and anomalies to their interaction history.

The first goal of this thesis is to trace the overall cluster formation history (CFH) of the MCs. This involves estimating the ages of clusters distributed throughout the MCs, with a focus on increasing coverage toward the outskirts with *Gaia* DR3 data. Also, the aim is to develop an improved field star decontamination (FSD) technique to effectively clean the cluster CMDs, thereby enabling precise age estimations. The second goal of the thesis is to develop a kinematic model of both the LMC and the SMC. The *Gaia* DR3 sources with PM information is the best among available data sets with accuracy and spatial coverage to perform the kinematic modeling of the MCs. In addition to age-based cluster groups, our study also modeled stars in various evolutionary stages, including young MS stars, red giants, and RC stars.

1.10 Overview of the thesis

The thesis is organized in the following way:

- **Chapter 1:** This chapter introduces the Magellanic System, covering the stellar population of the MCs, star clusters, kinematics and interaction history of the Clouds, through relevant literature study. The motivation and goals of the thesis are also outlined.

- **Chapter 2:** In this chapter, the datasets used in our studies, including the adopted star cluster catalogs and our approach to handling bulk archival data are presented. This chapter also details the research methodologies employed for the data analysis. The data and methods are outlined in Dhanush et al. (2024a), Dhanush et al. (2024b), and Dhanush et al. (2025).

- **Chapter 3:** Here, the results obtained from tracing the CFH of the MCs, including the age distribution of star clusters, the synchronized peaks of CF between the MCs, and the episodic and radial truncation of CF events to understand the evolution of both galaxies are presented. The content of this chapter is based on Dhanush et al. (2024a).

- **Chapter 4:** Here, the results from analyzing the internal kinematics of the LMC disk, modeled using star clusters and different stellar populations (both old and young), to study the disk's response to its recent interaction with the SMC are presented. The content of this chapter is based on Dhanush et al. (2024b).

- **Chapter 5:** Here, the first baseline kinematic model of the SMC, revealing the structure and morphology of the galaxy across its old and young stellar populations is presented. Additionally, we identify anomalous regions of the SMC affected by recent interactions with its larger companion (LMC). The content of this chapter is based on Dhanush et al. (2025).

- **Chapter 6:** This chapter summarizes the key conclusions of the thesis and outlines potential directions for future research.

Chapter 2

Data and Methodologies

The previous chapter presented an introduction to the MCs and discussed the motivation for studying them in this thesis. Our first goal is to parameterize the star clusters in the MCs, followed by kinematic modeling of the MCs with the cluster and other stellar populations using *Gaia* DR3 datasets. In this chapter, we provide an overview of the *Gaia* space telescope and discuss the methodologies we developed and adopted to achieve the goals of this thesis.

2.1 *Gaia*

The *Gaia* spacecraft is equipped with two optical telescopes, each featuring a 1.45 × 0.5 m^2 primary mirror, providing a combined light-collecting area of approximately 0.7 m^2. These telescopes observe two distinct sky regions separated by a fixed angle of 106.5° (as illustrated in Figure 2.1). A shared focal plane accommodates 106 charge-coupled devices (CCDs), each containing 4500 × 1966 pixels, amounting to an impressive total of ∼ 938 megapixels, as shown in Figure 2.2.

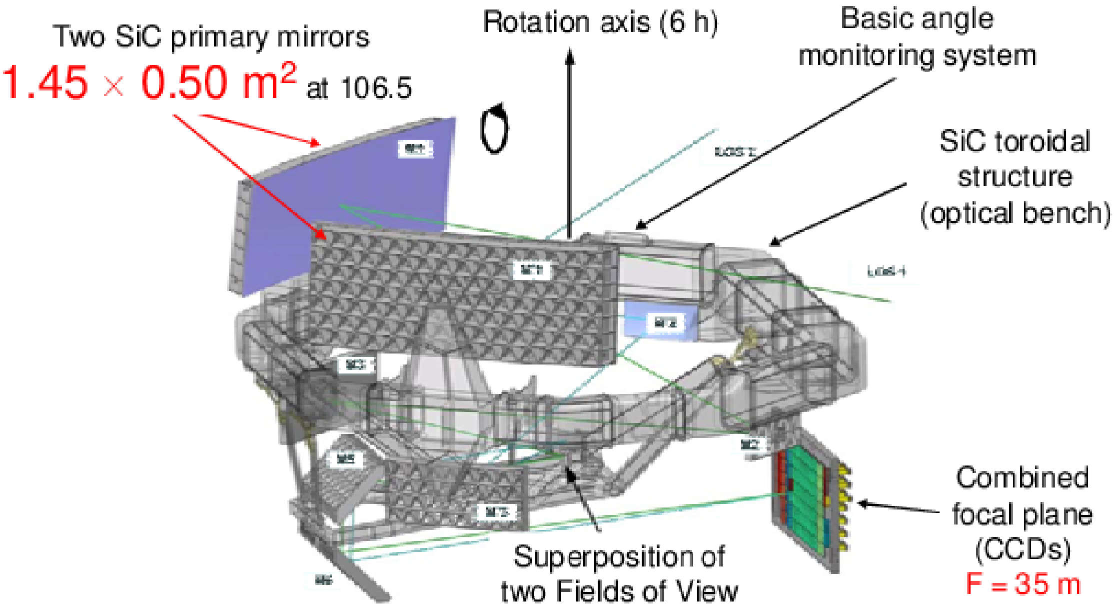

FIGURE 2.1: A schematic representation of the *Gaia* payload illustrating the two telescopic mirrors and associated instruments positioned on the optical bench. (Image Credit: EADS Astrium)

The focal plane of the *Gaia* spacecraft comprises five primary functional components: two CCDs each for the wavefront sensors and basic angle monitors used in calibration, 14 CCDs for the sky mapper responsible for detecting sources, 62 CCDs forming the astrometric field for high-precision measurements of stellar positions and motions, 14 CCDs dedicated to blue and red photometry for capturing spectral energy distributions, and 12 CCDs within the radial velocity spectrometer to assess stellar Doppler shifts. More details about these components and their roles are provided in Gaia Collaboration et al. (2016).

Gaia operates with three photometric bands: G spanning 330 to 1050 nanometers, G_{BP} covering 330 to 680 nanometers, and G_{RP} ranging from 640 to 1050 nanometers. It achieves a spatial resolution close to 0.4 arcseconds. The mission aims to compile a detailed catalog of roughly one billion stars, equivalent to around 1% of the MW's stellar population. This extensive dataset will be nearly complete for stars with G magnitudes up to 20 mag. Over its five-year operational timeline,

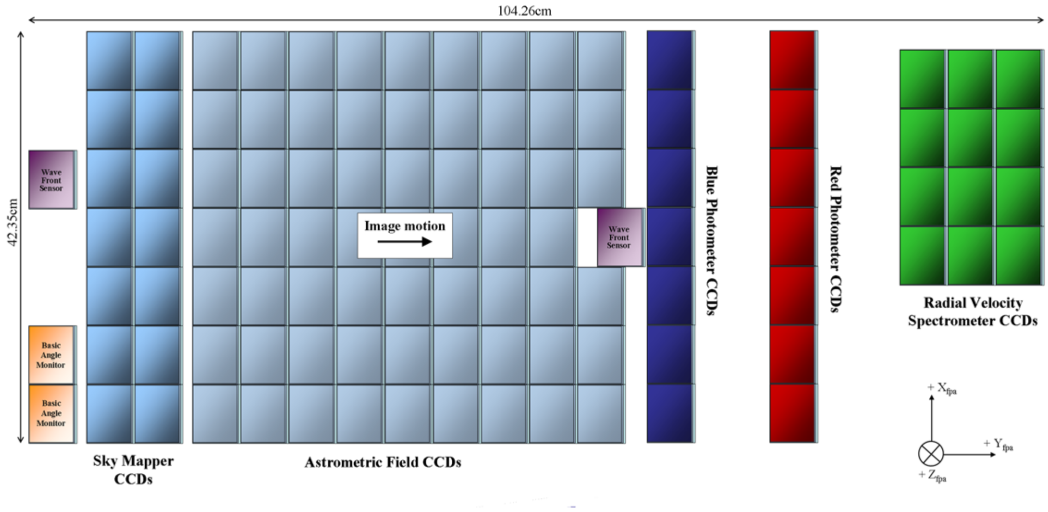

FIGURE 2.2: Illustration showing the layout of the *Gaia* telescope's focal plane. (Image credit: ESA)

Gaia observed each target around 70 times, enabling precise measurements of their positions, distances, velocities, and variations in brightness.

To date, the *Gaia* mission has produced three significant data releases, each corresponding to progressively longer observation periods. The initial release, *Gaia* DR1, became available in September 2016 and was based on 14 months of data collection, providing positions and brightness measurements for over 1.1 billion stars, though PM information was limited. The second release, *Gaia* DR2, published in April 2018, expanded the dataset to include positions, parallaxes, and PMs for $\sim$ 1.3 billion stars, utilizing 22 months of observations. The third release was split into two stages: *Gaia* EDR3, released in December 2020, offered improved positions, parallaxes, and PMs for more than two billion sources after 34 months of observations. The full *Gaia* DR3, made public in June 2022, built upon EDR3 by adding astrophysical parameters, variability data, and light curves, representing the most comprehensive dataset from the mission so far (Gaia Collaboration et al. 2023a; Babusiaux et al. 2023).

Gaia, launched in 2013, was initially planned to operate for five years. However, the spacecraft's systems and instruments performed exceptionally well, and it had enough fuel to continue operating. This allowed the ESA to extend the mission multiple times. *Gaia* continued observations until 10 January 2025. After downlinking all remaining data to Earth, the spacecraft was decommissioned on 27 March 2025. The upcoming *Gaia* Data Release 4 (Gaia DR4), based on 66 months of observations, is scheduled for release at the end of 2025. The mission has since entered a post-operations phase, during which the final Gaia Data Release, DR5, will be completed and published by the end of 2030.

The production of scientific community level *Gaia* catalog of sources is produced by a team of pan-European experts and software developers known as DPAC (Data Processing and Analysis Consortium). DPAC has been active since 2006, taking the tedious tasks to develop the data processing algorithms and maintain the IT infrastructure for *Gaia*. Further detailed information about *Gaia* can be found at the ESA website. *Gaia*-released data can be accessed through *Gaia* ESA Archive, and CDS-Vizier.

2.2 Research methodologies

In our studies, we performed several methods to analyze the *Gaia* data to arrive at our scientific results. These involve defining cluster workspaces and field star removal techniques to remove field stars from the cluster regions. Also, we use Markov Chain Monte Carlo (MCMC) optimization algorithms, which we developed in the C program to do the parameters optimization for clusters, and in the kinematic modeling of the LMC and SMC. These are discussed below.

2.2.1 Cluster workspaces

The workspace for each star cluster in the sky plane is defined such that it comprises a cluster region accompanied by one or more field regions. The workspace for each cluster depends on the choice of FSD algorithm suitable for its location, and it is a function of the cluster size and the presence of neighboring clusters. The method adopted for FSD depends on the availability of field star area around or near the cluster. Based on the above, we have considered four different types of field regions for FSD. The different types of cluster workspaces are shown in Figure 2.3. These are discussed below.

1. Group-1: These are isolated clusters with sufficient area available around them to define five concentric annular field regions of equal area. A graphical depiction of the workspace for isolated clusters is shown in Figure 2.3a. The field annuli are of external radii $\sqrt{n+1} \times r_c$ from the cluster center, where n is the number of annuli.
2. Group-2: In several isolated clusters, the outer annular field regions were found to overlap with a nearby cluster. We define Group-2 as partially isolated clusters, where the workspace of a cluster has up to four concentric annular field regions of equal area around the cluster.
3. Group-3: There were clusters where we could not take the annular field region around them, as even the first annular field region would overlap with a nearby cluster region. In such cases, as shown in Figure 2.3b, we have taken one circular comparison field near the cluster. Thus, the workspace comprises the cluster region and a nearby field region of the same area.
4. Group-4: A significant number of clusters have one overlapping neighbor in the LOS. Figure 2.3c shows the workspace for an overlapping pair of clusters as an example. The difference in their workspace from isolated clusters is

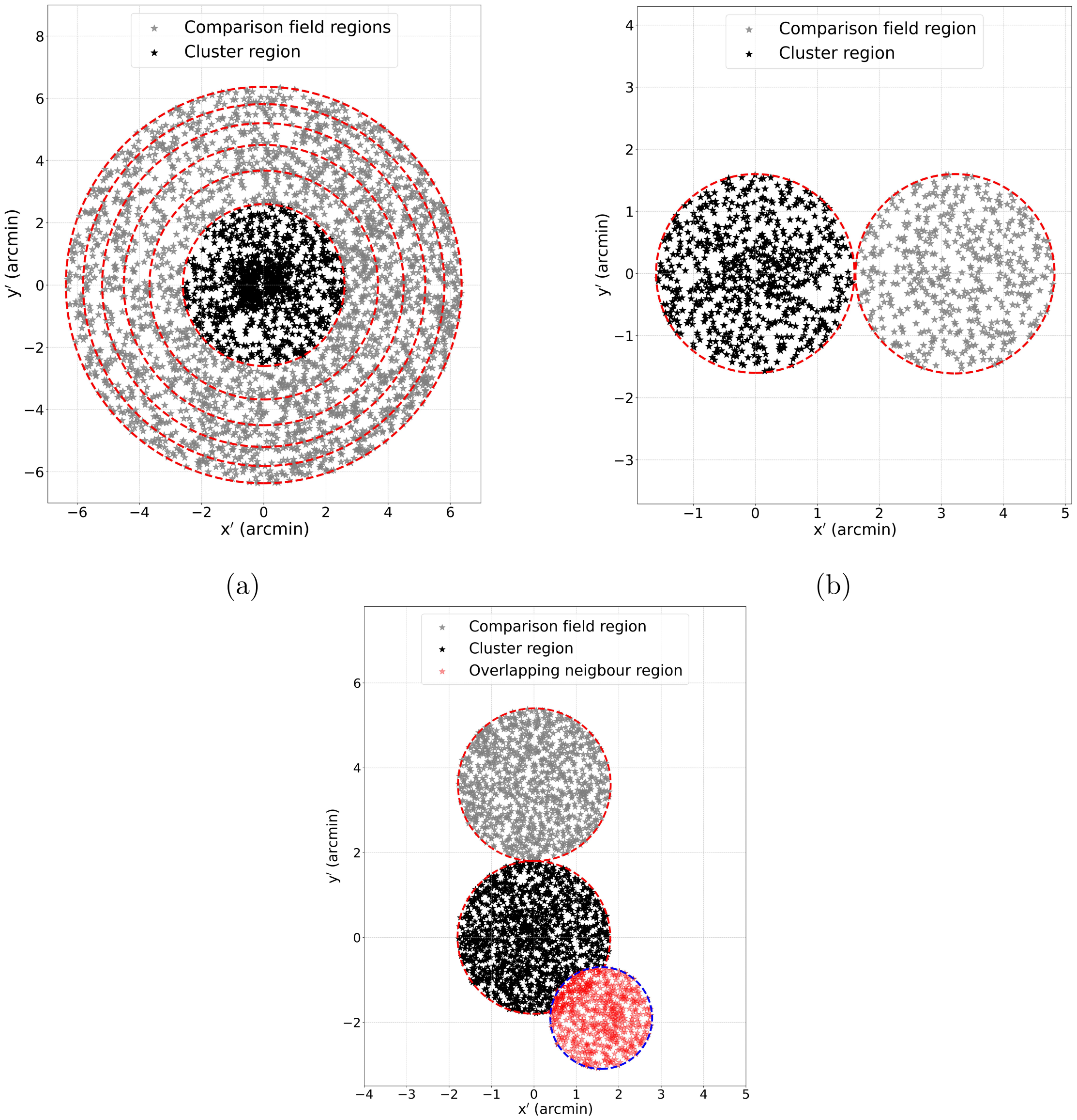

(a) (b)

(c)

FIGURE 2.3: Different types of cluster workspaces (as defined in subsection 2.2.1) for implementing FSD. a) Model workspace of the isolated cluster in the LOS, Group-1 and Group-2 clusters. The cluster region is shown with black stars. The nearby field regions are shown with grey stars, separated by concentric annular circles (dashed red circles). Group-1 clusters use all 5 field regions, and Group-2 clusters use 1 to a max of 4 field regions depending on their availability. b) Model workspace for a partially isolated cluster in the LOS, Group-3 clusters (black stars: cluster region, grey stars: nearby field region). c) Model workspace for an overlapping pair of clusters in the LOS, Group-4 clusters (black stars: cluster region, red stars: overlapping neighbor cluster region, grey stars: nearby field region).

in the selection of cluster region and the field region. For clusters with one neighbor, the neighboring cluster boundaries were ensured not to reside within a cut-off radius of $0.1\mathrm{r}_c$ from its center. The choice of the cut-off radius was based on trials and it ensured enough stars from the centrally dense regions of overlapping clusters while performing the parameter estimation. For these clusters, we removed the overlapping region with the neighboring cluster and used a nearby circular field region.

2.2.2 Field Star Decontamination

In our study, we used a modified version of FSD algorithm used by several authors (Pandey et al. 2007; Choudhury et al. 2015; N16) to clean the CMDs of the cluster region. We created $(G, G_{BP} - G_{RP})$ CMDs for the cluster region and the field region(s), for all the groups mentioned above. The CMD of a cluster region will have a combination of cluster and field stars, whereas the CMD of its field region(s) will have only the field stars. An algorithm was applied to the cluster CMDs to compare and remove field stars. To eliminate field stars from the cluster region, each star in the cluster CMD was matched with its nearest counterpart in the surrounding field CMD(s) and removed accordingly. This process involved searching for the closest field star within adaptive bins centered on each cluster star, starting with bin sizes of $[\Delta G, \Delta(G_{BP} - G_{RP})] = [0.02, 0.01]$ and increasing up to [0.5, 0.25] as needed. Those with counterparts in the field CMD(s) are considered as field stars in the cluster region and are removed from the CMD. Stars that remained in the cluster CMD after this statistical cleaning are most likely to be the cluster members and the CMD with such stars can be considered as a cleaned CMD(s).

In the case of Group-1 clusters, the algorithm takes advantage of the multiple field regions. For clusters in this group, we created 5 cleaned CMDs corresponding to using either all annular fields or with a reduced number of annuli up to a minimum of one. For example, 5-FSD CMD is defined as a cleaned CMD where a star from the cluster CMD did not find a counterpart in any one of the five annular field CMDs. Similarly, we created 4-FSD CMDs to 1-FSD CMD as explained above, using a correspondingly less number of field CMDs for a given cluster CMD. The same logic was implemented for Group-2 clusters with n<5 (where n, the number of associated field regions available for a given cluster) annular field regions to produce n-FSD CMDs for the same cluster, where n can take a maximum value of 4 and a minimum of value of 1. For Groups-1 & 2, we retained multiple cleaned CMDs for the same cluster at the end of this iteration. We note that the cleaned CMDs are affected by (1) less number of stars in the case of poor clusters and (2) variation in field star density. Both these result in the loss of features in the CMD and erroneous fits. Therefore, the CMD most suited for the cluster is decided after the parameter estimation with all the cleaned CMDs.

Now for the Group-3 clusters where a nearby circular field region by the side of the cluster is identified, we ensured that the field region does not overlap with any other neighboring cluster. In the case of Groups-3 & 4, only one cleaned CMD is created at the end of this iteration. We note that some parts of the field regions of different star clusters may be common across the Groups, particularly for those located nearby.

2.2.3 Markov Chain Monte Carlo with C

MCMC is a class of algorithms used to sample from complex probability distributions by constructing a Markov chain whose equilibrium distribution approximates the target distribution. As the chain progresses through more steps, the sample distribution closely matches the desired probability distribution. MCMC methods are beneficial for studying high-dimensional or complicated distributions that are difficult to analyze analytically.

In our study, we estimate four parameters while parameterizing each cluster, and in the kinematic modeling with the sources in the MCs, we estimate up to nine kinematic parameters. To achieve this, we use the MCMC optimization to find the models that best fit our datasets. We used the serial stretch move algorithm developed by Goodman & Weare (2010) to perform the MCMC sampling. The stretch move algorithm is primarily utilized in two ways: one in serial processing and the other in parallel processing. The usage of serial or parallel depends on the specific optimization problem.

Our study performs parameter optimization of 1990 star clusters in the MCs. Similarly, the kinematic modeling of the MCs makes use of ~ 60 data sets. This motivated us to develop the serial stretch move algorithm with a C program and assign each data set to each core available on the CPU. We find that the performance of our code is significantly better than the Python module, `emcee`, which works based on the same stretch move algorithm. A benchmark is provided in Figure 2.4, comparing our C code with `emcee` using several server-based and commercial CPUs. The benchmark time is provided for the kinematic modeling of the LMC (as detailed in section 4.3.1). The first advantage is the single-core performance of our code, which is on average significantly faster in commercial CPUs, even if they are several generations old. The second advantage is the possibility of distributing the different data sets serially at a time to the available cores, which speeds up the process compared to Python `emcee`.

For our workload, we used the commercial CPU, Intel i9-13900K with 24 cores, which helped to estimate cluster parameters for 24 clusters or run 24 kinematic modeling datasets distributed serially at a time. The serial implementation of MCMC is purely based on the type of workload, and in our study, it has more advantages as described above.

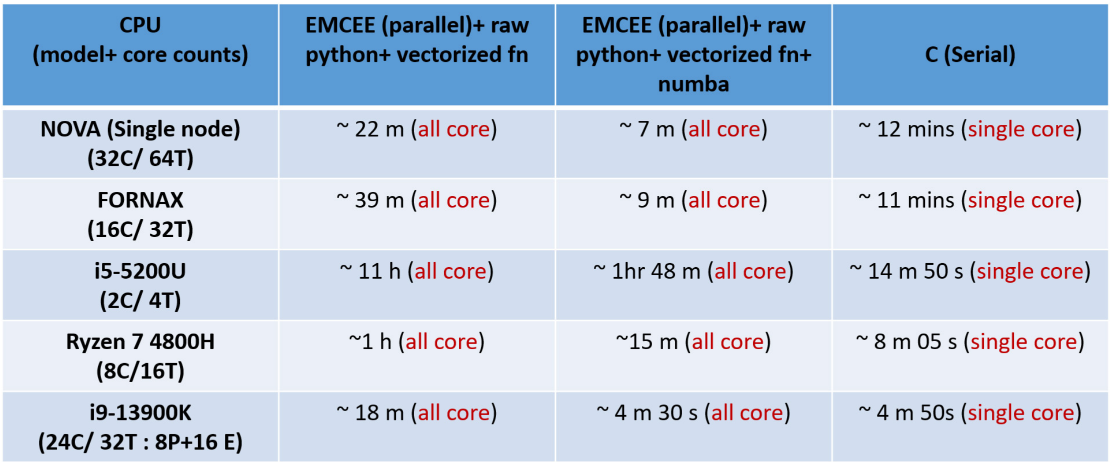

CPU (model+ core counts)	EMCEE (parallel)+ raw python+ vectorized fn	EMCEE (parallel)+ raw python+ vectorized fn+ numba	C (Serial)
NOVA (Single node) (32C/ 64T)	~ 22 m (all core)	~ 7 m (all core)	~ 12 mins (single core)
FORNAX (16C/ 32T)	~ 39 m (all core)	~ 9 m (all core)	~ 11 mins (single core)
i5-5200U (2C/ 4T)	~ 11 h (all core)	~ 1hr 48 m (all core)	~ 14 m 50 s (single core)
Ryzen 7 4800H (8C/16T)	~1 h (all core)	~15 m (all core)	~ 8 m 05 s (single core)
i9-13900K (24C/ 32T : 8P+16 E)	~ 18 m (all core)	~ 4 m 30 s (all core)	~ 4 m 50s (single core)

FIGURE 2.4: Benchmark of the MCMC sampler for the kinematic modeling of the LMC with star clusters as data sets. The first column shows the CPUs we tested, and the subsequent columns report the runtime for performing 2000-step iterations with 200 walkers, using different implementations of the stretch move algorithm: parallel with `emcee` and serial with C.

2.3 Theoretical models

In our studies, we used theoretical stellar isochrones to estimate the parameters of star clusters. Further, we adopted an analytical framework to model the PM of the LMC and the SMC. These are discussed below.

2.3.1 Isochrones

An isochrone represents the set of stars that are assumed to have formed simultaneously, with the same metallicity, but with varying initial masses on the H-R diagram or CMD. Since star clusters contain stars in different evolutionary stages and with different masses, their observed distribution on CMDs is most effectively represented using theoretical isochrones. These isochrones are used to derive key parameters of star clusters, such as age, reddening/extinction, distance, and metallicity, by comparing the theoretical models to the observed CMDs.

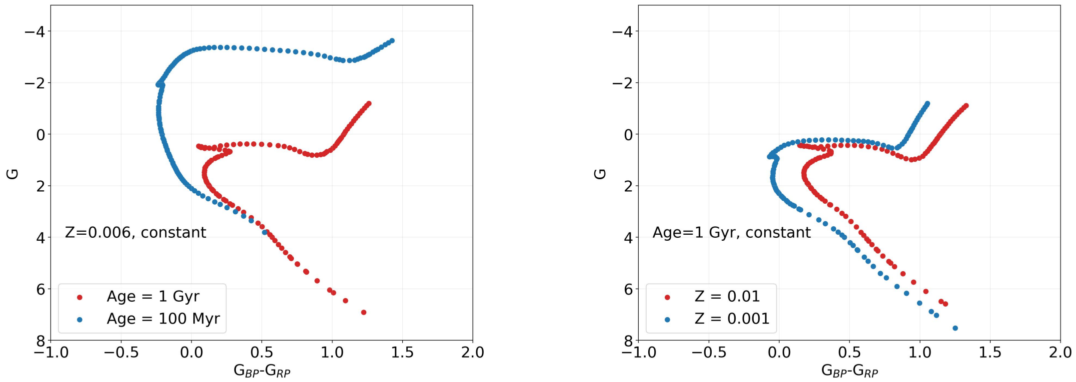

(a) (b)

FIGURE 2.5: The isochrones with different ages and metallicities are shown here. Panel (a) with Z = 0.006, Ages: 100 Myr (Blue), 1 Gyr (Red); Panel (b) with age of 1 Gyr, Z: 0.001 (Blue), 0.001 (Red)

In our analysis, we used PARSEC isochrones (Bressan et al. 2012) to model the cluster parameters, using the initial mass functions from Salpeter (1955) to generate the isochrones. We used the *Gaia* EDR3 photometric system available with the PARSEC, which is described in detail in Riello et al. (2021). Figure 2.5 shows a few model isochrones we used in the study. Panel (a) shows two isochrones at ages 100 Myr (Blue track) and 1 Gyr (Red track) at constant metal fraction, Z = 0.006. Panel (b) shows two isochrones at Z = 0.001 (Blue track) and Z = 0.01 (Red track) at a constant age of 1 Gyr. In our study, we considered stellar evolutionary phases from the MS to the RGB in the isochrone models, assuming the stars in each star cluster of the MCs (ages < 4 Gyr) stay within the limit of these evolutionary phases.

2.3.2 Kinematic model of the MCs

We performed the disk kinematic model of the LMC and the SMC using the analytical equations outlined by V02. These equations define the directional vectors of local PM in the West and North (μ_W, μ_N) in the sky plane using a series of 12 independent model parameters. The parameters selected for modeling the LMC encompass the inclination of the disk (i), the position angle of the line of nodes measured from West (θ), dynamic centers (α_0, δ_0), the amplitude of the tangential velocity of the galaxy's center of mass (v_t), the tangential angle made by v_t (θ_t), and three rotational parameters. In the case of the SMC, we fixed the kinematic centers and used two rotational parameters to model the kinematics. The rotational parameters are discussed later in this section. For the SMC, we modeled a dataset containing LOS velocity information, which enabled us to determine the systemic velocity ($v_{\rm sys}$) of its COM. The modeling aims to identify the most suitable values for these kinematic parameters. It is crucial to highlight that our datasets primarily contain PM data, which restricts our modeling to the translational velocity of the sources in the plane tangent to the sky plane, due to the absence of LOS velocity components. The analytical equations, which express μ_W and μ_N as functions of the described kinematic parameters, are provided below.

Figure 2.6 shows the schematic diagrams representing the velocity and coordinate systems which we use to model the μ_W and μ_N. Panel (a) illustrates the perspective of an observer viewing an arbitrary source in the galaxy, located at a distance D, which has an angular separation (ρ) from the kinematic center of the galaxy, situated at a mean distance of D_0. The velocity of this source with equatorial coordinates, (α, δ) on the sky plane, is primarily composed of three components. It consists of the LOS velocity (v_1) and the tangential plane velocity components (v_2, v_3) at the source location.

Panel (b) shows the source with (α, δ) and kinematic center (α_0, δ_0) at position

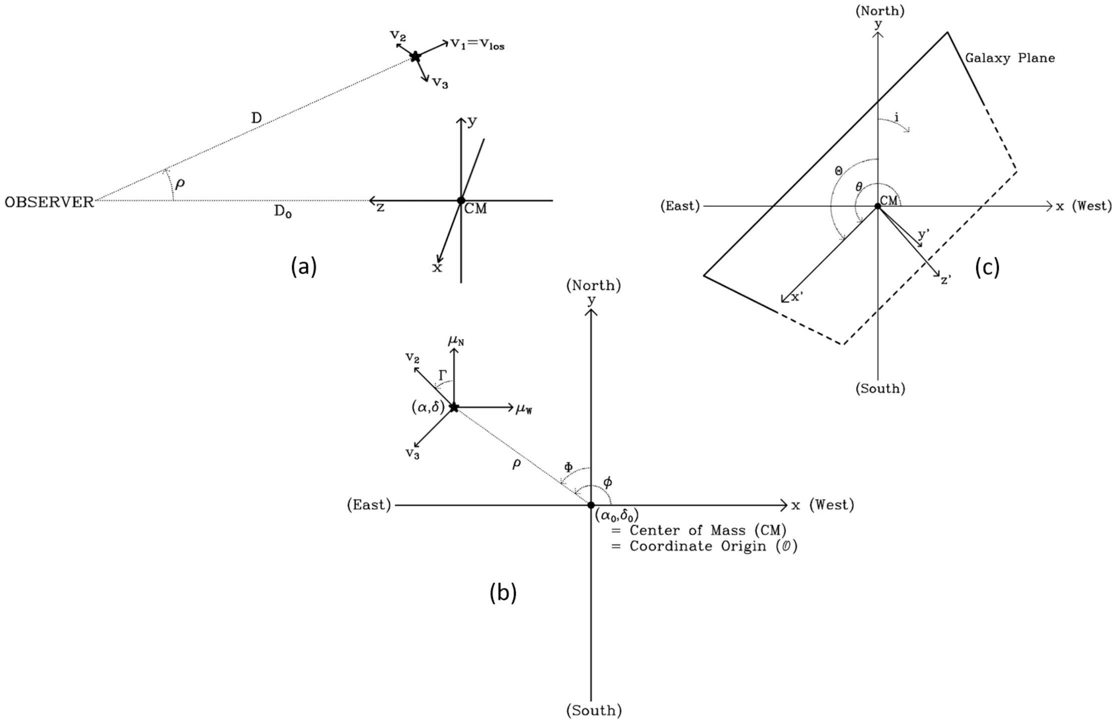

FIGURE 2.6: Depiction of the frames of reference for modeling the galaxy kinematics. Panel (a) shows the perspective of observer and an arbitrary source in the galaxy; panel (b) shows the sky plane perspective with PMs marked for the source; panel (c) shows the galaxy plane obtained after the clockwise rotation in i and θ.

angle, ϕ. The rotation angle between the (v_2, v_3) frame on the sky is Γ. We see the galaxy image as projected onto the sky plane. The PM we observe are the projected velocity components of v_2 and v_3 on the curved spherical surface. So we apply a coordinate transformation that incorporates the inclination (i) and the position angle of the line of nodes (θ) of the galaxy to the sky plane, as shown in panel (c). This transformation will allow us to express μ_W and μ_N in terms of v_2 and v_3. It is given by,

$$\begin{pmatrix}\mu_W \\ \mu_N\end{pmatrix} = \frac{\cos i \cos\rho - \sin i \sin\rho \sin(\phi - \theta)}{D_0 \cos i} \begin{pmatrix}-\sin\Gamma & -\cos\Gamma \\ \cos\Gamma & -\sin\Gamma\end{pmatrix} \begin{pmatrix}v_2 \\ v_3\end{pmatrix} \tag{2.1}$$

where,

$$\cos\Gamma = [\sin\delta \cos\delta_0 \cos(\alpha - \alpha_0) - \cos\delta \sin\delta_0] / \sin\rho$$

$$\sin\Gamma = [\cos\delta_0 \sin(\alpha - \alpha_0)] / \sin\rho$$

The velocity field model of a source in the galaxy can be primarily decomposed into three components: the COM velocity due to the spatial motions, the velocity associated with the precision and nutation (pn) due to the temporal variations of i and θ, and the internal motion (int) of the sources in the disk plane of the galaxy. Hence, (v_1, v_2, v_3) can be decomposed as,

$$\begin{pmatrix}v_1 \\ v_2 \\ v_3\end{pmatrix} = \begin{pmatrix}v_1 \\ v_2 \\ v_3\end{pmatrix}_{COM} + \begin{pmatrix}v_1 \\ v_2 \\ v_3\end{pmatrix}_{pn} + \begin{pmatrix}v_1 \\ v_2 \\ v_3\end{pmatrix}_{int} \tag{2.2}$$

The COM velocity can be expressed in terms of three parameters: v_{sys}, v_t, and θ_t. In our modeling, we assume that there is no precession and nutation of the galaxy, so we neglect the second term in equation 2.2. Further, using spherical trigonometry, the first and last terms in the equation can be written as,

$$\begin{pmatrix} v_1 \\ v_2 \\ v_3 \end{pmatrix}_{COM} = \begin{pmatrix} v_t \sin\rho \cos(\phi - \theta_t) + v_{sys} \cos\rho \\ v_t \cos\rho \cos(\phi - \theta_t) - v_{sys} \sin\rho \\ -v_t \sin(\phi - \theta_t) \end{pmatrix} \tag{2.3}$$

$$\begin{aligned} \begin{pmatrix} v_1 \\ v_2 \\ v_3 \end{pmatrix}_{int} &= \frac{V(R')}{[\cos^2 i \cos^2(\phi - \theta) + \sin^2(\phi - \theta)]^{1/2}} \\ &\times \begin{pmatrix} -\sin i \cos(\phi - \theta)[\cos i \cos\rho - \sin i \sin\rho \sin(\phi - \theta)] \\ \sin i \cos(\phi - \theta)[\cos i \sin\rho + \sin i \cos\rho \sin(\phi - \theta)] \\ -[\cos^2 i \cos^2(\phi - \theta) + \sin^2(\phi - \theta)] \end{pmatrix} \end{aligned} \tag{2.4}$$

where,

$$R' = \frac{D_0 \sin\rho[\cos^2 i \cos^2(\phi - \theta) + \sin^2(\phi - \theta)]}{\cos i \cos\rho - \sin i \sin\rho \sin(\phi - \theta)}$$

In equation 2.4, R′ represents the radial distance in the galaxy plane, and V(R′) represents the rotational velocity in the galaxy plane. The galaxy's rotation is parameterized differently, following the approaches of N22 and D18, based on their respective studies of the LMC and SMC. The adopted parametric forms for V(R′) are provided below.

$$V(R') = v_0[1 + (\frac{R_0}{R'})^{\eta}]^{-1/\eta}, \text{ for LMC} \tag{2.5}$$

$$V(R') = \frac{2}{\pi} v_f \arctan(\frac{R'}{R_f}), \text{ for SMC} \tag{2.6}$$

In equation 2.5 for the LMC, v_0 represents the amplitude of the saturated rotational velocity in the disk plane of the galaxy, R_0 represent the galaxy's scale radius, and η optimizes the turning point of rotation curve to saturation, aiding in tuning with sharper or gradual transition to v_0. In equation 2.6 for the SMC, v_f represents the asymptotic velocity from the rotational velocity in the disk plane of the galaxy, and R_f represents the galaxy's scale radius. The best fitting kinematics parameters for the galaxy are estimated based on the MCMC algorithm described in section 2.2.3, and detailed in Chapters 4 and 5.

Chapter 3

Tracing the cluster formation history of the Magellanic Clouds

3.1 Introduction

In this chapter, we focused on determining cluster parameters located in the outer regions of both MCs. Earlier study by G10 reported age estimates for 1193 clusters in the LMC and 324 in the SMC. Additionally, N16 and N18 provided age determinations for 1072 LMC clusters and 179 SMC clusters. Similarly, other studies have also contributed to age estimations of star clusters in the MCs(Chiosi et al. 2006; Palma et al. 2016; Piatti et al. 2018). However, these clusters are located towards the center of the MCs. The age estimations of the clusters distributed globally in the main body of the MCs are very important to trace the effect of their mutual interactions. This study is an attempt to produce a wide spatio-temporal CFH in the MCs.

This study has four main objectives: (1) to expand the catalog of well-characterized clusters in the MCs, with particular emphasis on the outskirts of the LMC; (2) To create an automated approach for determining cluster properties, such as age, extinction, metallicity, and distance from their CMDs; 3) To trace the Episodic Cluster Formation (ECF) history and obtain the signatures of interaction history between the MCs or with the MW; 4) To trace the density structures traced by clusters (such as bar/ spiral arm) as well as signatures of trigger/ shrinkage/ truncation of CF in the outer parts of the MCs.

This chapter is organized as follows. Section 3.2 outlines the data set and the steps taken for data reduction in this work. Section 3.3 details the automated techniques employed for estimating cluster parameters. In Section 3.4, we present our estimated age-extinction-metallicity-distance values for the clusters we characterized, along with the spatial age maps, ECF history, and radial cluster density profiles. The discussions based on our results are presented in Section 3.5, followed by Section 3.6, which covers the summary of our work. The results presented in this chapter are available in Dhanush et al. (2024a).

3.2 Data

This study used the data from the *Gaia* DR3 survey in G, G_{BP} and G_{RP} passbands. We considered 4041 star clusters taken from B08, S16 and S17 catalogs for this study, among which 3330 and 711 clusters belong to LMC and SMC, respectively. The central coordinates of the clusters, specified in Right Ascension (α) and Declination (δ), along with their radii (r_c), are taken from these catalogs. This study is focused on analyzing a large sample of star clusters that span a broad range of ages. As manual estimation of parameters is tiresome and liable to subjectivity, the entire process of cluster parameterization was automated. Before the automated parameterization was performed, we first selected clusters suitable for this study based on their position in the sky and the presence of neighboring/overlapping clusters in the LOS. The bulk handling of the *Gaia* archival data in our analyses was performed with the *Gaia* Asynchronous query services available in the `astroquery` (Ginsburg et al. 2019) python package.

The next stage involves cleaning star cluster data sets from field star contamination, where we used an FSD algorithm, which was obtained by modifying and improving the technique used by N16 (as detailed in the section 2.2.2). The following subsections detail the data reduction techniques we adopted in our study.

3.2.1 Classifications of clusters based on spatial overlap

The estimation of cluster membership is performed using the statistical subtraction of field stars using one or more nearby field regions for comparison. First and foremost, we need to ensure that the chosen field region is not a part of another cluster, as there may be a number of clusters located nearby. Therefore, each cluster is checked to identify star clusters that overlap in their spatial extend along the LOS.

We identified neighboring star clusters based on the angular separation between their centers. As a result, we classified star clusters as isolated and overlapping based on their spatial distribution in the LOS. The classification of star clusters as per the scheme is shown in Figure 3.1. Towards the central regions, many of the clusters appear to overlap in the LOS, as expected. The outer clusters are mostly isolated as they are well separated from each other. Figure 3.1a shows the isolated and spatially overlapping star clusters in the LOS. Out of 4041 cluster candidates, we have found 3019 isolated star clusters. The rest, 1022 clusters, were flagged as overlapping star clusters in the LOS. Also, each cluster is categorized based on the

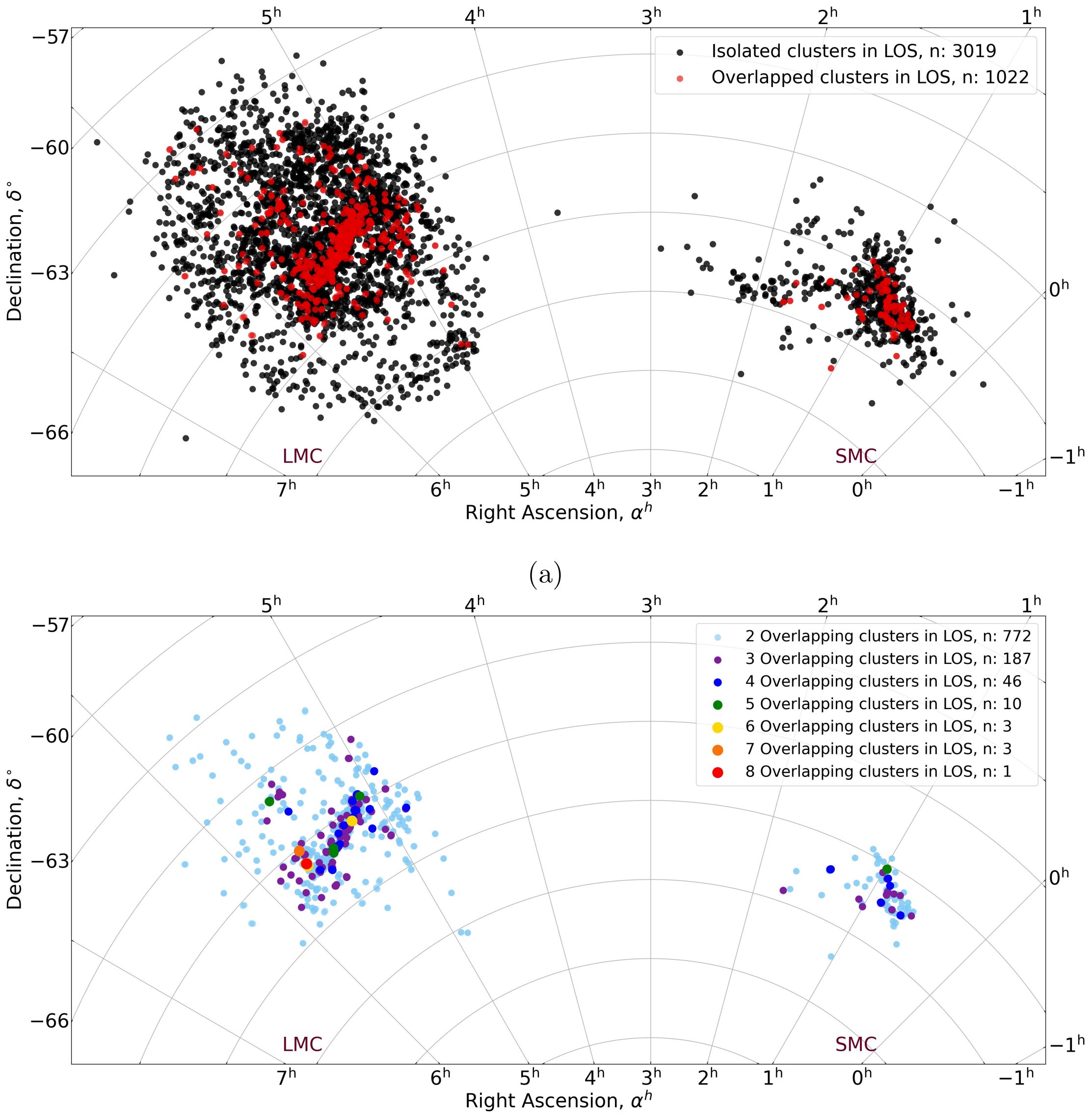

(a)

(b)

FIGURE 3.1: Spatial classification of star clusters in the MCs based on the LOS. a) The isolated clusters in the LOS (black dot) and overlapping clusters in the LOS (red dot) of the MCs in the sky plane. The number of clusters in each group is shown in the legend. b) The classification is based on the number (ranging from 2 to 8) of overlapping clusters in the LOS of the MCs color-coded as shown in the legend.

number of neighboring clusters overlapping into the cluster region. Figure 3.1b shows the classification based on the number of overlapping clusters ranging from 2 to 8. We note a large population of more than 4 overlapping clusters in the bar region of the LMC and a few such systems in the central SMC. The two-cluster overlap appears to have a wider spread but is confined to the inner regions.

The clusters classified based on spatial overlap need to be cleaned from the LOS field star contamination in the cluster regions. To perform the cleaning, we need to select the cluster workspaces for each clusters. We followed the procedure to select the workspaces in different groups, as detailed in section 2.2.1. We classified 2294 clusters in Group-1, 501 clusters in Group-2, 224 clusters in Group-3, and 772 clusters in Group-4. A total of 250 clusters were excluded from our classification due to their location in crowded regions of the galaxies, where they appear as overlapping clusters. Further, we applied certain selection criteria to select the *Gaia* sources within the 3791 workspaces. These are discussed below.

3.2.2 Selection criteria of *Gaia* sources in the workspace

The *Gaia* selection criteria for the sources in each cluster workspace are enumerated below.

1. Selected sources brighter than 20.5 mag in G.
2. Removed the NULL value sources in G_{BP} and G_{RP}.
3. Selected sources with RUWE (Re-normalized Unit Weight Error) < 1.4
4. Selected sources with $\leq 2\sigma$ of PM and parallax from the mean PM and parallax of all sources. Applied to cluster regions and each available field region in the workspace.

The G-band photometric uncertainties are up to $\sim$ 1 mmag for G$\leq$17 and 6 mmag for G$=$ 20. Meanwhile, the G$_{BP}$ and G$_{RP}$$>$ 20 mag have uncertainties greater than 50 mmag. For the reason, we considered sources brighter than 20.5 mag in our study, as we performed the parameter estimation accounting for the error in the magnitude and color of the sources. The *Gaia* data have NULL values for sources not satisfying the photometry selection criteria as mentioned in Riello et al. (2021), we removed such data points from each cluster workspace as well. The RUWE value < 1.4 is suggested by *Gaia* studies for the most probable singular sources in their catalog (Lindegren et al. 2018; Gaia Collaboration et al. 2023b).

The PM and parallax cut-off of $\leq 2\sigma$ we adopted helps in removing the highly deviant PM sources, most likely foreground MW contaminants from the dataset. The criteria were applied to cluster region and available field regions depending on the type of cluster workspace as mentioned in subsection 2.2.1. We note that the Gaia parallax is not a good distance estimator for sources located more than a few kpc, since the value lies very close to the parallax zero-point value (G21; Lindegren et al. 2021). But parallax is important to remove nearby MW sources that fall in the LOS of MC or MC cluster workspaces.

After applying the stated selection criteria as mentioned above, the workspaces and their associated data sets were fetched onto the local machine utilizing the *Gaia* Asynchronous query. The rest of the field star removal from the MCs was carried out with the FSD algorithm (as detailed in section 2.2.2). The cleaned clusters are ready for parameter estimation, these are discussed in the following section.

3.3 Estimation of cluster parameters.

At the end stage of FSD we obtained the cleaned cluster CMDs, which are now satisfactory to perform parameter estimation. We automated this stage by setting up prior age and extinction estimates for the clusters, followed by a set of selection criteria for the best-fitted CMDs with prior knowledge, and finally estimated the four cluster parameters with the MCMC sampling technique. The detailed procedures are provided below.

3.3.1 Setting up prior age and extinction estimates for the clusters

We used the cleaned CMDs to estimate the maximum likelihood of age by comparing them with theoretical isochrones. We used the PARSEC stellar evolutionary tracks (section 2.3.1) to generate the theoretical isochrones for our study. As per the previous studies, prior values of $Z_{\rm LMC} = 0.008$ and $Z_{\rm SMC} = 0.004$ were adopted as the LMC (N16 sample) and the SMC (N18 sample) metal fractions, respectively. The distance modulus (DM) to the center of the LMC was taken as 18.47 mag (Pietrzyński et al. 2019). The DM value for a given cluster in the LMC was modified by accounting for an inclination of $i = 23^\circ.26$ and a position angle of the line of nodes, $\Phi = 160^\circ.43$ (S22). In the case of the SMC, a value of 18.97 mag was assumed for all the clusters. Though there is a large depth in the SMC (Subramanian & Subramaniam 2009), this quantity cannot be incorporated as a function of any known parameters. Also, a few clusters in the bridge region were given attributes similar to the SMC.

As per the prior assumptions, we estimated the maximum likelihood of age, $\log(t)$ and extinction, A_G for the star clusters. We used an age range of 1 Myr to 10 Gyr ($\log(t) = 6$ to 10, respectively), with a spacing of $\Delta\log(t) = 0.05$ for fitting the isochrone models to the cleaned CMDs. For the interstellar extinction, we adopted a range of $A_G = 0$ to 0.836 mag (corresponding to a range of $A_V = 0$ to 1 mag), with a step size of $\Delta A_G = 0.01$ mag. The isochrone fitting to the observed CMD was an iterative process in the parameter space available for each cluster

CMD. First, all the theoretical isochrones of different $\log(t)$ and A_G values were pushed to the DM of the LMC and the SMC. Then we implemented a least square fitting method to the observed data points of the cluster CMD and the model isochrone points. The global minima of the least square deviations from about 80 models ($[\log(t)]/\Delta\log(t)$, constant $A_G = 0.45$) were found initially. Later, from the estimated initial fit parameters ($\log(t)_i, A_{G_i}$), we considered a reduced parameter space of $\log(t)$ range [$\log(t)_i - 0.6$ to $\log(t)_i + 0.6$] and A_G range [0 to 0.836 mag] to redo the least square fitting, we used this iteration to close the gap between the most likely model and the observed data. One more iteration was performed by removing the scattered field stars in the cleaned CMDs. We adopted a 1.5σ clip from the mean least square deviations to remove scattered data points. By doing so, convergence to a unique model with reduced error was achieved, with the best-fitting isochrone closely representing the features of the observed CMD.

The ordinary χ^2 minimization does not yield the best-fitting isochrone for the cluster CMD, as multiple combinations of parameters can give the minimum χ^2 values while fitting models to data (D'Antona et al. 2018; Souza et al. 2020). So, we defined an error-weighted modified χ^2 value to the fit for the clusters to define our selection criteria. The *Gaia* G magnitudes have errors of the order of $\sim 10^{-3}$ mag, corresponding to significantly less error in observed fluxes, resulting in high χ^2 values. As the error propagation in color ($G_{BP} - G_{RP}$) term is larger compared to the magnitude for a given star in the CMD, the error weighting was considered only on the color term, while estimating the χ^2 value of the best fitting isochrone model. We used three modified χ^2 options where the observed flux errors (corresponding to G_{BP}, G_{RP} magnitudes) of the stars were at least 2%, 4%, or 10% of the observed fluxes ($F_{i,o}$). After testing the fits with a smaller sample of clusters, we fixed the observed error in flux to be at least 4% and estimated the modified χ^2 values. For a CMD with data points of observed color ($c_{i,o}$) and model color ($c_{i,m}$), the modified chi-square (χ_f^2) is given by,

$$\chi_f^2 = \frac{1}{N-2}\sum_{i=1}^{N}\left\{\frac{(c_{i,o}-c_{i,m})^2}{s_i^2}\right\} \tag{3.1}$$

where

$$s_{i,o} = \sigma_{ci} \forall (\sigma_{fi} \geq 0.04 f_i), 0.04 \ \forall \ (\sigma_{fi} \leq 0.04 f_i),$$

Hence, we identified the best-fitting isochrones and the corresponding χ_f^2 values for all the cleaned CMDs. The age and extinction parameters corresponding to the best-fitting isochrone were estimated for all cleaned CMDs. In the case of Groups-3 & 4, only one cleaned CMD was created and therefore only one set of parameters was estimated per cluster. Two sample clusters and isochrone-fitted CMDs are shown in Figures 3.2 and 3.3.

In the case of Groups-1 & 2, where multiple annular field regions are used for FSD, the isochrone fitting along with the parameter estimation was performed on all the cleaned CMDs of a cluster. We found that star clusters in Groups-1 & 2 showed variation in the number of retained members in CMDs, depending on the number of annuli used in FSD. Depending on the spatial crowding in nearby field regions, the number of annular regions used for FSD was found to have a considerable effect on the cleaning process, even in the case of dense clusters and particularly for those in the central regions. In the case of isolated poor star clusters, a significant number of cluster members were not retained in the cleaned CMD if all five annular field regions were used. The above observations suggested that the choice of best cleaned CMD for a cluster should be made by considering, (1) the variation in the estimated parameters as a function of the number of annular field regions used in FSD, (2) over-subtraction of possible cluster members in the CMDs as a function of the number of annular fields used in FSD, (3) χ_f^2 value of the fit, and (4) visual goodness of isochrone fit to the cleaned CMD. We describe the adopted criteria to

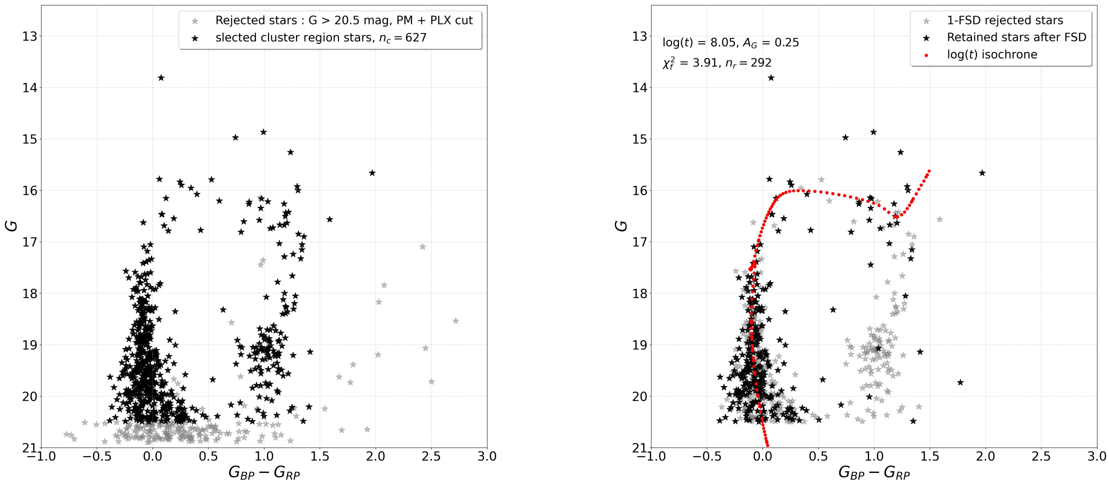

(a) NGC458, CMD of cluster region

(b) Cleaned and fitted CMD after 1-FSD

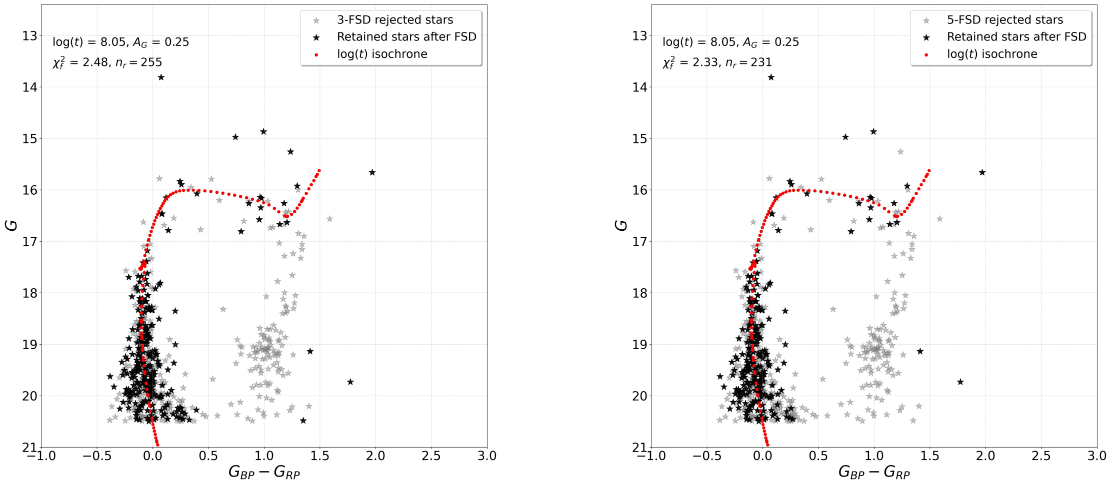

(c) Cleaned and fitted CMD after 3-FSD

(d) Cleaned and fitted CMD after 5-FSD

FIGURE 3.2: NGC458, a) Cluster CMD with initial selection criteria (PM, parallax, and G magnitude cut-offs). b) Cleaned CMDs (1-FSD, 3-FSD, and 5-FSD) with the parameters (log(t), A$_G$, and χ^2) estimated at DM = 18.977 are provided in each stages of FSD. In higher stages of FSD, the number of retained cluster members decreases because of the field star subtraction.

choose the best cleaned CMD for clusters belonging to Groups-1 & 2, in the next section.

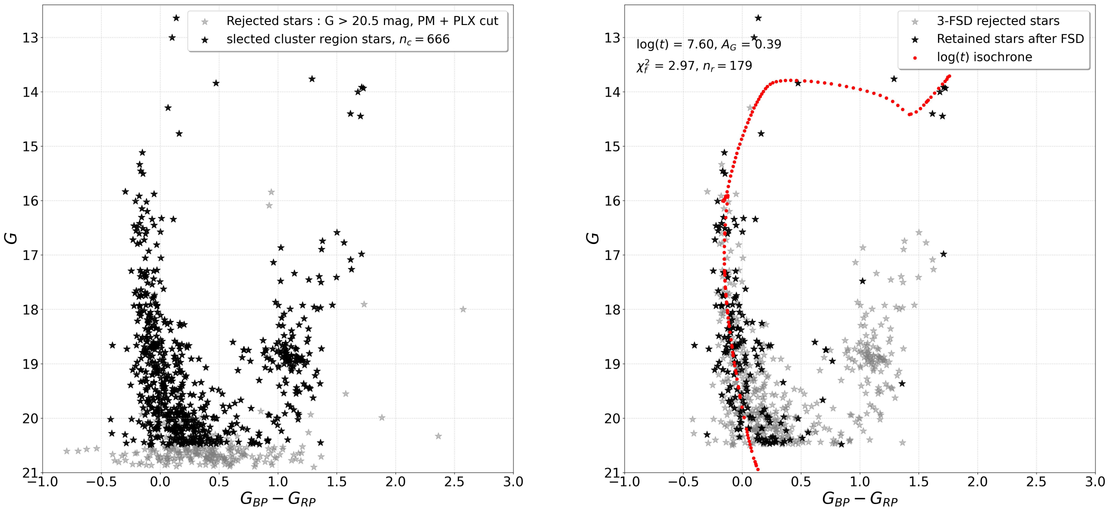

(a) NGC1735, CMD of cluster region

(b) Cleaned and fitted CMD after FSD

FIGURE 3.3: NGC1735: a) Cluster CMD with initial selection criteria (PM, parallax, and G magnitude cut-offs). b) The parameters ($\log(t)$, A_G, and χ^2) estimated at DM = 18.53 are provided. The cluster region after FSD shows a significant decrease in field stars.

3.3.2 Selection criteria for the cleaned cluster CMDs.

In the case of Groups-1 & 2 clusters, the cluster parameters and the χ_f^2 values differ for the n-FSD cleaned CMDs (n = 1 to 5) of the same cluster. In order to identify and retain the best isochrone-fitted cleaned CMD for a cluster, we implemented the following selection criteria in three steps:

(1) We applied a cut-off of $\chi_f^2 \leq 15$, based on a visual check of the fitted CMDs of a smaller sample of clusters to remove bad fits.

(2) We compared 3-FSD and 5-FSD CMDs for the same cluster and retained those clusters with age separation within $|\Delta \log(t)| \leq 0.1$ (absolute difference between 3-FSD and 5-FSD $\log(t)$), so that the number of field annuli used in the FSD did not influence the estimated age.

(3) We used a $|\Delta\chi_f^2| \leq 1$ (difference between 3-FSD and 5-FSD χ_f^2) to retain clusters that did not show a significant difference in the estimated parameters, such that the number of field annuli used in the FSD did not influence the quality of fit. Since the over-subtraction of cluster members generally happens more in the 5-FSD CMDs than in the 3-FSD CMDs, we selected the 3-FSD CMDs as the best-fit CMDs and the corresponding parameters for these clusters.

The plots comparing the $\log(t)$ and the χ_f^2 in the steps mentioned above for the various FSDs are shown in Figure 3.4.

In the case of clusters with $|\Delta\chi_f^2| > 1$, as per the criterion in step (3), but satisfying the criterion in step (2), we compared χ_f^2 values from 3-FSD and 5-FSD fits, then retained that with the lesser value of χ_f^2 and the corresponding parameters. This case suggests the possibility of over-subtraction of members in the 5-FSD. Clusters with $|\Delta\log(t)| > 0.1$ after step (2) suggest that the estimated parameters are impacted by the choice of FSD, which results from the number of annular regions used. Therefore, as a next step to reduce deviation in the estimated parameters, we compared the fits of the 4-FSD and 2-FSD CMDs as in the above-indicated step (2), followed by the same steps as for the 5-FSD and 3-FSD CMDs. Clusters with $|\Delta\log(t)| > 0.1$ in this step were then taken to the next step of 2-FSD and 1-FSD comparison. All clusters reaching this stage will have either parameter from the 2-FSD or 1-FSD fits.

The above series of procedures is expected to reduce any impact of the methods of FSD used in the estimation of the cluster parameters. We used two quantities, the deviation in age as well as the difference in χ_f^2, as control parameters to finally choose the number of annuli used in the FSD, instead of arbitrarily deciding the number of annuli for FSD. We believe that this helps to reduce erroneous parameter estimation due to variable field star density, over-subtraction of members in poor

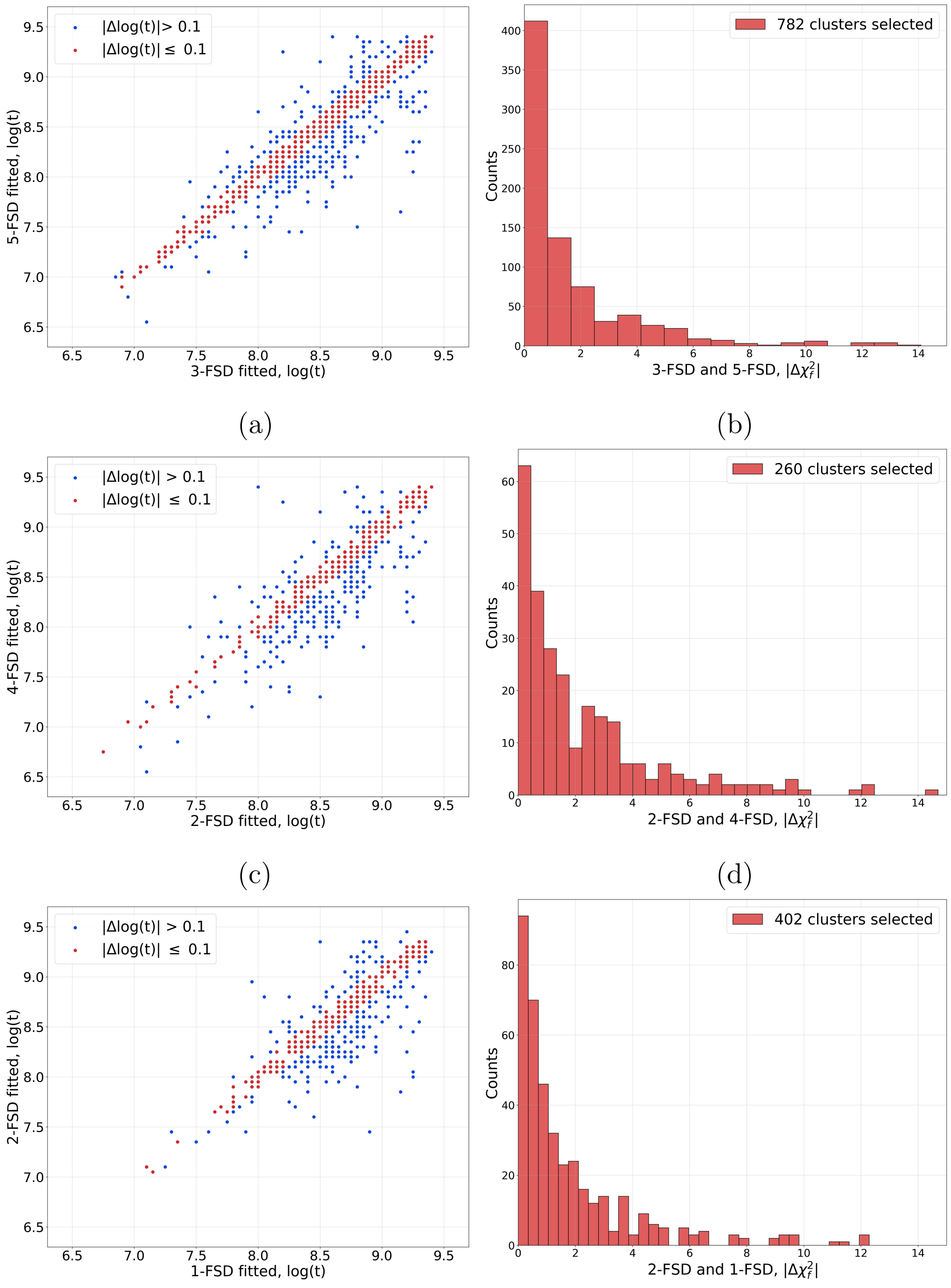

(a) (b)

(c) (d)

(e) (f)

FIGURE 3.4: The selection criterion discussed in subsection 3.3.2 for choosing the best cleaned CMD for clusters having multiple stages of FSD is shown here.

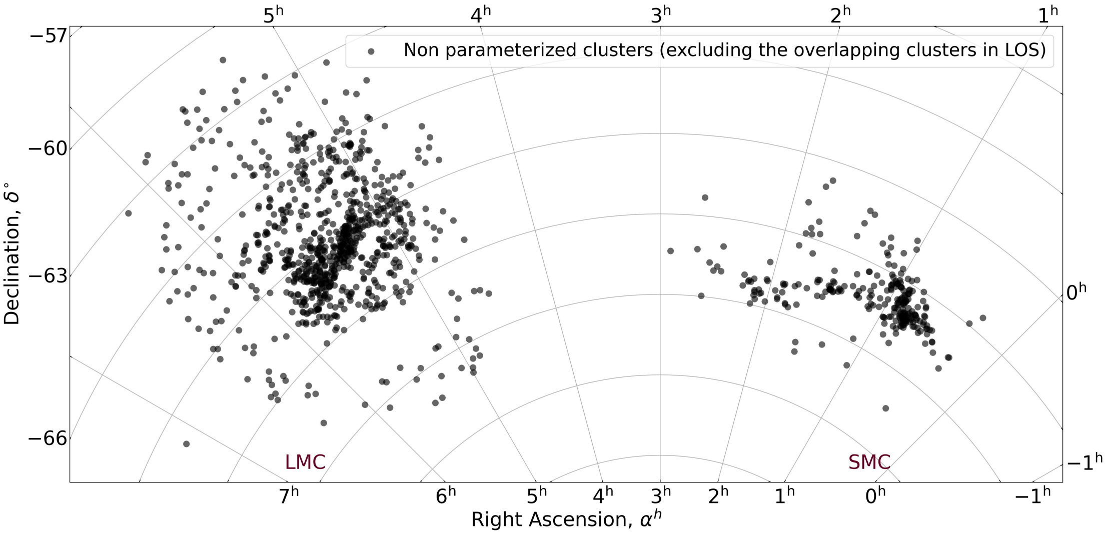

FIGURE 3.5: The above cluster locations (shown in black) are those we left out from parameterization. It includes 643 isolated clusters and 439 partially overlapping clusters in LOS. They are either poor clusters or residing in crowded regions of the galaxies, resulting in a cleaned CMD that cannot be parameterized.

clusters, and statistical fluctuation in field stars located in the dense regions of the MCs. In the case of Groups-3 & 4 clusters with only one CMD after FSD, we applied $\chi_f^2 \leq 20$ to filter in. Since the clusters in these two groups have only one field star region for FSD and are likely to introduce scatter in the CMDs, a slightly higher cut-off of χ_f^2 is justified.

Though the entire process was automated from FSD to isochrone fitting, a visual inspection of the final fitted CMDs was required to check for any spurious fits. Hence we inspected all the cluster CMDs after the completion of parameter estimation and manually rejected a few improperly cleaned/ fitted CMDs (26 clusters).

We note that we did not consider poor clusters with less than 8 stars in the cleaned CMDs, apart from the overlapping clusters, as mentioned earlier. The typical number of our cluster members, retained after FSD, averages to 40. We also did not retain clusters for which we were not able to get good fits (as decided by visual inspection) and/or with $\chi_f^2 > 20$. A map of the 1082 non-characterized clusters is shown in Figure 3.5.

The distribution of χ_f^2 for the finally selected CMDs of the retained 1990 clusters is shown in Figure 3.6. The peak of the distribution with more than 300 clusters is at $\sim \chi_f^2 = 1.25$, and about 1000 clusters ($\sim$ 50%) have χ_f^2 value within 1σ of the distribution. We conclude that these final fits are therefore satisfactory, based on the χ_f^2 values and visual inspection.

We estimated satisfactory parameters of 1990 clusters, of which 1710 are in the LMC and 280 are in the SMC. Out of the estimated parameters of clusters, 1651 clusters belong to Group-1, 169 clusters belong to Group-2, 117 clusters belong to Group-3, and 53 clusters belong to Group-4. We characterized 960 clusters ($\sim$ 48.2%) for the first time in comparison to the existing star cluster catalogs of the MCs (Pietrzynski & Udalski 2000, 1999; Chiosi et al. 2006; G10; Palma et al. 2016; N16; N18). Among these, 847 clusters ($\sim$ 49.5% of 1710) are in the LMC and 113 ($\sim$ 40.3% of 280) in the SMC. The following section deals with the MCMC sampling to arrive at the final estimates of age, extinction, DM, and metallicity of clusters from their prior assumptions.

3.3.3 MCMC sampling to estimate age, extinction, DM, and metallicity

The estimated age-extinction-metallicity-distance values associated with clusters are sensitive to the choice and combination of model parameter values. Also, in the previous section, age and extinction were estimated for a fixed value of metallicity and distance. So we used MCMC sampling method to arrive at the final estimates of all of the above four parameters.

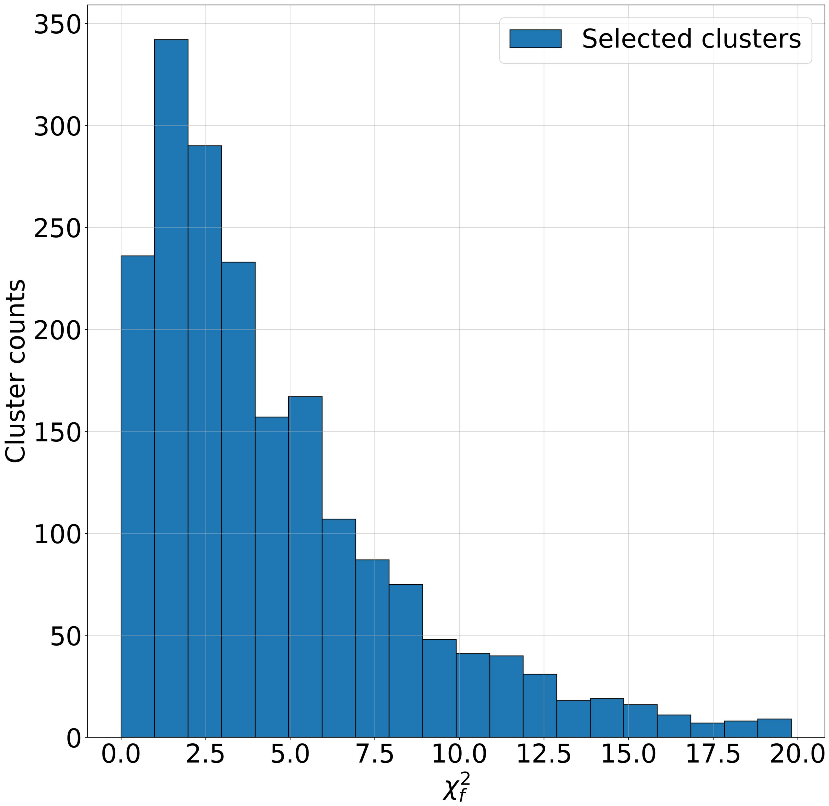

FIGURE 3.6: The χ^2_f distribution for the selected 1990 clusters, with a cut-off of $\chi^2_f \leq 20$ to retain the best isochrone-fitted cleaned CMD.

In order to perform an MCMC sampling, we defined a range for the parameters, within which the sampling is performed. As 960 clusters ($\sim$ 48% of 1990) are characterized for the first time, there are no other estimations available to constrain the parameter range. Hence the uniform priors were adopted for the extinction (A_G) and metallicity during the MCMC sampling. As the SMC is known to be more metal-poor than the LMC, we adopted a Z range of [0.0006 to 0.005] for the SMC, and [0.0015 to 0.01] for the LMC. The assumed Z range is consistent with the prior $Z_{\text{LMC}} = 0.008$ and $Z_{\text{SMC}} = 0.004$ that we adopted (subsection 3.3.1) for the SMC and LMC, respectively. We implemented bilinear interpolation using fine grid spacings in both parameters: an age step size of 0.02 in log(age) and a metallicity step size of 0.0002 in Z. This approach ensures precise generation of synthetic isochrones for each random age and metallicity value sampled during the MCMC iterations. The extinction (A_G) was allowed to vary from 0 to 0.836 and the DM to vary within 0.25 mag from the prior assumption. In the case of age, the sampling was confined within the 15% change from the maximum likelihood age estimated from the prior information. The goal was to get the expected change in A_G, Z, and DM from their prior assumptions and to obtain a robust age estimation.

The sampling likelihood function (LF) is defined to be the average χ^2_f associated with each CMD data point (magnitude, color, magnitude error, color error: $m_{i,o}$, $c_{i,o}$, sm_i, sc_i) and nearest isochrone model data points (model magnitude, model color: $m_{i,m}$, $c_{i,m}$). The sm_i, sc_i represent the scaled error values after taking the flux errors to be at least 4% of the observed flux values (as explained in subsection 3.3.1). And the LF is given in the following equation,

$$LF = \frac{-1}{N} \sum_{i=1}^{N} \left\{ \frac{(m_{i,o} - m_{i,m})^2}{{sm_i}^2} + \frac{(c_{i,o} - c_{i,m})^2}{{sc_i}^2} \right\} \tag{3.2}$$

The cleaned CMDs have the presence of randomly scattered field stars (as mentioned in subsection 2.2.2). For the reason, within the color-magnitude space for a given cluster, we considered stars within 1σ deviation with respect to the prior estimates (log(t), A_G, Z, DM) for that cluster.

The sampling uses a Bayesian approach with an ensemble of multiple walkers (20 walkers) with a stretch moves to explore the parameter space (section 2.2.3). In addition, the standard Metropolis-Hastings algorithm is also used for the proposal moves with a tuned acceptance ratio of 0.225 to 0.35 during the iteration phase. The iterations were performed with the mixture of different moves till the convergence was achieved in the posterior distribution of samples.

The sampled posterior distributions of a sample cluster (NGC458) is shown in Figure 3.7. The MCMC sampling mainly explores the parameter space in A_G, DM, and Z to find the range under which our age estimates have confidence. Also, MCMC sampling solves the expected values for A_G, DM, and Z with its

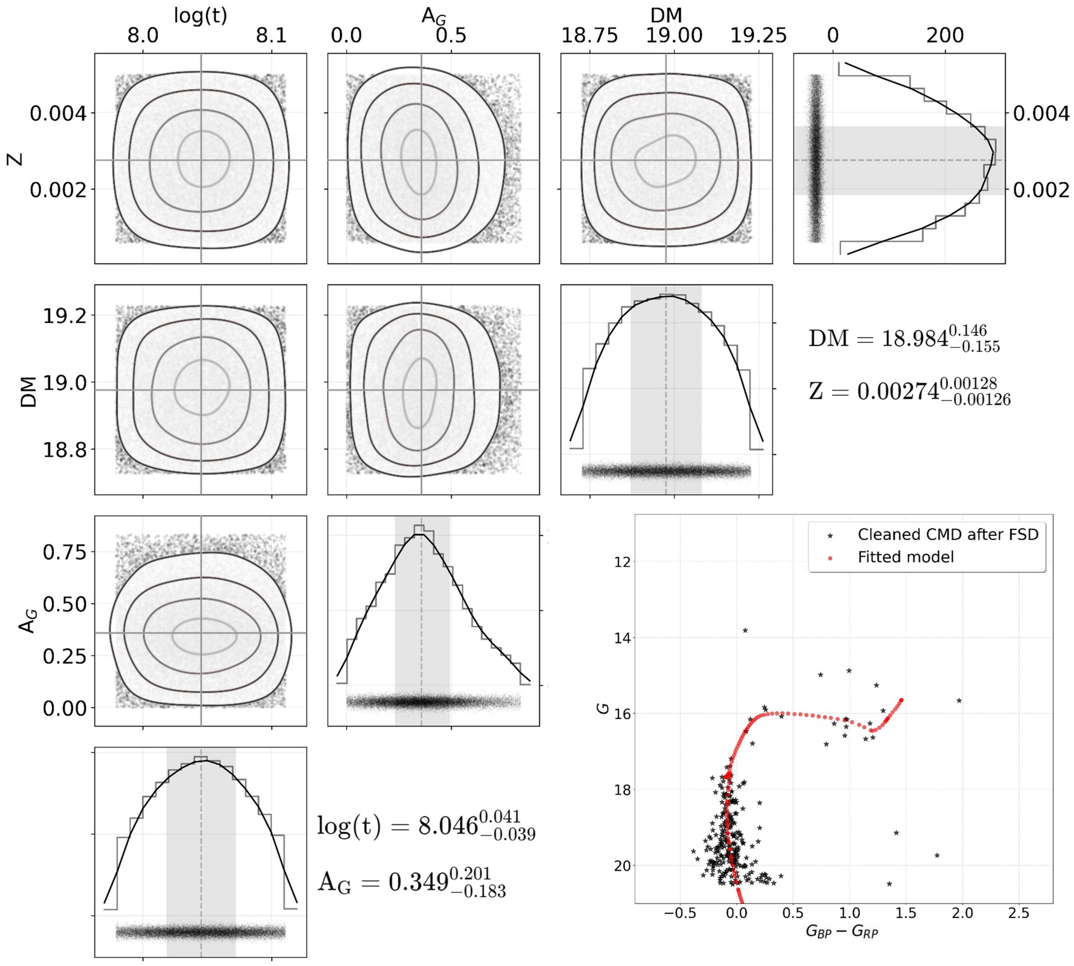

Figure 3.7: The sampled posterior distributions (corner plot) for the four-parameter estimation of cluster NGC458. The shaded regions in the histogram represent the 1σ region from the 50 percentile (dashed line in histograms) for $\log(t)$, A_G, DM, and Z. The 50 percentile values are chosen as the best parameter for the isochrone fitting. The cleaned CMD of NGC458 is fitted with the isochrone generated using the best-fit parameters.

uncertainties, which cannot be easily obtained using the ordinary χ^2 minimization.

3.4 Results

This is the first comprehensive study of star clusters in the MCs using the *Gaia* DR3 data, where the parameters are estimated using an MCMC sampling from the assumed priors. The clusters are parameterized after removing the field stars from the cluster CMD. Considering the uniform data coverage of the *Gaia* data, the exclusion of overlapping clusters in the LOS, and the implementation of the FSD by eliminating foreground stars and kinematically deviant sources, this study provides reliable parameters to explore the star cluster properties of the MCs. As mentioned in subsection 3.3.2, we estimated parameters for 1990 star clusters. This study identifies and characterizes 960 new clusters, the majority of which are situated in the outer parts of the MCs. In particular, the new clusters parametrized in the outskirts of the LMC significantly enhance our understanding of the galaxy, specifically beyond a distance of 4 kpc from its center.

To compare and understand the region-wise difference among clusters in various locations, the cluster coordinates need to be transformed from the skyplane to the galaxy plane. For the LMC, the cluster positions on the sky are projected onto the plane of the LMC disk using the transformation equations provided by van der Marel (2001). However, due to the complex morphology and unclear structure of the SMC, the cluster positions are retained in the Cartesian projection on the sky, centered on the SMC. The adopted central coordinates for both the LMC and SMC are taken from de Vaucouleurs & Freeman (1972b). The upcoming sections present the extinction and metallicity distributions, CFH, and the spatio-temporal map of clsuter distribution.

3.4.1 Extinction and metallicity maps

The extinction and the metallicity parameters for 1990 star clusters are presented here. The extinction histograms for the LMC and the SMC are shown in Figures 3.8a and 3.8c, with the mean extinction estimated as $\mu_e = 0.40 \pm 0.005$ mag and 0.38 ± 0.006 mag respectively. We adopted the constant R_V of 3.41 (Gordon et al. 2003) for the LMC and 2.72 (O'Donnell 1994) for the SMC in our reddening

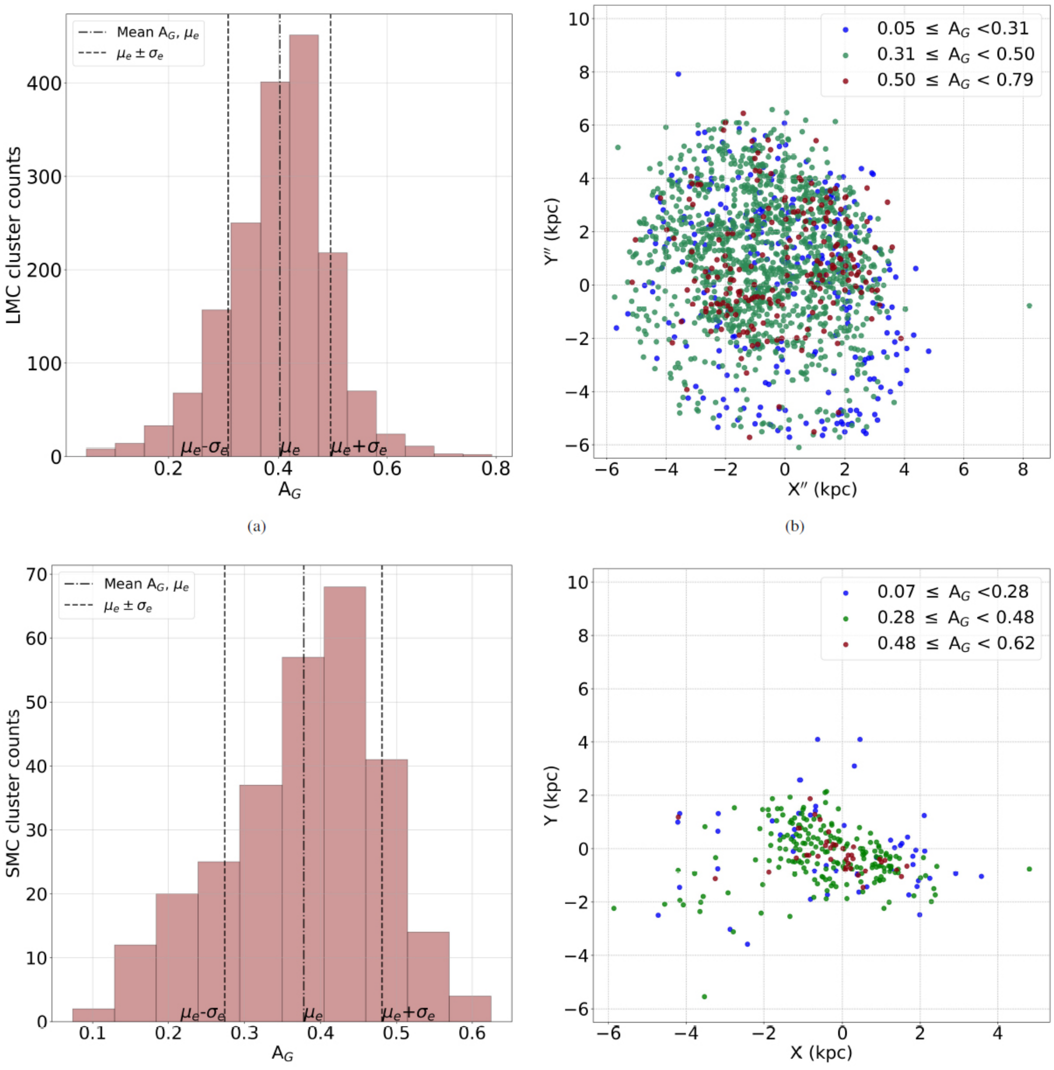

(a) (b)

(c) (d)

FIGURE 3.8: Spatial map and distribution of extinction (A_G) from the 1990 star clusters in the MCs. The bin width of 0.25× median error of cluster A_G estimations (50 percentile) is used here to generate the histograms. The three groups are color-coded based on the mean (μ_e) and standard deviation (σ_e) of A_G distribution as mentioned in subsection 3.4.1.

estimations. The mean reddening values in $E(B-V)$ are estimated as 0.14 ± 0.001 mag and 0.16 ± 0.003 mag for the LMC and the SMC, respectively. The spatial extinction maps of the LMC and the SMC clusters are shown in Figures 3.8b and 3.8d respectively, where three groups ($A_G < \mu_e - \sigma_e$, $\mu_e - \sigma_e \leq A_G < \mu_e + \sigma_e$, $A_G \geq \mu_e + \sigma_e$) are shown with blue, green and red colors, respectively. The central regions of the LMC and the SMC appear to have higher extinction than the outer regions. In the case of the LMC, a significant amount of clusters can be seen

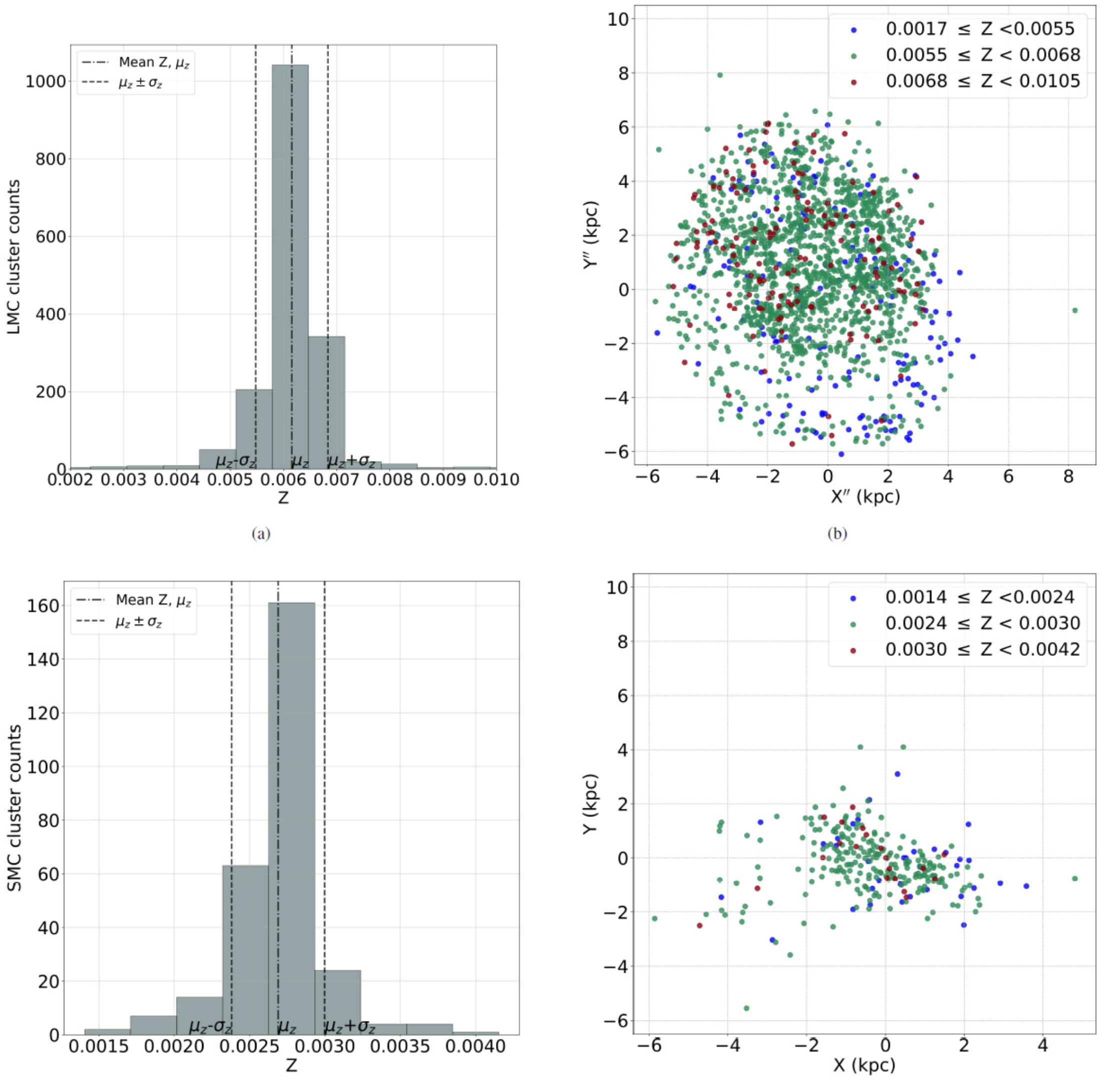

(a) (b)

(c) (d)

FIGURE 3.9: Spatial map and metallicity (Z) distribution of 1990 star clusters in the MCs. The bin width of 0.25 times the median error (50 percentile) in Z estimations are used here to generate the histograms. The three groups are color-coded based on the mean (μ_z) and standard deviation (σ_z) of Z distribution as mentioned in subsection 3.4.1.

towards the northern part, with higher extinction than in the South. The ring of clusters on the outskirts of the LMC has lower extinction than the rest. As this study has covered more clusters in the outer LMC, where the extinction/ reddening is low, the average values for the LMC also tend to be on the lower side.

The metal fraction (Z) is also estimated using the uniform priors about the prior knowledge ($Z = 0.008$ for the LMC and $Z = 0.004$ for the SMC) as mentioned in subsection 3.3.3. The distributions of the estimated Z are shown in Figures 3.9a and 3.9c for the LMC and the SMC clusters, respectively. We estimated a mean metal fraction, $\mu_z = 0.006 \pm 0.00002$ for the clusters in the LMC, and $\mu_z = 0.0027 \pm 0.00002$ for the clusters in the SMC. The spatial maps of Z for the LMC and the SMC clusters are shown in Figures 3.9b and 3.9d respectively, where three groups (Z$< \mu_z - \sigma_z$, $\mu_z - \sigma_z \leq$Z$< \mu_z + \sigma_z$, Z$\geq \mu_z + \sigma_z$) are shown with blue, green and red colors, respectively. In the LMC, the spatial plot shows a relatively larger number of metal-rich clusters (shown in red) towards the North and North-East of the galaxy, whereas the southern LMC has more of the metal-poor clusters (shown in blue). In the case of the SMC, the spatial plot shows metal enrichment towards the central regions compared to the outer regions. Based on this study, we recommend that the choice of Z value for isochrones to fit the CMDs of clusters with age $\leq$ 1 - 2 Gyr is 0.004 to 0.008 for the LMC and 0.0016 to 0.004 for the SMC.

The PARSEC models also give the [M/H] values corresponding to the Z values of the isochrones. Based on this, we calculated the mean [M/H] values to be -0.40 ± 0.001 dex and -0.76 ± 0.003 dex for the LMC and the SMC, respectively. We note that the mean [M/H] estimated here is for the case of clusters younger than 1-2 Gyr age.

The DM for each star cluster was constrained during MCMC sampling, allowing for a variation of 0.25 mag from the prior values. We note that the posterior values of DM did not show any significant deviation from their prior values. Since the young clusters mostly do not have the RGB population in the cleaned CMDs, the degeneracy of the DM, A_G, and $\log(t)$ is present in our estimates. But as mentioned in subsection 3.3.3, the parameter estimation is weighed to find the best age of the cluster and the expected variation of other cluster parameters.

3.4.2 Estimated age distribution and Episodic Cluster Formation in the MCs

The age distributions for the LMC and the SMC star clusters are shown in Figures 3.10a and 3.10b. In general, CF can be continuous or discontinuous in galaxies. When the CF is discontinuous, the CFH is likely to show peaks of CF episodes. In this study, we aim to detect these ECF and correlate the time scales with any external event in the galaxy. The spatial age map of the star clusters in the MCs is shown in Figure 3.10c on the sky plane, and they are segregated into four age groups in ranges of $\log(t)$, Age group-1: $[\geq 9.10, < 9.55]$, Age group-2: $[\geq 8.65, < 9.10]$, Age group-3: $[\geq 8.0, < 8.65]$, Age group-4: $[\geq 6.55, < 8.0]$. The grouping is made to track the age span from old to young clusters in the MCs, and they were visually selected based on the presence of prominent peaks in the ECF of the MCs.

In the LMC, the peaks of ECF are obtained at $\log(t) = 9.17 \pm 0.036$, 8.93 ± 0.036 corresponding to linear ages of $1.48^{+0.13}_{-0.12}$ Gyr and 851^{+76}_{-70} Myr respectively. In the SMC, the peaks of ECF are obtained at $\log(t) = 9.17 \pm 0.036$, 8.87 ± 0.036 and 8.17 ± 0.036 corresponding to linear ages of $1.48^{+0.13}_{-0.12}$ Gyr, 741^{+64}_{-60} Myr and 149^{+13}_{-12} Myr respectively. The first ECF peak coincides in both the Clouds, suggesting that both the galaxies experienced a burst of CF at ~ 1.5 Gyr. The second ECF peak in the LMC is found at ~ 851 Myr, whereas it is found at ~ 741 Myr in the SMC. Though there is a difference of 110 Myr between the second ECF in the LMC and the SMC, this is within 1σ error of the estimation. Therefore, we may consider this to be a synchronized CF peak at ~ 800 Myr in the MCs.

The four age groups (as shown in Figure 3.10c) help us to locate star clusters in the MCs based on their age. The first synchronized ECF peak of the MCs lies within the Age group-1. These clusters (shown in black) are widely distributed in both the MCs, having a large radial extent. Many can be seen in the outer regions,

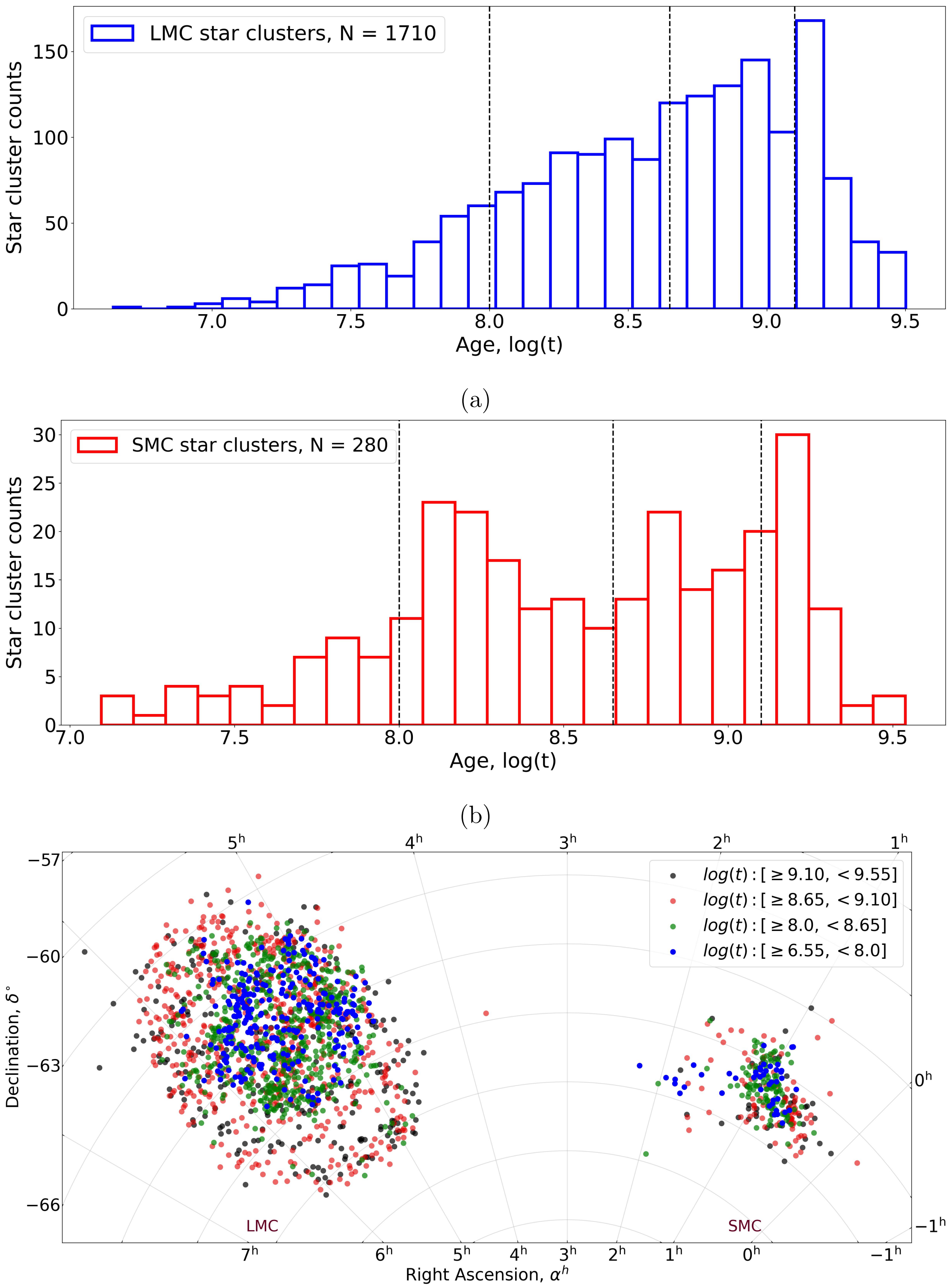

(a)

(b)

(c)

FIGURE 3.10: small Age distribution and spatial map of star clusters in the MCs. The bin width of 0.1 in $\log(t)$ is used to generate the age histograms, which is ∼ thrice the average median error in the $\log(t)$ estimations of the cluster as mentioned in subsection 3.4.2. The vertical lines in the histograms (a) and (b) show the margins of the age groups, which are grouped and shown in the spatial plot (c).

particularly in the LMC. Age group-2 consists of clusters (shown in red) showing a wider spatial distribution similar to the Age group-1, but with more clusters found towards the central regions of both the MCs. The Age group-2 includes the second synchronized ECF peak in the Clouds. Also, we notice a dip in ECF at ~ 1.26 Gyr between the first and second ECF peaks in both galaxies. There is evidence for an immediate bounce back in CF that resulted in the second synchronized CF, as seen by a significant peak in the LMC, but with a moderate peak in the SMC, though with a difference of 110 Myr. These peaks can be considered synchronized as it is within the margin of error. A decline in CF is detected after the 851 Myr peak in the LMC. In the Age group-3 (shown in green), the CF starts to shrink significantly towards the central regions of both the MCs. The CF shows a slow decline between 600 - 100 Myr in the case of the LMC, noting a small rise and fall in between. In the case of the SMC, the CF is found to increase for ages younger than 300 Myr, which peaks at $\sim 149^{+13}_{-12}$ Myr. Age group-4 (shown in blue) shows a significant shift of clusters to the North-East regions, away from the center of the LMC. Also, in this period, the Magellanic Bridge structure appears as a trail of young clusters from the South-East (SE) region of the SMC. Overall, we note a decline in the number of clusters formed in this age group.

A distinct radial shrinkage of CF is noticed in the MCs over the last 1 Gyr. Also, the propagation of CF is evident within the age groups. In the next section, we present the directional change in cluster distribution as a function of age within the MCs.

3.4.3 Spatio-temporal density map of star clusters

To trace the spatio-temporal density map of clusters, we produced a 2D-Gaussian kernel density estimation (KDE) within each age group. The cluster coordinates are taken with the conventions as mentioned in Section 4.4. Scott's rule was used to determine the optimum bandwidth for the KDE maps among the four age groups of MCs.

Figure 3.11 shows the spatial density distribution of the LMC clusters in the upper panel and their radial distribution in the middle and lower panels. The left-most map in the upper panel suggests a relatively large density of clusters in the eastern region of the LMC within the Age group-1. The density pattern spans from the South to the North, covering the East. The bar pattern is feebly visible, along with a patch of density enhancement in the West. The second map from the left, in the same panel, shows the density distribution of Age group-2, which shows that the cluster density peak shifts toward the North and North-West (NW) regions. We see a bar-like distribution in this age group, which was barely noticeable in the previous age group. We also notice a significant decrease in cluster density in the southern LMC. We notice that the patch of density enhancement in the West found in the Age group-1 extends to form an arc-like pattern in the NW in this age group. The overall radial extent of clusters in the LMC disk is more or less similar for Age groups-1 and 2.

In the case of the Age group-3 (as shown in the second map from the right, top panel), the density of clusters shifts dominantly towards the central and North-East (NE) regions, whereas most of the clusters in the South are located within $\sim$ 3 kpc, which is quite inward when compared to the Age group-2. We also note that, in the bar region, the cluster density shifts from the West to the East between the Age groups-2 and 3, such that the younger clusters are more in the eastern part of the bar. The western arm-like pattern still persists to a reduced extent. Further, in the Age group-4 (right-most map of the top panel), the South of the LMC shows the least number of clusters. The highest cluster density is found in the NE part, which started to appear in the Age group-3. In summary, we trace the cluster density in the LMC shifting from various quadrants, such as from the East to NW, then to NE, within the age range studied here. The bar of the LMC is clearly visible only in the Age groups-2 and 3 as a significant density enhancement.

The middle panel of Figure 3.11 shows the radial distribution of cluster counts in the four quadrants (local North, South, East, and West directions from left to right respectively). We note a wave-like pattern in the cluster count profiles rather than a monotonic decrease from the center to the outer regions. The peaks suggest local density enhancements and are likely tracing the spiral arms in the LMC. The profile shows double peaks in the South and East, whereas the North and West show one prominent peak. In the northern quadrant, the outer density peak at $\sim$ 4 - 6 kpc grows in the Age group-2, moves inward in the Age group-3 ($\sim$ 4 kpc), and further inward in the Age group-4 ($\sim$ 3kpc). We note a radial shrinkage of clusters from $\sim$ 8 kpc to $\sim$ 5 kpc in the northern quadrant. In the case of the southern quadrant, we note two peaks in the Age group-1, with a larger strength for the outer one at $\sim$ 6 kpc. In the Age group-2, the outer peak decreases and shrinks in the Age group-3, whereas the inner peak grows significantly. In the Age group-4, the outer peak disappears, and even the inner peak decreases. We notice a large reduction in the outer clusters in the Age groups-3 and 4, with a total shrinkage from $\sim$ 7 kpc to $\sim$ 3 kpc in the southern quadrant.

In the eastern quadrant, the outer peak at $\sim$ 5 kpc grows from the Age group-1 to 2. There appears to be a gradual inward shifting of this peak from $\sim$ 5 kpc to $\sim$ 2 kpc from the Age group-1 to 3. We notice a shrinkage of clusters from $\sim$ 7 kpc to $\sim$ 4 kpc. In the case of the western quadrant, the single peak is found to stay more or less at the same radial distance from the center. Also, we detect only a marginal shrinkage (from $\sim$ 6 kpc to $\sim$ 4 kpc). This is in sharp contrast to the rest of the quadrants. The processes responsible for the inward shifting of younger clusters may be ineffective in this quadrant.

As the LMC is known to move in the NE direction, the KDE plots for the NE,

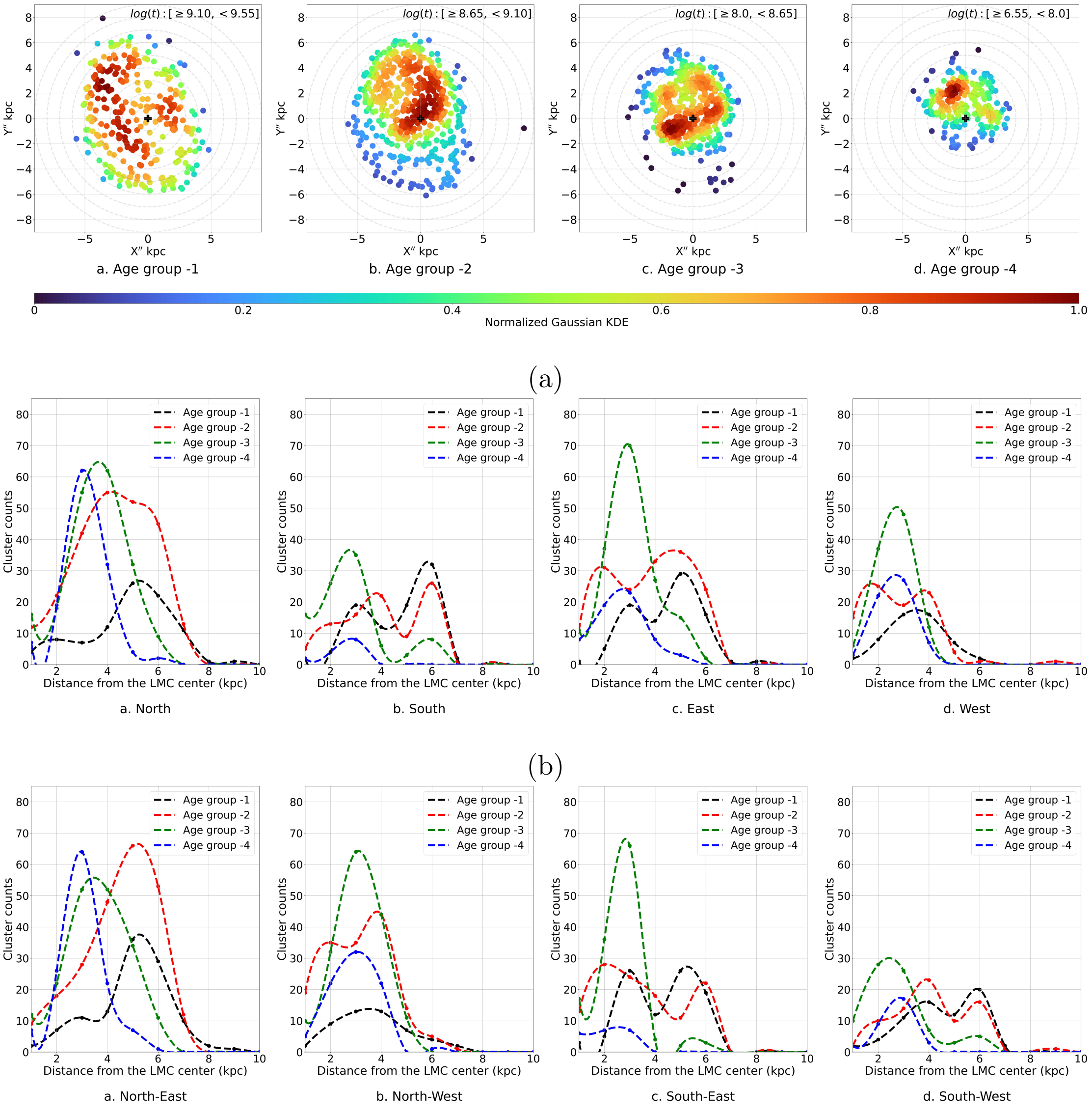

FIGURE 3.11: Spatio-temporal density and radial distribution of clusters in the LMC. a) The 2D Gaussian KDE is shown for the clusters within the four age groups (Age group-1, Age group-2, Age group-3, Age group-4). b) Radial cluster count profile for the four age groups in the four spatial quadrants (local North, South, East, and West) of the LMC plane. c) Radial cluster count profile for the four age groups in the local North-East, North-West, South-East, South-West directions of the LMC plane.

NW, South-East (SE), and South-West (SW) quadrants are shown in the bottom panel of 3.11c, to check the effect of the LMC's movement in the MW's halo. We notice a wavy pattern in all four quadrants in all age groups, likely to represent the spiral arms present in the LMC. The NE quadrant shows a peak at $\sim$ 5 kpc in Age group-1, which becomes prominent in the Age group-2. The peak stays more or less the same for the Age groups-2 and 1, but progressively moves inward to at $\sim$ 3 kpc. The radial extends also shrinks from $\sim$ 8 to $\sim$ 6kpc (with a sharp decline at $\sim$ 4 kpc) between the Age groups-2 and 4 in the last 450 Myr. In the NW quadrant, there is one single peak that more-or-less remains at the same radial distance in all age groups. We also do not notice any significant radial shrinkage of clusters in this quadrant, except from $\sim$ 6 - 5 kpc in the last 100 Myr.

In the SE quadrant, the profiles of Age groups-1 and 2 are more or less similar, with two peaks (an outer peak at $\sim$ 5 - 6 kpc and an inner peak at $\sim$ 2-3 kpc). We notice a distinct increase in the number of clusters in the inner peak for the Age group-3 (the peak at $\sim$ 3 kpc), along with an almost disappearance of the outer peak. In the Age group-4, the inner peak also shrinks and appears as a broad profile up to $\sim$ 4 kpc. The radial extend of this quadrant shrinks from $\sim$ 7 - 4 kpc, between the Age groups-2 and 4 in the last 450 Myr. In the case of the SW quadrant, we notice that there is less number of clusters populated in this quadrant with a wavy profile. The Age groups-1 and 2 appear similar with an outer peak at $\sim$ 6 kpc and an inner peak at $\sim$ 4 kpc. In the Age group-3, the outer peak reduces significantly to the extent that it almost disappears, whereas the inner peak is found to move inward to a radial distance of $\sim$ 3 kpc. The radial extend shrinks from $\sim$ 7 - 4 kpc between the Age groups-2 and 4 (last 450 Myr). In the case of the Age group-4, the inner peak reduces in strength but stays at the same radial distance. We note that except for the NW quadrant, all the other 3 quadrants have experienced considerable radial shrinkage, mostly in the last 450 Myr.

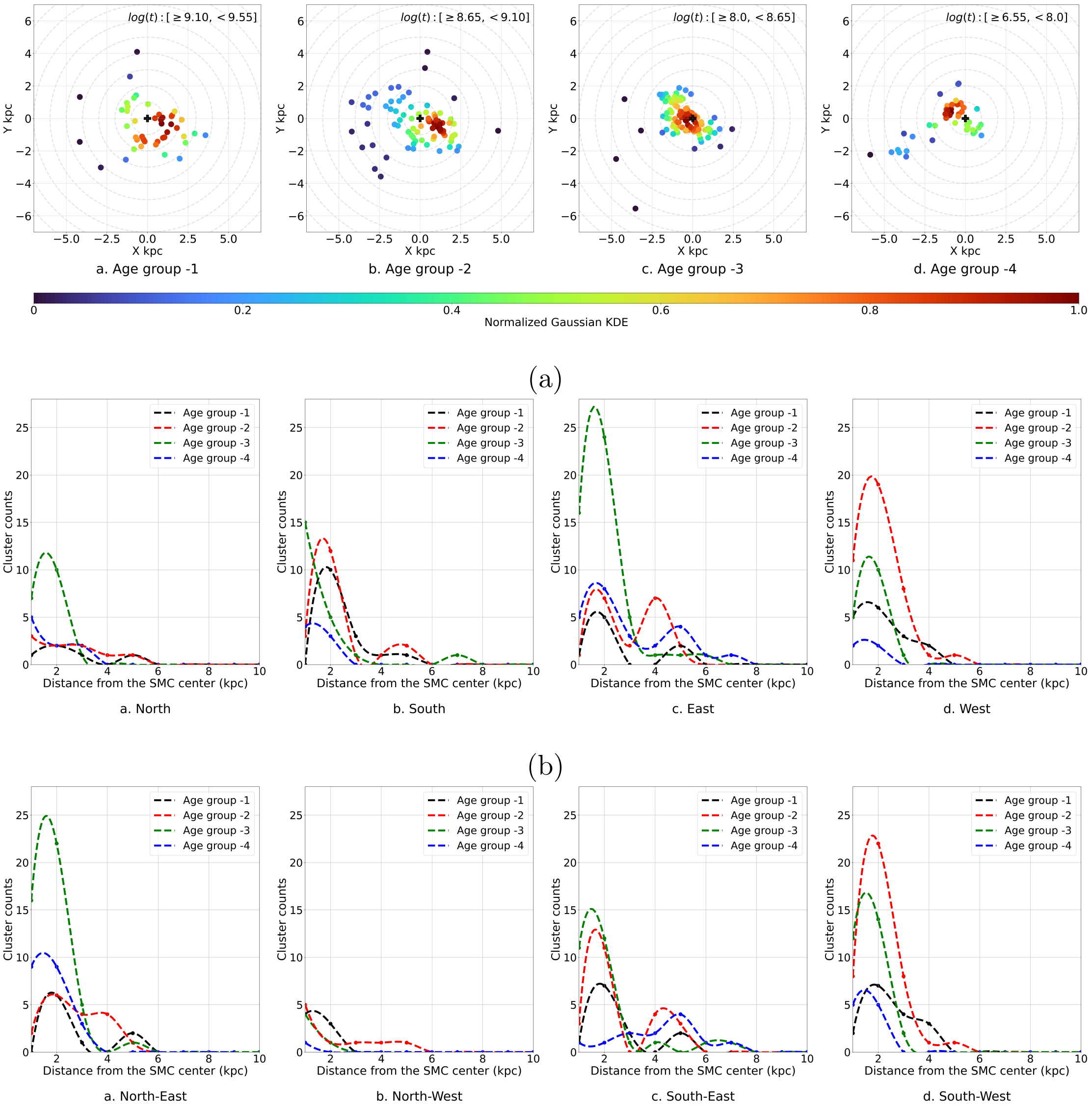

(c)

FIGURE 3.12: Spatio-temporal density and radial distribution of clusters in the SMC. a) The 2D Gaussian KDE is shown for the clusters within the four age groups (Age group-1, Age group-2, Age group-3, Age group-4). b) Radial cluster count profile for the four age groups in the four spatial quadrants (local North, South, East, and West) in the sky plane of the SMC. c) Radial cluster count profile for the four age groups in the local North-East, North-West, South-East, South-West directions in the sky plane of the SMC.

The cluster density is traced in the SMC sky plane as shown in Figure 3.12a. In the Age group-1 (shown in the leftmost panel), the cluster density is largest in the South and SW direction at $\sim$ 2 kpc from the SMC center. In the Age group-2 (second panel from the left), the cluster density shifts towards the central and SW regions at $\sim$ 2 kpc. Also, a scatter of old clusters can be noticed at $\sim$ 2 kpc to $\sim$ 5 kpc from the SMC center in the NE and SE regions in the Age groups-1 and 2. The density of clusters further shifts to the NE direction along with an increase in the central region, as evident from the Age group-3 (second panel from the right). In the Age group-4 (right-most panel), we notice a significant density in the NE region close to the center and a tail of clusters in the SE direction towards the LMC, which is the wing. We found that the cluster density in the SMC shifted from SW to NE and SE within the age groups studied here.

The radial cluster count profiles in the four quadrants of the SMC are traced in the middle panel (local North, South, East, West) and lower panel (local NE, NW, SE, SW) of Figure 3.12. In the northern quadrant, we notice a significant enhancement in the Age group-3 (100 - 450 Myr), whereas the count profiles of other age groups are more or less similar with less number of clusters. In the southern quadrant, we see a distinct peak in the Age group-1 and 2 at $\sim$ 2 kpc. This peak moves towards the center within the Age group-3, followed by a reduction in the cluster counts in the Age group-4. In the eastern quadrant, once again, we note a large enhancement in the Age group-3 (100 - 450 Myr), which is in fact the largest among all quadrants. This quadrant shows a wavy count profile with a similar radial distribution of clusters in the Age groups-1, 2, and 4. The Age group-4 clusters show an extended distribution populating the outer SMC. In the western quadrant, we note an increasing strength of the peak from the Age group-1 to 2, such that the highest peak in the Age group-2 (450 Myr - 1.26 Gyr) is found in this quadrant. The peak reduces progressively in the Age groups-3 and 4. Except in the eastern quadrant, all other quadrants show shrinkage of CF during the age groups considered here.

The NE quadrant shows the biggest peak in the Age group-3 (100-450 Myr), with similar profiles for the other age groups. The NW quadrant has the least number of clusters in all age groups. The SE quadrant shows a growing inner peak through the Age groups-1, 2, and 3. In the Age group-4, the entire profile changes to produce a peak at $\sim$ 5 kpc, populating the SMC wing and the extension to the MB. We also note the presence of the Age group-2 clusters in the SMC wing region. The SW quadrant shows the largest enhancement in the peak for the Age group-2 (450 Myr - 1.26 Gyr), which progressively reduces in the Age groups-3 and 4.

The NE quadrant has a significantly larger number of clusters than the NW across all age groups, suggesting a very low CF in the NW over the last 3.5 Gyr. The dominant peak in Age group-2 found in the South and SW quadrants suggests an enhancement in CF during 450 Myr - 1.26 Gyr. The South and SW regions of the SMC show an inward radial shrinkage of clusters from $\sim$ 6 kpc to $\sim$ 2 kpc in the last 450 Myr. On the other hand, the dominant peaks in Age group-3 found in the East and NE quadrants suggest an enhancement in CF during 100 - 450 Myr. The East and SE regions show the peak of CF at $\sim$ 5 kpc in Age group-4, which is suggestive of the formation of the wing and the extension to the Magellanic Bridge from the SMC in the last 100 Myr.

3.5 Discussion

In this study, we have considered clusters with one overlapping neighbor but excluded those with more than one overlapping neighbor in the LOS. Also, this study could not consider poor clusters (particularly in crowded regions), as they have scattered/ poor CMDs after the FSD. We could not characterize about 1000 clusters due to the above reasons. As shown in Figure 3.5, these clusters are found to be located more in the central regions with much less number in the outer regions. Many of them could also be just random density enhancements and not real clusters, as indicated by the poor number of cluster members. For example, N16, N18, and Choudhury et al. (2015) have found several such clusters. These clusters are unlikely to significantly alter the overall results derived in this study, particularly for the outer regions of the MCs. The central regions of both Clouds have more such excluded clusters. We expect the real clusters to be not so large in number and therefore may impact the CF statistics only to a small extent. Deeper photometric data are needed to study these poor clusters to increase the number of characterized clusters and to get a complete picture of CFH.

The data selection and the FSD algorithm are designed to effectively eliminate the MW source contamination. To check for any leftover contamination, we cross-matched the cleaned cluster sources from our study with the recent MC-MW source membership probability catalog by Jiménez-Arranz et al. (2023a, hereafter J23a) and Jiménez-Arranz et al. (2023b, hereafter J23b). The authors recommend two probability cut-off ($P_{\rm cut}$) values for MW source contamination in the MCs (in Section 2.3.3 of J23b). They suggest $P_{\rm cut} = 0.01$ for completeness in the LMC sample (that is, no LMC objects are missed at the price of an increased MW contamination), and $P_{\rm cut} = 0.52$ for the optimal sample with completeness and purity. While the aim of J23b is to make a master catalog of LMC sources with almost zero contamination of MW, our aim is to identify the star clusters located in the central region of MCs as well as in the outskirts and estimate their parameters to understand CFH. As we cannot afford to miss out on LMC stars, we adopted the $P_{\rm cut} = 0.01$ criteria to check the leftover MW source contamination. The cross-match showed that only a very small fraction, $\sim$ 1 - 2% of the final members are MW contaminants and mostly co-located with the cluster sequence in the CMD. We also re-estimated the cluster parameters for a sample of clusters after removing them. The estimated parameters do not change as our optimized parameter estimation technique is not affected by the removal of a very small number of sources.

We estimated the cluster parameters using an automated method, where the best fits are identified based on the χ^2_f value and MCMC sampling, followed by a visual inspection. The end product is the estimation of 4 parameters (age, extinction, distance, and metallicity) and their errors for 1990 clusters. Among these, we newly parameterized 960 clusters. The age estimation is robust within the expected range of the other three parameters that are constrained in the MCMC sampling. We also note a satisfactory comparison of ages and reddening from this study with those in the literature. In this section, we compare our cluster parameter estimates with the previous literature studies. Further, we discuss the results presented in Section 3.4 and highlight a few interesting details on the cluster ages and distribution in the MCs. These are discussed below.

3.5.1 Comparison of cluster parameters with the previous estimations

The estimated age-reddening values were compared with two major studies (G10; N16 and N18). We cross-matched 576 clusters from G10 and 585 clusters from N16 and N18. We used Spearman's rank correlation coefficient, ρ_s to compare the age estimations (as in Figures 3.13a and 3.13b). We estimated a positive correlation coefficient of $\rho_s = 0.69, 0.52$, suggesting that the age estimations of this study are comparable for the common clusters. The reddening estimations were compared with the above two studies, using histograms of reddening variations, $\Delta E(B-V)$, as shown in Figures 3.13c and 3.13d with constant R_V values as mentioned in subsection 3.4.1. The distribution of $\Delta E(B-V)$ is found to have a 1σ width of 0.06 mag, with the peak near 0.05 mag with respect to G10. This difference is statistically insignificant as it is of the order of the error in the current estimation. The distribution of $\Delta E(B-V)$ is found to be $\sim$ 0.0 mag with respect to N16 and

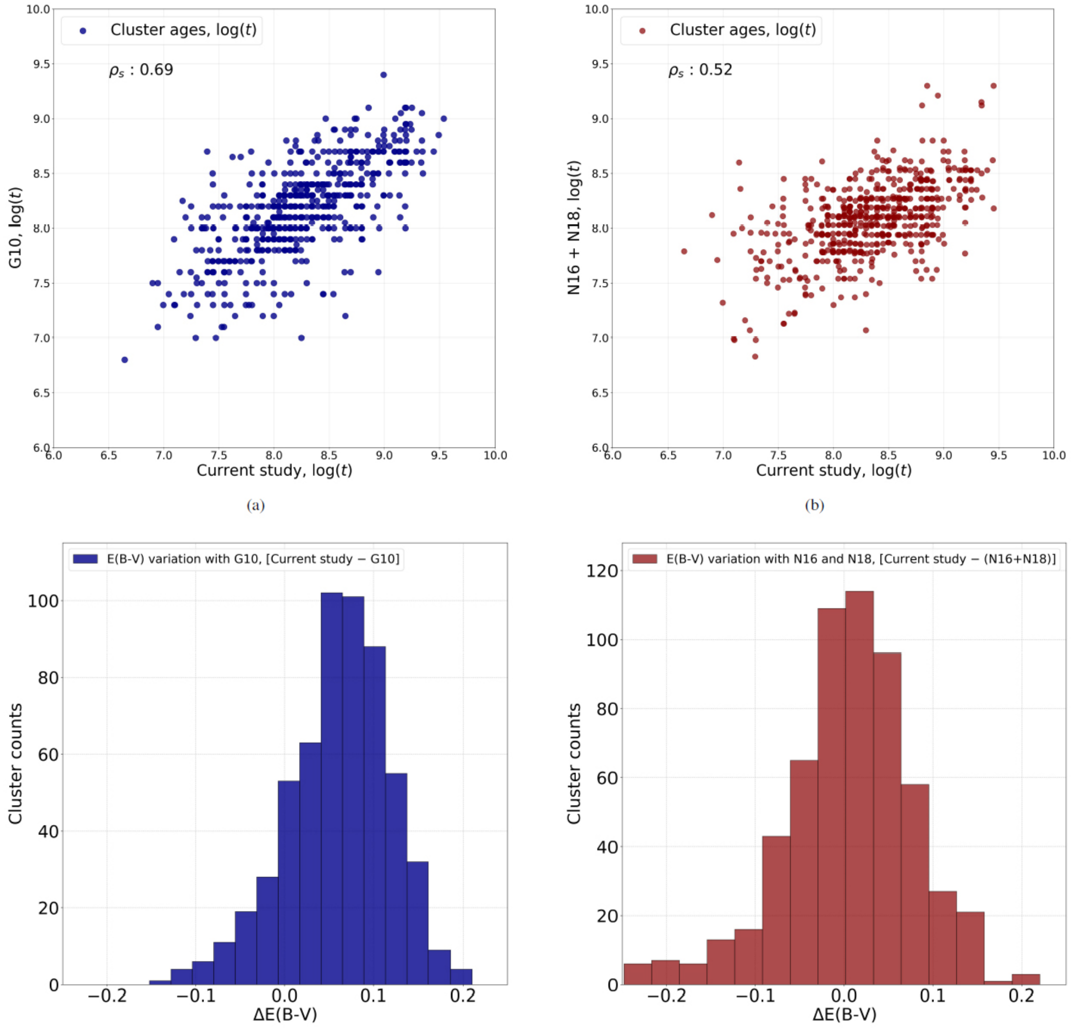

(a) (b)

(c) (d)

FIGURE 3.13: The age-reddening estimates from our current study compared with the literature (as mentioned in Section 3.5.1). The top panels (a and b) compare the age estimates from our study with Glatt et al. (2010), Nayak et al. (2016) and Nayak et al. (2018) (reference catalogs) using Spearman's rank correlation coefficient (ρ_s), in which we found positive correlations among the $\log(t)$ estimates as shown in the scatter plots. The reddening variation ($\Delta E(B-V)$) from our study is also compared with the reference catalogs and shown in the bottom panels (c and d).

N18. The age and reddening comparisons with G10, N16, and N18 are shown in Figure 3.13. These suggest that the age-reddening values more or less match the previous estimates. Hence the estimated parameters are similar to the previous studies and are reliable for inferring the cluster properties of the MCs.

There are not many estimations of [M/H], unlike the estimations of [Fe/H]. R18 estimated an [M/H] of ~ 0.65 dex ($Z \sim 0.0032$) for the SMC stellar population extending up to ~ 1 Gyr, which is very similar to our estimate. We also note that the range in Z or [M/H] is similar in both studies for ages less than $\log(t) < 9.1$.

3.5.2 Synchronized CF peaks and SFH of the MCs

To confirm the ages of synchronized CF episodes in the MCs, we generated normalized age distributions for clusters in both MCs, as presented in Figure 3.14. The age binning was set at $\delta \log(t) = 0.10$. The first and most prominent synchronized peak, at approximately 1.48 Gyr (l_1 and s_1), was observed in both Clouds. Additionally, a second synchronized peak was identified at ~ 851 Myr (l_2) in the LMC and ~ 741 Myr (s_2) in the SMC, with l_2 and s_2 showing only a small difference of ~ 110 Myr, well within the margin of error. This is the first time such synchronized peaks in CF are found for the Clouds at 1.5 Gyr and 800 Myr. This is possible due to the spatial coverage of *Gaia* data. Notably, a CF peak at ~ 149 million years (s_3) was observed as a significant peak in the SMC, while no corresponding peak was seen in the LMC. The wavy pattern in the profile for the SMC is due to the smaller number of clusters available to estimate the age distribution. A detailed comparison is provided below.

The first peak of synchronized CF is more or less in agreement with the peak of SFH at 2 Gyr obtained by Rubele et al. (2012), in the LMC. This peak of CF is likely to be due to the LMC-SMC interaction. The LMC's ring-like clusters in the outskirts are related to the possible LMC-SMC interaction (Choi et al. 2018) with the ages spanning within the Age groups-1 and 2 in our classification. The simulations by Salem et al. (2015) suggested that the outermost parts of the LMC were affected by the ram pressure stripping at ~ 1 Gyr ago. However, we found a global enhancement in CF in the MCs at ~ 800 Myr, so the ram-pressure stripping

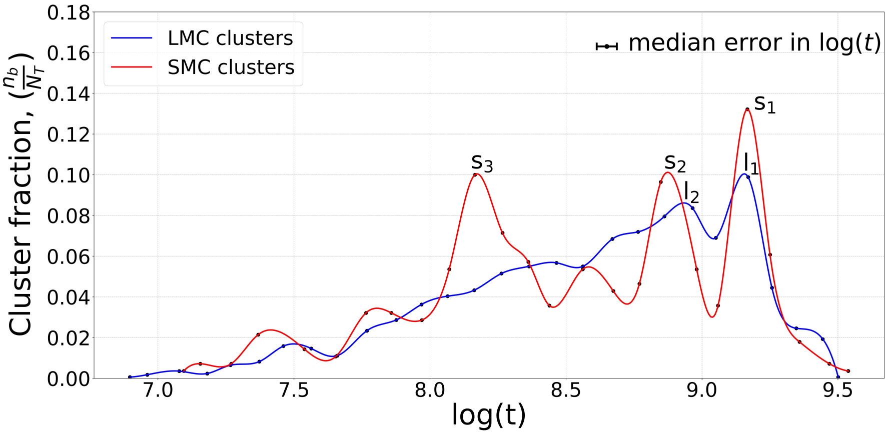

FIGURE 3.14: The ECF peaks obtained from the clusters we studied in the MCs. The age histograms of the LMC and the SMC from Fig 3.10a and 3.10b are normalized (n_b/N_T) with their total number, N_T (N_T =1710 (LMC), 280 (SMC)) and overplotted for comparison. The correlated peaks of CF are marked at ∼ 1.48 Gyr (l_1 and s_1), the other significant CF peaks in the LMC at ∼ 851 Myr (l_2), and in the SMC at ∼ 741 Myr (s_2), ∼ 149 Myr (s_3) are also marked. The median error in log(t) is also shown.

is likely to have started after this peak. However the second synchronized CF peak noticed in the LMC and the SMC is unlikely to be due to a common event, as no such mutual events are found/ expected at this period. This may be the response of the gaseous disk to the perturbation followed by a stochastic self-propagating star formation (Gerola & Seiden 1978). The recent study by Mazzi et al. (2021) also found two peaks in the star formation rate of the LMC, the first one between 1.6 - 4 Gyr and the second one between 0.63 - 1 Gyr. The two peaks of CF found for the LMC in this study are also consistent with our estimations.

The third peak of CF (s_3) in the SMC sets the upper limit of the recent interaction at ∼ 300 Myr and the lower limit at ∼ 150 Myr, in agreement with previous studies. A smaller peak of CF is noted in the SMC at ∼ 400 Myr, which is also noted in SFH by several authors. There are no significantly large peaks of CF in the LMC in the last 600 Myr. We note a marginal enhancement in the cluster numbers between 170 - 400 Myr (Figure 3.10a) in the LMC. The recent pericentric passage of the SMC about the LMC was reported at ∼ 150 Myr ago (Cullinane et al. 2022), and it is similar to the peak we obtained in our study for the SMC.

The CF of the SMC obtained in this study is likely to help constrain the recent interaction history, whereas the LMC (in particular, the outer LMC) does not show any significant impact in CF due to the recent interaction.

The comparison of our CF peak estimates with those of G10 for both the SMC and LMC reveals a close alignment, with differences of ∼ 100 Myr. Furthermore, the CF peaks identified in studies conducted by N16 and N18 also show consistency with our results. However, our study did not reproduce the younger CF peak of 125 MYr, which was previously reported in both the G10 and N16 studies. This may be because of the missing clusters in the inner LMC, that are not considered in this study due to crowding and insignificant number of cluster members after the FSD. Also, any disparities in CF peak values could potentially be attributed to changes in the metal fraction values used to estimate the ages of star clusters in previous studies.

Recent study of SFH of the MCs by Massana et al. (2022) suggested that the LMC-SMC had several synchronized star formations in the last ∼ 3.5 Gyr. They detected five star formation peaks in the SMC at ∼ 3, ∼ 2, ∼ 1.1, ∼ 0.45 Gyr ago, and an ongoing one. These time scales are in more or less good agreement with the ECF peaks at ∼1.5 Gyr (in both the MCs), ∼ 800 Myr (in both the MCs), and ∼ 149 (SMC) Myr that are found in this study.

3.5.3 Age-wise cluster density profiles and its implications

In our CF density profiles, the LMC exhibits a declining trend in star cluster distribution, particularly in its southern and SW regions. The decrease of star formation in the southern region for ages younger than 2 Gyr and recent active SFH in the North was reported previously by Ruiz-Lara et al. (2020) and Indu & Subramaniam (2011). These are in good agreement with the results obtained in this study. The outside-in quenching of star formation in the northern part of the LMC was found by Meschin et al. (2014), over a similar radial distance of 3.5 - 6.2 kpc, in the last 1 Gyr, which they conclude as due to either consumption of gas or ram-pressure stripping. This is in excellent agreement with the radial shrinkage found in this study.

The truncation of CF in the outer LMC is dominant for ages younger than Age group-2 clusters, which is at $\sim$ 500 Myr. The truncation could be due to a combination of various effects, such as consumption of gas due to star formation, ram pressure stripping, radial migration of the remnant gas due to loss of angular momentum and tidal stripping. We note that the most severe truncation is in the southern LMC, whereas the motion of the LMC is in the NE direction.

The map of star formation rate in the LMC as shown in Figure 5 of Mazzi et al. (2021) is in good agreement with the KDE maps presented in our study. The spatial extent as well as the variation in star formation rates are well correlated for the corresponding age groups. Their maps also show a significant decline in the NE regions in the last 500 Myr, likely to be due to the ram-pressure effect.

It is curious to note that the western LMC is the least affected and hardly shows any shrinkage. On the other hand, the extent of the disk in the oldest group is much smaller in the West when compared to the other regions. We also note that this study has comparable East-West coverage with respect to Ruiz-Lara et al. (2020), whereas the North-South coverage is much larger. We note that the outer LMC plays a major role in its global CF for ages older than 1 Gyr. In contrast, the inner LMC plays a major role in deciphering the recent star formation, particularly for ages $\leq$ 500 Myr. Therefore, it is important to include the outer LMC while estimating the global SFH of the LMC.

The motion of the LMC implies that any headwind from the MW's circumgalactic medium would compress or impact the NE part of the LMC disk. In this quadrant, HI profile truncates at ~ 6.2 kpc (Putman et al. 2003), in contrast to a much extended stellar profile (van der Marel 2001), ruling out a tidal truncation of HI (as tides would truncate both gas and stars, Salem et al. 2015). Therefore, this truncation of HI in the NE quadrant is indeed evidence of ram-pressure stripping (Salem et al. 2015). The shifting of younger stars to the North and NE was noticed by Indu & Subramaniam (2011), and they suggested that the recent star formation is impacted by the motion of the LMC in the MW's halo. The radial cluster counts in the North and NE presented in this study (Figures 3.11b and 3.11c) are in good agreement with the above. The radial shift of the CF peak in the last 450 Myr is probably suggestive of the gas compression in the NE due to the LMC's motion.

Several authors have reported spiral arms in the North of the LMC (de Vaucouleurs & Freeman 1972a; Mackey et al. 2016), and the origin of spiral structure is associated with the interaction between the MCs (B12; Besla et al. 2016; Yozin & Bekki 2014). The LMC bar shows up as a density enhancement in the Age group-2, and there are more clusters in the East of the bar in the Age group-3 compared to the Age group-2. The SFH of the regions closer to the LMC bar region (South-East Arm, North-West Arm, Blue Arm, North-West Void) are previously studied by Harris & Zaritsky (2009).

We also note that the wavy pattern in the cluster count profile persists across the age groups and in all the quadrants, suggesting of long-lasting spiral pattern. This finding aligns well with the results from the field star analysis by Ruiz-Lara et al. (2020), who reported indications of long-lasting stability in the spiral arms of the LMC, tracing their formation back to over 2 Gyr ago. However, we add that the location of the spiral arms is found to move inwards for younger ages over the last 1 Gyr. The cluster count profiles have demonstrated their ability to trace the probable spiral arms as a function of age in the LMC.

In the case of the SMC, the CF peak shifted from the SW for Age group-1 to NE for Age group-4. We note that the SMC has far less number of clusters and the results may not be as strong as the LMC due to poor statistics. The study by J16 with the age map of classical cepheids has found the NE part of the SMC to be younger compared to the SW, which is in agreement with our study. Also, the density map (Figure 3.12a) for the Age group-3 for SMC, the features identified by Y19 (in their Figure 7 for the SMC) can be noticed, such as the central bar, the NE and SW extensions (except the wing, that is seen only in the Age group-4). Our study traces the KDE of younger clusters extending from SW to NE for ages younger than 1 Gyr, and it is similar to the KDE map traced by Sun et al. (2018). The CF in the SMC is dominated in the South and West during 450 Myr - 3.5 Gyr, and in the North and East during the last 450 Myr. Overall, a general shrinkage of CF is noticed in the SMC. The SMC wing as well as the extension to the Magellanic Bridge are traced by clusters younger than 100 Myr. If the wing and Magellanic Bridge are formed during the last interaction at 150 Myr, then these clusters might be formed in-situ from the HI gas pulled out of the SMC during the last interaction.

The catalog of 1990 clusters containing the cluster name, coordinates, and the estimated parameters (age, extinction, metallicity, and DM) along with the 16^{th} and 84^{th} percentiles (lower and upper uncertainty bounds) is made available as an online catalog (Online link: catalog in MRT Format).

3.6 Summary

We summarize the results of this study below:

1. We characterized 1990 clusters (1710 in the LMC and 280 in the SMC)

using the *Gaia* DR3 data, where 847 clusters in the LMC and 113 clusters in the SMC are parameterized for the first time (when compared to 7 existing catalogs). The age-extinction-metallicity-DM parameters estimated here are based on an automated fitting of the CMDs after the removal of field stars, which act as prior values. We implemented an MCMC sampling technique to derive the final parameters along with the errors. The MCMC sampling mainly explores the parameter space in A_G, DM, and Z to find the range under which our age estimates have confidence.

2. The LMC has several clusters that overlap in the LOS. We categorized clusters into isolated, singly overlapping and triple overlapping, etc. This study considers a majority of single clusters ($\sim$ 83%) as well as those with only one overlapping cluster in the LOS. We note that more than 2 overlapping clusters are mostly in the inner regions of the MCs.

3. This study could not characterize 1082 clusters that presented either a scattered CMD after FSD or a CMD with less than 8 members after FSD. These clusters are located mostly in the inner regions of the MCs. We note that many of them are likely to be very poor clusters or random density enhancements. The average number of member stars retained after FSD is 40, for the 1990 clusters that are characterized.

4. The mean extinction A_G is estimated to be 0.4±0.005 mag and 0.38±0.006 mag for the LMC and the SMC, respectively. We note that the LMC sample has more outer clusters with relatively less extinction.

5. We estimated a mean metal fraction, $\mu_z = 0.0060 \pm 0.00002$ for the clusters in the LMC, and $\mu_z = 0.0027 \pm 0.00002$ for the clusters in the SMC. The corresponding mean [M/H] values are estimated as -0.40 ± 0.001 dex and -0.76 ± 0.003 dex for the LMC and the SMC, respectively. We recommend that the choice of Z value for isochrones to fit the CMDs of clusters with age $\leq$ 1 - 2 Gyr is 0.004 to 0.008 for the LMC and 0.0016 to 0.004 for the SMC.

6. For the first time, this study estimated two synchronized peaks in CF in the MCs. The first one is at $\sim$ 1.5 Gyr, likely to be due to their first mutual interaction. The second synchronized CF peak at $\sim$ 740-850 Myr is likely to be of internal origin in the galaxies, as there is no known interaction during this period.

7. The cluster count profiles in all the quadrants of the LMC show a wavy pattern with peaks, instead of a monotonic decrease from the center to the outer regions over the age range explored in this study (up to 3.5 Gyr). This is suggestive of the presence of spiral arms as noted by several studies in the literature. In this study, we trace an inward shifting of these peaks (possible spiral arms) to the inner LMC for younger ages.

8. The cluster count profiles show that there is a significant radial shrinkage in the cluster distribution in the LMC in the last 450 Myr. The KDE maps as well as the cluster count profiles provide evidence for ram-pressure stripping in the NE quadrant due to the movement of the LMC in the MW's halo.

9. Radial shrinkage of the LMC disk and truncation of outer CF is noted, typically from outer at $\sim$ 8 kpc to inner at $\sim$ 4 kpc. We find a significant shrinkage in CF in the South, NE, and SE in the last 450 Myr. The West and NW quadrants, on the other hand, show no significant shrinkage.

10. We note a severe truncation of CF in the southern LMC in the last 450 Myr, likely to be due to the combined effect of multiple factors, such as consumption of gas due to star formation, ram pressure stripping, radial migration of the remnant gas due to loss of angular momentum and tidal stripping, etc.

11. The recent interaction at $\sim$ 150 Myr has impacted the SMC with a CF peak, whereas no such peak is found in the LMC. We note an enhanced CF in the central, NE of the SMC and the northern LMC during this period.

12. The CF in the SMC appears to be enhanced in the South and West during 450 Myr - 3.5 Gyr, whereas the CF gets enhanced in the North and East in the last 450 Myr. The shrinkage of CF in the SMC is noted from $\sim$ 6 kpc to $\sim$ 3 kpc in the NE, NW, and SW of the SMC, mostly in the last 450 Myr.

13. This study therefore brings out a very detailed view of the CF in the LMC and SMC in the last 3.5 Gyr. The outer LMC clusters have provided a unique mapping of the CFH. This study provides some important insight into the CF episodes and their link with the LMC-SMC-MW interactions.

Chapter 4

Disk response of the LMC to the recent LMC-SMC collision

4.1 Introduction

There have been several studies aimed at the kinematic modeling of the LMC (V02; W20; G21) resulting in an estimation of a range in structural parameters, as the modeled/ estimated parameters are known to vary with respect to the age and nature of the stellar population traced (W20). Even though the LMC is known to host a rotation-supported disk, the kinematic parameters of the LMC are also known to vary with respect to the radial coverage of the study as well (N22). The stellar motion in the outskirts of the SMC indicates a probable direct collision between the SMC and the LMC at $\sim$ 100 to 250 Myr ago (Z18). Modeling the internal kinematics of the LMC is therefore necessary to reveal the response of its disk to the direct collision with the SMC.

In Chapter 3, we detailed the parameterization of 1710 star clusters in the LMC, which we performed after the field stars were decontaminated from the cluster regions. The PM of the cluster estimated using the median PM value of the members therefore presents a golden data set to explore the LMC disk kinematics. As the ages of these clusters are already estimated, the data set will allow us to explore the dependency of kinematic properties on the age of the cluster. Our previous study also identified a nearby field region for all the 1710 clusters, and this population can be used as a control/ comparison population. This study therefore explores the LMC disk kinematics using these unique data sets.

This study aimed to model the LMC disk and estimate the kinematic parameters using a robust MCMC method, to explore the model dependency on various factors such as age, and to check how the modeling depends on the spatial coverage of the population as well as the richness of clusters. The kinematic parameters of the LMC disk are derived for the first time using star clusters in this study. We also quantify the residual PM after fitting the model and trace the kinematic outliers among clusters.

The chapter is arranged as follows. In Section 4.2, we describe the data sets used for our modeling. In Section 4.3, we present the model of the LMC along with the assumptions underlying our analysis. In Section 4.4, we present the estimated kinematic parameters of our data sets, followed by the estimation of the residual PM. The discussions based on our results are presented in Section 4.5, followed by Section 4.6, which summarizes our work. The results presented in this chapter are available in Dhanush et al. (2024b).

4.2 Data

The initial selection of data sets includes the 1710 cluster regions and nearby field regions from the *Gaia* DR3 data. First, we calculated the median of the PM and its standard error for stars within each cluster and their associated field region in both the RA and DEC directions. Then, we applied a PM cutoff of < (median PM+3σ) based on the PM distribution of field regions. We used it for clusters and field regions both to eliminate a few outliers in the galaxy that show relatively large PM. We retained 1705 clusters after this selection. The primary modeling was performed using the clusters and their associated field regions following this selection process. We further performed kinematic modeling with data sets based on the control population, cluster richness, cluster age, and spatial coverage of the LMC. The details of these data sets are enumerated below.

1. The control population for the model is obtained from the CMDs of field regions associated with each cluster. The choice of control population was made to understand the kinematic nature of the cluster and field population. We chose the young MS stars within the window of $G < 19.5$ mag and (G_{BP}-G_{RP}) < 0.5, then RC stars based on the selection criteria from CMD of the LMC sources as mentioned in S22. Several field regions associated with clusters do not have significant young MS stars in the CMD. We put a cut-off of young MS stars $\geq$5 to further select the samples for the control population. We are left with 1484 candidates in the four categories for modeling, the clusters, nearby field regions, young MS stars, and RC stars. Out of this final selection, we note that the $\sim$ 75% of the field regions considered have young MS stars and RC stars with a strength of 20 and 50 stars, respectively.

2. We note that the average number of members in each cluster in our study is $\sim$ 40. To investigate potential biases in the data sets, we conducted modeling of groups based on the cluster members' strength across a range from 10 to

60 members, with intervals of 10. The field regions associated with these richness groups were also modeled to compare with the nature of clusters. We created 12 models for the cluster groups and field groups based on cluster richness.

3. To understand the age dependency of the kinematic parameters, we performed modeling with respect to clusters spanning from older to younger age groups. We used age groups in ranges of $\log(t)$, Age group-1: $[\geq 9.10, < 9.55]$, Age group-2: $[\geq 8.65, < 9.10]$, Age group-3: $[\geq 8.0, < 8.65]$, and Age group-4: $[\geq 6.55, < 8.0]$ (as mentioned in Chapter 3, section 3.4.2). The associated nearby field regions were also modeled with respect to each age group. It is to be noted that the age-wise grouping is only valid for the clusters, and the associated field regions are age-wise heterogeneous but analyzed for comparison.

4. We investigated the variations in kinematic parameters concerning the spatial extent of the LMC. Employing circular regions, we analyzed clusters and associated field regions, ranging from 2° to 7° in increments of 0.5° from the kinematic center on the sky plane. We used the kinematic center that we calculated from the primary model encompassing clusters and field stars for the radially separated groups.

Table 4.1 summarizes the data sets that are modeled. The subsequent section covers the implementation of the kinematic model using the above data sets.

4.3 Kinematic model of the LMC

We performed the kinematic disk model of the LMC corresponding to the observed median PM for the data sets referenced in Section 4.2. We followed the analytical

Table 4.1: The data sets used in the kinematic model of the LMC are summarized here. The length (L_d) and the number (N_d) of data sets are provided as well. Clusters and associated field regions are labeled based on the cluster richness in the 3^{rd} row, such as C_{10} representing clusters with 10 or more stars, and so on. A total of 48 data sets are used in our study to perform the kinematic modeling.

Data set	$\mathbf{L}_d$	$\mathbf{N}_d$
Clusters, Nearby field regions (Primary sample)	1705	2
Clusters, Nearby field regions, Young MS stars, RC stars (Control sample)	1484	4
$C_{10,..,60}$, $F_{10,..,60}$ (groups based on cluster richness)	1581, 973, 643, 455, 334, 257	12
Cluster age groups, Nearby field regions	316, 579, 551, 260	8
Clusters, Nearby field regions (groups based on spatial coverage, radii: 2° to 7°, step size: 0.5°)	372, 560, 551, 768, 958, 1104, 1263, 1401, 1604, 1667, 1688	22

framework detailed in section 2.3.2 for modeling the kinematics of the LMC. The parameters od for our model include the inclination of the LMC disk (i), the position angle of the line of nodes measured from West (θ), dynamic centers (α_0, δ_0), the amplitude of the tangential velocity of the LMC's center of mass (v_t), the tangential angle made by v_t (θ_t), scale radius (R_0), optimization factor (η), and the amplitude of the rotational velocity (v_0). Our modeling process is aimed at determining the most fitting values for these nine kinematic parameters. It's important to note that our modeling was confined to the LMC's sky plane due to the absence of LOS velocity components in our data sets.

We assumed that there is no precession and nutation of the LMC disk within the spatial coverage of the galaxy (less than 7°) considered in this study (V02; N22). We assumed the RA and DEC of the field regions associated with each cluster to have the same spatial coordinates as the cluster centers. Also, we assumed a fixed distance of 49.59 kpc (P20) to the LMC center, D_0 and a LOS velocity of the COM, v_{sys}, as 262.2 km s^{-1} (V02). The following subsection deals with the method and estimation of the best-fitting kinematic parameters for the data sets summarized in Table 4.1.

4.3.1 Modeling procedure

We found the best-fitting 48 models and the associated kinematic parameters for 48 data sets referenced in Table 4.1. We performed the fitting of the parameters using the MCMC serial stretch move sampling algorithm as explained in section 2.2.3. A similar MCMC approach is used in the studies by W20, C22 and N22. The observed PM for the sources in data sets are along the RA and DEC directions, but the model formulation is for the PM in the West and North directions. For that, we took the negative of the source median PM in the RA direction. Now the model PM ($M_{W,m}$, $M_{N,m}$) and the observed PM ($M_{W,o}$, $M_{N,o}$) can be used to construct the log-likelihood function ($\ln\mathcal{L}$), which can be used with the associated West and North direction standard errors of observed data sets ($\sigma_{W,o}$,$\sigma_{N,o}$) to sample the best fitting parameter with MCMC. The equation for $\ln \mathcal{L}$ is given by,

$$\begin{aligned}\ln \mathcal{L} = -0.5 \sum_{i=1}^{n} \Bigg[& \ln\left(2\pi\sigma^2_{W,o,i}\right) + \frac{\left(\mu_{W,o,i} - \mu_{W,m,i}\right)^2}{\sigma^2_{W,o,i}} \\ & + \ln\left(2\pi\sigma^2_{N,o,i}\right) + \frac{\left(\mu_{N,o,i} - \mu_{N,m,i}\right)^2}{\sigma^2_{N,o,i}} \Bigg]\end{aligned} \tag{4.1}$$

The priors for the model were uniformly chosen, except for the rotation velocity amplitude, v_0, for which we used a Gaussian prior of 76 km s^{-1} (van der Marel & Kallivayalil 2013; G21; N22). When working with modeling datasets based on cluster age groups, we note that the spatial distribution of clusters in the sky plane is not homogeneous. This results in the non-convergence of η in its posterior sampling distributions while performing the MCMC with a uniform prior. To avoid this, we employed Gaussian weighting on η specifically for these age-based datasets, using the corresponding value of the parameter estimated from the primary model encompassing all cluster and field regions.

We executed 2000 steps of MCMC iteration involving 200 walkers evolving sequentially at each step. From the sampled posterior values for the nine parameters, we focused on the final 50%, calculating their median alongside the 16^{th} and 84^{th} percentile errors for estimation. In the following section, we present the comprehensive results obtained from the above modeling procedures.

4.4 Results

This is the first 2D kinematic model of the LMC employing clusters and neighboring field regions with *Gaia* DR3 data. The data coverage of the LMC considered in this study is within $\sim 7^\circ$ from the LMC center. The primary modeling is performed with 1705 clusters and nearby field regions, estimating nine best-fitting

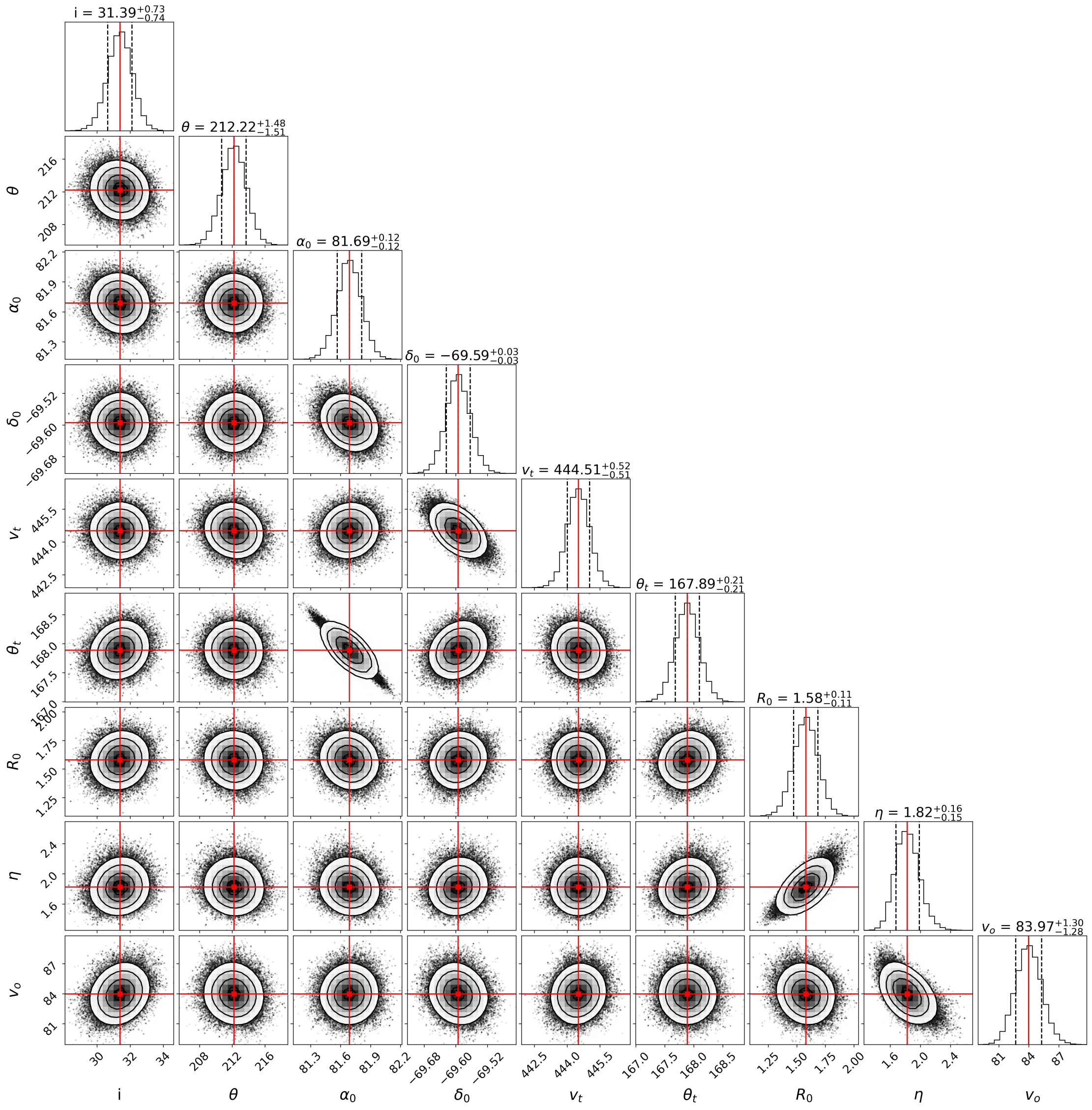

FIGURE 4.1: The corner plot representing the sampled posterior distribution of nine kinematic parameters for the primary cluster data set is shown here. The vertical red lines represent the median values, and the black dashed lines represent the 16th and 84th percentiles.

model parameters defining the kinematic properties of the LMC. Figures 4.1 and 4.2 show the sampled posterior distribution of the parameters for clusters and nearby field regions, respectively. We also performed the parameter estimation for the rest of the data sets mentioned in Table 4.1.

In the following subsections, we provide the estimated kinematic parameters obtained for all the modeled data sets. Additionally, we present the residual PM

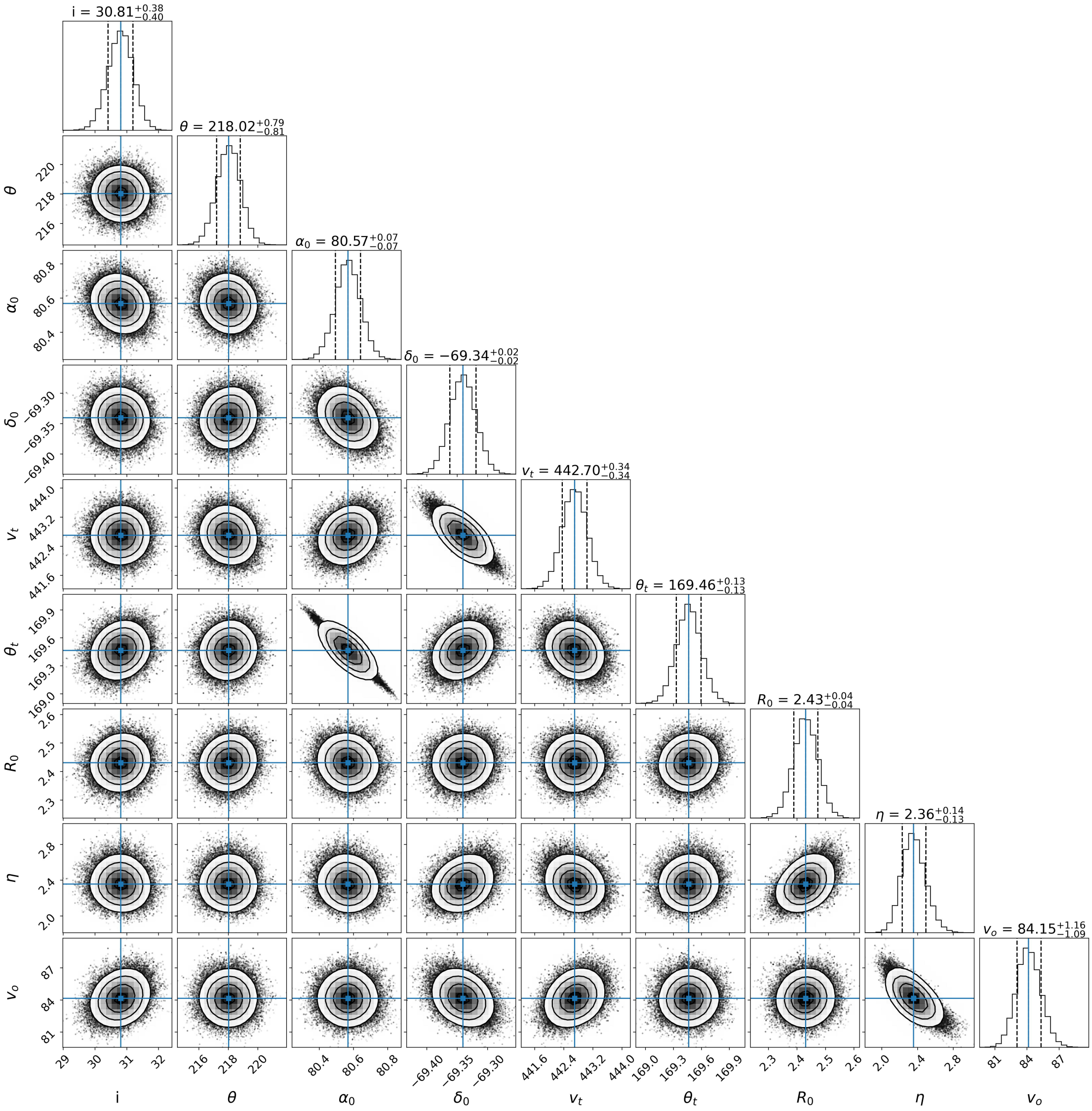

FIGURE 4.2: The corner plot representing the sampled posterior distribution of nine kinematic parameters for the primary field data set is shown here. The vertical blue lines represent the median values, and the black dashed lines represent the 16th and 84th percentiles.

derived from comparing the model and observed data.

TABLE 4.2: The kinematic best-fitting parameters obtained for the LMC from the primary model of clusters and nearby field regions are tabulated below.

Data	i (deg)	Θ (deg)	α_0 (deg)	δ_0 (deg)	v_t (km s^{-1})	θ_t (deg)	R_0 (kpc)	η	v_0 (km s^{-1})
Clusters	$31.39^{+0.73}_{-0.74}$	$122.22^{+1.48}_{-1.51}$	$81.69^{+0.12}_{-0.12}$	$-69.59^{+0.03}_{-0.03}$	$444.51^{+0.52}_{-0.51}$	$167.89^{+0.21}_{-0.21}$	$1.58^{+0.11}_{-0.11}$	$1.82^{+0.16}_{-0.15}$	$83.97^{+1.3}_{-1.28}$
Nearby field	$30.81^{+0.38}_{-0.4}$	$128.02^{+0.79}_{-0.81}$	$80.57^{+0.07}_{-0.07}$	$-69.34^{+0.02}_{-0.02}$	$442.7^{+0.34}_{-0.34}$	$169.46^{+0.13}_{-0.13}$	$2.43^{+0.04}_{-0.04}$	$2.36^{+0.14}_{-0.13}$	$84.15^{+1.16}_{-1.09}$

4.4.1 Cluster and Field kinematics

Table 4.2 provides the estimated kinematic parameters for the primary model involving clusters and field stars. The position angle of the line of nodes is conventionally measured from the North of the galaxy, whereas the modeling we performed involved measuring from the West. Therefore, we define the position angle of the line of nodes measured from North (PA) as Θ, which is (θ-90°) throughout the sections. The COM PM values in the West and the North directions ($\mu_{W,com}$ and $\mu_{N,com}$) can be obtained using the estimated tangential velocity vector estimated in our models (using v_t and θ_t and Equation 10 in V02). The orthographic projections of the sky coordinate and PM vectors are performed using equations 1, 2, and 3, as mentioned in G21. Figure 4.3 shows the bulk motion and rotation of the LMC obtained with clusters and field by subtracting the COM PM values estimated from the model. Below we compare the notable kinematic properties of clusters and field regions obtained from the modeling.

- $\mu_{W,com}$ and $\mu_{N,com}$ were estimated as 1.849 ± 0.003 mas yr^{-1} and 0.397 ± 0.007 mas yr^{-1} for the clusters. Similarly, for the field regions, the values are 1.851 ± 0.002 mas yr^{-1} and 0.344 ± 0.004 mas yr^{-1}. These values suggest no significant difference between the observed COM PM between cluster and field.

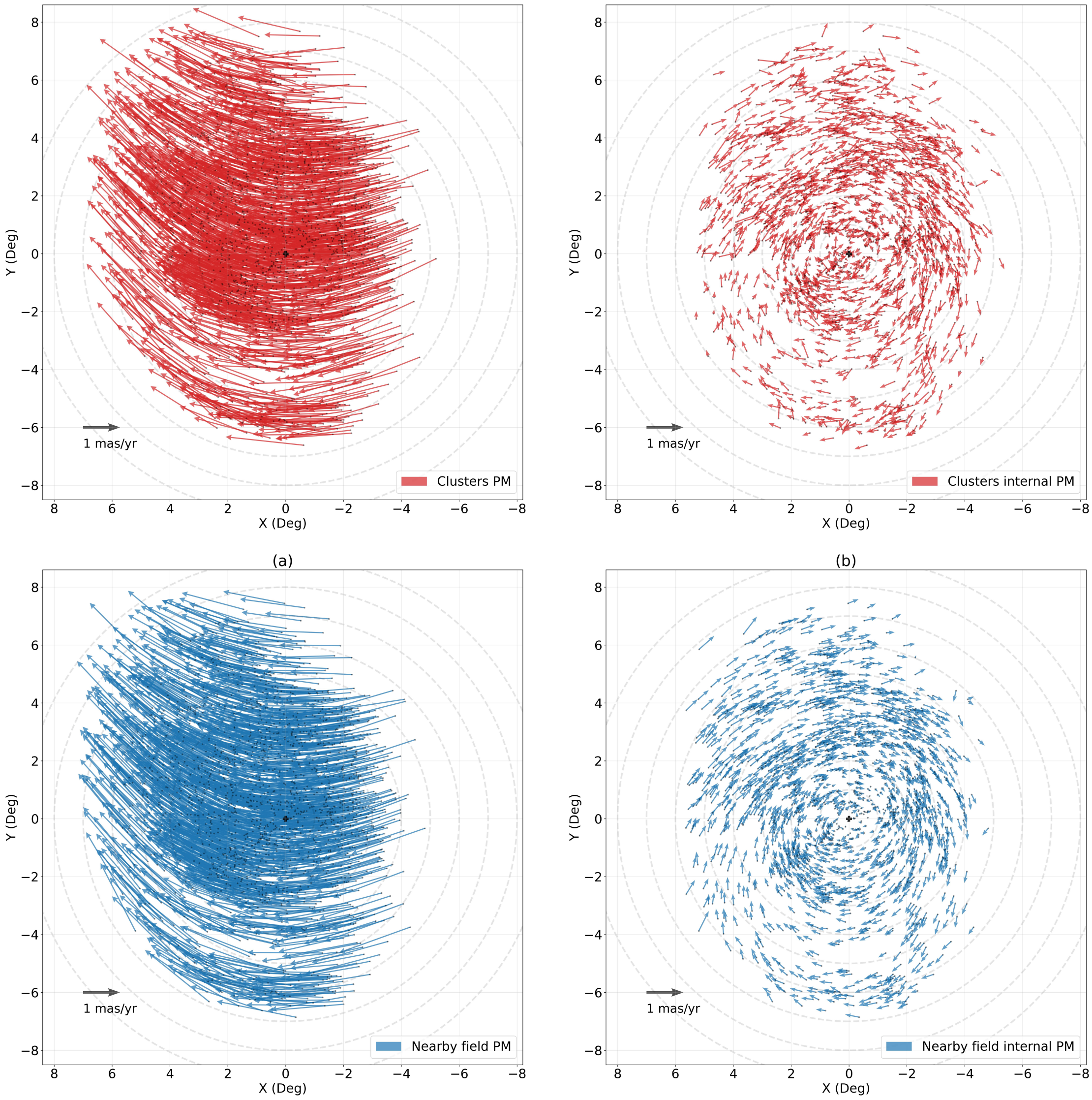

(a) (b)

(c) (d)

FIGURE 4.3: The observed PM plots for the clusters and field in the LMC sky plane are shown here. (a) Observed bulk motion of clusters; (b) Internal rotation PM of clusters; (c) Observed bulk motion of field; (b) Internal rotation PM of field.

- We note an offset of 28±8 arcmin between the dynamic centers (α_0, δ_0) of the cluster and field.
- Estimated Θ values of $122^\circ.22^{+1.48}_{-1.51}$ for clusters and $128^\circ.02^{+0.79}_{-0.81}$ for field regions point to an offset of $5^\circ.8 \pm 1^\circ.7$ between them, while the inclination, i, remains almost similar.
- The modeled rotational parameters, R_0 and η_0 appear to be larger for field regions compared to clusters, while the v_0 remains almost similar.

Two major notable differences in the kinematic properties obtained are, (1) for the value of R_0, where clusters have a relatively low value when compared to the field population, and (2) a significant offset in the dynamic centers of cluster and field population. In the next sub-section, we look into the control population we used in our model to understand the kinematic nature of the cluster and field population.

4.4.2 Comparison with control population

Table 4.3 provides the estimated kinematic parameters for the control population as mentioned in Section 4.2. Below we compare the cluster and field with the young MS stars and RC stars to understand their kinematic nature.

- $\mu_{W,com}$ and $\mu_{N,com}$ appear to be similar in all the data sets of the control population without any significant difference.
- The value of α_0 for the field and RC population are the same within errors, whereas the value of δ_0 shows a difference. The α_0 for clusters shows a significant offset in comparison to other populations. In general, the younger population tends to show a southern and eastward dynamic center.

Table 4.3: The kinematic best-fitting parameters obtained for the LMC based on the control sample (clusters, field population, young MS stars, RC stars) are tabulated below.

Data	i	Θ	α_0	δ_0	v_t	θ_t	R_0	η	v_0
	(deg)	(deg)	(deg)	(deg)	(km s^{-1})	(deg)	(kpc)		(km s^{-1})
Clusters	$31.11^{+0.82}_{-0.81}$	$120.27^{+1.65}_{-1.64}$	$81.71^{+0.13}_{-0.13}$	$-69.6^{+0.03}_{-0.03}$	$445.01^{+0.58}_{-0.59}$	$167.86^{+0.22}_{-0.22}$	$1.63^{+0.11}_{-0.11}$	$1.88^{+0.17}_{-0.15}$	$83.95^{+1.3}_{-1.3}$
Nearby field	$30.83^{+0.4}_{-0.41}$	$127.7^{+0.81}_{-0.8}$	$80.59^{+0.08}_{-0.08}$	$-69.35^{+0.02}_{-0.02}$	$442.93^{+0.37}_{-0.37}$	$169.43^{+0.14}_{-0.14}$	$2.45^{+0.04}_{-0.04}$	$2.35^{+0.14}_{-0.13}$	$84.56^{+1.21}_{-1.16}$
Young MS	$33.26^{+0.56}_{-0.57}$	$115.45^{+0.99}_{-0.99}$	$80.99^{+0.08}_{-0.08}$	$-69.64^{+0.02}_{-0.02}$	$446.65^{+0.43}_{-0.42}$	$169.5^{+0.15}_{-0.14}$	$1.29^{+0.08}_{-0.08}$	$1.5^{+0.1}_{-0.09}$	$90.92^{+1.26}_{-1.18}$
Red Clump	$31.1^{+0.44}_{-0.44}$	$135.84^{+0.91}_{-0.89}$	$80.68^{+0.11}_{-0.11}$	$-69.21^{+0.03}_{-0.03}$	$441.6^{+0.48}_{-0.46}$	$169.01^{+0.2}_{-0.19}$	$2.99^{+0.05}_{-0.05}$	$3.24^{+0.28}_{-0.24}$	$81.39^{+1.21}_{-1.18}$

- Estimated values of $\Theta = 115^\circ.45^{+0.99}_{-0.99}$ and $i = 33^\circ.26^{+0.56}_{-0.57}$ for the young MS population appear distinct from other data sets in the control population. RC population has the largest value of Θ ($135^\circ.84$).
- We note a significant shift in R_0, $|\Delta R_0| \approx 1.7$ kpc between young MS and RC population. A corresponding change of η is observed as well. We also estimate a larger value for $v_0 = 90.92^{+1.26}_{-1.18}$ km s^{-1} for the young MS population in comparison with the other data sets.

As observed in the previous comparison (subsection 4.4.1), the value of Θ appears to be changing across the control population. Notably, the clusters and young MS population show a relatively small value in comparison to the field and RC population. Specifically, the R_0 for the cluster and young MS population falls within the range of 2 kpc, while the field and RC population have values exceeding 2 kpc.

The model parameters estimated for the cluster and the control samples are used to obtain the values of rotational velocity (V$_{rot}$) of the LMC. Figure 4.4 shows the spatial distribution of V$_{rot}$ among the clusters, field stars, Young stars, and RC population. Though the overall appearance of the plots is similar, we note

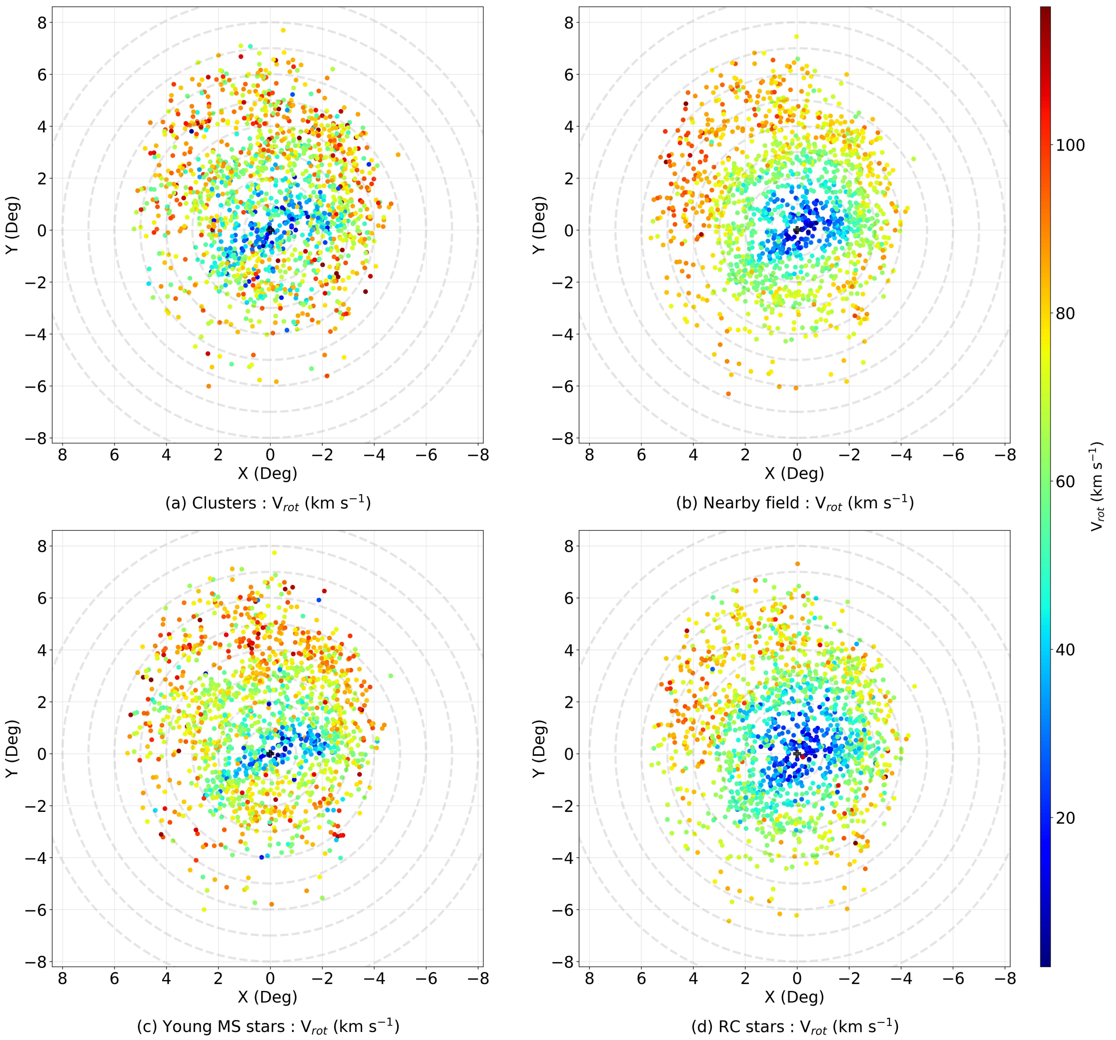

(a) Clusters : V$_{rot}$ (km s^{-1})

(b) Nearby field : V$_{rot}$ (km s^{-1})

(c) Young MS stars : V$_{rot}$ (km s^{-1})

(d) RC stars : V$_{rot}$ (km s^{-1})

FIGURE 4.4: Spatial distribution of the rotational velocity (V$_{rot}$) of the LMC for the clusters and the three control populations are depicted here.

that clusters (panel a) and the young MS stars (panel c) appear to have similar spatial distributions of V$_{rot}$, whereas the field (panel b) and the RC stars (panel d) appear to have similar V$_{rot}$ distribution. We also note that the elongated bar feature is more prominent in the V$_{rot}$ maps of clusters and young MS stars.

This suggests that the kinematic model of the LMC depends on the age of the population. In the subsequent subsection, we look into the kinematic model of the LMC with data sets of different ages, using the cluster age groups and nearby field regions as mentioned in Section 4.2.

TABLE 4.4: The kinematic best-fitting parameters obtained for the LMC based on the cluster age groups and nearby field regions are tabulated below. As mentioned in Section 4.2, the associated field population for each cluster age group is age-wise heterogeneous.

Data	i (deg)	Θ (deg)	α_0 (deg)	δ_0 (deg)	v_t (km s^{-1})	θ_t (deg)	R_0 (kpc)	η	v_0 (km s^{-1})
C_{AG-1}	$31.56^{+1.22}_{-1.3}$	$145.25^{+2.93}_{-3.01}$	$80.84^{+0.38}_{-0.38}$	$-69.19^{+0.13}_{-0.14}$	$440.57^{+1.49}_{-1.52}$	$169.02^{+0.63}_{-0.63}$	$3.14^{+0.18}_{-0.22}$	$5.61^{+1.76}_{-1.4}$	$78.63^{+1.4}_{-1.33}$
F_{AG-1}	$31.11^{+0.78}_{-0.79}$	$137.44^{+1.67}_{-1.67}$	$80.68^{+0.18}_{-0.19}$	$-69.19^{+0.06}_{-0.06}$	$439.83^{+0.76}_{-0.75}$	$169.14^{+0.33}_{-0.32}$	$2.84^{+0.08}_{-0.08}$	$5.44^{+0.97}_{-0.81}$	$77.21^{+1.12}_{-1.04}$
C_{AG-2}	$28.33^{+1.33}_{-1.45}$	$133.87^{+3.34}_{-3.42}$	$81.64^{+0.27}_{-0.27}$	$-69.6^{+0.07}_{-0.07}$	$445.16^{+1.17}_{-1.11}$	$168.04^{+0.46}_{-0.45}$	$2.17^{+0.2}_{-0.21}$	$2.52^{+0.46}_{-0.36}$	$80.63^{+1.52}_{-1.51}$
F_{AG-2}	$30.79^{+0.72}_{-0.72}$	$130.17^{+1.61}_{-1.63}$	$80.7^{+0.15}_{-0.15}$	$-69.25^{+0.04}_{-0.04}$	$442.59^{+0.62}_{-0.63}$	$169.18^{+0.27}_{-0.27}$	$2.52^{+0.07}_{-0.08}$	$2.87^{+0.29}_{-0.25}$	$81.03^{+1.3}_{-1.28}$
C_{AG-3}	$35.36^{+1.2}_{-1.31}$	$111.11^{+2.08}_{-2.04}$	$81.59^{+0.21}_{-0.21}$	$-69.6^{+0.05}_{-0.05}$	$445.2^{+0.9}_{-0.9}$	$168.31^{+0.36}_{-0.35}$	$1.34^{+0.17}_{-0.16}$	$2.06^{+0.34}_{-0.27}$	$81.31^{+1.51}_{-1.49}$
F_{AG-3}	$29.89^{+0.72}_{-0.73}$	$123.5^{+1.41}_{-1.46}$	$80.36^{+0.12}_{-0.12}$	$-69.34^{+0.03}_{-0.03}$	$443.01^{+0.56}_{-0.55}$	$169.84^{+0.22}_{-0.22}$	$2.28^{+0.06}_{-0.07}$	$2.34^{+0.18}_{-0.16}$	$81.88^{+1.47}_{-1.43}$
C_{AG-4}	$33.34^{+1.87}_{-2.04}$	$118.39^{+2.98}_{-3.16}$	$81.29^{+0.26}_{-0.26}$	$-69.68^{+0.08}_{-0.08}$	$444.4^{+1.65}_{-1.59}$	$168.33^{+0.46}_{-0.46}$	$1.98^{+0.17}_{-0.18}$	$3.69^{+0.85}_{-0.64}$	$79.6^{+1.62}_{-1.56}$
F_{AG-4}	$30.38^{+1.06}_{-1.1}$	$125.54^{+1.75}_{-1.84}$	$80.6^{+0.2}_{-0.2}$	$-69.57^{+0.06}_{-0.06}$	$445.6^{+1.14}_{-1.13}$	$169.5^{+0.37}_{-0.36}$	$2.54^{+0.1}_{-0.11}$	$3.1^{+0.4}_{-0.35}$	$81.96^{+1.54}_{-1.5}$

4.4.3 Age dependent kinematics of the LMC

The age-dependent variation of the kinematic parameters of the LMC was estimated using the data sets mentioned in Section 4.2. Table 4.4 provides the estimated kinematic parameters for the cluster and nearby field data sets based on the cluster age groups. Below, we compare their kinematic properties.

- As noted in the previous subsections, the COM PM shows minimal variations across different age groups. Even slight variations in the parameter v_t estimated as in Table 4.4 for different age groups do not result in substantial shifts in $\mu_{W,com}$ and $\mu_{N,com}$.

- The clusters ranging in age from $\sim$ 100 Myr to 1.25 Gyr show a small offset in the (α_0, δ_0) to the South-East with respect to the older clusters, as evident from C_{AG-2} and C_{AG-3}. Meanwhile, the nearby field population in these age groups shows variation only in the South.

- Θ attains its minimum value of $111^\circ.11^{+2.08}_{-2.04}$ for the C_{AG-3}, with field also showing a similar trend. Notably, the i ($35^\circ.36^{+1.2}_{-1.31}$) for C_{AG-3} is the largest when compared to other age groups. In the case of the field regions, we do not detect any significant shift in i, but a smaller shift in Θ is noted.
- In the cluster data sets, the minimum value of R_0 is estimated to be $1.34^{+0.17}_{-0.16}$ kpc for the C_{AG-3}, while its maximum value occurs at $3.14^{+0.18}_{-0.22}$ kpc for the C_{AG-1}. Similarly, in the field data sets, there is a comparable pattern with the minimum and maximum values of $2.28^{+0.06}_{-0.07}$ kpc and $2.84^{+0.08}_{-0.08}$ kpc for F_{AG-3} and F_{AG-1}, respectively. η also shows a similar trend in the age-based data sets.
- The values of v_0 remain relatively consistent across all datasets, and any observed changes are not significant, as they are within the margin of errors.

As noted in the above comparison, there is a noticeable deviation of kinematic parameters for the cluster age groups, in contrast to the datasets of the field region associated with each age group. The comparison presented in this section has shown that the dependence of kinematic parameters on the age of the population is indeed present, and the variations are statistically significant. In the following subsections, we further investigate the dependence of estimated parameters on the cluster richness as mentioned in Section 4.2.

4.4.4 Influence of cluster richness on the kinematic model

Table 4.5 shows the estimated kinematic parameters for the data sets based on cluster richness, as outlined in Section 4.2. The cluster data sets and the nearby

Table 4.5: The kinematic best-fitting parameters obtained for the LMC based on the cluster richness and their nearby field regions are tabulated below.

Data	i	Θ	α_0	δ_0	v_t	θ_t	R_0	η	v_0
	(deg)	(deg)	(deg)	(deg)	(km s^{-1})	(deg)	(kpc)		(km s^{-1})
C_{10}	$31.78^{+0.72}_{-0.75}$	$122.19^{+1.48}_{-1.52}$	$81.7^{+0.13}_{-0.13}$	$-69.61^{+0.03}_{-0.03}$	$444.87^{+0.55}_{-0.54}$	$167.87^{+0.22}_{-0.22}$	$1.59^{+0.11}_{-0.11}$	$1.85^{+0.17}_{-0.15}$	$83.99^{+1.3}_{-1.24}$
F_{10}	$30.78^{+0.4}_{-0.41}$	$127.85^{+0.82}_{-0.79}$	$80.59^{+0.07}_{-0.08}$	$-69.35^{+0.02}_{-0.02}$	$442.82^{+0.35}_{-0.35}$	$169.43^{+0.14}_{-0.14}$	$2.41^{+0.04}_{-0.04}$	$2.34^{+0.14}_{-0.13}$	$84.15^{+1.17}_{-1.14}$
C_{20}	$31.76^{+0.85}_{-0.88}$	$119.48^{+1.73}_{-1.73}$	$81.85^{+0.14}_{-0.14}$	$-69.62^{+0.03}_{-0.03}$	$444.81^{+0.58}_{-0.61}$	$167.59^{+0.24}_{-0.23}$	$1.47^{+0.12}_{-0.12}$	$1.81^{+0.18}_{-0.16}$	$82.89^{+1.34}_{-1.33}$
F_{20}	$30.18^{+0.49}_{-0.49}$	$127.05^{+0.94}_{-0.97}$	$80.59^{+0.09}_{-0.09}$	$-69.34^{+0.02}_{-0.02}$	$442.55^{+0.4}_{-0.4}$	$169.43^{+0.16}_{-0.16}$	$2.41^{+0.05}_{-0.05}$	$2.55^{+0.18}_{-0.16}$	$82.22^{+1.19}_{-1.15}$
C_{30}	$31.62^{+0.94}_{-0.98}$	$119.72^{+1.91}_{-1.94}$	$82.06^{+0.14}_{-0.14}$	$-69.63^{+0.04}_{-0.04}$	$445.06^{+0.65}_{-0.64}$	$167.23^{+0.24}_{-0.24}$	$1.31^{+0.14}_{-0.13}$	$1.69^{+0.18}_{-0.16}$	$82.59^{+1.39}_{-1.39}$
F_{30}	$29.86^{+0.55}_{-0.55}$	$127.06^{+1.13}_{-1.13}$	$80.72^{+0.1}_{-0.1}$	$-69.33^{+0.03}_{-0.03}$	$442.4^{+0.46}_{-0.46}$	$169.19^{+0.19}_{-0.18}$	$2.42^{+0.05}_{-0.05}$	$2.58^{+0.19}_{-0.18}$	$81.9^{+1.27}_{-1.24}$
C_{40}	$31.04^{+1.04}_{-1.08}$	$118.5^{+2.09}_{-2.12}$	$82.2^{+0.16}_{-0.17}$	$-69.61^{+0.04}_{-0.04}$	$445.07^{+0.7}_{-0.66}$	$166.97^{+0.28}_{-0.28}$	$1.34^{+0.14}_{-0.15}$	$1.68^{+0.19}_{-0.17}$	$82.04^{+1.47}_{-1.42}$
F_{40}	$28.81^{+0.63}_{-0.64}$	$126.27^{+1.31}_{-1.37}$	$80.82^{+0.11}_{-0.11}$	$-69.33^{+0.03}_{-0.03}$	$442.28^{+0.5}_{-0.51}$	$169.04^{+0.2}_{-0.2}$	$2.35^{+0.06}_{-0.06}$	$2.52^{+0.2}_{-0.19}$	$80.96^{+1.32}_{-1.26}$
C_{50}	$31.05^{+1.13}_{-1.24}$	$116.34^{+2.27}_{-2.3}$	$82.36^{+0.17}_{-0.17}$	$-69.65^{+0.04}_{-0.04}$	$445.58^{+0.73}_{-0.74}$	$166.76^{+0.29}_{-0.29}$	$1.15^{+0.15}_{-0.15}$	$1.59^{+0.19}_{-0.17}$	$81.29^{+1.52}_{-1.47}$
F_{50}	$28.94^{+0.69}_{-0.72}$	$126.19^{+1.5}_{-1.53}$	$81.06^{+0.12}_{-0.12}$	$-69.37^{+0.03}_{-0.03}$	$442.56^{+0.51}_{-0.53}$	$168.66^{+0.21}_{-0.21}$	$2.18^{+0.07}_{-0.07}$	$2.37^{+0.21}_{-0.18}$	$80.25^{+1.38}_{-1.31}$
C_{60}	$29.75^{+1.35}_{-1.4}$	$116.94^{+2.6}_{-2.69}$	$82.5^{+0.18}_{-0.17}$	$-69.69^{+0.05}_{-0.04}$	$445.95^{+0.77}_{-0.75}$	$166.49^{+0.29}_{-0.3}$	$0.95^{+0.16}_{-0.15}$	$1.43^{+0.19}_{-0.16}$	$80.06^{+1.56}_{-1.58}$
F_{60}	$28.13^{+0.77}_{-0.8}$	$127.28^{+1.76}_{-1.77}$	$81.34^{+0.12}_{-0.12}$	$-69.42^{+0.04}_{-0.04}$	$442.91^{+0.58}_{-0.56}$	$168.16^{+0.22}_{-0.22}$	$2.07^{+0.08}_{-0.08}$	$2.12^{+0.19}_{-0.17}$	$80.47^{+1.44}_{-1.46}$

field regions are modeled based on cluster richness, which helped in checking for any kinematic changes in the model based on poor and rich clusters.

Figure 4.5 shows the variation of the kinematic parameters corresponding to different cluster and field groups based on cluster richness. We note an offset of dynamic centers from poor to rich clusters in the increasing RA directions for both clusters and field populations. Meanwhile, the shift of COM PM for poor to rich clusters is seen increasing in North and West directions. Similarly, estimates for Φ, Θ, R_0, and v_0 show a decrease from C/F10 to C/F60 groups (as seen in Table 4.5). However, a notable deviation becomes apparent in the kinematic parameters when considering entire cluster groups compared to field groups. This once again

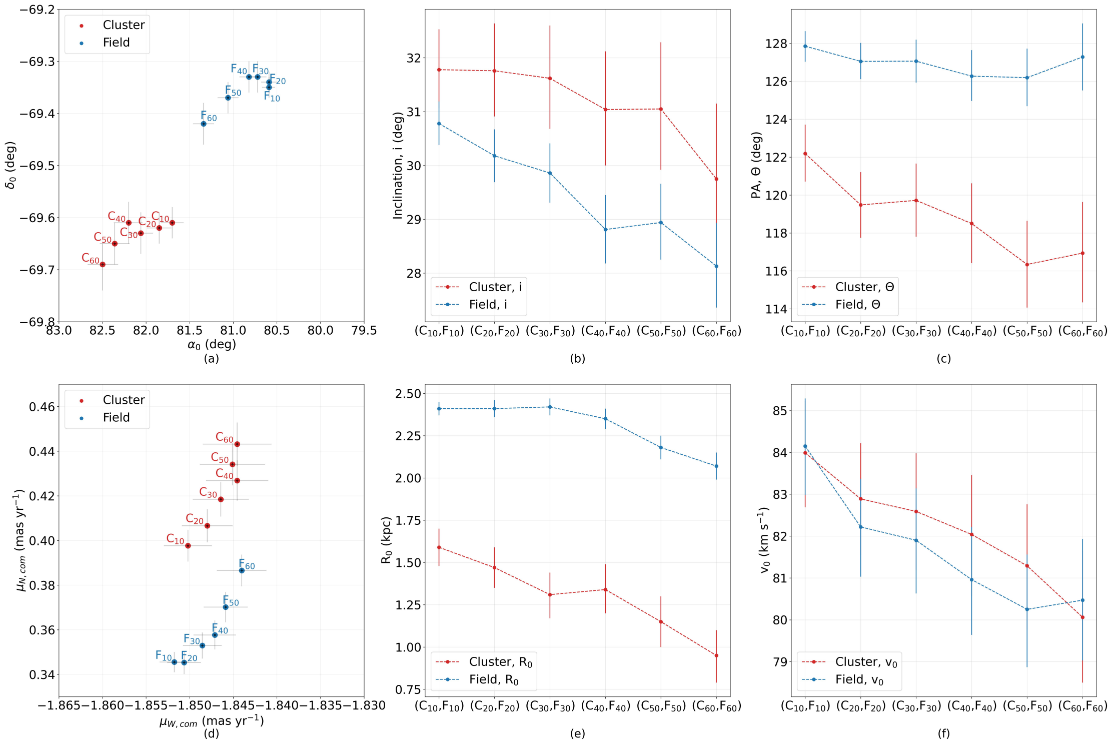

FIGURE 4.5: The variation of kinematic parameters based on cluster richness is shown here. Estimated parameters for cluster groups (C_{10} to C_{60}) and nearby field groups (F_{10} to F_{60}) are shown in red and blue colors from Panel (a) to (f). (a) Variation in (α_0, δ_0); (b) Variation in i; (c) Variation in Θ; (d) Variation in ($\mu_{W,com}$, $\mu_{N,com}$); (e) Variation in R_0; (f) Variation in v_0.

indicates that the kinematic model for clusters and the field population indeed manifests distinct kinematic properties. We also note that the cluster richness groups do not have similar spatial coverage. Overall, we do detect variation in the COM PM, dynamic center, i, and R_0, which may partially be due to the spatial coverage, and the variation in Θ is statistically insignificant.

4.4.5 Impact of the LMC's spatial coverage on kinematic properties

Table 4.6 shows the estimated kinematic parameters for the data sets based on the spatial coverage of the LMC. The circular regions of radii increase from 2° to

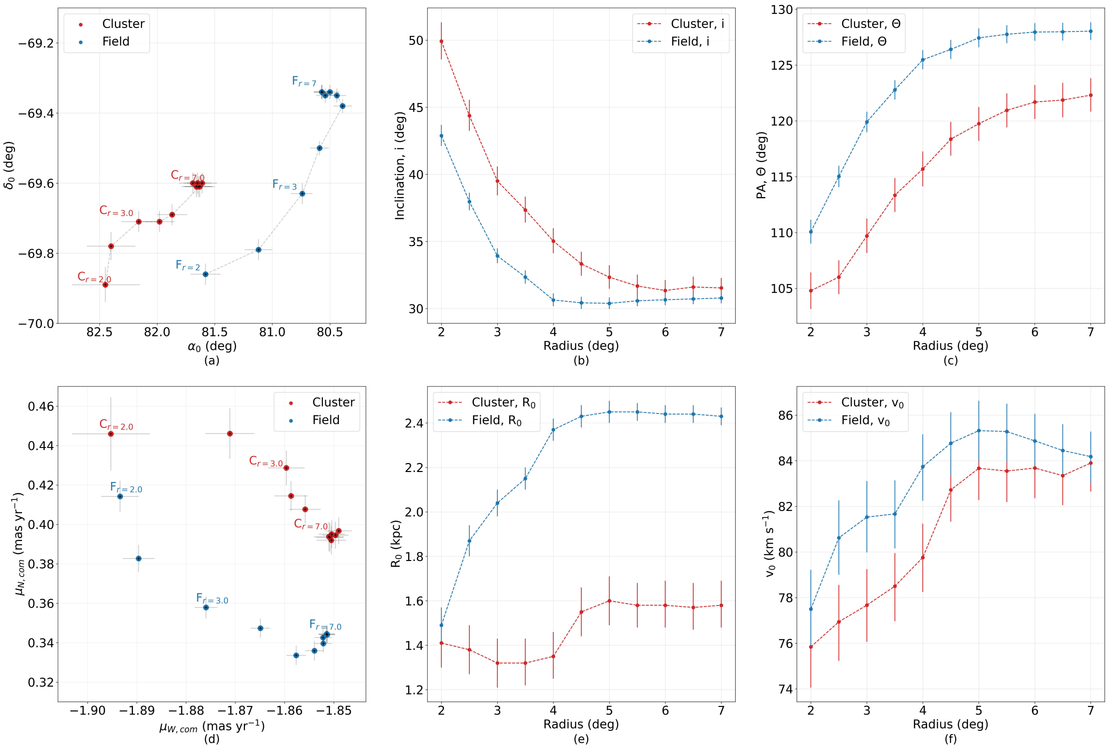

FIGURE 4.6: The variation of kinematic parameters based on the spatial coverage of the LMC is shown here. Estimated parameters for different spatial coverage from 2° to 7° with a step size of 0.5° from the center (based on the primary model) of the LMC are shown here. The corresponding cluster data sets ($C_{r=2}$ to $C_{r=7}$) and nearby field data sets ($F_{r=2}$ to $F_{r=7}$)are shown in red and blue colors from Panel (a) to (f). (a) Variation in (α_0, δ_0); (b) Variation in i; (c) Variation in Θ; (d) Variation in ($\mu_{W,com}$, $\mu_{N,com}$); (e) Variation in R_0; (f) Variation in v_0.

7° with a step size of 0.5° from the kinematic center (from the primary model, see Table 4.2) of the LMC were used to perform the modeling.

Figure 4.6 shows the radial variation of the kinematic parameters in the case of clusters and nearby field regions. Within the radii considered in this study, there is a notable offset in the amplitude of PM, of the order of $\sim$ 0.06 mas yr^{-1} in ($\mu_{W,com}$, $\mu_{N,com}$) between the inner and outer cluster/field regions. Similarly, we note a positional offset of $\sim$ 0.4° for clusters and $\sim$ 0.6° for the field between the estimated values of α_0 and δ_0. The value of i steeply decreases from the inner to outer radii, from $\sim$ 50° to $\sim$ 32° in the case of clusters, and $\sim$ 43° to $\sim$ 31° in the case of field population. Meanwhile, the value of Θ increases from inner

Table 4.6: The kinematic best-fitting parameters obtained for the LMC based on the spatial coverage of the LMC with clusters and nearby field regions are tabulated below.

Data	i	Θ	α_0	δ_0	v_t	θ_t	R_0	η	v_0
	(deg)	(deg)	(deg)	(deg)	(km s^{-1})	(deg)	(kpc)		(km s^{-1})
$C_{r[2.0]}$	$49.93^{+1.36}_{-1.41}$	$104.79^{+1.64}_{-1.63}$	$82.45^{+0.3}_{-0.29}$	$-69.89^{+0.05}_{-0.05}$	$457.7^{+1.59}_{-1.56}$	$166.76^{+0.53}_{-0.56}$	$1.41^{+0.11}_{-0.12}$	$3.38^{+0.99}_{-0.67}$	$75.84^{+1.78}_{-1.81}$
$F_{r[2.0]}$	$42.89^{+0.77}_{-0.8}$	$110.07^{+1.06}_{-1.07}$	$81.58^{+0.13}_{-0.13}$	$-69.86^{+0.03}_{-0.03}$	$455.62^{+0.82}_{-0.76}$	$167.66^{+0.24}_{-0.24}$	$1.49^{+0.09}_{-0.08}$	$1.57^{+0.13}_{-0.12}$	$77.5^{+1.76}_{-1.72}$
$C_{r[2.5]}$	$44.38^{+1.13}_{-1.17}$	$106.01^{+1.53}_{-1.5}$	$82.4^{+0.21}_{-0.21}$	$-69.78^{+0.04}_{-0.04}$	$452.18^{+0.96}_{-0.96}$	$166.59^{+0.38}_{-0.39}$	$1.38^{+0.11}_{-0.11}$	$2.69^{+0.52}_{-0.41}$	$76.94^{+1.71}_{-1.62}$
$F_{r[2.5]}$	$37.97^{+0.64}_{-0.66}$	$115.03^{+0.96}_{-0.96}$	$81.12^{+0.12}_{-0.12}$	$-69.79^{+0.03}_{-0.03}$	$453.23^{+0.69}_{-0.68}$	$168.55^{+0.21}_{-0.21}$	$1.87^{+0.07}_{-0.07}$	$1.93^{+0.15}_{-0.13}$	$80.62^{+1.62}_{-1.64}$
$C_{r[3.0]}$	$39.51^{+1.07}_{-1.08}$	$109.7^{+1.53}_{-1.55}$	$82.16^{+0.15}_{-0.15}$	$-69.71^{+0.03}_{-0.03}$	$448.62^{+0.76}_{-0.78}$	$167.02^{+0.27}_{-0.27}$	$1.32^{+0.11}_{-0.11}$	$2.19^{+0.33}_{-0.27}$	$77.67^{+1.61}_{-1.58}$
$F_{r[3.0]}$	$33.93^{+0.54}_{-0.56}$	$119.91^{+0.92}_{-0.91}$	$80.74^{+0.09}_{-0.1}$	$-69.63^{+0.03}_{-0.03}$	$448.94^{+0.49}_{-0.49}$	$169.2^{+0.17}_{-0.17}$	$2.04^{+0.06}_{-0.06}$	$2.03^{+0.14}_{-0.12}$	$81.53^{+1.55}_{-1.58}$
$C_{r[3.5]}$	$37.35^{+0.94}_{-0.99}$	$113.34^{+1.49}_{-1.54}$	$81.98^{+0.13}_{-0.13}$	$-69.71^{+0.03}_{-0.03}$	$447.66^{+0.71}_{-0.68}$	$167.43^{+0.23}_{-0.23}$	$1.32^{+0.1}_{-0.11}$	$2.09^{+0.27}_{-0.23}$	$78.5^{+1.53}_{-1.45}$
$F_{r[3.5]}$	$32.35^{+0.49}_{-0.5}$	$122.78^{+0.86}_{-0.86}$	$80.59^{+0.08}_{-0.08}$	$-69.5^{+0.02}_{-0.02}$	$445.93^{+0.41}_{-0.41}$	$169.45^{+0.15}_{-0.15}$	$2.15^{+0.05}_{-0.05}$	$2.13^{+0.14}_{-0.13}$	$81.67^{+1.51}_{-1.47}$
$C_{r[4.0]}$	$35.03^{+0.9}_{-0.96}$	$115.7^{+1.56}_{-1.57}$	$81.87^{+0.13}_{-0.13}$	$-69.69^{+0.03}_{-0.03}$	$446.66^{+0.66}_{-0.66}$	$167.61^{+0.23}_{-0.22}$	$1.35^{+0.1}_{-0.11}$	$1.95^{+0.22}_{-0.2}$	$79.76^{+1.51}_{-1.48}$
$F_{r[4.0]}$	$30.64^{+0.46}_{-0.49}$	$125.48^{+0.85}_{-0.87}$	$80.39^{+0.08}_{-0.08}$	$-69.38^{+0.02}_{-0.02}$	$443.67^{+0.42}_{-0.41}$	$169.82^{+0.15}_{-0.15}$	$2.37^{+0.05}_{-0.05}$	$2.29^{+0.14}_{-0.13}$	$83.74^{+1.49}_{-1.42}$
$C_{r[4.5]}$	$33.33^{+0.88}_{-0.91}$	$118.37^{+1.48}_{-1.54}$	$81.63^{+0.13}_{-0.13}$	$-69.61^{+0.03}_{-0.03}$	$444.86^{+0.63}_{-0.64}$	$167.99^{+0.23}_{-0.23}$	$1.55^{+0.11}_{-0.11}$	$1.94^{+0.19}_{-0.17}$	$82.72^{+1.39}_{-1.34}$
$F_{r[4.5]}$	$30.43^{+0.45}_{-0.45}$	$126.41^{+0.87}_{-0.85}$	$80.44^{+0.08}_{-0.08}$	$-69.35^{+0.02}_{-0.02}$	$442.91^{+0.38}_{-0.39}$	$169.73^{+0.14}_{-0.15}$	$2.43^{+0.05}_{-0.05}$	$2.29^{+0.14}_{-0.13}$	$84.77^{+1.43}_{-1.36}$
$C_{r[5.0]}$	$32.34^{+0.86}_{-0.89}$	$119.75^{+1.53}_{-1.5}$	$81.61^{+0.13}_{-0.13}$	$-69.6^{+0.03}_{-0.03}$	$444.66^{+0.62}_{-0.6}$	$168.04^{+0.22}_{-0.22}$	$1.6^{+0.11}_{-0.11}$	$1.9^{+0.18}_{-0.16}$	$83.67^{+1.39}_{-1.35}$
$F_{r[5.0]}$	$30.39^{+0.42}_{-0.44}$	$127.44^{+0.83}_{-0.85}$	$80.5^{+0.08}_{-0.08}$	$-69.34^{+0.02}_{-0.02}$	$442.65^{+0.36}_{-0.36}$	$169.61^{+0.14}_{-0.14}$	$2.45^{+0.05}_{-0.05}$	$2.27^{+0.13}_{-0.13}$	$85.32^{+1.32}_{-1.31}$
$C_{r[5.5]}$	$31.68^{+0.81}_{-0.85}$	$120.95^{+1.52}_{-1.52}$	$81.64^{+0.12}_{-0.13}$	$-69.61^{+0.03}_{-0.03}$	$444.8^{+0.56}_{-0.57}$	$168.0^{+0.22}_{-0.22}$	$1.58^{+0.1}_{-0.1}$	$1.86^{+0.17}_{-0.15}$	$83.55^{+1.36}_{-1.29}$
$F_{r[5.5]}$	$30.58^{+0.41}_{-0.42}$	$127.76^{+0.8}_{-0.82}$	$80.54^{+0.08}_{-0.08}$	$-69.35^{+0.02}_{-0.02}$	$442.79^{+0.36}_{-0.37}$	$169.52^{+0.14}_{-0.14}$	$2.45^{+0.04}_{-0.04}$	$2.28^{+0.13}_{-0.13}$	$85.28^{+1.32}_{-1.22}$
$C_{r[6.0]}$	$31.35^{+0.76}_{-0.78}$	$121.69^{+1.52}_{-1.53}$	$81.66^{+0.13}_{-0.13}$	$-69.61^{+0.03}_{-0.03}$	$444.79^{+0.53}_{-0.55}$	$167.95^{+0.21}_{-0.22}$	$1.58^{+0.1}_{-0.11}$	$1.84^{+0.17}_{-0.15}$	$83.68^{+1.32}_{-1.25}$
$F_{r[6.0]}$	$30.66^{+0.4}_{-0.41}$	$127.96^{+0.78}_{-0.8}$	$80.57^{+0.08}_{-0.07}$	$-69.34^{+0.02}_{-0.02}$	$442.68^{+0.34}_{-0.35}$	$169.47^{+0.14}_{-0.14}$	$2.44^{+0.04}_{-0.04}$	$2.3^{+0.14}_{-0.13}$	$84.87^{+1.26}_{-1.19}$
$C_{r[6.5]}$	$31.61^{+0.75}_{-0.77}$	$121.87^{+1.54}_{-1.54}$	$81.65^{+0.12}_{-0.12}$	$-69.6^{+0.03}_{-0.03}$	$444.59^{+0.54}_{-0.53}$	$167.96^{+0.21}_{-0.21}$	$1.57^{+0.1}_{-0.11}$	$1.87^{+0.17}_{-0.16}$	$83.35^{+1.3}_{-1.24}$
$F_{r[6.5]}$	$30.72^{+0.39}_{-0.4}$	$127.99^{+0.79}_{-0.8}$	$80.57^{+0.07}_{-0.07}$	$-69.34^{+0.02}_{-0.02}$	$442.66^{+0.34}_{-0.33}$	$169.47^{+0.13}_{-0.13}$	$2.44^{+0.04}_{-0.04}$	$2.34^{+0.14}_{-0.13}$	$84.45^{+1.14}_{-1.15}$
$C_{r[7.0]}$	$31.54^{+0.73}_{-0.74}$	$122.31^{+1.47}_{-1.52}$	$81.69^{+0.12}_{-0.12}$	$-69.6^{+0.03}_{-0.03}$	$444.55^{+0.54}_{-0.52}$	$167.89^{+0.21}_{-0.21}$	$1.58^{+0.1}_{-0.11}$	$1.84^{+0.16}_{-0.15}$	$83.9^{+1.25}_{-1.24}$
$F_{r[7.0]}$	$30.79^{+0.39}_{-0.39}$	$128.04^{+0.78}_{-0.8}$	$80.57^{+0.07}_{-0.07}$	$-69.34^{+0.02}_{-0.02}$	$442.7^{+0.34}_{-0.34}$	$169.46^{+0.13}_{-0.13}$	$2.43^{+0.04}_{-0.04}$	$2.36^{+0.14}_{-0.13}$	$84.18^{+1.14}_{-1.1}$

to outer radii, from ∼ 108° to ∼ 122° in the case of clusters, and ∼ 110° to ∼ 128° in the case of field population. The rotational parameters, R_0 and v_0 after 5° show convergence to the values estimated as in the primary model (see Table 4.2). Therefore, the estimated parameters show a significant radial dependence for both clusters and field populations.

4.4.6 Residual PM of the LMC: Cluster vs Field

The residual PM value for the clusters and nearby field populations is found by subtracting the net modeled PM from the net observed PM values. The residual PM vectors for clusters and field regions are plotted in the X-Y plane as shown in Figure 4.7, panels (a) and (b), respectively. Clusters show larger residual PM in the spatial plot when compared with the field population. The spatial residual plot for clusters shows relatively large residuals in the bar region and in the northern LMC, whereas such large residuals are not found in the corresponding plot for the field population. The residual PM amplitudes (|Residual PM|) of both the clusters and the nearby field are used to generate the probability distribution plot as in Figure 4.7, panel (c) depicting the distribution of their values. We obtained a Root Mean Square (RMS) value of 0.146±0.002 mas yr^{-1} for clusters and 0.069±0.001 mas yr^{-1} for the nearby field population. The RMS distribution of clusters shows a broader profile, while the field shows a narrower one.

4.5 Discussion

In this study, we performed the kinematic modeling of the LMC using 1705 star clusters and nearby field regions for the first time. We also created an extensive additional 46 models using two control samples (young MS stars and RC stars),

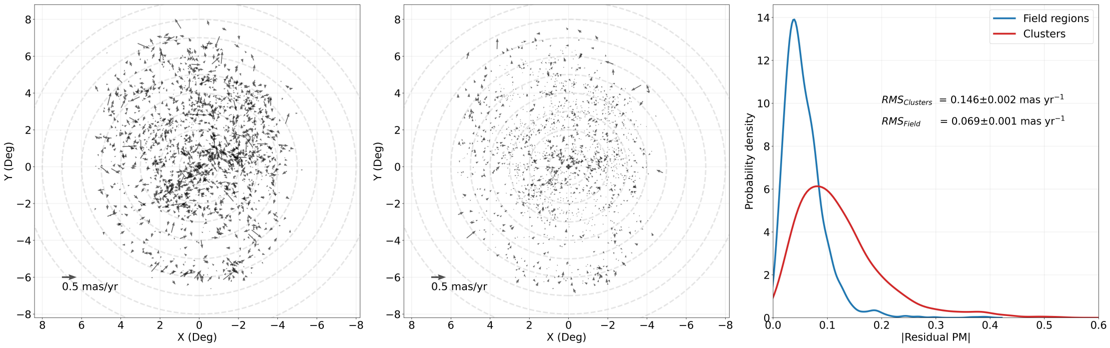

(a) Spatial plot of Residual PM vectors for clusters (b) Spatial plot of Residual PM vectors for field (c) |Residual PM| distribution

Figure 4.7: Residual PM of clusters and field population. (a) Spatial plot of residual PM vectors for the clusters; (b) Spatial distribution of residual PM vectors for the field population; (c) The Gaussian KDE showing the distribution of the |Residual PM|.

different cluster age groups and nearby fields, cluster richness groups, and samples with varying spatial coverage of the LMC. The clusters were cleaned using field star contamination and found less than 2% of MW source contamination in each cluster while cross-matching with the MW/ LMC source catalog by J23b. The median value of the PM is used for the study for both clusters and fields and hence is unlikely to be affected by the foreground MW contamination.

In the following subsections, we discuss the important results we obtained from the modeling. We compare the estimated kinematic parameters with the previous studies, analyze the rotation curve of the LMC for the control samples, trace the spatial variation of residual PM across the LMC, analyze the kinematic outliers from the model, and comment on the kinematic variation in parameters based on cluster age.

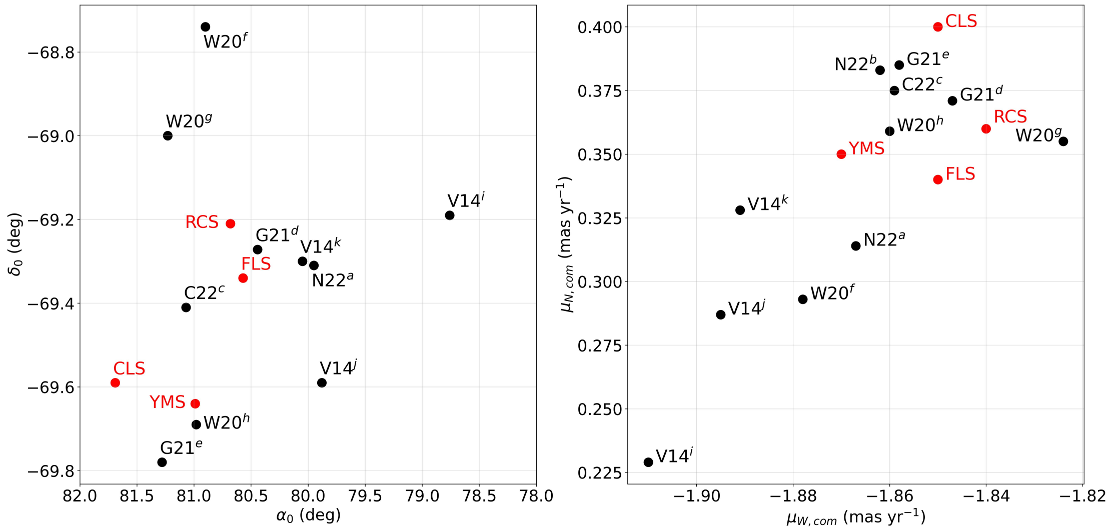

FIGURE 4.8: The parameter space of the estimated (α_0, δ_0) and ($\mu_{W,com}$, $\mu_{N,com}$) are compared with the reference studies (Table 4.7) are provided in panels (a) and (b), respectively. The corresponding estimated parameters for the clusters (CLS), field (FLS), young MS stars (YMS), and RC stars (RCS) are marked with red dots along with labels. The reference studies are marked with black dots along with labels.

4.5.1 Comparison of kinematic properties with previous studies

The estimated kinematic parameters of the LMC are compared with those from previous studies, mainly in which either the authors estimated the kinematic centers and COM PM values or adopted them. First we compare the estimations of (α_0, δ_0), ($\mu_{W,com}$, $\mu_{N,com}$), i, and Θ from studies by N22, C22, G21, W20, and V14. The parameters estimated are tabulated in Table 4.7 along with estimations from this study for comparison.

Figure 4.8 shows the distribution of (α_0, δ_0) and ($\mu_{W,com}$, $\mu_{N,com}$) estimations from the literature studies as mentioned above, along with the estimations from this study. We can notice a significant variation in the values of (α_0, δ_0) from various studies. Our estimations (shown in red) are located well within the range of other estimations, except the α_0 for the cluster population. Most clusters ($\sim 75\%$) used

TABLE 4.7: Comparison of the estimated kinematic parameters with previous studies. The first two rows list the estimations from this study.

α_0	δ_0	$\mu_{W,\mathbf{com}}$	$\mu_{N,\mathbf{com}}$	i	Θ	Reference
(deg)	(deg)	(deg)	(deg)	(deg)	(deg)	
$81.69^{+0.12}_{-0.12}$	$-69.59^{+0.03}_{-0.03}$	$-1.849^{+0.003}_{-0.003}$	$0.397\ ^{+0.007}_{-0.007}$	$31.39^{+0.73}_{-0.74}$	$122.22^{+1.48}_{-1.51}$	Clusters
$80.57^{+0.07}_{-0.07}$	$-69.34^{+0.02}_{-0.02}$	$-1.851^{+0.002}_{-0.002}$	$0.344\ ^{+0.004}_{-0.004}$	$30.81^{+0.38}_{-0.40}$	$128.02^{+0.79}_{-0.81}$	Field
$79.95^{+0.22}_{-0.23}$	$-69.31^{+0.12}_{-0.11}$	$-1.867^{+0.008}_{-0.008}$	$0.314^{+0.014}_{-0.014}$	$33.5^{+1.2}_{-1.3}$	$129.8^{+1.9}_{-1.9}$	N22 ^{a}
81.07	-69.41	$-1.862^{+0.002}_{-0.002}$	$0.383^{+0.002}_{-0.002}$	$28.7^{+1.4}_{-1.5}$	$126.0^{+2.5}_{-2.6}$	N22 ^{b}
80.443	-69.272	-1.859	0.375	$23.396^{+0.493}_{-0.501}$	$138.856^{+1.360}_{-1.370}$	C22 ^{c}
81.07	-69.41	-1.847	0.371	33.28	130.97	G21 ^{d}
81.28	-69.78	-1.858	0.385	34.08	129.92	G21 ^{e}
80.90 ± 0.29	-68.74 ± 0.12	-1.878 ± 0.007	0.293 ± 0.018	25.6 ± 1.1	135.6 ± 3.3	W20 ^{f}
81.23 ± 0.04	-69.00 ± 0.02	-1.824 ± 0.001	0.355 ± 0.002	26.1 ± 0.1	134.1 ± 0.4	W20 ^{g}
80.98 ± 0.07	-69.69 ± 0.02	-1.860 ± 0.002	0.359 ± 0.004	29.4 ± 0.4	152.0 ± 1.0	W20 ^{h}
78.76 ± 0.52	-69.19 ± 0.25	-1.910 ± 0.020	0.229 ± 0.047	39.6 ± 4.5	147.4 ± 10.0	V14 ^{i}
79.88 ± 0.83	-69.59 ± 0.25	-1.895 ± 0.024	0.287 ± 0.054	34.0 ± 7.0	139.1 ± 4.1	V14 ^{j}
80.05 ± 0.34	-69.30 ± 0.12	-1.891 ± 0.018	0.328 ± 0.025	26.2 ± 5.9	154.5 ± 2.1	V14 ^{k}

(N22 ^{a} : Estimated using VMC data; N22 ^{b} : Estimated with fixed (α_0, δ_0) based on G21, using VMC data; C22 ^{c} : Estimated with fixed (α_0, δ_0) and COM PM, using RC population with *Gaia* EDR3; G21 ^{d} : Estimated with *Gaia* EDR3; G21 ^{e} : Estimated with fixed (α_0, δ_0), using *Gaia* EDR3; W20 ^{f} : Estimated using carbon stars, with SkyMapper DR1; W20 ^{g} : Estimated using RGB stars, with SkyMapper DR1; W20 ^{h} : Estimated using Young stars, with SkyMapper DR1; V14 ^{i} : Estimated with the third epoch of *Hubble Space Telescope* (HST) data, using PM; V14 ^{j} : Estimated with the third epoch of HST data, using PM + v_{LOS} of old stars; V14 ^{k} : Estimated with the third epoch of HST data, using PM + v_{LOS} of young stars.)

for the modeling in this study are of ages younger than 1 Gyr (D24). Due to this, the estimated values of (α_0, δ_0) for clusters are closer to the estimation by W20 using the young stellar population. Meanwhile, the estimation from the young MS population is much closer to the W20 estimations. The field population and RC population are closely in agreement with the recent studies by G21, V14, N22, and C22. The offset of (α_0, δ_0) in the older and younger stellar population was previously noted by W20.

The $\mu_{W,com}$ and $\mu_{N,com}$ values for the clusters and field population also align with the recent studies by N22, C22, G21, and W20 in a similar manner. Notably, the clusters show a relatively larger PM in the North direction when compared to the field. However, the kinematic centers and COM PM are distinct for the clusters and field population.

The values of i and Θ estimated in this study are compared with the previous studies (see Table 4.7) and are more or less in agreement. However, the kinematic parameters such as i and Θ are known to vary with respect to the coverage of the LMC (N22). The variations, as seen from the table, also contribute to the coverage. In this study, for the first time, we studied the variation of kinematic parameters as a function of the spatial coverage of the LMC using star clusters, as described in the subsection 4.4.5. The inner regions of the LMC show a larger inclination with respect to outer regions, which is already noted in the study by S22 using RC population.

The following section discusses the rotational parameters (v_0, R_0) and rotation curves of the LMC for various populations.

4.5.2 Rotation of the LMC

The rotation curves for the clusters, nearby fields, young MS stars, and RC stars from the control sample (as mentioned in subsection 4.4.2) in the LMC plane, after deprojection are shown in Figure 4.9 (a. Clusters, b. Nearby field, c. young MS stars, d. RC stars). The running average for the data points is made with a bin resolution of 0.25 kpc, and shown in red. The fitted model is shown with the blue curve. The rotational velocity amplitude (v_0) does not show a significant variation across the clusters and field population. The estimated v_0 for clusters, fields, and RC stars are consistent with the estimates by W20. The young MS stars in our study show a slightly larger v_0 ($\sim$ 91 km s^{-1}) when compared to the RC stars. However, it is consistent with the observed v_0($\sim$ 90 km s^{-1}) for the younger population studied by N22.

In the cluster age-dependent kinematic model (subsection 4.4.3), the variation of R_0 for cluster age groups is provided. The age group C$_{AG-3}$ (log(age) = 8.0 - 8.65) and young MS stars from the control population show reduced values of R_0 at $1.34^{+0.17}_{-0.16}$ kpc and $1.29^{+0.08}_{-0.08}$ kpc, respectively. This is suggestive of a steeper rise of the rotational velocity when compared to the older population. The decreased R_0 for these age groups may imply a redistribution of mass, leading to a higher mass density in the central regions. Also, in the youngest group C$_{AG-4}$ (log(age) = 6.55 - 8.0), the cluster density in the galaxy shifts towards the North-East regions (D24). In C$_{AG-4}$, there is a shift in the value of R_0 to a slightly higher value of $1.98^{+0.17}_{-0.18}$ kpc. The field population near clusters is dominated by the older population, hence the R_0 value remains high.

Panel (a) of Figure 4.10 shows all the four model velocity profiles fitted to the control population provided in Figure 4.9. The v_0 for the control population is almost identical ($\sim$ 81 to 84 kms^{-1}), whereas the value for the young MS stars remains slightly higher ($\sim$ 91 kms^{-1}). It is clear from this figure that the clusters and young MS stars show a steeper rise of the V$_{rot}$ suggesting an increased mass density in the inner regions. A similar trend of small R_0 in the case of the younger population and larger R_0 in the case of the older population is noted in the study by W20. The variation in the value of R_0 with respect to population may be due to the effect of the evolution of the bar and its activity with time, resulting in the redistribution of mass in the inner regions.

Notably, the dispersion of the rotation velocity profile resides at $\sim$ 23 km s^{-1} and $\sim$ 11 km s^{-1} up to 6 kpc in the case of clusters and field population, respectively. In the case of the young MS population, there is a larger σ_{rot} of $\sim$ 22 km s^{-1} up to 2 kpc, then a slight decline and further rises after 4 kpc. Meanwhile, the RC population has a σ_{rot} of $\sim$ 20 km s^{-1} within 1 kpc and slowly declines and levels off at $\sim$ 12 km s^{-1} afterward. The larger dispersion values in the central 2 kpc might be due to the non-circular motions due to the bar.

Panel (b) of Figure 4.10 shows the radial variation of the V$_{rot}/\sigma_{rot}$ ratio for the four control population. As all of the population have similar V$_{rot}$ (except slightly higher value for the young MS stars), the higher values observed for the field stars suggest a relatively low σ_{rot}. The RC population has a similar profile, though with a slightly lower ratio (suggesting a relatively large σ_{rot}). The young MS stars have a more or less similar profile till $\sim$ 3 kpc, and we note a lower value of the ratio beyond this radius (suggesting a relatively large σ_{rot}). The cluster has a shallow profile and lowest value for the ratio, suggestive of the highest value of σ_{rot} at all radii. Overall, the low value of σ_{rot} the field population points to the minimal disk heating for this population. However, the ratios suggest that young clusters and young stars have relatively large velocity dispersion, which is suggestive of relatively recent perturbation(s) in the LMC disk. This may point to the heating of the gas in the disk (resulting in the formation of stars with similar kinematics). The heating may be due to internal perturbations, such as the bar and spiral arms, or external perturbation, which is the interaction with the SMC.

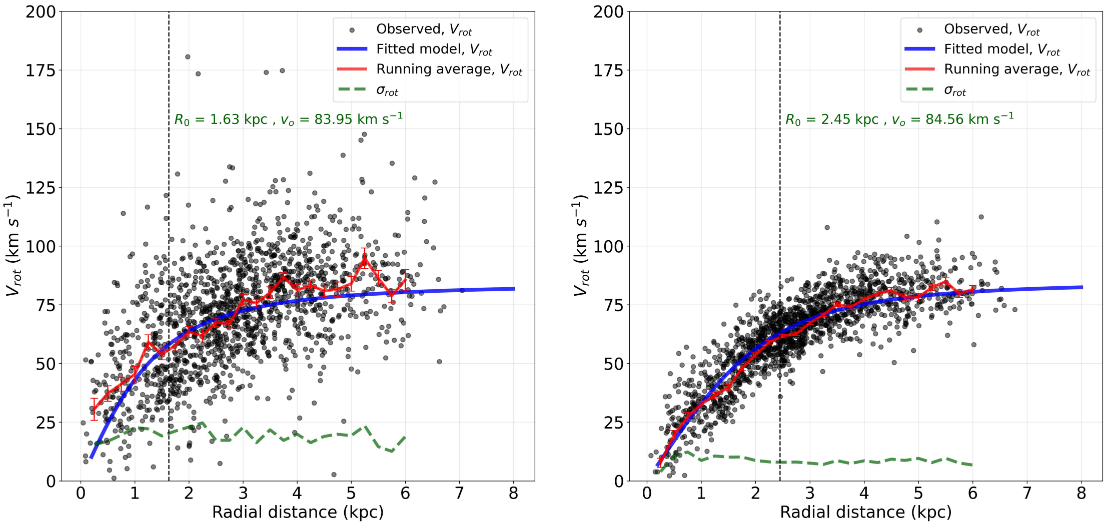

(a) Clusters

(b) Nearby field

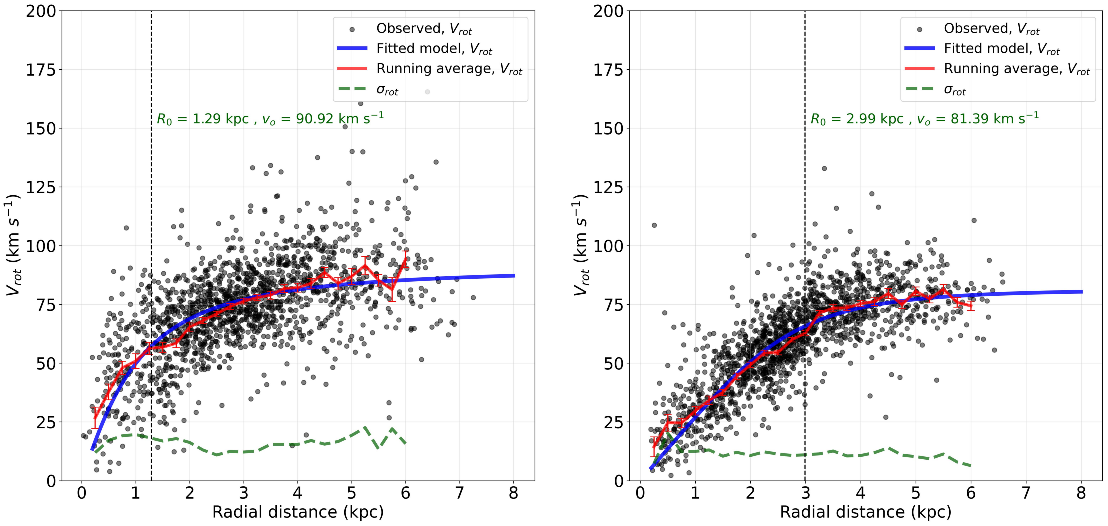

(c) Young MS stars

(d) RC stars

FIGURE 4.9: The rotation curve of the LMC based on the parameter estimation for the control sample (Clusters, Nearby field, young MS stars, and RC stars) are plotted in panels (a) to (d). The magnitude of the rotational velocity in the LMC plane (V_{rot}) is shown with black dots in each panel. The red curve represents the running average over the observed V_{rot} with a bin size of 0.25 kpc, and the blue curve shows the best-fitting model depending on the rotational parameters (v_0, R_0, η) estimated for each data set (see Table 4.3).

The rotational velocity maps shown in Figure 4.4 closely match with the velocity maps from G21. Additionally, the variation in slope between evolved and younger populations observed in Figure 4.10a is consistent with G21. However, there is a discrepancy in the rotation velocity dispersion profiles when compared to G21.

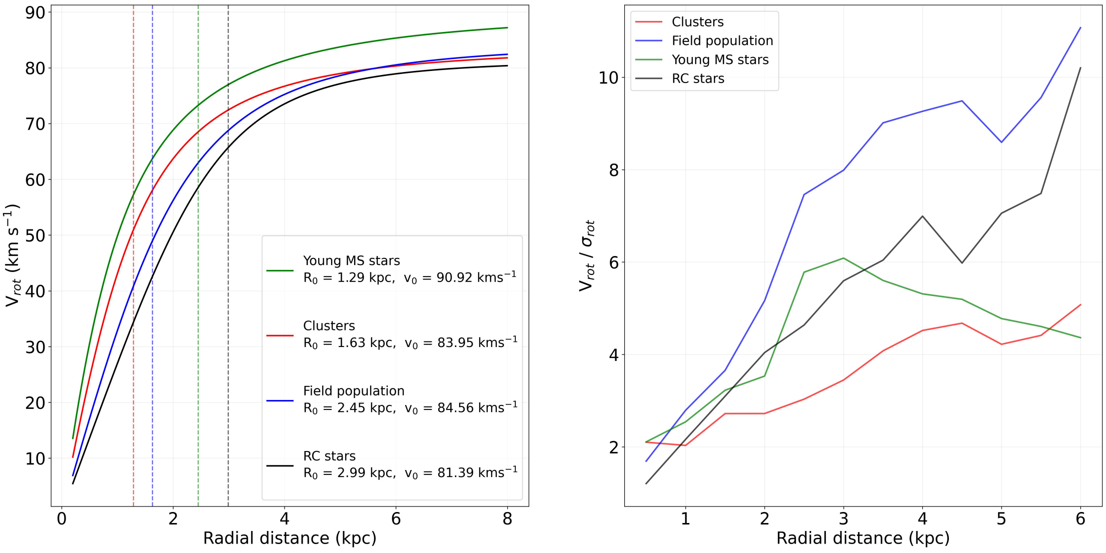

(a) (b)

FIGURE 4.10: Variataion of R_0 and V_{rot}/σ_{rot} for the control population (Clusters, Nearby field, young MS stars, and RC stars). (a) Modeled velocity profiles showing the variation in R_0 across the control sample; (b) Variation of V_{rot}/σ_{rot} across the control sample, estimated using a bin size of 0.4 kpc in radii.

4.5.3 Spatial variation of residual PM: Clusters and Field

In order to trace regions with large variations in the residual PM, the mean |Residual PM| is traced for different radii (1 to 6° with a bin size of 1° using annular regions) as shown in Figure 4.11. We observe a similar trend in radial variation of mean |Residual PM| for both the clusters and field population, though the values are significantly different. For inner radii less than 2°, the mean residual PM of the LMC is larger for both populations, likely to be due to the presence of the bar. Beyond 2°, we note a decline in mean residual PM, and it increases after 4°. This could be due to the presence of spiral arms in the galaxy, where dense star formation is noted. However, there is a clear signature of larger residual PM for clusters when compared to the field population.

The residual PM RMS profiles in Figure 4.7 can be compared with the study by C22 based on the numerical simulations by B12 with a population older than 1 Gyr. Figure 8 in C22 has provided the predicted $log\mathrm{RMS}_{|\mathrm{Residual\ PM}|}$ as a function

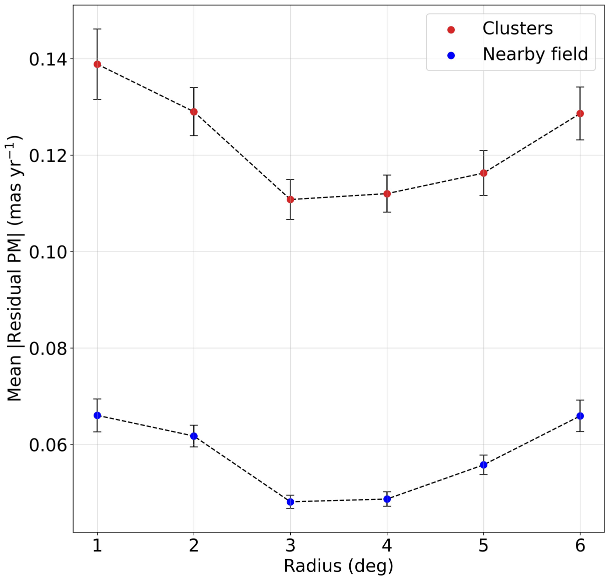

FIGURE 4.11: The radial variation of mean |Residual PM| in the sky plane. Annular regions with a bin size of 1° are used. Mean |Residual PM| of clusters and field population are marked with red and blue dots, respectively.

of the impact parameter (P in kpc) and impact timing (T in Myr) of the recent LMC-SMC interaction. We adopted the value of T as 149 Myr, based on the significant CF peak in the SMC as observed in Figure 3.10 to estimate the likely value of P. We note the assumed value of T is also in good agreement with the estimate by Z18, who suggests a recent direct collision between the LMC and the SMC at 147 Myr ago. The field $log\mathrm{RMS}_{|\mathrm{Residual\ PM}|}$ of -1.611 and -1.219 from the primary model and control sample support the Future 40 and Future 60 models provided in C22. We estimate that the impact parameter, P, must reside at less than 3 kpc, and most likely match with the impact parameter of 2 kpc as per B12 simulations. However, the RC stars in the control sample show a larger residual (0.08 mas yr^{-1}) compared to the estimates of C22 (0.058 mas yr^{-1}). We note that our model involves treating the COM PM and kinematic centers as free parameters, unlike C22. Hence a direct comparison of our results with C22 may be unrealistic.

The clusters and young stars show larger disk heating, with $log\mathrm{RMS}_{|\mathrm{Residual\ PM}|}$ of -0.853 and -0.957. This suggests that the young population is more perturbed, unlike the RC stars and other field stars. Also, the clusters, irrespective of age, show larger residual PM. The kinematic deviant clusters are analyzed in the next section.

4.5.4 Kinematically deviant clusters: Tracing the regions of larger residual PM

The residual PM distribution of clusters, as shown in Figure 4.7a suggests that some clusters have a large residual PM. We traced clusters with significantly large residuals ($>3\sigma$ of |Residual PM|) and identified the region with the highest density of such clusters, as illustrated in Figure 4.12(a) with the 2D Gaussian KDE. We find a significant density of clusters in the North-West at $\sim$ 1-2° with large residual PM. The bar region extending from North-West to South-East of the LMC shows relatively large residuals in PM.

We note several outlier clusters in the observed v_{rot} profile (Figure 4.9) of the LMC. The clusters falling outside the 3σ margin from the running average of the v_{rot} profile are treated as outliers. Their locations are traced, and their internal PM is plotted in Figure 4.12b.

The residual PM vectors are plotted in Figure 4.12c for clusters with the relative angular difference (θ_r) between the observed and modeled internal motion greater than 45° and 90°. The red vectors indicate clusters with $\theta_r > 90°$, suggestive of counter-rotation. These are dominantly seen in the North-West of the galaxy. The deviant clusters also trace the non-circular motion of the bar.

The North-West region with the largest residual PM is located between a radial distance of 1-2°. The same location also shows the presence of counter-rotating clusters. This region has PM deviation both in angle (panel c) and in value (panel

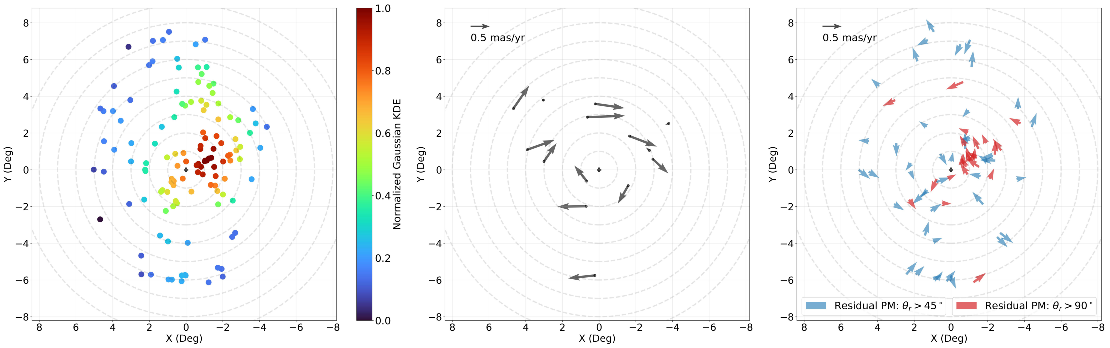

(a) Spatial KDE: clusters >3σ of Residual PM distribution (b) Internal PM vectors: clusters >3σ and <3σ in V_{rot} profile (c) Residual PM vectors: Clusters with deviant internal PM

FIGURE 4.12: The clusters of larger residual PM are plotted here. (a) Spatial 2D Gaussian KDE of cluster locations with $> 3\sigma$ of |Residual PM|; (b) Internal PM vectors of clusters $> 3\sigma$ and $< 3\sigma$ in V_{rot} profile of Figure 4.9(a); (c) Residual PM vectors of clusters with model and observed internal PM vectors differing by $\theta_r > 45^\circ$ and $\theta_r > 90^\circ$

.

a), pointing to the region experiencing an event of perturbation. As this region is located at an impact distance similar to that estimated by C22 and in this study, we speculate that this may be the area that experienced the largest impact due to the recent LMC-SMC collision. We also note that there could also be other reasons, such as perturbations that could occur at the ends of the bar, but a similar disturbance is not seen at the eastern end of the bar. Hence bar perturbation may not be the reason for this disturbance.

4.5.5 Kinematic variation of parameters in the younger clusters

The kinematic model of the LMC for different age groups is studied as in subsection 4.4.3. We note the kinematic parameters of the LMC, mainly the i, Θ, and R_0, show variation in the younger age group C_{AG-3} (100-440 Myr). To further investigate the change in kinematic parameters, we split the C_{AG-3} into two groups (one from 100 to 200 Myr and the other from 200 to 440 Myr) and performed the kinematic modeling. The variation of i, Θ, and R_0 are shown in Figure 4.13.

The age group from 100 to 200 Myr shows the largest inclination ($\sim 39^{\circ}$) compared to other age groups. Meanwhile, we note the smallest Θ value ($\sim 105^{\circ}$) in this age range when compared to other age ranges. The cluster density shifted towards central regions of the LMC in the age group C_{AG-3} and towards North-East in C_{AG-4} (D24). We note this effect in the variation of R_0 to the inner radii of the galaxy, as shown in Figure 4.13c. The value of R_0 reaches 1.1 kpc for clusters of age between 100 to 200 Myr. A similar effect is seen in the nearby young population, where the value reaches 0.5 kpc. Meanwhile, the field population shows smaller i and lesser variation in R_0 compared to other age groups. The kinematic model of cluster groups based on richness also shows this trend of variation in R_0. The younger and richer clusters with more than 60 members are located more toward the central regions of the galaxy as well. We note R_0 smaller than 1 kpc at this cluster group. In summary, we note that the i, Θ, and R_0 values for clusters and young MS stars in the age range 100-200 Myr are distinct from the other groups. A possible reason for this deviation is discussed in subsection 4.5.7.

4.5.6 Kinematic signatures of the LMC bar

The spatial PM plots of clusters and field population, as shown in Figure 4.3, do not bring out the bar feature explicitly. The residual PM plots, as shown in Figure 4.7, on the other hand, show the bar feature, though more prominent in the case of clusters. The radial gradient of the residual PM (Figure 4.11, panel a) shows a large gradient in the bar region, pointing to residuals resulting from kinematics related to the bar. The residual PM plots shown in Figure 4.12 (panels a and c) show the possible presence of non-circular motions in the bar region. A significant reduction in the value of R_0 for clusters and young MS stars with respect to RC stars (see Figure 4.10a) is probably related to the mass distribution within the inner 2 kpc, where the bar is present. The fact that the younger population reaches the maximum value of V_{rot} in a shorter radius when compared to the older population points to a redistribution of mass, most likely due to the evolution of the bar.

In summary, this study has traced three kinematic signatures of the LMC bar, relatively large residual PM in the inner 2° radius for both clusters and field population, the presence of non-circular motion among star clusters, and a decrease of R_0 as a result of the possible evolution of the bar. Recently, J23b also found that the dynamics of the inner disk are dominated by the bar.

4.5.7 Effect of the recent LMC-SMC interaction on the LMC disk

The panels (a) and (c) of Figure 4.12, show that though there are kinematically deviant clusters spread through the LMC disk, there is a specific location where the deviation is maximum. Panel (c) indicates that the same location also shows the presence of cluster motion in all directions, suggesting a possible specific external disturbance. It is therefore important to identify the source of the disturbance identified in this study.

It is possible that this disturbance is caused by the LMC-SMC collision at ~ 150 Myr ago as the radial distance of this region from the center also matches the value of the impact factor of the LMC-SMC collision as derived by C22. The age-dating of the disturbance, as shown in Figure 4.13 suggests a significant shift in inclination i, PA, and R_0 for clusters in the age range 100-200 Myr. The kinematic parameters of clusters younger than this period are more similar to the overall disk properties. This is an indication that the clusters formed during this period have significantly different kinematic parameters. We speculate that this is the first evidence of direct collision in the LMC disk and the spatial and temporal kinematic disturbance, matching with the predicted time and location

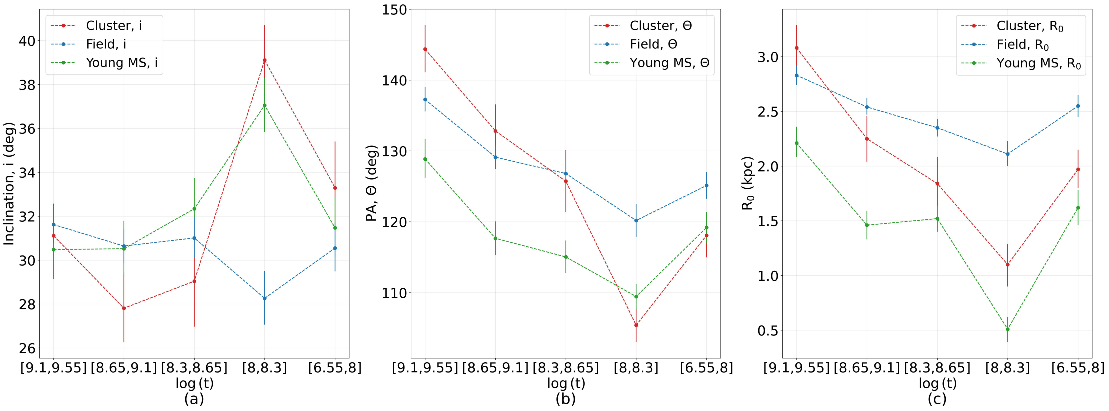

FIGURE 4.13: The variation of i, Θ, and R_0 with respect to the cluster age groups (subsection 4.5.5) are shown here. Red, Blue, and Green markers are used for clusters, fields, and young MS stars, respectively. (a) Variation of i; (b) Variation of Θ and (c) Variation of R_0 are shown for 5 age groups. The age groups are valid only for clusters (Section 4.2). The field and the young MS stars are age-wise heterogeneous but located near the clusters within each age group.

of the LMC-SMC collision. We also speculate that the interaction mainly affected the gas, and the clusters and stars born from the disturbed gas bear the signature of the perturbation.

4.6 Summary

We summarise the results and conclusions from this comprehensive study of the LMC disk kinematics using *Gaia* DR3 data.

1. We performed the kinematic model of the LMC that corresponds to the observed median PM using 1705 star clusters and field regions. This is a comprehensive study with a total of 48 data sets analyzed to create 48 models to study the dependence of the kinematic model on various parameters.

2. The model PM for the tracers in the data sets is formulated based on the equations outlined by V02. The model parameters estimated include inclination of the LMC disk (i), the position angle of the line of nodes (Θ), dynamic centers (α_0, δ_0), the amplitude of the tangential velocity of the LMC's center of mass (v_t), the tangential angle made by v_t (θ_t), scale radius (R_0), optimization factor (η), and the amplitude of the rotational velocity (v_0). We assumed a fixed distance to the LMC center and a line-of-sight velocity of the COM, v_{sys}. The fitting of the parameters was performed by an MCMC technique, and model parameters were estimated for all datasets listed in Table 4.1.

3. This is the first 2D kinematic model of the LMC employing clusters and neighboring field regions with *Gaia* DR3 data. The data coverage of the LMC considered in this study is within $\sim 7^\circ$ from the LMC center. The parameters estimated in this study show good agreement with estimations in the literature when the comparison is made between similar populations.

4. There is no significant difference between the observed COM PM between cluster and field. We note an offset of 28±8 arcmin between the dynamic centers (α_0, δ_0) of the cluster and field. Estimated Θ values of $122^\circ.22^{+1.48}_{-1.51}$ for clusters and $128^\circ.02^{+0.79}_{-0.81}$ for field regions point to an offset of $5^\circ.8\pm1.7$ between them, while the inclination, i, remains almost similar. The modeled rotational parameters, R_0 and η_0 appear to be larger for field regions compared to clusters, while the v_0 remains almost similar.

5. We also estimated the kinematic model parameters for two control populations, RC stars and young MS stars. We find that the younger population tends to show a southern and eastward dynamic center and a relatively smaller value of R_0. We also note a varying value of Θ across the control population.

6. This study establishes that the kinematic model of the LMC disk varies with the age of the cluster population used for the estimation, in contrast to the surrounding field population.

7. The estimated parameters show a significant radial dependence for both cluster and field population. The value of i steeply decreases from the inner to outer radii, from $\sim 50°$ to $\sim 32°$ for clusters, and $\sim 43°$ to $\sim 31°$ for field population. The value of Θ increases from inner to outer radii, from $\sim 108°$ to $\sim 122°$ for clusters, and $\sim 110°$ to $\sim 128°$ for field population. The rotational parameters, R_0 and v_0 after $5°$ show convergence to the values estimated from the full sample.

8. Clusters show larger PM residuals when compared with the field population. The RMS distribution of the residual PM for clusters shows a broader profile, while the corresponding distribution for the field shows a narrower one.

9. The rotational velocity amplitude (v_0) for clusters, fields, and RC stars ($\sim$ 81 to 84 km s^{-1}) are consistent with the estimates by W20. The young MS stars in our study show a slightly larger v_0 ($\sim$ 91 km s^{-1}) when compared to the RC stars, as also noted by N22.

10. The modeled rotational parameters, R_0 and η_0 appear to be larger for field population when compared to clusters, while the v_0 remains almost similar. We note a significant shift in R_0 of ≈ 1.7 kpc between young MS and RC population. The variation in the value of R_0 with respect to population may be due to the redistribution of mass in the inner regions, and it may be due to the evolution of the bar and its activity over time.

11. The dispersion of the rotation velocity is found to be ~ 23 km s^{-1} for clusters, and is likely to have contributions from the bar and spiral arms. The value of $\sim$ 11 km s^{-1} for field population is relatively low and suggests insignificant stellar disk heating. Young MS stars show a relatively large velocity dispersion, similar to clusters.

12. The residual PM for the cluster and the field decreases from the center up to 3°, then increases beyond 4°. The increased value in the inner 2° region is likely to be the effect of the bar. We also detect evidence for non-circular motion in the bar region among the clusters.

13. Location of kinematically deviant clusters show an increased density in the North-West side. We also trace the presence of a number of counter-rotating clusters, mainly in the same region.

14. We detect a specific kinematic perturbation between 2-3° from the center in the North-West direction. We also note a significant shift in the i, Θ, and R_0 of clusters in the age range of 100-200 Myr. This spatial and temporal disturbance matches with the impact factor and the time of the LMC-SMC collision as estimated by C22 and this study.

Chapter 5

Investigating the morphology and kinematics of the SMC

5.1 Introduction

In this chapter, we inspect the 2D kinematic structure of the SMC using a disk model. Previous studies indicate that the distribution of younger and older populations within the SMC differs significantly (D18; Z21; N21). Thus, the morphology and kinematics of the SMC vary depending on the specific tracer population used in the study. Previous kinematic models did not adequately address the estimated LOS depth of the SMC. To comprehend the substantial LOS depth, morphology, and structure of the SMC, it is essential to model the kinematics of the galaxy as a function of different populations (both young and old). In this study, we address these aspects by presenting a 2D model of the SMC that incorporates various populations, both young and old, utilizing data from *Gaia* DR3. Additionally, we develop a 3D model of the SMC using Red Giants that have LOS velocity (v_{los}) information as well.

In this study, we aim to achieve the following: (1) to develop a base kinematic disk model of the SMC that aligns with the observed kinematics of both young and old stars in the galaxy; (2) to detect the signatures of rotation in the SMC, based on the age of the stellar population; (3) to estimate the kinematic disk parameters, which aid in revealing the orientation, galaxy plane morphology, and LOS features of the SMC; (4) to investigate the tidal interaction/influence on the SMC by the LMC, based on the kinematic response of both young and old population. Addressing these points will offer insights into the structural and kinematic evolution of the SMC within the Magellanic system.

The chapter is arranged as follows. In Section 5.2, we describe the datasets used for our modeling. In Section 5.3, we describe the procedures of our kinematic model. In Section 5.4, we present the estimated kinematic parameters of our datasets, followed by the estimation of the residual PM. The discussions based on our results are presented in Section 5.5, followed by Section 5.6, which summarizes our work. The results presented in this chapter are available in Dhanush et al. (2025).

5.2 Data

To model the young and old population of the SMC, we used the cleaned SMC *Gaia* DR3 catalog provided in the study by J23a, which is produced based on a robust neural network classifier. We retained the sources with Probability, P $\geq$ 0.31 for optimal selection of the SMC sources, as recommended by the authors. We selected the SMC sources within a box of $7^\circ.5$ centered on the SMC. We adopted the optical center of the SMC (α_0 = $13^\circ.05$ and δ_0 = $-72^\circ.83$, de Vaucouleurs & Freeman 1972a) in our modeling. We then classified the SMC sources into sub-samples as Young MS 1 (YMS1, ages < 50 Myr), Young MS 2 (YMS2, 50 < age <

400), Young MS 3 (YMS3, mixed ages reaching up 1-2 Gyr), and RGB, based on the polygon selections in the CMD of the SMC as provided in Section 2.3.2 of G21. We also selected the RC population from the CMD based on the selection criterion mentioned in S22. The selected sub-samples are highlighted and displayed on the CMD, as shown in Figure 5.1. Since these datasets lack LOS velocity information, we cross-matched the J23a catalog with the Red Giants catalog by Dobbie et al. (2014, hereafter D14) and found 3545 stars, which have LOS velocity information as well.

Additionally, we incorporated the dataset of 280 parameterized star clusters in the SMC from our previous study, as described in Chapter 3. The SMC cluster sample used in this work spans ages from $\sim$ 12 Myr to 3.4 Gyr. These clusters were divided into three age groups: (1) Young clusters (CLSY - ages $<$ 400 Myr, 143 clusters), (2) Intermediate age clusters (CLSI - 400 Myr $<$ ages $<$ 1 Gyr, 65 clusters), and (3) Old clusters (CLSO - ages $>$ 1 Gyr, 72 clusters).

The sources shown in Figure 5.1 are orthographically projected with the SMC center, using the equations outlined in G21. We used a bin size of $0^\circ.25$ to bin the sources and calculated the median PM and their corresponding standard errors for each bin. We retained bins with more than 5 stars, which resulted in 140 YMS1, 372 YMS2, 1093 YMS3, 1288 RGB, and 1731 RC bins as the final datasets for the modeling. The bin size and minimum number of stars per bin are determined through multiple trials with different bin sizes and star counts. The optimal combination is selected based on the visual clarity of features observed in the vector point diagram of bulk PM and residual PM (see Section 5.4). The radial coverage of Red Giants from D14 is mostly within $\sim 3^\circ$ of the SMC, so we model them as individual sources rather than binning the data. For clusters, we calculated the median PM and the associated standard error of stars within each cluster.

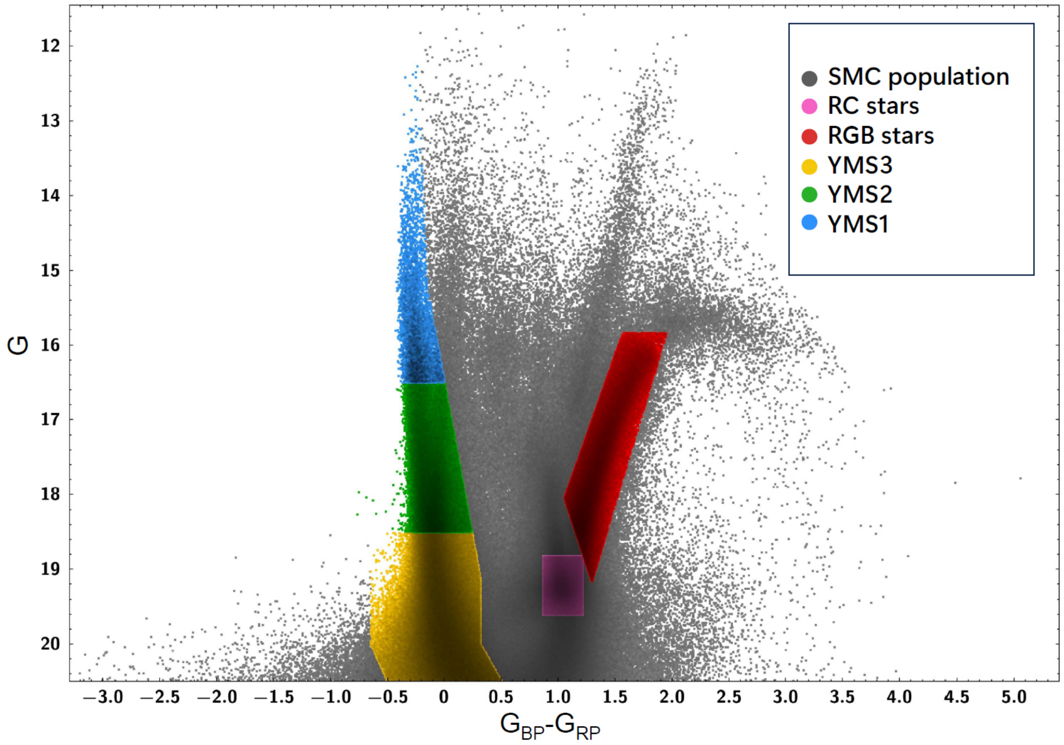

FIGURE 5.1: The CMD illustrating the selection of various stellar populations in the SMC as defined in section 2 is presented here. The populations are highlighted in corresponding colors: RC stars (pink), RGB stars (red), YMS3 (yellow), YMS2 (green), and YMS1 (light blue).

The datasets mentioned above are used for modeling the SMC. The modeling procedures are described in the following section.

5.3 Kinematic model of the SMC

The analytical approach of the modeling is similar to that of the LMC (as in Chapter 4). The parameters selected for our model encompass the inclination of the SMC disk (i), the position angle of the line of nodes measured from West (θ), the amplitude of the tangential velocity of the SMC's center of mass (v_t), the tangential angle made by v_t (θ_t), scale radius (R_f), the asymptotic velocity (v_f), and the systemic velocity (v_{sys}). Our modeling process is aimed at determining the best-fitting values for these kinematic parameters. It should be noted that the disk we expect to trace is the projected distribution of the ellipsoidal SMC along its semi-major and semi-minor axes.

The following subsection describes the modeling procedure employed to estimate the best-fitting kinematic parameters for the datasets discussed in Section 5.2.

5.3.1 Modeling procedure

The best-fitting kinematic parameters of the SMC were estimated using the MCMC serial stretch move sampling algorithm as detailed in section 2.2.3. The implementation of MCMC is similar to the approach used for the kinematic model of the LMC (Chapter 4, section 4.3.1). The model PM ($\mu_{W,m}$, $\mu_{N,m}$) and the observed PM ($\mu_{W,o}$, $\mu_{N,o}$) are used to construct the log-likelihood function ($\ln \mathcal{L}$), which can be used with the associated West and North direction standard errors of observed datasets ($\sigma_{W,o}$,$\sigma_{N,o}$) to sample the best fitting parameter with MCMC. For Red Giants with observed LOS velocities ($\mathrm{v}_{los,o}$) and associated errors ($\sigma_{los,o}$), we include the model LOS velocity ($\mathrm{v}_{los,m}$) in the $\ln \mathcal{L}$ as well. The equation for $\ln \mathcal{L}$ is given by,

$$\begin{aligned}\ln \mathcal{L} = -0.5 \sum_{i=1}^{n} \Bigg[& \ln\left(2\pi\sigma^2_{W,o,i}\right) + \frac{\left(\mu_{W,o,i} - \mu_{W,m,i}\right)^2}{\sigma^2_{W,o,i}} \\ & + \ln\left(2\pi\sigma^2_{N,o,i}\right) + \frac{\left(\mu_{N,o,i} - \mu_{N,m,i}\right)^2}{\sigma^2_{N,o,i}} \\ & + \ln\left(2\pi\sigma^2_{los,o,i}\right) + \frac{\left(v_{los,o,i} - v_{los,m,i}\right)^2}{\sigma^2_{los,o,i}} \Bigg] \end{aligned} \tag{5.1}$$

It is to be noted that the last two terms in equation 5.1 are excluded for the eight datasets that lack v_{los} information. Additionally, we consider two primary variants of the model: one that includes the rotation component of the observed PMs and one that does not. Both variants are tested across each dataset to determine which best represents the different stellar populations of the SMC. The final model for each population is chosen based on the variant (with or without rotation) that shows convergence in the posterior distribution of the sampled parameters. For datasets lacking $\mathrm{v}_{los,o}$, the v_{sys} is fixed at 145.6 km s^{-1} (V02), but it is treated as a free parameter otherwise. The kinematic center is fixed at α_0 = 13°.05 and δ_0 = -72°.83, which is the optical center adopted to select the coverage of the SMC in this study (Section 5.2). The priors for the i, θ, v_t, and v_f were uniformly chosen, while R_f was assigned a Gaussian prior centered at 1.1 kpc (D18), with an extended 3σ range to effectively explore the parameter space.

We executed 2000 steps of MCMC iteration involving 200 walkers evolving sequentially at each step. From the sampled posterior values for the parameters, we focused on the final 50%, calculating their median alongside the 16^{th} and 84^{th} percentile errors for parameter estimation. In the following section, we present the results obtained from the above modeling procedures.

5.4 Results

In this study, we present a 2D kinematic model of the SMC by analyzing various SMC populations using *Gaia* DR3 data. These populations include YMS1, YMS2, YMS3, RC, RGB, CLSY, CLSI, and CLSO. The study covers a radius within ∼ 7°.5 from the SMC center. Additionally, we develop a 3D disk model of the SMC using Red Giants and their LOS velocities estimated by D14. The modeling indicates that rotation in the SMC is present in the YMS1, YMS2, CLSY, and CLSI. In contrast, CLSO, YMS3, RGB, RC, and Red Giants with v_{los} in the SMC, show no evidence of significant rotation. Figure 5.2 shows the sampled posterior distribution of the kinematic parameters for the YMS1. Figure 5.3 presents a

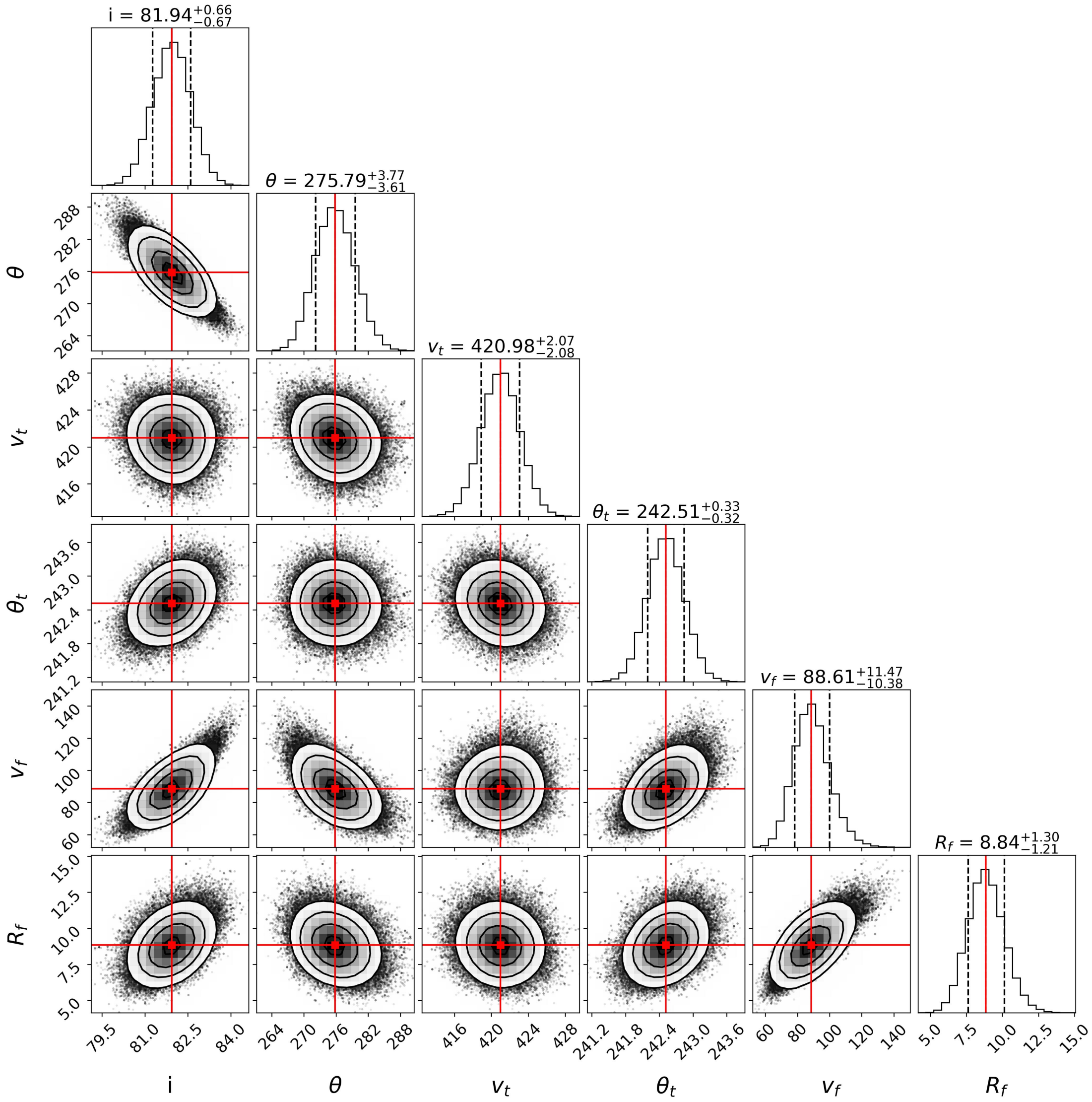

FIGURE 5.2: The corner plot representing the sampled posterior distribution of kinematic parameters for the YMS1 is shown here. The vertical red lines represent the median values, and the black dashed lines represent the 16th and 84th percentiles.

comparison of the sampled posterior distributions of the kinematic parameters for the RGB population without v_{los} and the Red Giants with v_{los}. The best-fitting kinematic parameters for all the datasets considered in this study are tabulated in Table 5.1.

In the following subsections, we detail the results from our models, corresponding to different SMC populations. We highlight some notable features in each

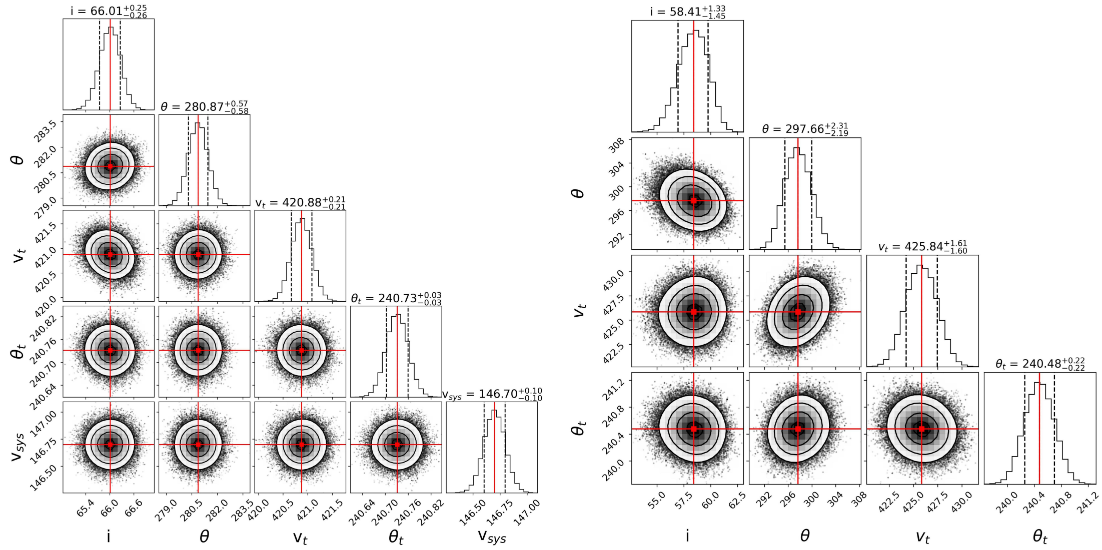

(a)

(b)

FIGURE 5.3: The corner plot representing the sampled posterior distribution of kinematic parameters for the Red Giants with v$_{los}$ (panel a) and RGB without v$_{los}$ (panel b) are shown here. The vertical red lines represent the median values, and the black dashed lines represent the 16th and 84th percentiles.

TABLE 5.1: The estimated kinematic parameters for nine populations in our study are provided here. The position angle of the line of nodes is measured from the north ($\Theta = \theta - 90°$).

Data	i	Θ	v_t	θ_t	v_f	R_f	v_{sys}
	(deg)	(deg)	(km s^{-1})	(deg)	(km s^{-1})	(kpc)	(km s^{-1})
YMS1	$81.94^{+0.66}_{-0.67}$	$185.79^{+3.77}_{-3.61}$	$420.98^{+2.07}_{-2.08}$	$242.51^{+0.33}_{-0.32}$	$88.61^{+11.47}_{-10.38}$	$8.84^{+1.30}_{-1.21}$	fixed
YMS2	$77.68^{+0.90}_{-0.91}$	$188.92^{+4.19}_{-4.17}$	$434.21^{+3.04}_{-2.92}$	$240.97^{+0.40}_{-0.39}$	$49.32^{+10.91}_{-9.44}$	$5.85^{+1.65}_{-1.52}$	fixed
YMS3	$71.34^{+1.38}_{-1.64}$	$200.29^{+4.55}_{-4.45}$	$447.52^{+5.37}_{-5.53}$	$241.20^{+0.59}_{-0.59}$	-	-	fixed
CLSY	$79.93^{+0.78}_{-0.80}$	$180.46^{+3.44}_{-3.32}$	$422.80^{+1.39}_{-1.40}$	$241.26^{+0.20}_{-0.19}$	$66.59^{+11.28}_{-10.23}$	$7.12^{+1.40}_{-1.31}$	fixed
CLSI	$74.80^{+1.46}_{-1.73}$	$182.14^{+5.44}_{-5.33}$	$420.80^{+2.32}_{-2.30}$	$241.28^{+0.31}_{-0.30}$	$49.73^{+13.69}_{-12.18}$	$6.33^{+1.86}_{-1.72}$	fixed
CLSO	$63.30^{+2.35}_{-2.78}$	$240.44^{+4.65}_{-5.16}$	$419.58^{+1.88}_{-1.94}$	$240.65^{+0.24}_{-0.23}$	-	-	fixed
RGB	$58.41^{+1.33}_{-1.45}$	$207.66^{+2.31}_{-2.19}$	$425.84^{+1.61}_{-1.60}$	$240.48^{+0.22}_{-0.22}$	-	-	fixed
RC	$58.20^{+1.51}_{-1.68}$	$202.00^{+3.22}_{-3.07}$	$421.91^{+2.31}_{-2.28}$	$241.18^{+0.32}_{-0.32}$	-	-	fixed
Red Giants (D14)	$66.01^{+0.25}_{-0.26}$	$190.87^{+0.57}_{-0.58}$	$420.88^{+0.21}_{-0.21}$	$240.73^{+0.03}_{-0.03}$	-	-	$146.70^{+0.10}_{-0.10}$

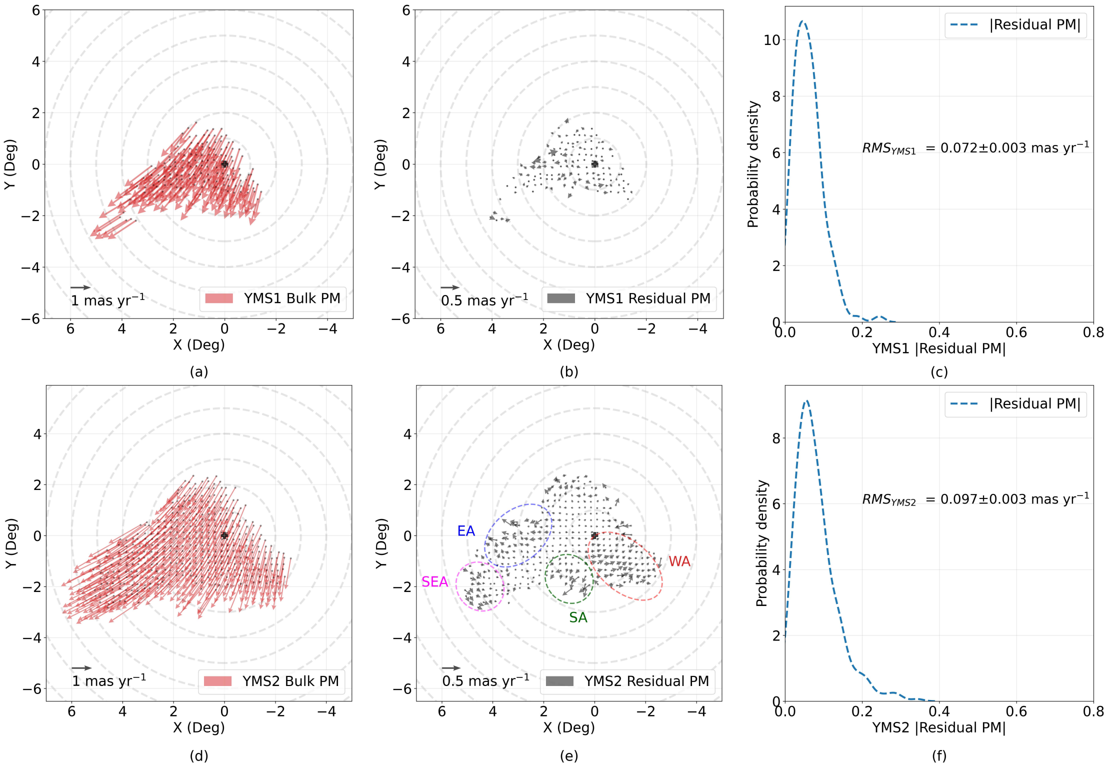

(a) (b) (c)

(d) (e) (f)

FIGURE 5.4: The observed PM (panels a and d), residual PM vectors (panels b and e), and distribution of |residual PM| (panels c and f) for the YMS1&2 are shown here. The EA, SEA, SA, and WA regions identified in the residual PM map of YMS2 are highlighted.

population and also present the residual PM map and its distribution.

5.4.1 YMS1 and YMS2

The observed bulk PM of the YMS1 and YMS2 in the skyplane are shown in Figure 5.4, panels (a) and (d), respectively. We found these populations support rotation components in their bulk PM. However, we estimated a larger v_f and R_f for YMS1 (~ 89 km s^{-1} and 9 kpc, respectively) compared to the YMS2 population (~ 49 km s^{-1} and 6 kpc, respectively). Meanwhile, the estimated COM PM values in the west and north directions ($\mu_{W,com}$, $\mu_{N,com}$) for YMS1 (-0.657±0.008, -1.262±0.007) and YMS2 (-0.712±0.010, -1.283±0.010) do not show any significant deviation. The estimated i shows an offset of 4°.26±1°.13, while the position angle of the line of nodes, measured from north Θ ($\theta - 90°$) does not show any significant variation.

Panels (b) and (e) in the Figure 5.4 depict the residual PM (Observed PM - Model PM) for YMS1 and YMS2, respectively. We visually detected four anomalies in the residual PM map of YMS2 by identifying large deviations in the amplitude and direction of the residual vectors. These include the East Anomaly (EA), which is significant beyond $\sim 2°$ with residual PM directed towards east and northeast; the South East Anomaly (SEA), located in the southeast and extending beyond $\sim 4°$, where residual PM is directed towards south with indication for counter rotation; the South Anomaly (SA), found in the southern region beyond $\sim 1°$, where residual PM is directed towards the southeast; and the more prominent West Anomaly (WA), which extends from the central regions of the SMC to the southwest, with residual PM directed westward. YMS1 exhibits significantly less pronounced SEA, WA, and SA, though the EA is still evident.

The magnitude of the residual PM distributions (|residual PM|) for YMS1 and YMS2 are presented in panels (c) and (f), respectively. The RMS values are estimated as 0.072±0.003 mas yr^{-1} for YMS1 and 0.097±0.003 mas yr^{-1} for YMS2, respectively.

5.4.2 YMS3

Figure 5.5, panel (a) shows the observed bulk PM of YMS3. The spatial distribution of stars in YMS3 is more spatially spread than YMS1 and YMS2. This population does not exhibit significant rotation in their bulk PM, as the model variant that includes rotation fails to achieve convergence in the MCMC sampler. We estimated a slightly larger ($\mu_{W,com}$, $\mu_{N,com}$) for YMS3 (-0.728±0.016, -1.325±0.018) when compared to YMS1&2, notably in the south direction. Also,

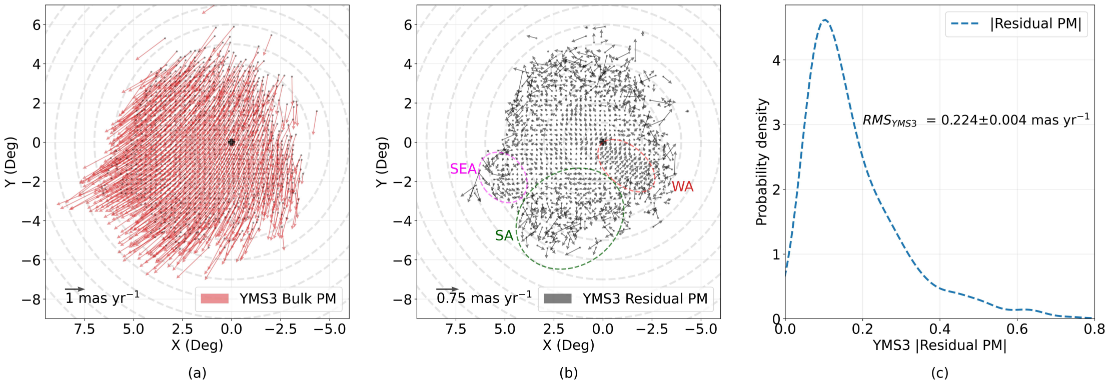

Figure 5.5: The observed PM (panel a), residual PM vectors (panel b), and distribution of |residual PM| (panel c) for the YMS3 are shown here. The SEA, SA, and WA regions identified in the residual PM map of YMS3 are highlighted.

the estimated i ($\sim 71°$) for YMS3 is lower, and Θ ($\sim 200°$) is slightly larger when compared to YMS1&2.

Panel (b) shows the spatial residual PM for YMS3. The SEA, SA, and WA are present in YMS3. However, the WA in YMS3 shows the northwest-directed motion of residuals, unlike the west-directed motion observed in YMS2. Additionally, the SA in YMS3 extends $\sim 6°$ further south than in YMS2. Also, the northern and southern outskirts of YMS3 exhibit higher residual PM magnitudes compared to YMS2. As a result, YMS3 shows a broader |residual PM| distribution in panel (c), with an RMS value of 0.224±0.004 mas yr^{-1}.

5.4.3 Clusters

The clusters belonging to CLSY and CLSI show rotation signatures. We estimated v_f and R$_f$ to be ~ 67 km s^{-1} and ~ 7 kpc, respectively, for CLSY, and ~ 50 km s^{-1} and ~ 6 kpc, respectively, for CLSI. This is consistent with the estimated kinematics of the YMS1 and YMS2. We also note the absence of significant rotation in the case of older clusters (CLSO with ages > 1 Gyr), similar to the kinematics of YMS3. The COM PM does not show any significant deviation among the cluster

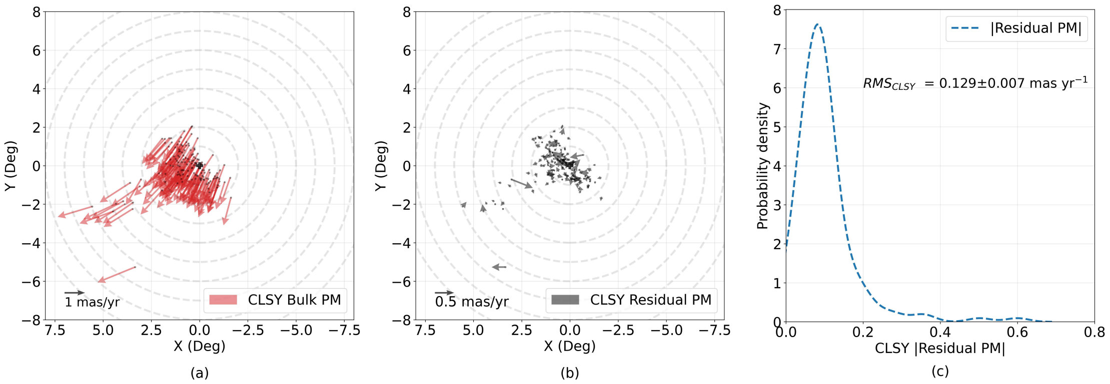

FIGURE 5.6: The observed PM (panel a), residual PM vectors (panel b), and distribution of |residual PM| (panel c) for the CLSY are shown here.

groups as well as with respect to YMS1 and YMS2 populations. However, the estimated i decreases from ∼ 80° for CLSY (young) to ∼ 63° for CLSO (old), meanwhile Θ increases from ∼ 180° to ∼ 240°, similar to the trend seen in the young MS population.

Figure 5.6, panel (a) shows the observed bulk PM for the clusters belonging to the CLSY group. The clusters in our study are predominantly located in the eastern region of the SMC. Panels (b) and (c) show the spatial map and distribution of the magnitude of residual PM for CLSY. We note the residual PM vectors overall display a relatively more random orientation, along with several clusters showing a larger magnitude of residuals. The distribution of |residual PM| for CLSY gives an RMS value of 0.129±0.007 mas yr^{-1}, which is less compared to YMS3, but more than that was found for YMS1&2. Due to the sparseness, we do not detect the EA, SEA, SA, and WA in the cluster distribution. Also, we do not show the residual PM maps for CLSI and CLSO due to their sparse distribution in our sample.

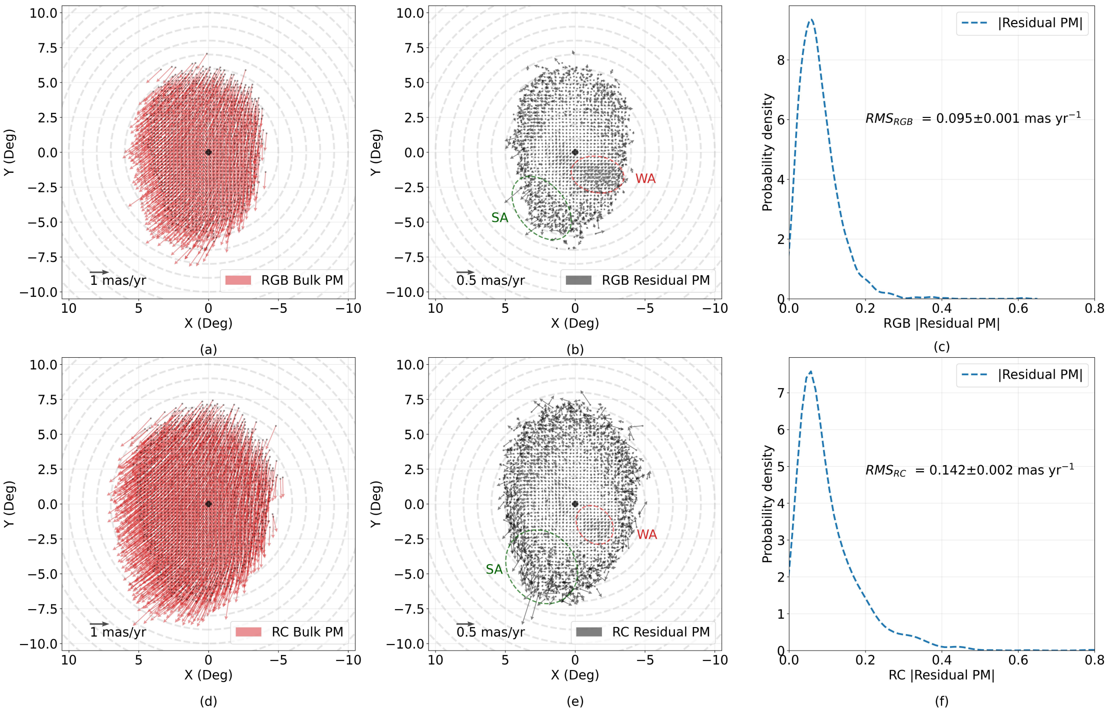

FIGURE 5.7: The observed PM (panels a and d), residual PM vectors (panels b and e), and distribution of |residual PM| (panels c and f) for the RGB and RC are shown here. The SA and WA regions identified in the RGB and RC residual PM maps are highlighted.

5.4.4 RGB and RC

Figure 5.7 presents the spatial map of the observed bulk PM for RGB and RC populations in panels (a) and (d), respectively. The spatial coverage of RGB and RC are similar, although RC extends slightly more towards the outskirts of the SMC. They do not support rotational components in their bulk PM. The estimated COM PM values for RGB and RC are comparable and do not exhibit significant deviations when compared to other populations, except for YMS3. However, the estimated i is smaller, $\sim 58^\circ$, while the Θ is estimated to be larger than 200°.

Panels (b) and (e) in Figure 5.7 depict the spatial maps of residual PM vectors for the RGB and RC, respectively. The EA identified in YMS2 is observed beyond $\sim 3^\circ$ and is slightly shifted northeast for both RGB and RC. Additionally, the SA anomaly extends beyond $\sim 4^\circ$ to the south. However, the WA is more prominently evident for RGB than for RC. In the outskirts of the SMC, residual PMs are notably pronounced in the RC, especially in the northern and southern regions.

The distributions of |residual PM| for RGB and RC are shown in panels (c) and (f), respectively. The RC displays a higher RMS value of 0.142±0.002 mas yr^{-1}, compared to 0.095±0.001 mas yr^{-1} for RGB.

5.4.5 Red Giants with LOS velocities

The estimated parameters for Red Giants with radial velocities (v_{los}) do not significantly deviate from the model parameters estimated for the RGB and RC populations without v_{los}. The i ($\sim 66^\circ$) and Θ($\sim 191^\circ$) of the Red Giants are slightly deviant from the 2D model values for the RGB and RC, though these are still notably different from those of the younger MS population. Despite these differences, we do not observe any significant offset in the COM PM for Red Giants relative to the other populations. We estimated a systemic velocity (v_{sys}) of $146.70^{+0.10}_{-0.10}$ for the Red Giants, which is closer to the assumed value of 145.6 km s^{-1} used in the 2D modeling of other datasets. Since the radial coverage of Red Giants with v_{los} is smaller ($\sim 3^\circ$) and we modeled individual stars rather than binning them, we do not discuss the residual PM maps.

The various populations in the SMC exhibit distinct kinematic properties, which aid in understanding the kinematic structure of the SMC based on age. In the following section, we discuss the intriguing details that emerge from our modeling.

5.5 Discussion

In this study, we have carried out kinematic modeling of the SMC by analyzing nine different stellar populations, including YMS1, YMS2, YMS3, CLSY, CLSI, CLSO, RGB, RC, and Red Giants.

In the following subsections, we discuss the key results from our modeling. We compare the estimated kinematic parameters with those from previous studies, analyze the morphology of the galaxy, examine anomalies in the galaxy's internal motion, and explore the tidal evolution of the SMC.

5.5.1 kinematic parameters

The estimated values of ($\mu_{W,com}$, $\mu_{N,com}$) of the SMC from our study are compared with those from previous studies by Costa et al. (2011, hereafter C11), K13, van der Marel & Sahlmann (2016, hereafter V16), Z18, G18, D20, and N21 in Table 5.2 and illustrated in Figure 5.8. The COM PM values for clusters (CLSY, CLSI, CLSO), RGB, RC, and Red Giants (with v_{los}) do not show significant offsets with respect to the recent estimates (D20 and N21). However, YMS1, YMS2, and YMS3 progressively exhibit offsets in the parameter space, with YMS3 displaying the largest offset.

We note that the YMS3 population has ages between 1-2 Gyr, whereas YMS1&2 are younger than 400 Myr. Also, the YMS3 shows a significantly high COM PM directed southward (see Table 5.2 and Figure 5.8). The largest southward shift seen in the YMS3 could be linked to the encounter between the LMC and the SMC about 1.5 Gyr ago, an interaction peak identified in our previous study (Chapter 2, section 3.4.2). This may be a sign that these stars probably retain the kinematic

Table 5.2: Comparison of the estimated COM PM with previous studies. The first nine rows list the estimations from this study.

$\mu_{W,com}$ (mas yr^{-1})	$\mu_{N,com}$ (mas yr^{-1})	Reference
-0.657±0.008	-1.262±0.007	YMS1
-0.712±0.010	-1.283±0.010	YMS2
-0.728±0.017	-1.325±0.018	YMS3
-0.704±0.004	-1.252±0.005	CLSY
-0.687±0.005	-1.247±0.008	CLSI
-0.683±0.008	-1.236±0.006	CLSO
-0.695±0.006	-1.252±0.005	RGB
-0.687±0.008	-1.249±0.008	RC
-0.687±0.008	-1.249±0.008	Red Giants
-0.743±0.027	-1.233±0.012	N21
-0.721±0.024	-1.222±0.018	D20
-0.82±0.10	-1.21±0.03	Z18
-0.797±0.030	-1.220±0.030	G18
-0.874±0.066	-1.229±0.047	V16
-0.772±0.063	-1.117±0.061	K13
-0.93±0.14	-1.25±0.11	C11

disturbance to the gas from which they are born, as a result of the interaction. The CLSO (ages > 1 Gyr) does not show this trend since the clusters are smaller in number in this group.

The estimated value of i for most of the old to young population in our study ranges from $\sim 58^\circ$ to 82°, meanwhile Θ ranges from $\sim 185^\circ$ to 202°. This range aligns with the findings of Z21 using *Gaia* DR2 data, which reported a value of i between 50° and 80° and a Θ of $\sim 180^\circ$. S15 estimated (i, Θ) of $\sim (64^\circ, 155^\circ)$ using cepheids. Meanwhile, D18 estimated these values to be $\sim (51^\circ, 66^\circ)$, using HI gas. The sparse distribution of CLSO, along with the central concentration of clusters in our sample results in a larger Θ value ($\sim 240^\circ$). However, Our estimations tentatively suggest a decreasing value of i and an increasing value of Θ with the increase in age of the tracer population.

The bin sizes for binning the *Gaia* data were set at $0^\circ.25$ to visually identify the features seen in the PM and residual PM maps (Section 5.2). Modifying the bin sizes, either by increasing or decreasing, as well as altering the minimum requirement of 5 stars per bin for estimating the median PM, does not substantially affect the parameter estimates in this study. We modified the bin sizes and the minimum number of stars per bin but found that the parameter estimates do not change significantly across all the populations. Therefore, the estimated COM PM and viewing angles (i and Θ) for the SMC in our study are reliable and consistent with the findings of previous studies.

5.5.2 Internal rotation of the SMC

The younger populations show evidence of internal rotation in the SMC. The value of v_f we estimated in this study are ~ 89 and 49 km s^{-1} for YMS1 and YMS2, respectively. However, in our study, we estimated a larger R_f of ~ 9 and 6 kpc for

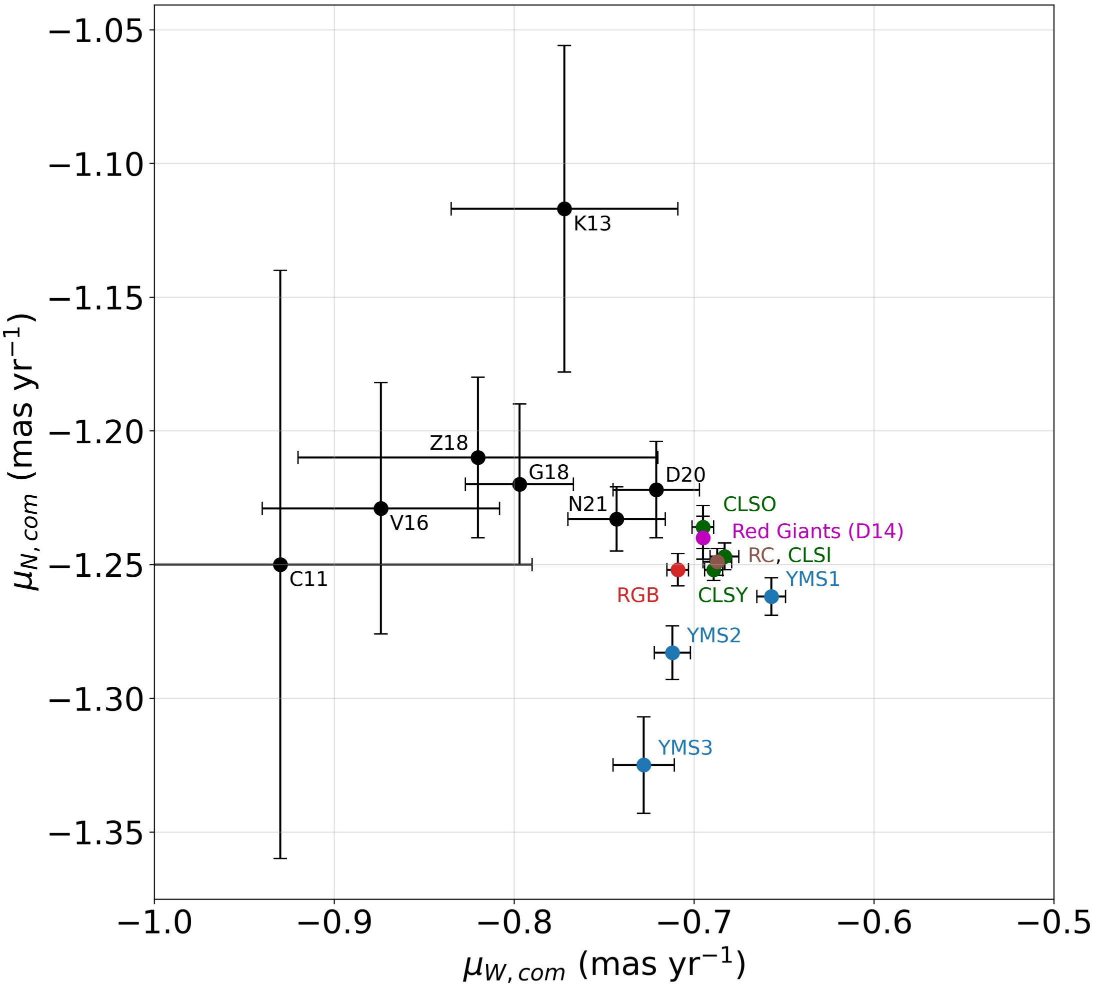

FIGURE 5.8: The parameter space of the estimated ($\mu_{W,com}$, $\mu_{N,com}$) is compared with the reference studies provided in Table 5.2). The corresponding estimated parameters for the YMS1, YMS2, and YMS3 are marked with blue dots. Clusters are marked with green dots. RGB, RC, and Red Giant red, brown, and magenta dots, respectively. The reference studies are marked with black dots. Error bars are provided as well.

YMS1 and YMS2, respectively, compared to the estimates by D18 (R$_f$ $\sim$ 1.1 kpc). A comparable trend is observed in the case of CLSY and CLSI. We were not able to fit the rotation component for the YMS3, CLSO, RGB, and RC, but we noted a partial convergence of v$_f$ below 8 km s^{-1}, which is not reliable as the error in the estimations is of the order of 10 km s^{-1} (noted in YMS1&2). This suggests that the rotation in the old population is significantly less, and can be assumed to have no rotation. This is consistent with the study by Z21, which found a moderate or slow rotation of $\sim$ 10 km s^{-1} in the central regions of the SMC using Red Giant

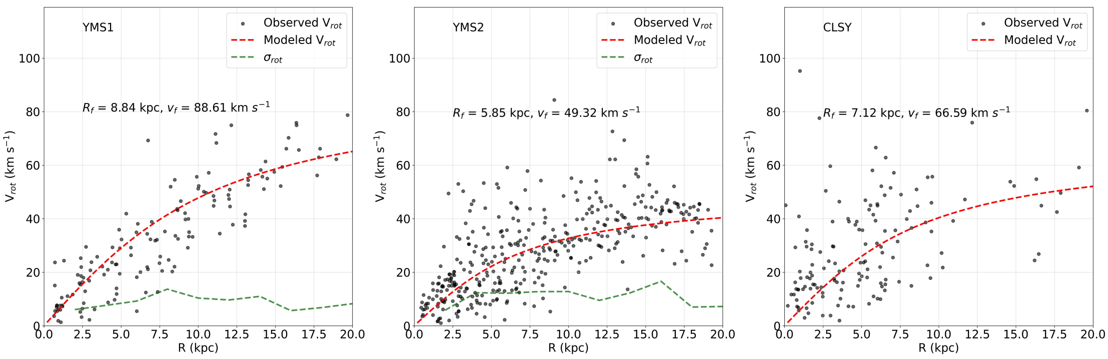

(a) (b) (c)

FIGURE 5.9: The rotation velocity (V_{rot}) profile of the SMC is shown for YMS1 (panel a), YMS2 (panel b), and CLSY (panel c) in the SMC plane. Black dots represent the observed V_{rot}, while the red dashed curve denotes the modeled V_{rot}. The dispersion (σ_{rot}) of the observed V_{rot} for YMS1 and YMS2 populations are shown with the green dashed curve.

stars.

Figure 5.9, panels (a) and (b) show the rotation velocity profile for the YMS1, YMS2, and CLSY respectively. The rotation velocity within the SMC plane (V_{rot}) is presented as a function of the galactocentric distance (R, in kpc). We also estimated an average rotational dispersion (σ_{rot}) of $\sim$ 9 km s^{-1} and 11 km s^{-1} for YMS1 and YMS2, respectively. This was done using a binning interval of 2 kpc along the disk radius. In CLSY, the absence of enough clusters beyond the radius of 11 kpc prevents the estimation of σ_{rot}. The smaller values of σ_{rot} suggest a disk morphology for the younger population (YMS1&2). The extension of R to $\sim$ 20 kpc or more indicates that the disk structure of the SMC is notably more stretched along the galaxy plane for the younger populations compared to its appearance in the sky plane.

For the cluster groups CLSY and CLSI, we found evidence of rotation consistent with the YMS1&2 populations. However, the cluster samples in the wing region of the SMC are sparse in our study, leading to variations in i and Θ between the young clusters (CLSY and CLSI) and the young MS populations (YMS1&2).

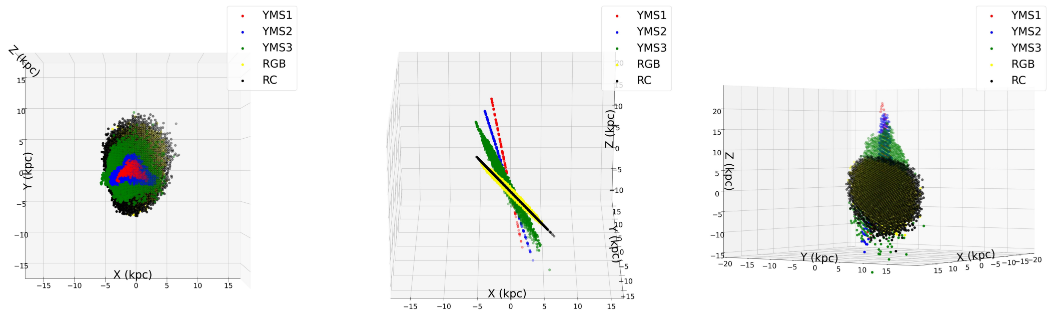

(a) (b) (c)

FIGURE 5.10: The distribution of YMS1, YMS2, YMS3, RGB, and RC populations in our study are color-coded and depicted here. (a) populations in the sky plane perspective (X-Y plane), (b) X-Y-Z perspective 1: (R_1, R_2) = (90°, 20°), (c) (b) X-Y-Z perspective 2: (R_1, R_2) = (90°, 120°). R_1 represents a clockwise rotation about the X-axis of the sky plane perspective, followed by R_2, which is a subsequent clockwise rotation about the new Y-axis.

In the next section, we present the in-plane morphology of the SMC based on our model.

5.5.3 Morphology of the SMC

Figure 5.10 shows the 3D perspective of the SMC for different populations (YMS1, YMS2, YMS3, RGB, and RC) based on the disk models we obtained in our study. The distances in X-Y-Z (in kpc) are estimated based on the fixed center (α_0 = 13°.05; δ_0 = -72°.83) and the mean distance (D_0 = 62.44 kpc) to the galaxy center. Panel (a) shows the density distributions of different populations as observed in the sky plane, where the negative X and Y directions are the East and South directions, respectively. Panel (b) shows the X-Y-Z perspective of the SMC, which is attained by the clockwise rotation of 90° about the X axis (Y=0), R_1 = 90° and followed by another clockwise rotation of 20° about the new Y axis, R_2 = 90°. This keeps much of the population on the edge-on perspective, which also reflects their varying values of i for the disk. The RC and RGB disk has an offset of more than 19° with the YMS1&2. Panel (c) shows an alternative X-Y-Z perspective of the

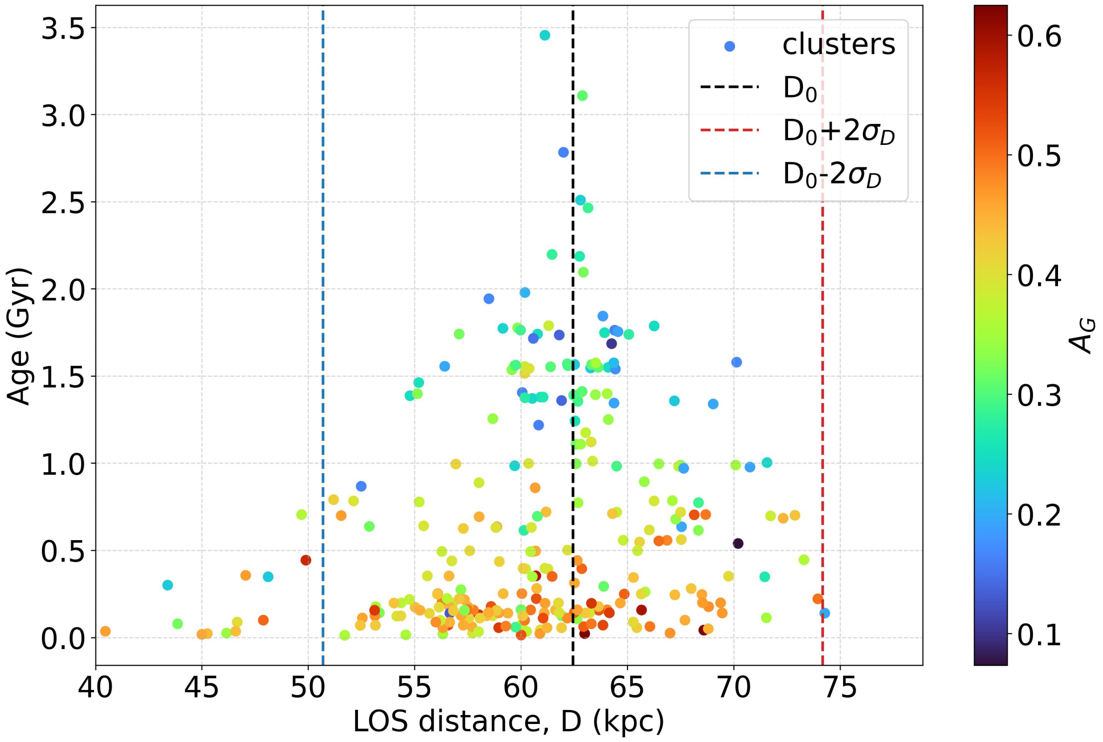

FIGURE 5.11: The age distribution of clusters (CLSY, CLI, and CLSO) is shown here according to their LOS distance (D), with each cluster color-coded based on extinction in the *Gaia* G band (A_G). $D_0 = 62.44$ kpc is the adopted mean distance to the SMC, with σ_D representing the standard deviation in D based on the disk model.

SMC for $R_1 = 90°$ and $R_2 = 120°$, obtained after performing the rotations from the sky plane perspective from panel (a). The selection of R_1 and R_2 is arbitrary and it only serves to visualize the disk's inclination and the spatial distribution of different populations on the galaxy plane.

The triangular density distribution of the young population (YMS1&2) in the sky plane appears similar to that of the observed density distribution of HI in the SMC (Stanimirović et al. 2004). The distribution of the older population (RGB and RC) in our study appears elliptical in the sky plane (Figure 5.10, panel a). Also, the previous studies suggest that the old population of the SMC is distributed in a spheroidal or ellipsoidal shape (Harris & Zaritsky 2004; R18; Y19). Our model indicates a highly inclined morphology for the SMC across all populations. We find that YMS1 and YMS2 are rotation-supported, while for the old population, we likely traced a projected geometry of ellipsoidal distribution along the semi-major and semi-minor axes. Notably, D14 estimated a LOS dispersion of ~ 26 km s^{-1} for the Red Giants we used in our study. This implies that the SMC probably has a flattened ellipsoidal distribution, where the younger populations (YMS1 and YMS2) have rotation-supported disk structures.

Panels (b) and (c) in Figure 5.10 reveal the LOS depth of the SMC based on the disk morphology obtained in this study for both young and old populations. Figure 5.11 shows the estimated LOS distance (D, in kpc) of clusters (CLSY, CLSI, and CLSO) in our study plotted against their age (in Gyr). The data is color-coded according to extinction in the *Gaia* G band (A_G), where the ages and A_G are taken from our first study (Chapter 3). We compare this plot with a similar plot by Piatti (2021, P21) using clusters in the outer northeast of the SMC. We note a trail of young clusters ($<$ 200 Myr) in Figure 5.11 along the decreasing LOS distance (East of the SMC), which was noted in P21 as well. These clusters are also oriented along the wing region of the SMC, suggesting they were formed after the recent SMC-LMC interaction. The estimation of cluster ages in our previous study (Chapter 3) did not take disk morphology into account. Hence, we re-estimated the ages of clusters using the current LOS distances obtained using the disk model of clusters. However, we observed minor differences in the estimates that fall within the margins of error for age estimation. The LOS depth for clusters, determined from the estimated inclination relative to the center, is $\sim$ 20 kpc to the east and $\sim$ 12 kpc to the west.

Our model suggests that the LOS depth for the RC and RGB populations extends $\sim$ 11 kpc to both the east and west of the SMC. In contrast, the LOS extension of the young populations (YMS1, YMS2, YMS3) in the west surpasses 15 kpc, with the eastern side of YMS1 extending to $\sim$ 20 kpc. The studies by J16 and R17 previously reported the younger population of the SMC to have LOS elongation of $\sim$ 20 kpc. In essence, our models trace that both the younger and older populations

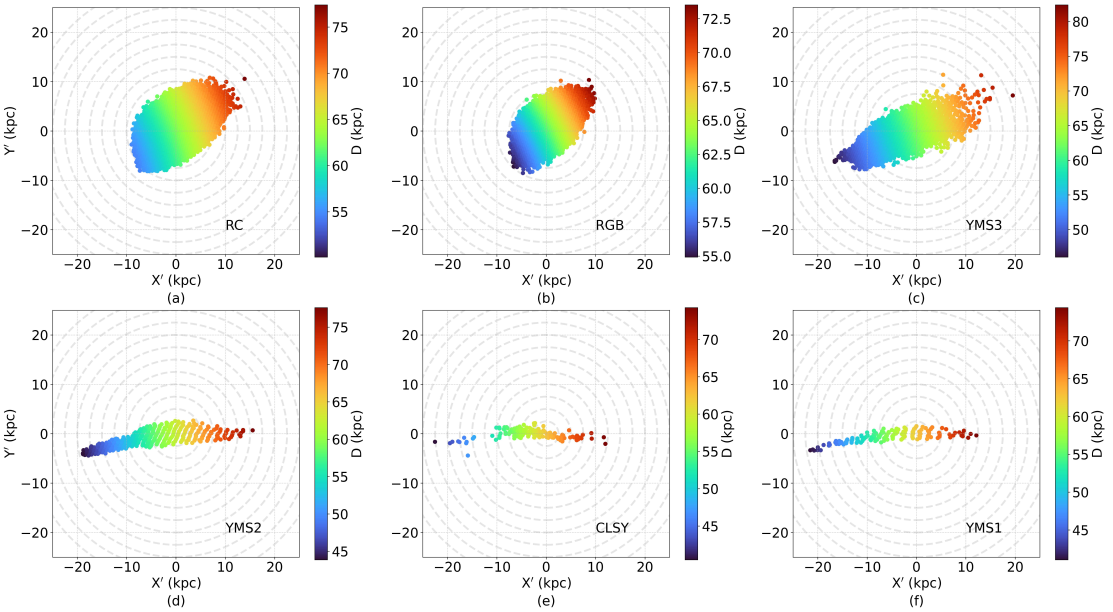

FIGURE 5.12: The morphology of the SMC is shown in the disk plane (primed coordinates) of the galaxy. Panels from (a) to (f) show RC, RGB, YMS3, YMS2, CLSY, and YMS1, respectively. The sources in each population are color-coded with LOS distance (D, in kpc) as well.

have a larger LOS depth, consistent with the previous observations.

To better visualize the disk plane of the SMC, we present the RC, RGB, YMS3, YMS2, CLSY, and YMS1 within their best-fitted disk plane of the galaxy (X′-Y′ axes), as shown in Figure 5.12. Each population's disk plane is rotated counter-clockwise by their corresponding i and about the PA of the line of node axis. Also, each source is color-coded based on the LOS distance (D, in kpc) as well. This perspective aligns the disk plane with the standard East, West, North, and South directions of the sky plane, facilitating a comparison of the disk plane and its appearance in the sky. Starting with the RC and RGB populations, we observe that the SMC extends up to $\sim$ 10 kpc from its center. The YMS3 population, which is 1-2 Gyr old, is more spread out, but elongated compared to the RC and RGB, reaching over $\sim$ 17 kpc from the SMC center. In contrast, the YMS1, YMS2, and CLSY, which are less than 400 Myr old, exhibit an even larger stretch in their disk distribution. These populations are significantly more elongated along the X′ axis compared to the Y′ axis, extending up to $\sim$ 20 kpc from the center, with YMS1 and CLSY spanning more than 22 kpc. However, we estimated a small dispersion of ~ 10 km s^{-1} in the rotation profiles for the YMS1 & 2 (Figure 5.9, panels a and b). This suggests that the young SMC likely has a disk structure that is not very thick. Additionally, the appearance of the RC and RGB indicates a more compact ellipsoidal structure compared to the young populations.

In the following section, we will investigate the anomalies identified in the residual PM maps in conjunction with the SMC's morphology.

5.5.4 Anomalies in the kinematics and tidal evolution of the SMC

The anomalies we identified in the residual PM map of YMS2 (Section 5.4) are evident in both the young and the old populations. The SEA, which represents a stellar population in counter rotation is noticed for the first time in the SMC, and it is prominent across the YMS1, YMS2, and YMS3. The appearance of counter-rotation in the residual could arise due to the slower rotation of the population with respect to the model (This is explored further in detail later). The EA indicates the motion of groups of stars away from the SMC and directed to the LMC along the young bridge of the SMC. We note the clusters in the east wing are mostly of ages less than 200 Myr, they also have residual PM aligned towards the younger bridge. However, the SA shows the residual PM vectors of the stellar population aligning to the south in the SMC outskirts, probably connecting to the old bridge.

The eastward movement of stars in the younger population toward the younger bridge was previously noted in the study by N21 and aligns with our findings. Figure 16 of G21 illustrates comparable movements of both old and young populations toward the older and younger bridges, respectively, which is consistent with our findings. The residual PM features located beyond ~ 5° to ~ 8° for RGB

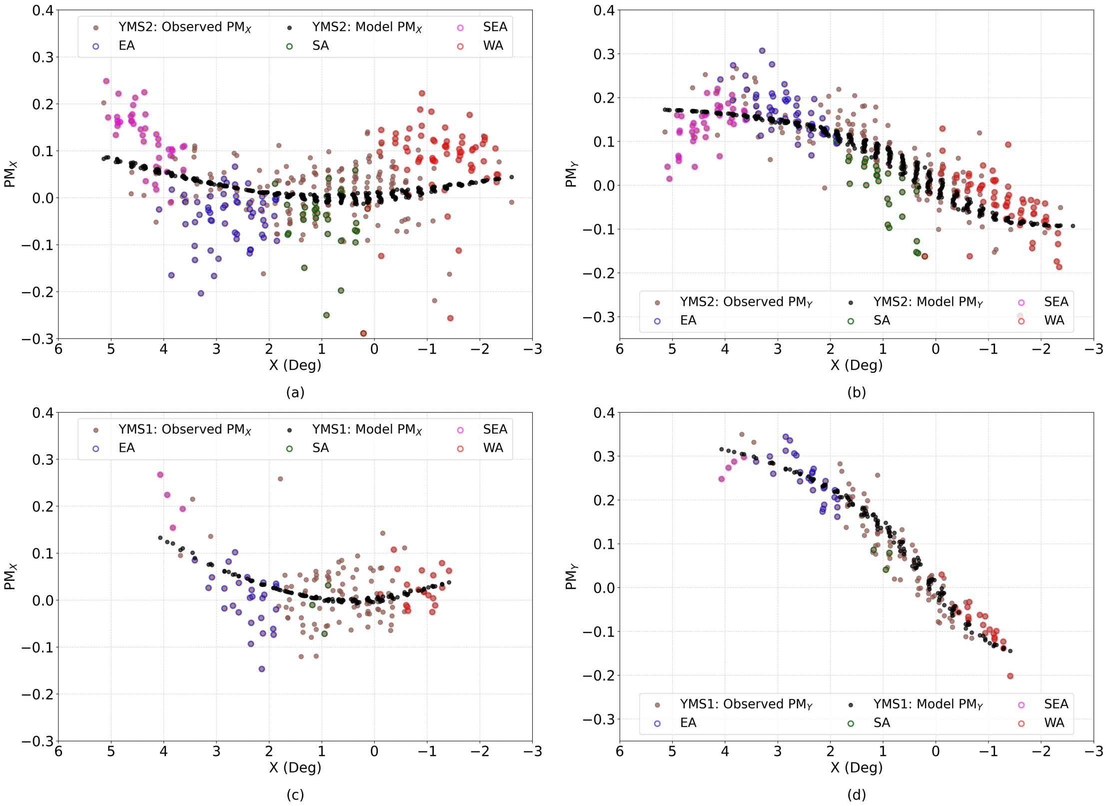

(a) (b) (c) (d)

FIGURE 5.13: Comparison of the internal PM components (PM_X, PM_Y) along the X direction of the sky plane for YMS2&1 are shown here. Observed PM_X and PM_Y are represented by brown dots, while their corresponding model predictions are indicated by black dots. The SEA, EA, SA, and WA binned stars identified for YMS2 (see subsection 5.4.1) are marked with magenta, blue, green, and red circles, respectively.

and RC (as shown in Figure 5.7, panels b and e) show similarities to the trends observed by Cullinane et al. (2023) for the offset population of RGB stars in the SMC outskirts, as depicted in their Figure 4.

The WA is observed in the central regions and extends mostly westward in the SMC, which is evident in both young and old populations (YMS2, YMS3, RGB, and RC). The west-directed motion of these populations is consistent with the studies by Niederhofer et al. (2018) and Dias et al. (2022b). The motion is directed to the west halo of the SMC, a tidal feature suggested by Dias et al. (2016). The west halo is later associated with the counter bridge of the SMC (Tatton et al. 2021), which loops behind the SMC from southwest to northeast of the galaxy.

The anomalies observed point out that the galaxy is showing tangential anisotropy in PM across all the populations. We further analyze the observed internal PM$_X$ and PM$_Y$ along the X direction for YMS2&1, aiming to assess their respective contributions to these four anomalies. In Figure 5.13, panels (a) and (c) illustrate the variation in the X component of the internal PM (PM$_X$) for YMS2 and YMS1 along the X direction in the sky plane. Meanwhile, panels (b) and (d) depict the variation in the Y component of the internal PM (PM$_Y$) for YMS2 and YMS1 along the same X direction in the sky plane. The color-coding for anomalies in both YMS1 and YMS2 across each panel is based on the EA, SEA, SA, and WA regions identified in YMS2. This facilitates a region-to-region comparison between YMS2 and YMS1.

The SEA is found to have larger values of (PM$_X$) indicative of an inward motion, and lower values for (PM$_Y$) indicative of slower rotation, particularly for regions at X $\sim$ 4° and beyond as seen in panels (a) and (b). Furthermore, the SEA region in YMS1, as shown in panels (c) and (d), noticeably has a reduced number of bins compared to YMS2. This suggests that the disk's rotation is attaining stability in the youngest population (YMS1). The SEA prominently emerges from the YMS3 population (ages $\sim$ 1 to 2 Gyr) and is not so evident in RGB and RC. This suggests that the SEA is predominantly detected in the populations with $\sim$ 50 Myr to 2 Gyr age range. Our models indicate that the SMC's rotation starts with the YMS2 population, suggesting that the SEA may be pointing to a gas in-fall from the outskirts into the southeastern region of the SMC, where stars formed from this gas retaining the in-falling gas kinematics. We therefore classify the SEA to be an infalling feature, rather than a counter-rotating feature.

The EA reveals larger negative values in PM$_X$, and it is evident in both YMS2 and YMS1. The inner bins in the east between $\sim$ 2° and 4° of YMS2 show large negative observed PM$_X$ values, suggesting the eastward directed motion. This implies that stars in these bins are being pulled eastward towards the LMC. In the YMS1 population, the bins of stars in the central regions between 1° and 3° exhibit similar eastward motion, along with larger negative values for PM_X. This points to the tidal signature in the RA direction likely resulting from the SMC interacting with the LMC.

The SA reveals the flow of stars towards the south of the SMC, which is prominent in the YMS2 population, and only marginally present in the YMS1. The outward motion of binned stars to the south is also observed in the YMS3, RGB, and RC populations, suggesting that this is likely associated with the old bridge of the SMC.

The WA appears prominently in YMS2 but not in YMS1. The more positive values of PM_X observed for WA when compared to the model, are suggestive of a westward motion. There is a marginally higher value for these populations in the PM_Y when compared to the model suggesting a northward motion. A predominantly westward motion of stars present in YMS2 is missing in YMS1. If the gas in these regions is also affected by this motion, then the gas can escape the SMC through the western halo. This could explain the contribution of gas to the Magellanic stream which in turn could explain the absence of stars in YMS1 for values of $X < -1°$ (panel c). Notably, all the anomalies (SEA, EA, SA, and WA) show greater anisotropy in PM_X than in PM_Y, which is a result of the line of interaction with the LMC. Additionally, the variation of PM_X and PM_Y along the Y direction shows similar anomalies.

The morphology of the young SMC, as seen in the SMC plane, appears to be extensively stretched in the east-west direction. This stretching is starting to appear in the YMS3 population and is full-blown in the distribution of YMS2 population. The contrasting distribution of the RC/ RGB (panel a/b) to the YMS2 (panel d) in Figure 5.12 highlights the skewed stellar distribution. The morphological change is suggestive of a stretched distribution of the gas that is formed in the younger populations. We explore the possible connection of this feature with the tidal effects of the LMC-SMC interaction. The eastward motion is likely to be associated with the recent interactions between the LMC and the SMC, as evidenced by the eastward stretch across all populations. Similarly, the westward motion is evident across all populations, but less pronounced in the YMS1. These two interaction signatures, which are acting along the same line, but in opposite directions in the SMC's internal PM suggest that its elongation is a result of the significant tidal stretching, particularly from the recent interaction, as it is most pronounced in YMS2. Moreover, the increased inclination of the younger population has resulted in smaller LOS distances in the eastern part, along with a significant reduction in the extent of the SMC in the north-south direction. All these point to a significant tidal influence from its larger companion. The fact that all anomalies exhibit more deviation in the X-direction of the PM is also suggestive of extensive tidal signatures across the SMC. The tangential anisotropy on the PM of the SMC has previously been observed in the RA direction of the galaxy, which is associated with the tidal disruption of the dwarf galaxy due to the gravitational influence of the LMC (Klimentowski et al. 2007; D18; Hota et al. 2024). Similarly, several studies have reported tidal stripping or stretching of the SMC (Piatti 2021b; N21; El Youssoufi et al. 2023), which aligns with the picture of the SMC emerging from our models. The counter-rotating signature that is identified in this study for the first time is unlikely to be a tidal signature, but a hydrodynamic one probably from the gas-infall in the course of the morphological evolution of the SMC.

This study provides baseline models estimated from the median motion as traced by the majority of stellar populations across the SMC. The anomalies detected in the residual PM of the different stellar populations are likely to be the major outliers as they are shown by the bulk of the population. This study therefore does not detect kinematic and structural outliers that exist in smaller fractions of the population across the SMC. Therefore, we note that the base models derived here will be very helpful in detecting kinematic and structural outlier (minority) populations that exist in the SMC. The unique PM pattern identified in this study can aid numerical simulations to pinpoint the details of the interaction between the MCs. However, the anomalies seen in the residual PM maps of this study need further investigation, such as a 3D model including radial velocity for all populations to fully comprehend the dynamic evolution of the SMC.

5.6 Summary

We summarize the results and conclusions derived from the disk model of the SMC using *Gaia* DR3 data.

- We performed the kinematic model of the SMC using nine different populations to investigate the galaxy's morphology. Eight populations were used to derive a 2D model using PM from *Gaia* DR3 and one was used to derive a 3D model using PM (*Gaia* DR3) and radial velocities. The data coverage of the SMC considered in this study is within $\sim 7^\circ.5$ from the galaxy center.
- The best-fitting kinematic parameters of the SMC were estimated using an MCMC method. The parameters estimated in this study, such as the inclination of the SMC disk (i), the position angle (PA) of the line of nodes measured from West (θ), the amplitude of the tangential velocity of the SMC's COM (v_t), the tangential angle made by v_t (θ_t), scale radius (R_f), the asymptotic velocity (v_f), and the systemic velocity (v_{sys}) show good agreement with estimations in the literature when comparisons are made between similar populations.

- The COM PM for the entire population exhibits minimal variation, except in YMS3, where the southward motion is larger than other populations. This may be a signature of the LMC-SMC interaction $\sim$ 1-2 Gyr ago.
- We estimated the i to range from $\sim 58^\circ$ to 82°, and Θ range from $\sim 180^\circ$ to 240° among the young and old population of the SMC. We observe that i decreases with age, while Θ increases.
- We estimated a v_f of $\sim$ 89 km s^{-1} for YMS1 and 49 km s^{-1} for YMS2, with corresponding R_f of $\sim$ 9 kpc and 6 kpc. A similar trend is observed for CLSY and CLSI. This suggests that both YMS1 and YMS2 show a rotation-supported disk structure for ages less than 400 Myr. In contrast, the older populations (YMS3, RGB, RC, CLSO, and Red Giants) do not exhibit significant rotation and are likely pressure-supported.
- The young MS population (YMS1 and YMS2) shows an elongated structure in the galaxy plane, with a rotational velocity dispersion of $\sim$ 11 km s^{-1}, suggesting a flattened rotating structure for the SMC.
- Our models reveal a larger LOS extension for the SMC reaching up to $\sim$ 30 kpc across the different stellar populations (old and young).
- We identified several anomalies on the residual PM of YMS2, which are the East Anomaly (EA), South East Anomaly (SEA), South Anomaly (SA), and West Anomaly (WA). The SEA identified for the first time is suggestive of an infalling population possibly having a hydrodynamic origin. The SA is likely associated with the old bridge, the EA and WA appear to be of tidal origin.
- This study also brings out the morphological change in the SMC over its evolution. The extensive east-west stretch seen in the young population is likely to be due to the skewed distribution of gas in the SMC resulting from the recent interactions.

- This preferential stretching in the X-direction is also noted in the young stars. The internal rotation of the young population along the X-direction (PM_X) of the SMC exhibits greater tangential anisotropy than in the Y-direction, suggesting that the galaxy is being tidally stretched due to the influence of the LMC.

Chapter 6

Conclusions & Future Work

In this thesis, we analyzed star clusters and various stellar populations within the MCs utilizing data from *Gaia* DR3. Our study involved determining parameters for 1710 clusters in the LMC and 280 clusters in the SMC to map the CFH of these galaxies. Additionally, we modeled the kinematics of the MCs using proper motion for the stellar population in the galaxies. We used star clusters to model the kinematics for the first time. This chapter summarizes the main findings and conclusions of the thesis and outlines several promising directions for future research.

6.1 Evidence for the interaction history of the MCs from cluster age-dating

We parametrized 847 new LMC and 113 new SMC clusters, where the newly parameterized clusters in the LMC are in the outskirts. The age distribution of the clusters obtained in our study in the LMC and SMC traced the peaks of CF from $\sim$ 4 Myr to 3.5 Gyr. The correlated CF peaks are noted in LMC and SMC at $\sim$ 1.5 Gyr, and we believe it is associated with one of the past encounters of the LMC and the SMC. We notice a dip at $\sim$ 1.25 Gyr in CF between the first and second CF peaks in both galaxies. Afterward, there is a bounce back in CF in both galaxies, with a significant peak in both the galaxies at $\sim$ 800 Myr, associated with another interaction between the dwarfs or global instability of their disks. Further, we detect a peak at $\sim$ 150 Myr in the SMC, which is found consistent with the recent LMC-SMC direct collision.

The spatial age map of the star clusters in the MCs was segregated into four age groups in ranges of $\log(t)$, Age group-1: $[\geq 9.10, < 9.55]$, Age group-2: $[\geq 8.65, < 9.10]$, Age group-3: $[\geq 8.0, < 8.65]$, Age group-4: $[\geq 6.55, < 8.0]$. The grouping tracked the age span from old to young clusters in the MCs. Notably, we found the shrinkage of CF of younger clusters towards the central regions of the galaxies. The spatial KDE of the clusters based on age revealed intriguing details about the MCs. In the oldest age group ($\sim$ 1.25 Gyr - 3.5 Gyr) of the LMC, the southern arm of the galaxy is prominently evident, extending towards the central region and further north. In the later age range of $\sim$ 446 Myr to 1.25 Gyr, the cluster density becomes more pronounced in the northern regions, revealing the prominent northern arm of the galaxy. However, the younger age groups (ages $<$ 446 Myr) show radial shrinkage towards the center, and the youngest age group shows active CF towards the central northeast regions. In the younger age groups, the southwest region lacks CF, likely due to ram pressure stripping of the LMC during its current pericentric passage around the MW. In the SMC, a similar shift in cluster density is observed. The tidal interaction between the LMC and SMC is evident as the young bridge or wing of the SMC appears in the youngest age group (ages $<$ 100 Myr), with clusters forming a trail extending toward the eastern region of the SMC.

6.2 Investigating the disk response of the LMC to its interaction with the SMC

We estimated the kinematic parameters for the clusters, field stars, young stars, and RC stars in the LMC. The kinematic properties of the clusters in our sample showed a similar trend as the young stars. The clusters in our sample are mostly young, where 75% of clusters are with ages less than 1 Gyr. The field stars showed kinematics similar to that of the old population, the RC stars. We identified that the clusters have large disk heating compared to the old population. We compared the RMS profiles of the clusters and field population in our study with the models from the simulation of B12, and found the recent LMC-SMC direct collision impact parameter to be within 1 to 5 kpc from the center of the LMC disk.

We modeled the rotation curve for the clusters, field, young stars, and RC population in the LMC. The notable change is in the scale radius (R_0), where younger populations have smaller values compared to older populations, signifying the redistribution of mass within the galaxy during its evolution. Also, we found a disturbance of the LMC disk in the central southwest regions, likely associated with the recent LMC-SMC collision. Several clusters at the site of larger residuals show counterclockwise rotation as well. The inclination of the clusters aged between 100 to 200 Myr and their nearby young stars show distinct and larger values compared to other nearby age groups. The radial variation of the kinematic parameters of the LMC also reveals that the inner disk of the LMC is more inclined towards us than the outer regions. The dynamic centers of the young and old population also show a significant offset in our models, suggesting the tidal interaction/ collision with the SMC affected the LMC, and it is evident in our kinematics of the LMC.

6.3 Exploring the kinematic and morphological evolution of the SMC

In our study, the kinematic model of the SMC revealed rotation signatures for the population younger than 400 Myr, and the older population did not show any significant rotation. The estimated inclination for the younger population shows larger values ($\sim 81^\circ$) and the position angle of the line of node is aligned almost north-south for all the population. The modeled RC and RGB disk has an offset of more than 19° with the YMS1&2. We also estimated the large LOS extension of the SMC disk, even the stretching of the disk in its plane, which is associated with the tidal interaction with the SMC.

We identified several anomalies in the SMC disk across all modeled populations. In the residual PM map of the young population (50 Myr $<$ ages $<$ 400 Myr), we visually detected four distinct anomalies based on significant deviations in the amplitude and direction of the residual vectors. These include the East Anomaly (EA), South East Anomaly (SEA), South Anomaly (SA), and West Anomaly (WA). The SEA has been identified for the first time, likely linked to a hydrodynamic origin, possibly from gas infall contributing to the formation of the SMC's disk structure. The EA is observed across all populations, with the motion of stars from the eastern region toward the SMC's eastern side being associated with the tidal interaction with the LMC. The SA is linked to the SMC's old bridge structure. The WA is observed in both young and old populations, associated with the western halo and the counter-bridge of the SMC. Tangential anisotropy in the rotation velocity is most notable along the RA direction, highlighting the tidal influence of the LMC on the SMC. Our models indicate that while the SMC is undergoing tidal disruption by the LMC, its younger stellar populations are simultaneously attempting to establish a stable, rotation-supported disk structure.

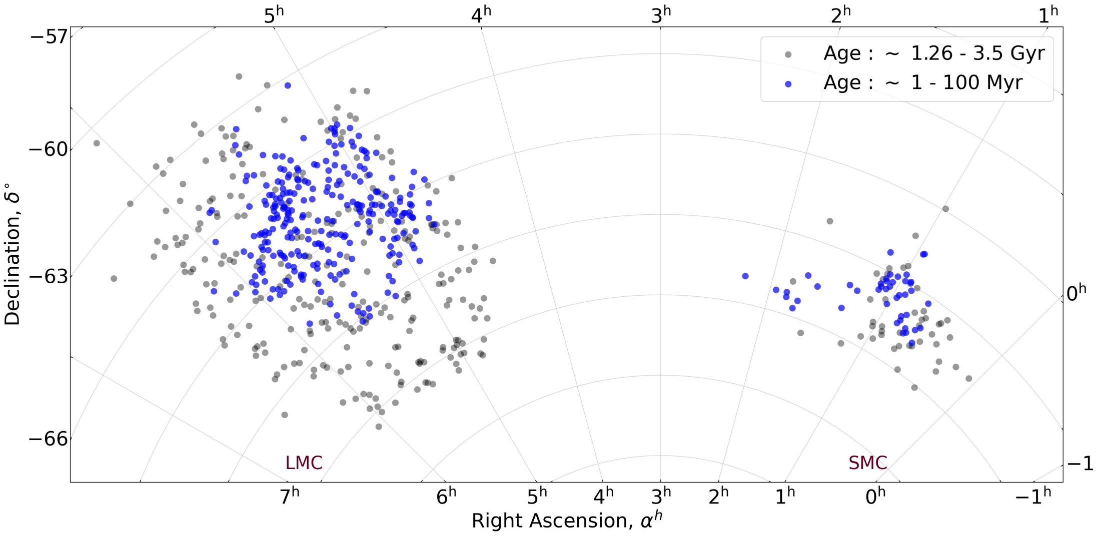

FIGURE 6.1: The spatial maps of the oldest and youngest cluster groups in our study are highlighted. Radial radial shrinkage CF is clearly evident in both MCs. The older clusters are distributed relatively uniformly across the MCs, whereas the younger clusters are concentrated toward the central and northeastern regions in both Clouds.

6.4 Thesis Conclusions

Our thesis explores the history of interaction and the evolutionary details of MCs. The age distribution of clusters in the MCs from our study highlights the triggers of star formation during their mutual interactions. The development of spiral arms, the central bar region, and recent star formation in the northeastern part of the LMC appear to have occurred during different epochs of the Clouds' interaction. Figure 6.1 shows the spatial age map of the oldest and the youngest group of clusters parametrized in our study. The truncation of CF at youngest ages indicates that the LMC, being more massive than the SMC, has been significantly influenced by ram pressure stripping. This process has expelled gas from the LMC's southwestern regions, leading to a concentration of star formation in the central and northeastern regions over the recent epochs, consistent with its closer approach and motion toward the MW.

Figure 6.2 illustrates different perspectives of the modeled disk for the LMC star

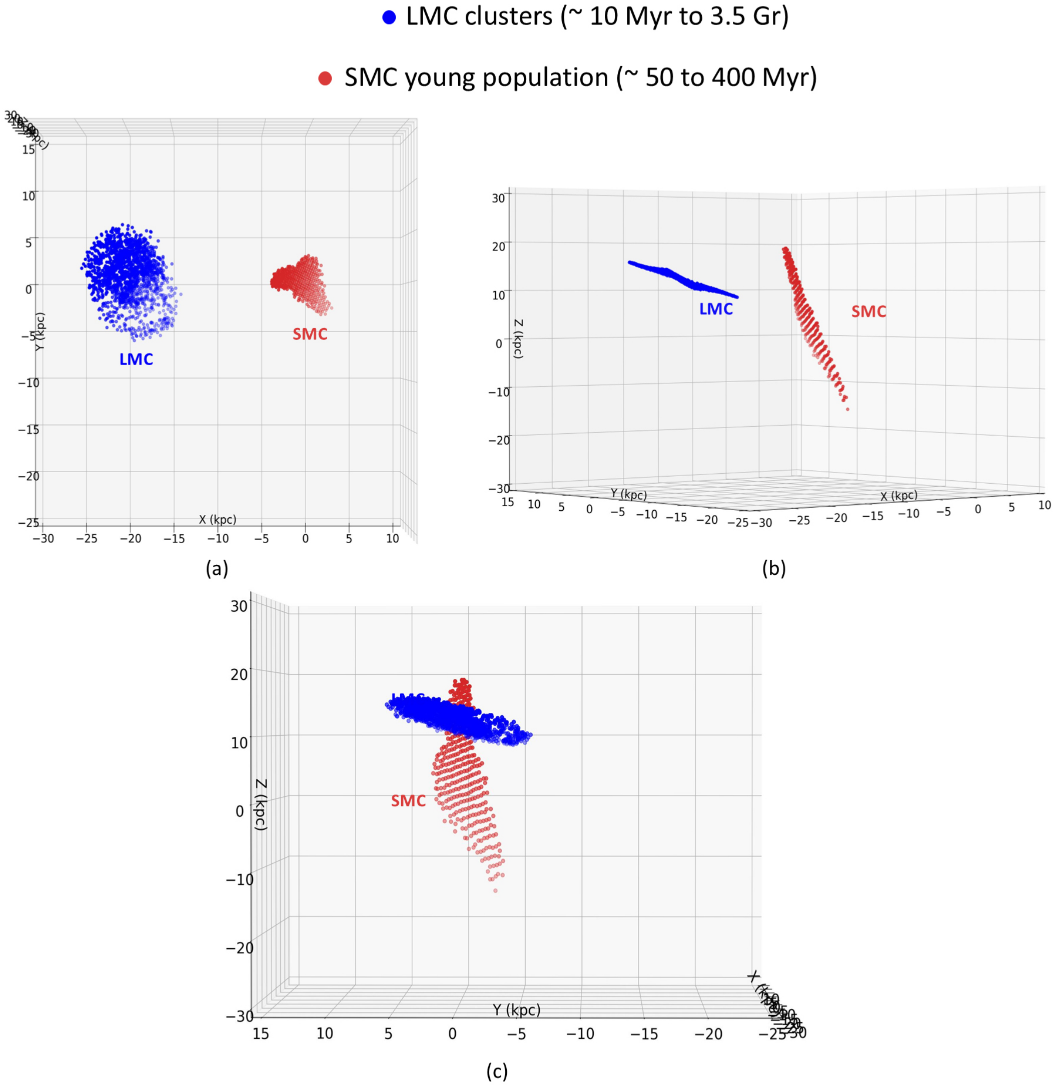

FIGURE 6.2: The disk model obtained for the LMC clusters and SMC YMS2 populations (as provided in Chapters 4 and 5) are shown together with different perspectives, where the SMC center is chosen as the center of reference. The rotation conventions for the perspectives are detailed in section 5.5.3. (a) Sky plane perspective of the LMC and the SMC population, (b) X-Y-Z perspective showing the LOS depth of the SMC: (R_1, R_2) = (90°, 40°), (c) Another X-Y-Z perspective of the MCs: (R_1, R_2) = (90°, 90°)

clusters (spanning $\sim$ 10 Myr to 3.5 Gyr) and the younger stellar population of the SMC (ranging from $\sim$ 50 to 400 Myr), as revealed by our analysis. The skewedness in the spatial distribution of young population in the SMC is already demonstrated in morphology map shown Figure 5.12, hence only the young population is shown in Fig 6.2 to show how it is positioned with respect to the LMC. The sky plane (panel a) and LOS perspectives (panels b, c) are provided to highlight the elongated disk of the SMC. The kinematic analysis of both galaxies indicates that the collision between the MCs had a more significant effect on the SMC than on the LMC. The SMC exhibits pronounced evidence of tidal forces, with its disk being elongated and influenced by the LMC. The probable site of this recent interaction is $\sim$ 2 kpc from the SMC's center, corresponding to a peak in CF around 150 Myr ago. This tidal encounter disrupted the gas in both galaxies, leading to its removal from their main bodies and subsequent ejection into the Magellanic Stream. This is evident from the WA we note for stars in the SMC, and the lack of CF at LMC in the southwest for ages $<$ 200 Myr. The baseline kinematic model of the SMC, developed for the first time in our study, will serve as a critical tool for N-body simulations of the Clouds. Furthermore, the details uncovered about the dwarf-dwarf-host galaxy interactions within the nearby Magellanic system can be used as a template for studying similar processes in extragalactic systems.

6.5 Future Studies

Several future projects we plan to pursue are briefly described below.

- In addition to *Gaia*, we have the SMASH, which is a deep optical sky survey. This survey utilizes the DECam to map 480 square degrees of the sky in ugriz bands at $\sim$ 24 magnitude. The main objective of SMASH is to detect faint, extended stellar populations associated with the halos and tidal remnants of the MCs. Our study involves using an automated method to parameterize the cluster in the MCs. The same methods developed in this study can be used to parameterize the clusters with SMASH as well.

- We plan to study the overlapping clusters in the LOS, as classified in our study (Chapter 3). The ages and metallicities of the clusters will reveal whether they formed together or independently. These overlapping groups of clusters are located in the dense regions of the MCs, making them challenging to study. To parameterize the overlapping clusters, we plan to develop machine learning algorithms and convolutional neural network classifiers to determine the members corresponding to each cluster.

- The gravitational interaction between the MCs causes disturbances in the LMC's bar, and the characteristics of the bar are expected to change depending on the ages of the stellar populations present. The spatially resolved rotational velocity profiles traced by the young and old populations, as derived from our kinematic model of the LMC (Chapter 4), reveal distinct bar morphologies. This suggests that the LMC bar is influenced by the mutual interaction between the MCs. To investigate this further, we plan to apply Fourier decomposition to the rotational velocity map in the galaxy plane of the LMC, to characterize the bar length and strength, and to identify any asymmetries induced by the interaction.

- We plan to conduct N-body simulations based on the disk configurations of the LMC and SMC derived from the kinematic models presented in this thesis. These simulations will allow us to investigate the future evolution of the Clouds and their infall into the MW's halo. Additionally, hydrodynamic simulations will be incorporated to account for the effects of ram pressure stripping and the gas/ material contribution to the Magellanic Stream.

Bibliography

Archinal, B. A., & Hynes, S. J. 2003, Star Clusters

Astropy Collaboration, Robitaille, T. P., Tollerud, E. J., et al. 2013, *Astron. Astrophys.*, 558, A33, doi: 10.1051/0004-6361/201322068

Baade, W. 1944, *Astrophys. J.*, 100, 137, doi: 10.1086/144650

Babusiaux, C., Fabricius, C., Khanna, S., et al. 2023, *Astron. Astrophys.*, 674, A32, doi: 10.1051/0004-6361/202243790

Bekki, K., & Chiba, M. 2005, Monthly Notices of the Royal Astronomical Society, 356, 680, doi: 10.1111/j.1365-2966.2004.08510.x

Belokurov, V., Erkal, D., Deason, A. J., et al. 2017, *Mon. Not. Roy. Astron. Soc.*, 466, 4711, doi: 10.1093/mnras/stw3357

Besla, G., Kallivayalil, N., Hernquist, L., et al. 2007, The Astrophysical Journal, 668, 949, doi: 10.1086/521385

Besla, G., Kallivayalil, N., Hernquist, L., et al. 2010, *Astrophys. J. Lett.*, 721, L97, doi: 10.1088/2041-8205/721/2/L97

—. 2012, *Mon. Not. Roy. Astron. Soc.*, 421, 2109, doi: 10.1111/j.1365-2966.2012.20466.x

Besla, G., Martínez-Delgado, D., van der Marel, R. P., et al. 2016, *Astrophys. J.*, 825, 20, doi: 10.3847/0004-637X/825/1/20

Bica, E., Bonatto, C., Dutra, C. M., & Santos, J. F. C. 2008, *Mon. Not. Roy. Astron. Soc.*, 389, 678, doi: 10.1111/j.1365-2966.2008.13612.x

Bica, E., Maia, F. F. S., Oliveira, R. A. P., et al. 2022, *Mon. Not. Roy. Astron. Soc.*, 517, L41, doi: 10.1093/mnrasl/slac108

Bland-Hawthorn, J., & Gerhard, O. 2016, *Ann. Rev. Astron. Astrophys.*, 54, 529, doi: 10.1146/annurev-astro-081915-023441

Bressan, A., Marigo, P., Girardi, L., et al. 2012, *Mon. Not. Roy. Astron. Soc.*, 427, 127, doi: 10.1111/j.1365-2966.2012.21948.x

Cantat-Gaudin, T., Jordi, C., Vallenari, A., et al. 2018, *Astron. Astrophys.*, 618, A93, doi: 10.1051/0004-6361/201833476

Cantat-Gaudin, T., Anders, F., Castro-Ginard, A., et al. 2020, *Astron. Astrophys.*, 640, A1, doi: 10.1051/0004-6361/202038192

Carrera, R., Gallart, C., Aparicio, A., & Hardy, E. 2011, *Astron. J.*, 142, 61, doi: 10.1088/0004-6256/142/2/61

Castro-Ginard, A., Jordi, C., Luri, X., et al. 2020, *Astron. Astrophys.*, 635, A45, doi: 10.1051/0004-6361/201937386

Chiosi, E., Vallenari, A., Held, E. V., Rizzi, L., & Moretti, A. 2006, VizieR Online Data Catalog, J/A+A/452/179

Choi, Y., Olsen, K. A. G., Besla, G., et al. 2022, *Astrophys. J.*, 927, 153, doi: 10.3847/1538-4357/ac4e90

Choi, Y., Nidever, D. L., Olsen, K., et al. 2018, *Astrophys. J.*, 866, 90, doi: 10.3847/1538-4357/aae083

Choi, Y., Nidever, D. L., Olsen, K., et al. 2018, The Astrophysical Journal, 869, 125, doi: 10.3847/1538-4357/aaed1f

Choudhury, S., Subramaniam, A., & Cole, A. A. 2016, *Mon. Not. Roy. Astron. Soc.*, 455, 1855, doi: 10.1093/mnras/stv2414

Choudhury, S., Subramaniam, A., Cole, A. A., & Sohn, Y. J. 2018, *Mon. Not. Roy. Astron. Soc.*, 475, 4279, doi: 10.1093/mnras/sty087

Choudhury, S., Subramaniam, A., & Piatti, A. E. 2015, The Astronomical Journal, 149, 52, doi: 10.1088/0004-6256/149/2/52

Choudhury, S., Subramaniam, A., & Piatti, A. E. 2015, *Astron. J.*, 149, 52, doi: 10.1088/0004-6256/149/2/52

Cioni, M. R. L., Habing, H. J., & Israel, F. P. 2000, *Astron. Astrophys.*, 358, L9, doi: 10.48550/arXiv.astro-ph/0005057

Cioni, M. R. L., Clementini, G., Girardi, L., et al. 2011, *Astron. Astrophys.*, 527, A116, doi: 10.1051/0004-6361/201016137

Costa, E., Méndez, R. A., Pedreros, M. H., et al. 2011, The Astronomical Journal, 141, 136, doi: 10.1088/0004-6256/141/4/136

Craig, P., Chakrabarti, S., Baum, S., & Lewis, B. T. 2021, arXiv e-prints, arXiv:2107.09791, doi: 10.48550/arXiv.2107.09791

Cullinane, L., Mackey, A., Costa, G., et al. 2022, Monthly Notices of the Royal Astronomical Society, 510, 445, doi: 10.1093/mnras/stab3350

Cullinane, L. R., Mackey, A. D., Da Costa, G. S., Koposov, S. E., & Erkal, D. 2023, *Mon. Not. Roy. Astron. Soc.*, 518, L25, doi: 10.1093/mnrasl/slac129

D'Antona, F., Caloi, V., & Tailo, M. 2018, Nature Astronomy, 2, 270, doi: 10.1038/s41550-018-0408-1

de Boer, K., & Seggewiss, W. 2008, Stars and Stellar Evolution

de Vaucouleurs, G., & Freeman, K. C. 1972a, Vistas in Astronomy, 14, 163, doi: 10.1016/0083-6656(72)90026-8

—. 1972b, Vistas in Astronomy, 14, 163, doi: 10.1016/0083-6656(72)90026-8

Deb, S., Kurbah, K., Singh, H. P., et al. 2019, *Mon. Not. Roy. Astron. Soc.*, 489, 3725, doi: 10.1093/mnras/stz2328

Deb, S., Singh, H. P., Kumar, S., & Kanbur, S. M. 2015, Monthly Notices of the Royal Astronomical Society, 449, 2768, doi: 10.1093/mnras/stv358

De Leo, M., Carrera, R., Noël, N. E. D., et al. 2020, Monthly Notices of the Royal Astronomical Society, 495, 98, doi: 10.1093/mnras/staa1122

Dhanush, S. R., Subramaniam, A., Nayak, P. K., & Subramanian, S. 2024a, Monthly Notices of the Royal Astronomical Society, stae096, doi: 10.1093/mnras/stae096

Dhanush, S. R., Subramaniam, A., & Subramanian, S. 2024b, The Astrophysical Journal, 968, 103, doi: 10.3847/1538-4357/ad4453

—. 2025, The Astrophysical Journal, 980, 73, doi: 10.3847/1538-4357/ada55f

Dias, B., Kerber, L., Barbuy, B., Bica, E., & Ortolani, S. 2016, *Astron. Astrophys.*, 591, A11, doi: 10.1051/0004-6361/201527558

Dias, B., Angelo, M. S., Oliveira, R. A. P., et al. 2021, *Astron. Astrophys.*, 647, L9, doi: 10.1051/0004-6361/202040015

Dias, B., Parisi, M. C., Angelo, M., et al. 2022a, *Mon. Not. Roy. Astron. Soc.*, 512, 4334, doi: 10.1093/mnras/stac259

—. 2022b, *Mon. Not. Roy. Astron. Soc.*, 512, 4334, doi: 10.1093/mnras/stac259

Diaz, J. D., & Bekki, K. 2012, *Astrophys. J.*, 750, 36, doi: 10.1088/0004-637X/750/1/36

Di Teodoro, E. M., McClure-Griffiths, N. M., Jameson, K. E., et al. 2018, Monthly Notices of the Royal Astronomical Society, 483, 392, doi: 10.1093/mnras/sty3095

Dobbie, P. D., Cole, A. A., Subramaniam, A., & Keller, S. 2014, *Mon. Not. Roy. Astron. Soc.*, 442, 1663, doi: `10.1093/mnras/stu910`

Donor, J., Frinchaboy, P. M., Cunha, K., et al. 2020, *Astron. J.*, 159, 199, doi: `10.3847/1538-3881/ab77bc`

El Youssoufi, D., Cioni, M.-R. L., Bell, C. P. M., et al. 2019, *Mon. Not. Roy. Astron. Soc.*, 490, 1076, doi: `10.1093/mnras/stz2400`

El Youssoufi, D., Cioni, M.-R. L., Kacharov, N., et al. 2023, *Mon. Not. Roy. Astron. Soc.*, 523, 347, doi: `10.1093/mnras/stad1339`

Ettorre, G., Mazzi, A., Girardi, L., et al. 2025, *Mon. Not. Roy. Astron. Soc.*, 539, 2537, doi: `10.1093/mnras/staf591`

Forbes, D. A., Read, J. I., Gieles, M., & Collins, M. L. M. 2018, *Mon. Not. Roy. Astron. Soc.*, 481, 5592, doi: `10.1093/mnras/sty2584`

Foreman-Mackey, D. 2017, corner.py: Corner plots, Astrophysics Source Code Library, record ascl:1702.002

Gaia Collaboration, Prusti, T., de Bruijne, J. H. J., et al. 2016, *Astron. Astrophys.*, 595, A1, doi: `10.1051/0004-6361/201629272`

Gaia Collaboration, Helmi, A., van Leeuwen, F., et al. 2018, *Astron. Astrophys.*, 616, A12, doi: `10.1051/0004-6361/201832698`

Gaia Collaboration, Luri, X., Chemin, L., et al. 2021, *Astron. Astrophys.*, 649, A7, doi: `10.1051/0004-6361/202039588`

Gaia Collaboration, Vallenari, A., Brown, A. G. A., et al. 2023a, *Astron. Astrophys.*, 674, A1, doi: `10.1051/0004-6361/202243940`

Gaia Collaboration, Arenou, F., Babusiaux, C., et al. 2023b, *Astron. Astrophys.*, 674, A34, doi: `10.1051/0004-6361/202243782`

Gardiner, L. T., & Hawkins, M. R. S. 1991, *Mon. Not. Roy. Astron. Soc.*, 251, 174, doi: 10.1093/mnras/251.1.174

Gardiner, L. T., Sawa, T., & Fujimoto, M. 1994, Monthly Notices of the Royal Astronomical Society, 266, 567, doi: 10.1093/mnras/266.3.567

Gerola, H., & Seiden, P. E. 1978, *Astrophys. J.*, 223, 129, doi: 10.1086/156243

Ginsburg, A., Sipőcz, B. M., Brasseur, C. E., et al. 2019, *Astron. J.*, 157, 98, doi: 10.3847/1538-3881/aafc33

Girardi, L. 2016, *Ann. Rev. Astron. Astrophys.*, 54, 95, doi: 10.1146/annurev-astro-081915-023354

Girardi, L., & Salaris, M. 2001, *Mon. Not. Roy. Astron. Soc.*, 323, 109, doi: 10.1046/j.1365-8711.2001.04084.x

Glatt, K., Grebel, E. K., & Koch, A. 2010, *Astron. Astrophys.*, 517, A50, doi: 10.1051/0004-6361/20101418710.48550/arXiv.1004.1247

Goodman, J., & Weare, J. 2010, Communications in Applied Mathematics and Computational Science, 5, 65, doi: 10.2140/camcos.2010.5.65

Gordon, K. D., Clayton, G. C., Misselt, K. A., Landolt, A. U., & Wolff, M. J. 2003, *Astrophys. J.*, 594, 279, doi: 10.1086/376774

Graczyk, D., Pietrzyński, G., Thompson, I. B., et al. 2020, *Astrophys. J.*, 904, 13, doi: 10.3847/1538-4357/abbb2b

Hammer, F., Yang, Y. B., Flores, H., Puech, M., & Fouquet, S. 2015, The Astrophysical Journal, 813, 110, doi: 10.1088/0004-637X/813/2/110

Harris, C. R., Millman, K. J., van der Walt, S. J., et al. 2020, *Nature*, 585, 357, doi: 10.1038/s41586-020-2649-2

Harris, J., & Zaritsky, D. 2004, *Astron. J.*, 127, 1531, doi: 10.1086/381953

Harris, J., & Zaritsky, D. 2004, The Astronomical Journal, 127, 1531, doi: 10.1086/381953

—. 2009, The Astronomical Journal, 138, 1243, doi: 10.1088/0004-6256/138/5/1243

Harris, J., & Zaritsky, D. 2009, *Astron. J.*, 138, 1243, doi: 10.1088/0004-6256/138/5/1243

Harris, W. E. 2010, arXiv e-prints, arXiv:1012.3224, doi: 10.48550/arXiv.1012.3224

Haschke, R., Grebel, E. K., & Duffau, S. 2012, *Astron. J.*, 144, 107, doi: 10.1088/0004-6256/144/4/107

Hidalgo, S. L., Aparicio, A., Skillman, E., et al. 2011, *Astrophys. J.*, 730, 14, doi: 10.1088/0004-637X/730/1/14

Holtzman, J. A., Gallagher, III, J. S., Cole, A. A., et al. 1999, *Astron. J.*, 118, 2262, doi: 10.1086/301097

Hota, S., Subramaniam, A., Nayak, P. K., & Subramanian, S. 2024, UVIT Study of the MAgellanic Clouds (U-SMAC) II. A Far-UV catalog of the Small Magellanic Cloud: Morphology and Kinematics of young stellar population. https://arxiv.org/abs/2409.13605

Hunt, E. L., & Reffert, S. 2021, *Astron. Astrophys.*, 646, A104, doi: 10.1051/0004-6361/202039341

—. 2023, *Astron. Astrophys.*, 673, A114, doi: 10.1051/0004-6361/202346285

—. 2024, *Astron. Astrophys.*, 686, A42, doi: 10.1051/0004-6361/202348662

Hunter, J. D. 2007, Computing in Science and Engineering, 9, 90, doi: 10.1109/MCSE.2007.55

Iben, Jr., I. 1991, *Astrophys. J. Suppl.*, 76, 55, doi: 10.1086/191565

Indu, G., & Subramaniam, A. 2011, *Astron. Astrophys.*, 535, A115, doi: 10.1051/0004-6361/201117298

—. 2015, *Astron. Astrophys.*, 573, A136, doi: 10.1051/0004-6361/201321133

Jacyszyn-Dobrzeniecka, A. M., Skowron, D. M., Mróz, P., et al. 2016, *Acta Astronomica, 66, 149, doi: 10.48550/arXiv.1602.09141*

—. 2017, Acta Astronomica, 67, 1, doi: 10.32023/0001-5237/67.1.1

Jacyszyn-Dobrzeniecka, A. M., Mróz, P., Kruszyńska, K., et al. 2020, The Astrophysical Journal, 889, 26, doi: 10.3847/1538-4357/ab61f2

Jiménez-Arranz, Ó., Romero-Gómez, M., Luri, X., & Masana, E. 2023a, Astron. Astrophys., 672, A65, doi: 10.1051/0004-6361/202245720

Jiménez-Arranz, Ó., Romero-Gómez, M., Luri, X., et al. 2023b, Astron. Astrophys., 669, A91, doi: 10.1051/0004-6361/202244601

Kalirai, J. S., & Richer, H. B. 2010, Philosophical Transactions of the Royal Society of London Series A, 368, 755, doi: 10.1098/rsta.2009.0257

Kallivayalil, N., van der Marel, R. P., & Alcock, C. 2006, Astrophys. J., 652, 1213, doi: 10.1086/508014

Kallivayalil, N., van der Marel, R. P., Besla, G., Anderson, J., & Alcock, C. 2013, The Astrophysical Journal, 764, 161, doi: 10.1088/0004-637X/764/2/161

Kelley, L. Z. 2021, The Journal of Open Source Software

Kim, S., Staveley-Smith, L., Dopita, M. A., et al. 1998, Astrophys. J., 503, 674, doi: 10.1086/306030

Kippenhahn, R., & Weigert, A. 1990, Stellar Structure and Evolution

Kippenhahn, R., Weigert, A., & Weiss, A. 2013, Stellar Structure and Evolution, doi: 10.1007/978-3-642-30304-3

Klimentowski, J., Łokas, E. L., Kazantzidis, S., et al. 2007, Monthly Notices of the Royal Astronomical Society, 378, 353, doi: 10.1111/j.1365-2966.2007.11799.x

Kruijssen, J. M. D., Dale, J. E., & Longmore, S. N. 2015, Mon. Not. Roy. Astron. Soc., 447, 1059, doi: 10.1093/mnras/stu2526

Krumholz, M. R., McKee, C. F., & Bland-Hawthorn, J. 2019, Ann. Rev. Astron. Astrophys., 57, 227, doi: 10.1146/annurev-astro-091918-104430

Kuhn, M. A., Hillenbrand, L. A., Sills, A., Feigelson, E. D., & Getman, K. V. 2019, Astrophys. J., 870, 32, doi: 10.3847/1538-4357/aaef8c

Lam, S. K., Pitrou, A., & Seibert, S. 2015, in Proceedings of the Second Workshop on the LLVM Compiler Infrastructure in HPC, 1–6

Lee, J. C., Whitmore, B. C., Thilker, D. A., et al. 2022, The Astrophysical Journal Supplement Series, 258, 10, doi: 10.3847/1538-4365/ac1fe5

Lindegren, L., Hernández, J., Bombrun, A., et al. 2018, Astron. Astrophys., 616, A2, doi: 10.1051/0004-6361/201832727

Lindegren, L., Klioner, S. A., Hernández, J., et al. 2021, Astron. Astrophys., 649, A2, doi: 10.1051/0004-6361/202039709

Lucchini, S. 2024, Astrophys. Space Sci., 369, 114, doi: 10.1007/s10509-024-04377-5

Lucchini, S., D'Onghia, E., Fox, A. J., et al. 2020, Nature, 585, 203, doi: 10.1038/s41586-020-2663-4

Lucchini, S., D'Onghia, E., & Fox, A. J. 2021, The Astrophysical Journal Letters, 921, L36, doi: 10.3847/2041-8213/ac3338

Mackey, A. D., Koposov, S. E., Erkal, D., et al. 2016, Monthly Notices of the Royal Astronomical Society, 459, 239, doi: 10.1093/mnras/stw497

Massana, P., Ruiz-Lara, T., Noël, N. E. D., et al. 2022, Mon. Not. Roy. Astron. Soc., 513, L40, doi: 10.1093/mnrasl/slac030

Massari, D., Koppelman, H. H., & Helmi, A. 2019, Astron. Astrophys., 630, L4, doi: 10.1051/0004-6361/201936135

Mazzi, A., Girardi, L., Zaggia, S., et al. 2021, Mon. Not. Roy. Astron. Soc., 508, 245, doi: 10.1093/mnras/stab2399

McClure-Griffiths, N. M., Pisano, D. J., Calabretta, M. R., et al. 2009, Astrophys. J. Suppl., 181, 398, doi: 10.1088/0067-0049/181/2/398

Meschin, I., Gallart, C., Aparicio, A., et al. 2014, Mon. Not. Roy. Astron. Soc., 438, 1067, doi: 10.1093/mnras/stt2220

Milone, A. P., Bedin, L. R., Piotto, G., & Anderson, J. 2009, Astron. Astrophys., 497, 755, doi: 10.1051/0004-6361/200810870

Milone, A. P., Cordoni, G., Marino, A. F., et al. 2023, Astron. Astrophys., 672, A161, doi: 10.1051/0004-6361/202244798

Misawa, T., Charlton, J. C., Kobulnicky, H. A., Wakker, B. P., & Bland-Hawthorn, J. 2009, The Astrophysical Journal, 695, 1382, doi: 10.1088/0004-637X/695/2/1382

Muller, E., & Bekki, K. 2007, Monthly Notices of the Royal Astronomical Society: Letters, 381, L11, doi: 10.1111/j.1745-3933.2007.00356.x

Muraveva, T., Subramanian, S., Clementini, G., et al. 2017, Monthly Notices of the Royal Astronomical Society, 473, 3131, doi: 10.1093/mnras/stx2514

Myeong, G. C., Vasiliev, E., Iorio, G., Evans, N. W., & Belokurov, V. 2019, Mon. Not. Roy. Astron. Soc., 488, 1235, doi: 10.1093/mnras/stz1770

Myers, N., Donor, J., Spoo, T., et al. 2022, Astron. J., 164, 85, doi: 10.3847/1538-3881/ac7ce5

Nayak, P. K., Subramaniam, A., Choudhury, S., Indu, G., & Sagar, R. 2016, Mon. Not. Roy. Astron. Soc., 463, 1446, doi: `10.1093/mnras/stw2043`

Nayak, P. K., Subramaniam, A., Choudhury, S., & Sagar, R. 2018, Astron. Astrophys., 616, A187, doi: `10.1051/0004-6361/201732227`

Nidever, D. L., Majewski, S. R., & Butler Burton, W. 2008, Astrophys. J., 679, 432, doi: `10.1086/587042`

Niederhofer, F., Cioni, M. R. L., Rubele, S., et al. 2018, Astron. Astrophys., 613, L8, doi: `10.1051/0004-6361/201833144`

Niederhofer, F., Cioni, M.-R. L., Rubele, S., et al. 2021, Monthly Notices of the Royal Astronomical Society, 502, 2859, doi: `10.1093/mnras/stab206`

Niederhofer, F., Cioni, M.-R. L., Schmidt, T., et al. 2022, Mon. Not. Roy. Astron. Soc., 512, 5423, doi: `10.1093/mnras/stac712`

O'Donnell, J. E. 1994, Astrophys. J., 422, 158, doi: `10.1086/173713`

Oliveira, R. A. P., Maia, F. F. S., Barbuy, B., et al. 2023, Mon. Not. Roy. Astron. Soc., 524, 2244, doi: `10.1093/mnras/stad1827`

Palma, T., Gramajo, L. V., Clariá, J. J., et al. 2016, Astron. Astrophys., 586, A41, doi: `10.1051/0004-6361/201527305`

Pandey, A. K., Sharma, S., Upadhyay, K., et al. 2007, Pub. Astron. Soc. Japan, 59, 547, doi: `10.1093/pasj/59.3.547`

Peng, C. Y., Impey, C. D., Rix, H.-W., et al. 2006, Astrophys. J., 649, 616, doi: `10.1086/506266`

Piatti, A. E. 2021, Monthly Notices of the Royal Astronomical Society, 509, 3462, doi: `10.1093/mnras/stab3190`

Piatti, A. E. 2021, Astron. Astrophys., 650, A52, doi: `10.1051/0004-6361/202140643`

Piatti, A. E., Cole, A. A., & Emptage, B. 2018, Mon. Not. Roy. Astron. Soc., 473, 105, doi: `10.1093/mnras/stx241810.48550/arXiv.1709.05244`

Pietrzynski, G., & Udalski, A. 1999, Acta Astronomica, 49, 157, doi: `10.48550/arXiv.astro-ph/9906339`

—. 2000, Acta Astronomica, 50, 337, doi: `10.48550/arXiv.astro-ph/0010360`

Pietrzyński, G., Graczyk, D., Gallenne, A., et al. 2019, Nature, 567, 200, doi: `10.1038/s41586-019-0999-4`

Pontoppidan, K. M., Barrientes, J., Blome, C., et al. 2022, Astrophys. J. Lett., 936, L14, doi: `10.3847/2041-8213/ac8a4e`

Prialnik, D. 2009, An Introduction to the Theory of Stellar Structure and Evolution

Putman, M. E., Staveley-Smith, L., Freeman, K. C., Gibson, B. K., & Barnes, D. G. 2003, Astrophys. J., 586, 170, doi: `10.1086/344477`

Putman, M. E., Gibson, B. K., Staveley-Smith, L., et al. 1998, Nature, 394, 752, doi: `10.1038/29466`

Rathore, H., Choi, Y., Olsen, K. A. G., & Besla, G. 2025, Astrophys. J., 978, 55, doi: `10.3847/1538-4357/ad93ae`

Rezaeikh, S., Javadi, A., Khosroshahi, H., & van Loon, J. T. 2014, Mon. Not. Roy. Astron. Soc., 445, 2214, doi: `10.1093/mnras/stu1807`

Riello, M., De Angeli, F., Evans, D. W., et al. 2021, Astron. Astrophys., 649, A3, doi: `10.1051/0004-6361/202039587`

Ripepi, V., Cioni, M.-R. L., Moretti, M. I., et al. 2017, Monthly Notices of the Royal Astronomical Society, 472, 808, doi: `10.1093/mnras/stx2096`

Ripepi, V., Chemin, L., Molinaro, R., et al. 2022, Mon. Not. Roy. Astron. Soc., 512, 563, doi: `10.1093/mnras/stac595`

Rodríguez, M. J., Feinstein, C., Baume, G., et al. 2022, Monthly Notices of the Royal Astronomical Society, 519, 3357, doi: `10.1093/mnras/stac3806`

Rubele, S., Kerber, L., Girardi, L., et al. 2012, Astron. Astrophys., 537, A106, doi: `10.1051/0004-6361/201117863`

Rubele, S., Pastorelli, G., Girardi, L., et al. 2018, Mon. Not. Roy. Astron. Soc., 478, 5017, doi: `10.1093/mnras/sty1279`

Ruiz-Lara, T., Gallart, C., Monelli, M., et al. 2020, Astron. Astrophys., 639, L3, doi: `10.1051/0004-6361/202038392`

Rusakov, V., Monelli, M., Gallart, C., et al. 2021, Monthly Notices of the Royal Astronomical Society, 502, 642, doi: `10.1093/mnras/stab006`

Saha, A., Olszewski, E. W., Brondel, B., et al. 2010, Astron. J., 140, 1719, doi: `10.1088/0004-6256/140/6/1719`

Salaris, M., & Girardi, L. 2002, Mon. Not. Roy. Astron. Soc., 337, 332, doi: `10.1046/j.1365-8711.2002.05917.x`

Salem, M., Besla, G., Bryan, G., et al. 2015, Astrophys. J., 815, 77, doi: `10.1088/0004-637X/815/1/77`

Salpeter, E. E. 1955, Astrophys. J., 121, 161, doi: `10.1086/145971`

Saroon, S., & Subramanian, S. 2022, Astron. Astrophys., 666, A103, doi: `10.1051/0004-6361/202141435`

Silva-Villa, E., Adamo, A., Bastian, N., Fouesneau, M., & Zackrisson, E. 2014, Mon. Not. Roy. Astron. Soc., 440, L116, doi: `10.1093/mnrasl/slu028`

Sitek, M., Szymański, M. K., Skowron, D. M., et al. 2016, Acta Astronomica, 66, 255, doi: `10.48550/arXiv.1609.08175`

Sitek, M., Szymański, M. K., Udalski, A., et al. 2017, Acta Astronomica, 67, 363, doi: `10.32023/0001-5237/67.4.5`

Skowron, D. M., Skowron, J., Udalski, A., et al. 2021, The Astrophysical Journal Supplement Series, 252, 23, doi: 10.3847/1538-4365/abcb81

Soszyński, I., Dziembowski, W. A., Udalski, A., et al. 2011, Acta Astronomica, 61, 1, doi: 10.48550/arXiv.1105.6126

Souza, S. O., Kerber, L. O., Barbuy, B., et al. 2020, The Astrophysical Journal, 890, 38, doi: 10.3847/1538-4357/ab6a0f

Spano, M., Mowlavi, N., Eyer, L., et al. 2011, Astron. Astrophys., 536, A60, doi: 10.1051/0004-6361/201117302

Stanek, K. Z., & Garnavich, P. M. 1998, in American Astronomical Society Meeting Abstracts, Vol. 193, American Astronomical Society Meeting Abstracts, 106.05

Stanimirović, S., Staveley-Smith, L., & Jones, P. A. 2004, Astrophys. J., 604, 176, doi: 10.1086/381869

Subramaniam, A. 2003, The Astrophysical Journal, 598, L19, doi: 10.1086/380556

Subramaniam, A. 2004, Astron. Astrophys., 425, 837, doi: 10.1051/0004-6361:20047006

—. 2005, Astron. Astrophys., 430, 421, doi: 10.1051/0004-6361:20041279

Subramaniam, A., Gorti, U., Sagar, R., & Bhatt, H. C. 1995, Astron. Astrophys., 302, 86

Subramaniam, A., & Sagar, R. 1999, The Astronomical Journal, 117, 937, doi: 10.1086/300716

Subramaniam, A., & Subramanian, S. 2009, Astrophys. J. Lett., 703, L37, doi: 10.1088/0004-637X/703/1/L37

Subramanian, S., & Subramaniam, A. 2009, Astron. Astrophys., 496, 399, doi: `10.1051/0004-6361/200811029`

Subramanian, S., & Subramaniam, A. 2011, The Astrophysical Journal, 744, 128, doi: `10.1088/0004-637X/744/2/128`

Subramanian, S., & Subramaniam, A. 2013, in Astronomical Society of India Conference Series, Vol. 9, Astronomical Society of India Conference Series, 63–66

Subramanian, S., & Subramaniam, A. 2015, Astron. Astrophys., 573, A135, doi: `10.1051/0004-6361/201424248`

Sun, N.-C., de Grijs, R., Cioni, M.-R. L., et al. 2018, Astrophys. J., 858, 31, doi: `10.3847/1538-4357/aabc50`

Tatton, B. L., van Loon, J. T., Cioni, M. R. L., et al. 2021, Mon. Not. Roy. Astron. Soc., 504, 2983, doi: `10.1093/mnras/staa3857`

Taylor, M. 2011, TOPCAT: Tool for OPerations on Catalogues And Tables, Astrophysics Source Code Library, record ascl:1101.010

Usher, C., Caldwell, N., & Cabrera-Ziri, I. 2024, Mon. Not. Roy. Astron. Soc., 528, 6010, doi: `10.1093/mnras/stae282`

van der Marel, R. P. 2001, Astron. J., 122, 1827, doi: `10.1086/323100`

van der Marel, R. P., Alves, D. R., Hardy, E., & Suntzeff, N. B. 2002, Astron. J., 124, 2639, doi: `10.1086/343775`

van der Marel, R. P., & Kallivayalil, N. 2013, The Astrophysical Journal, 781, 121, doi: `10.1088/0004-637X/781/2/121`

van der Marel, R. P., & Kallivayalil, N. 2014, Astrophys. J., 781, 121, doi: `10.1088/0004-637X/781/2/121` van der Marel, R. P., & Sahlmann, J. 2016, The Astrophysical Journal Letters, 832, L23, doi: 10.3847/2041-8205/832/2/L23

Vasiliev, E. 2019, Mon. Not. Roy. Astron. Soc., 484, 2832, doi: 10.1093/mnras/stz171

Vasiliev, E. 2023, Monthly Notices of the Royal Astronomical Society, stad2612, doi: 10.1093/mnras/stad2612

Virtanen, P., Gommers, R., Oliphant, T. E., et al. 2020, Nature Methods, 17, 261, doi: 10.1038/s41592-019-0686-2

Wan, Z., Guglielmo, M., Lewis, G. F., Mackey, D., & Ibata, R. A. 2020, Mon. Not. Roy. Astron. Soc., 492, 782, doi: 10.1093/mnras/stz3493

Westerlund, B. E. 1997, The Magellanic Clouds

Whitmore, B. C., Lee, J. C., Chandar, R., et al. 2021, Mon. Not. Roy. Astron. Soc., 506, 5294, doi: 10.1093/mnras/stab2087

Yang, Y., Hammer, F., Fouquet, S., et al. 2014, Mon. Not. Roy. Astron. Soc., 442, 2419, doi: 10.1093/mnras/stu931

Yoshizawa, A. M., & Noguchi, M. 2003, Monthly Notices of the Royal Astronomical Society, 339, 1135, doi: 10.1046/j.1365-8711.2003.06263.x

Yozin, C., & Bekki, K. 2014, Monthly Notices of the Royal Astronomical Society, 443, 522, doi: 10.1093/mnras/stu1132

Zaritsky, D. 2004, Astrophys. J. Lett., 614, L37, doi: 10.1086/425312

Zaritsky, D., Harris, J., Grebel, E. K., & Thompson, I. B. 2000, Astrophys. J. Lett., 534, L53, doi: 10.1086/312649

Zaritsky, D., Harris, J., & Thompson, I. 1997, Astron. J., 114, 1002, doi: 10.1086/118531

Zaritsky, D., Harris, J., Thompson, I. B., & Grebel, E. K. 2004, Astron. J., 128, 1606, doi: `10.1086/423910`

Zivick, P., Kallivayalil, N., & van der Marel, R. P. 2021, The Astrophysical Journal, 910, 36, doi: `10.3847/1538-4357/abe1bb`

Zivick, P., Kallivayalil, N., van der Marel, R. P., et al. 2018, Astrophys. J., 864, 55, doi: `10.3847/1538-4357/aad4b0`

Zivick, P., Kallivayalil, N., van der Marel, R. P., et al. 2018, The Astrophysical Journal, 864, 55, doi: `10.3847/1538-4357/aad4b0`